

<https://doi.org/10.15388/vu.thesis.729>

<https://orcid.org/0000-0003-2248-5195>

VILNIUS UNIVERSITY

CENTER FOR PHYSICAL SCIENCES AND TECHNOLOGY

Augustinas Petrulėnas

# Femtosecond Pulse Generation in the 1.1 – 3 $\mu\text{m}$ Range by Parametric and Stimulated Raman Amplification of Supercontinuum

**DOCTORAL DISSERTATION**

Natural Sciences,  
Physics (N 002)

VILNIUS 2025

The dissertation was prepared between 2020 and 2024 at the Laser Technologies department of the Center for Physical Sciences and Technology in the Solid State Laser laboratory. The research was supported by the Research Council of Lithuania and The North Atlantic Treaty Organization (NATO).

**Academic Supervisor** – Dr. Aleksėj M. Rodin (Center for Physical Sciences and Technology, Natural Sciences, Physics, N 002).

This doctoral dissertation will be defended at a public meeting of the Dissertation Defense Panel:

**Chairman** – Dr. Arūnas Varanavičius (Vilnius University, Natural Sciences, Physics, N 002).

**Members:**

Dr. Roman Antipenkov (ELI Beamlines Facility, Czech Republic, Natural Sciences, Physics, N 002),

Prof. Dr. Arkady Major (University of Manitoba, Canada, Natural Sciences, Physics, N 002),

Dr. Kęstutis Regelskis (Center for Physical Sciences and Technology, Natural Sciences, Physics, N 002),

Assoc. Prof. Dr. Julius Vengelis (Vilnius University, Natural Sciences, Physics, N 002).

The dissertation shall be defended at a public meeting of the Dissertation Defense Panel at 11 am on 21<sup>st</sup> February 2025 in the meeting room of the Physics Institute, Center for Physical Sciences and Technology.

Address: Savanoriu ave. 231, Vilnius, Lithuania

Tel. +370 5 266 1640; e-mail: office@ftmc.lt

The text of this dissertation can be accessed at the libraries of Center for Physical Sciences and Technology and Vilnius University, as well as on the website of Vilnius University:

[www.vu.lt/lt/naujienos/ivykiu-kalendorius](http://www.vu.lt/lt/naujienos/ivykiu-kalendorius)

<https://doi.org/10.15388/vu.thesis.729>

<https://orcid.org/0000-0003-2248-5195>

VILNIAUS UNIVERSITETAS  
FIZINIŲ IR TECHNOLOGIJOS MOKSLŲ CENTRAS

Augustinas Petrulėnas

Femtosekundinių impulsų generacija  
1.1 – 3  $\mu\text{m}$  ruože, stiprinant  
superkontinuumą parametriniuose ir  
priverstinės Ramano sklaidos  
stiprintuvuose

**DAKTARO DISERTACIJA**

Gamtos moklai  
Fizika (N 002)

VILNIUS 2025

Disertacija rengta 2020 – 2024 metais Fizinių ir technologijos mokslų centro Lazerinių technologijų skyriuje, Kieto kūno lazerių laboratorijoje. Mokslinius tyrimus rėmė Lietuvos mokslo taryba ir Šiaurės Atlanto sutarties organizacija (NATO).

**Mokslinis vadovas** – Dr. Aleksėj M. Rodin (Fizinių ir technologijos mokslų centras, gamtos mokslai, fizika, N 002)

Gynimo Taryba:

**Pirmininkas** – Dr. Arūnas Varanavičius (Vilniaus universitetas, gamtos mokslai, fizika, N 002).

**Nariai:**

Dr. Roman Antipenkov (ELI Beamlines Facility, Čekijos Respublika, gamtos mokslai, fizika, N 002),

Prof. dr. Arkady Major (Manitobos universitetas, Kanada, gamtos mokslai, fizika, N 002),

Dr. Kęstutis Regelskis (Fizinių ir technologijos mokslų centras, gamtos mokslai, fizika, N 002),

Doc. dr. Julius Vengelis (Vilniaus universitetas, gamtos mokslai, fizika, N 002),

Disertacija ginama viešame Gynimo tarybos posėdyje 2025 m. Vasario 21 d. 11 val. Fizinių ir technologijos mokslų centro, Fizikos instituto posėdžių salėje. Adresas: Savanorių pr. 231, Vilnius, Lietuva, tel. +370 5 266 1640; el. paštas: [office@ftmc.lt](mailto:office@ftmc.lt)

Disertaciją galima peržiūrėti Vilniaus universiteto ir Fizinių ir technologijos mokslų centro bibliotekose bei VU interneto svetainėje adresu:

<https://www.vu.lt/naujienos/ivykiu-kalendorius>

## CONTENT

INTRODUCTION.....	9
THE GOAL OF THE THESIS.....	11
RESEARCH OBJECTIVES.....	11
SCIENTIFIC NOVELTY.....	11
PRACTICAL VALUE .....	12
STATEMENTS TO DEFEND .....	13
LAYOUT OF THE THESIS .....	13
APPROBATION.....	14
AUTHOR’S CONTRIBUTION.....	19
CO-AUTHOR’S CONTRIBUTION .....	19
1. LITERATURE OVERVIEW.....	20
1.1. Methods for generating ultrashort SWIR pulses .....	20
1.2. Overview of OPCPA setups operating in the SWIR range.....	22
1.3. Fundamentals of optical parametric amplification.....	27
1.4. Transient stimulated Raman scattering in the NIR–SWIR ranges .....	29
1.4.1. Fundamentals of stimulated Raman scattering.....	29
1.4.2. Transient stimulated Raman scattering and amplification .....	36
1.4.3. Transient SRS bandwidth expansion .....	39
2. HIGH-ENERGY OPCPA OPERATING IN THE SWIR RANGE .....	42
2.1. High-energy single-picosecond pump source .....	42
2.2. Generation of supercontinuum seed in the SWIR range .....	45
2.3. Analysis of optimal OPCPA configuration in the SWIR range .....	46
2.4. Control of signal pulses in the SWIR OPCPA.....	49
2.5. Experimental setup of three-stage SWIR OPCPA .....	51
2.6. Optimization of seed pulse width and OPCPA gain bandwidth .....	52
2.7. High-energy three-stage OPCPA operating in the SWIR range .....	57
2.8. OPCPA with integrated AOPDF operating in the SWIR range.....	60
2.9. Excitation of supercontinuum in the MWIR range for gas sensing ...	64

2.10. Summary of the results .....	66
3. TRANSIENT SRRS IN THE NEAR IR RANGE.....	68
3.1. Setup for cascade transient SRRS in compressed hydrogen .....	69
3.2. Performance of SRRS in hydrogen on the pump beam polarization .	71
3.3. Dependence of SRRS on pump energy and hydrogen pressure.....	73
3.4. Transient SRRS amplification of SC seed in compressed hydrogen .	76
3.5. Compression of SRRS pulses amplified in a hydrogen cell.....	79
3.6. Setup for studying broadband TSRCPA in KGW crystals .....	80
3.7. Spectral synthesis in a two-stage TSRCPA based on KGW crystals.	81
3.8. Summary of the results .....	84
4. COLLINEAR SWIR OPCPA COMBINED WITH TSRCPA .....	85
4.1. Setup for TSRCPA combined with SWIR OPCPA in KGW crystal.	85
4.2. Investigation of SWIR TSRCPA in the KGW crystal .....	87
4.3. Setup for investigation of SWIR SRRS in compressed hydrogen .....	92
4.4. Investigation of transient SWIR SRRS in compressed hydrogen .....	94
4.5. Summary of the results .....	99
MAIN RESULTS AND CONCLUSIONS .....	101
SANTRAUKA .....	102
Įvadas .....	102
Disertacijos tikslas ir uždaviniai.....	104
Mokslinis tyrimų naujumas .....	104
Praktinė nauda .....	105
Ginamieji teiginiai.....	106
Aprobacija .....	107
Literatūros apžvalga .....	108
Rezultatai.....	110
Pagrindiniai rezultatai ir išvados .....	126
BIBLIOGRAPHY .....	128
CURRICULUM VITAE .....	152

## ACKNOWLEDGEMENT

First, I would like to express my heartfelt gratitude to my scientific supervisor, Dr. Aleksėj Rodin, for inviting me to join the research at the Solid State Laser laboratory eight years ago, and for his continued support throughout this time. I am especially grateful for the inspiring freedom in shaping my research path, the favorable conditions for creative exploration, and for the example of dedication to the mission on the way to success.

I would also like to thank Dr. Paulius Mackonis for his insightful discussions, innovative ideas and fresh perspectives on my research work. His collaboration in co-authoring scientific publications was invaluable, and his contributions greatly enriched them.

I am sincerely grateful to Augustė Černekytė for her invaluable assistance in conducting experiments at the final stage of the research, persistence and diligence in overcoming difficulties.

Thanks to Dr. Julijanas Želudevičius from the Fiber Laser laboratory for assistance in repairing the fiber components of the experimental setup.

Lastly, I am deeply grateful to my family for their unwavering support and patience throughout my studies. Without their encouragement, this work would not have been possible.

## LIST OF ABBREVIATIONS

- AOPDF** – acousto-optic programmable dispersive filter  
**ASE** – amplified spontaneous emission  
**BiBO** – Bismuth Triborate,  $\text{BiB}_3\text{O}_6$   
**BBO** – Beta-Barium Borate,  $\beta\text{-BaB}_2\text{O}_4$   
**CPA** – chirped pulse amplification (or amplifier)  
**CEP** – carrier-envelope phase  
**CM** – chirped mirrors  
**DFG** – difference frequency generation  
**FROG** – frequency-resolved optical gating  
**FTL** – Fourier transform limited  
**FOD** – fourth-order dispersion  
**FWHM** – full width at half maximum  
**GDD** – group delay dispersion  
**GVD** – group velocity dispersion  
**HCF** – hollow-core fiber  
**HHG** – high harmonic generation  
**KGW** – Potassium Gadolinium Tungstate,  $\text{KGd}(\text{WO}_4)_2$   
**LIDT** – laser induced damage threshold  
**LWIR** – long-wavelength infrared range (8 – 15  $\mu\text{m}$ )  
**MWIR** – mid-wavelength infrared range (3 – 8  $\mu\text{m}$ )  
**Nd:YAG** – Neodymium-doped Yttrium Aluminum Garnet,  $\text{Nd}:\text{Y}_3\text{Al}_5\text{O}_{12}$   
**NIR** – near-infrared range (0.75 – 1.4  $\mu\text{m}$ )  
**NOPA** – non-collinear optical parametric amplifier  
**OPA** – optical parametric amplification (or amplifier)  
**OPO** – optical parametric oscillator  
**OPCPA** – optical parametric chirped-pulse amplification (or amplifier)  
**PPLN** – periodically poled Lithium Niobate  
**SC** – white light supercontinuum  
**SPM** – self-phase modulation  
**SRA** – stimulated Raman amplification (or amplifier)  
**SRS** – stimulated Raman scattering  
**SRRS** – stimulated rotational Raman scattering  
**SWIR** – short-wavelength infrared range (1.4 – 3  $\mu\text{m}$ )  
**Ti:Sa** – Titanium-doped sapphire ( $\text{Ti}^{3+}:\text{Al}_2\text{O}_3$ )  
**TOD** – third-order dispersion  
**TSRCPA** – transient stimulated Raman chirped-pulse amplification  
**YAG** – Yttrium Aluminum Garnet,  $\text{Y}_3\text{Al}_5\text{O}_{12}$



## INTRODUCTION

The development of lasers since their introduction in the 1960s [1] has been driven by diverse needs in scientific, medical and industrial fields [2]. A significant milestone in the design of ultrafast lasers was the discovery by Nobel laureates D. Strickland and G. Mourou of chirped pulse amplification (CPA) [3], which made it possible to achieve TW peak powers. This invention paved the way for numerous applications in strong field physics [2], such as the generation of isolated attosecond pulses, electron acceleration, and the study of wave packet dynamics in atoms and molecules. Laser sources with pulse widths of tens of femtoseconds are now available in scientific laboratories, with a growing number of applications and an ever-expanding user base.

Modern lasers cover a wide range of the electromagnetic spectrum, spanning from ultraviolet to long-wavelength infrared (LWIR). However, in recent years there has been a growing interest in wavelengths from  $\sim 2 \mu\text{m}$  to terahertz (THz). This spectral range is rich in specific features for molecular identification in chemical analysis, environmental monitoring, medical diagnostics, process control, safety, security, and defense applications [4]. Currently, special attention is paid to femtosecond laser sources operating in the short-wavelength and mid-wavelength infrared (SWIR–MWIR) ranges, covering from  $\sim 1.4$  to  $\sim 3 \mu\text{m}$  and from  $\sim 3$  to  $\sim 8 \mu\text{m}$ , respectively. In addition to molecular sensing, high-intensity lasers in this spectral range can be used in fundamental strong field physics, providing shorter attosecond pulses [5], higher THz generation efficiency [6], and improved discrimination between tunneling and multiphoton processes [7]. Intense SWIR–MWIR lasers have also recently been used for molecular structure imaging [8] and material processing [9]. Tabletop attosecond light sources operate on the basis of high harmonic generation (HHG), driven by intense few-cycle laser pulses in noble gases. These sources of high-energy photons are of interest for direct probing of biological molecules in aqueous solutions [10] and tracking electronic, vibrational, rotational [11] and magnetization [12] dynamics. Although the maximum photon energy achievable with HHG [13], as well as the energy cutoff of field-driven photoemitted electrons [14] are scaled as  $\lambda^2$ , the overall conversion efficiency decreases [15], so that each spectral range corresponds to an optimal driver wavelength. Thus, there is a reasonable compromise in SWIR laser wavelength for producing coherent soft X-rays in the water window between 284 and 543 eV [16,17]. Also, ultrashort SWIR–MWIR pulses facilitate detailed studies of atomic and molecular dynamics [18,19], allowing visualization of molecular structures [20]. In the medical field,

SWIR–MWIR lasers are used for precise localized tissue incision and removal by exploiting the strong absorption properties [21]. This enables surgical interventions with micrometer precision, thereby minimizing collateral damage and the risk of functional impairment. The use of  $\sim 2\ \mu\text{m}$  lasers provides superior results in welding polymers with high tensile strength compared to shorter wavelength sources [22]. Military applications of SWIR–MWIR lasers include the targeting and directed infrared countermeasures to disrupt guidance systems [23].

The prevailing approach to obtaining ultrashort pulses in the SWIR–MWIR ranges involves the use of nonlinear methods coupled with readily available femtosecond and picosecond Nd or Yb pump lasers at a wavelength of  $\sim 1\ \mu\text{m}$  [24–26]. In particular, the advancement of high-energy, few-cycle SWIR lasers relies on optical parametric chirped-pulse amplification (OPCPA) operating in the degeneracy range at  $\sim 2\ \mu\text{m}$ . However, most SWIR OPCPA designs developed to date are complex and relatively expensive. These systems use active phase control based on an acousto-optic programmable dispersive filter (AOPDF) and separate laser sources for seed and pump, with the inherent stability degradation and the need for precise synchronization between the two lasers [25]. To make SWIR femtosecond lasers widely available and reliable in operation, it is important to investigate and develop alternative, simpler and low-cost approaches to OPCPA.

Another way to expand the spectrum of commercially available lasers to the SWIR–LWIR ranges could be stimulated Raman scattering (SRS), which has been well studied in the steady-state regime with nanosecond pump pulses [27]. Notably, unlike four-wave mixing, difference frequency generation (DFG) or optical parametric amplification (OPA), SRS is not constrained by phase matching. However, the SRS efficiency in the transient regime is significantly reduced [28], calling for the exploration of new approaches to generating SWIR pulses.

Thus, this study considers a high peak power SWIR OPCPA setup driven by a Yb:YAG laser with a pulse width of  $\sim 1.3\ \text{ps}$ . The primary goal of developing this OPCPA with a broadband supercontinuum (SC) seed source was to achieve the best conversion efficiency while maintaining simplicity and low cost. These efforts resulted in an easily reproducible multi-mJ OPCPA setup operating in the SWIR range with outstanding efficiency. Approaches to increasing the SRS conversion efficiency under highly transient conditions with expansion of the spectral range in the near infrared (NIR) and SWIR ranges were also investigated. In particular, a two-stage stimulated Raman amplifier (SRA) is considered, where adjacent Stokes components are amplified in successive stages. Furthermore, it is shown that

transient SRS combined with SWIR OPCPA allows to increase the idler intensity. In summary, this work explores the synergy of combining various nonlinear effects to efficiently generate SWIR femtosecond pulses.

## THE GOAL OF THE THESIS

The goal of the thesis was to investigate and develop femtosecond laser setups operating in the SWIR range based on the phenomena of supercontinuum, OPCPA and transient SRS in compressed gases and crystals.

## RESEARCH OBJECTIVES

To achieve the goal, the following work tasks were defined:

1. To investigate and develop a few-cycle, multi-mJ OPCPA setup operating in the SWIR range near  $\sim 2 \mu\text{m}$  with  $\sim 1.3$  ps pump pulses from a Yb:YAG laser using broadband SC radiation as a seed source.
2. To study the capabilities of cascaded stimulated rotational Raman scattering (SRRS) combs in compressed hydrogen to extend the spectrum of  $\sim 1.3$  ps pump pulses at 1030 nm into the SWIR range using a broadband SC seed and to evaluate the Stokes pulse compression.
3. To investigate the syntheses of adjacent vibrational Stokes modes by transient SRS in KGW crystals using  $\sim 1.3$  ps pump pulses at 1030 nm and a broadband SC seed, and to evaluate the compression of the amplified pulses with tailored spectra in the NIR range.
4. Explore collinear SWIR OPCPA setup in combination with transient vibrational SRS in KGW crystal and SRRS in compressed hydrogen to achieve spectral extension with energy transfer into SWIR and MWIR ranges, respectively.

## SCIENTIFIC NOVELTY

1. An optimized multi-mJ BiBO crystal SWIR OPCPA setup operating near  $\sim 2 \mu\text{m}$  demonstrated an outstanding pump-to-signal conversion efficiency of up to  $\sim 25\%$  in the last stage, followed by pulse compression to  $\sim 38$  fs without active spectral phase control. These results were achieved for the first time using SWIR supercontinuum seed pulses obtained with the same single-picosecond OPCPA pump laser at 1030 nm.

2. For the first time, transient cascade SRRS combs in compressed hydrogen were obtained with an efficiency of up to ~52% and multi-mJ pulses covering the difficult-to-reach ~1.1 – 1.4  $\mu\text{m}$  wavelength range using ~1.3 ps pump pulses at 1030 nm.
3. Spectral synthesis of adjacent vibrational Stokes in sequential KGW crystals was demonstrated for the first time, leading to a ~23-fold increase in the composite bandwidth of amplified SC pulses compared to pump pulses and a conversion efficiency of ~35%.
4. Combining SWIR OPCPA with transient stimulated Raman chirped-pulse amplification (TSRCPA) in KGW crystals provided for the first time the idler energy build-up with a signal-to-idler conversion efficiency of up to ~25%.
5. Investigations of SWIR OPCPA in combination with TSRCPA in compressed hydrogen revealed that positively chirped broadband SC seed pulses contribute to the extension of the SRRS spectral bandwidth to longer wavelengths compared to negatively chirped ones.

## PRACTICAL VALUE

These studies lead to the development of a few-cycle, multi-mJ OPCPA setup operating in the SWIR range near ~2  $\mu\text{m}$ . The optimized design includes a Yb:YAG pump laser, broadband SC generation, AOPDF, three OPCPA stages based on BiBO crystals, and pulse compressor. A cost-effective implementation of this setup without using AOPDF provides similar output parameters except for slightly longer pulses. The developed intense SWIR source can be adapted into remote sensing LIDARs to detect atmospheric pollutants, biochemicals and hazardous gases. In particular, the filamentation of intense SWIR–MWIR pulses paves the way for the long-range detection of molecules such as H<sub>2</sub>O, CO<sub>2</sub>, CO, and NH<sub>4</sub>. This setup can also be used to generate soft X-rays and, at higher repetition rates of the pump source, will allow satellite communications in the atmospheric transparency window.

Furthermore, SRRS in compressed hydrogen represents a fairly simple and cost-effective approach to generate multi-mJ pulses shorter than ~150 fs and even down to ~15 fs in the wavelength range from ~1.1 to ~1.4  $\mu\text{m}$  for a number of applications, including nonlinear microscopy.

Moreover, the combination of collinear OPCPA with TSRCPA in gases and crystals studied in this work can serve as a simple way for increasing the idler pulse energy. Considering the importance of carrier-envelope phase (CEP) stable pulses in HHG, attosecond pulse generation and other strong-field physics experiments, this technique can provide simple yet high-performance few-cycle laser sources operating in the SWIR–MWIR range. Finally, the integration of SWIR OPCPA with transient SRRS in compressed hydrogen resulted in a significant extension of the output pulse spectrum to  $\sim 3 \mu\text{m}$ . Such laser sources are in demand for spectroscopy, remote sensing and medical diagnostics. In addition, this approach can be extended to generate LWIR pulses for applications in molecular spectroscopy, atmospheric remote sensing, and seeding of TW-class  $\text{CO}_2$  amplifiers.

### STATEMENTS TO DEFEND

1. The broadband SWIR SC seed pulses generated by single-picosecond pump pulses at 1030 nm are well suited for a passively synchronized three-stage BiBO OPCPA setup. This approach allows the generation of multi-mJ SWIR pulses compressed in a glass block to a few optical cycles.
2. Using a broadband SC seed source and circularly polarized single-picosecond pump pulses at 1030 nm under high hydrogen pressure enables highly efficient cascade SRRS in the difficult-to-reach  $\sim 1.1 - 1.4 \mu\text{m}$  wavelength range while suppressing vibrational SRS.
3. The NIR TSRCPA bandwidth can be expanded by more than  $\sim 20$  times using spectral synthesis of adjacent vibrational modes in KGW stages, compared to single-picosecond pump pulses with partial compression of spectrally tailored pulses.
4. Collinear SWIR OPCPA setup combined with TSRCPA enables efficient signal-to-idler energy transfer in the KGW crystal, while transient SRRS in compressed hydrogen with positively chirped SC seed pulses allows spectrum extension beyond  $\sim 3 \mu\text{m}$  by generating higher-order rotational Stokes.

### LAYOUT OF THE THESIS

The doctoral dissertation consists of four principal chapters:

The first chapter reviews the literature on SWIR OPCPA and SRS setups. It begins with a discussion of current SWIR femtosecond pulse generation techniques, then analyzes their inherent challenges and potential OPCPA configurations, and presents recent advances in SWIR OPCPA design. The basic principles behind SRS are then explained and unexplored opportunities for generating intense femtosecond pulses in the SWIR range using SRS are discussed.

The second chapter describes the developed SWIR OPCPA setup using ~1.3 ps pump pulses at 1030 nm and broadband SC seed pulses. This section outlines the calculations used in the design, compares the effect of chirp variation on the OPCPA performance, and justifies the feasibility of the setup for spectroscopic application. Furthermore, the possibilities for improving the OPCPA design are discussed.

The third chapter is divided into two parts, each reflecting different approaches to the generation of intense femtosecond NIR pulses using SRS, applicable also in the SWIR range. The first part presents the results of a study of transient cascaded SRRS in compressed hydrogen using ~1.3 ps pump pulses at 1030 nm and broadband SC seed. The second part explores the spectral synthesis of the TSRCPA bandwidth in successive stages based on KGW crystals.

The fourth chapter presents the results of TSRCPA integration into the SWIR OPCPA. It describes the features of signal-to-idler energy transfer using both transient vibrational SRS in KGW crystal and SRRS in compressed hydrogen, and presents the energy, spectral, and temporal characterization of the output pulses. In addition, the differences observed when conjugating oppositely chirped pulses are discussed.

## APPROBATION

The research results presented in the thesis were published in 4 scientific papers [A1–A4] and 3 conference proceedings [A5–A7], and together with co-authors the results were presented at 13 international conferences [C1–C13].

**Scientific papers directly related to the thesis that have been peer-reviewed and indexed in Clarivate Web of Science (WoS):**

**A1 A. Petrulėnas, P. Mackonis and A. M. Rodin, Synthesis of adjacent Stokes spectra in a two-stage transient stimulated Raman chirped-pulse amplifier. Crystals 12 (7), 888 (2022).**

- A2** **A. Petrulėnas**, P. Mackonis and A. M. Rodin, Signal-to-idler energy conversion from 1.9 to 2.3  $\mu\text{m}$  by transient stimulated Raman chirped-pulse amplification. *Optics Letters* **48** (7), 1598–1601 (2023).
- A3** **A. Petrulėnas**, P. Mackonis and A. M. Rodin, High-efficiency bismuth borate-based optical parametric chirped pulse amplifier with  $\sim 2.1$  mJ, 38 fs output pulses at  $\sim 2150$  nm. *High Power Laser Science and Engineering*, **11**, e27 (2023).
- A4** **A. Petrulėnas**, P. Mackonis, A. Černeckytė and A. M. Rodin, Amplification of supercontinuum seed pulses at  $\sim 1078 - 1355$  nm by cascade rotational SRS in compressed hydrogen. *Applied Science*, **13** (24), 13087 (2023).

**Scientific papers directly related to the thesis (conference proceedings):**

- A5** **A. Petrulėnas**, P. Mackonis, A. M. Rodin and V. Girdauskas, IR-supercontinuum seeded efficient two-stage transient stimulated Raman amplification in KGW with pulse compression. *Proc. SPIE* **11670**, 1167017 (2021).
- A6** **A. Petrulėnas**, P. Mackonis, A. M. Rodin, 1800 – 2400 nm OPCPA based on BiBO with signal-to-idler conversion by transient stimulated Raman chirped pulse amplification. *Proc. SPIE* **11867**, 118670L (2021).
- A7** **A. Petrulėnas**, P. Mackonis, A. M. Rodin and A. Černeckytė, Cost-effective femtosecond laser source at 1800 – 3400 nm wavelengths based on multistage nonlinear conversion. *Proc. SPIE* **12092**, 1209204 (2022).

**Others scientific papers:**

- A8** A. M. Rodin, P. Mackonis and **A. Petrulėnas**, Ultrafast NIR-SWIR lasers with transient stimulated Raman chirped pulse amplification for advanced LIDAR. *Proc. of SPIE* **11525**, 15251W (2020).
- A9** P. Mackonis, **A. Petrulėnas**, A. M. Rodin, V. Girdauskas and A. Michailovas, Two-stage transient stimulated Raman chirped-pulse amplification in  $\text{KGd}(\text{WO}_4)_2$  with compression to 145 fs. *Optics Letters* **45** (24), 6627- 6630 (2020).

**A10** P. Mackonis, **A. Petrulėnas**, A. M. Rodin and V. Girdauskas, VIS-to-NIR multiple output sub-TW class modular laser based on OPCPA and TSRCPA. *Proc. of SPIE* **11664**, 116640N (2021).

**A11** A. M. Rodin, A. Černekytė, P. Mackonis, **A. Petrulėnas**, Optimizing self-seeded perfluorooctane SBS compressor configurations to achieve ~90 ps high-energy pulses. *Photonics*, **10** (9) 1060 (2023).

**International conferences (presented by thesis author):**

**C1** **A. Petrulėnas**, P. Mackonis, A. M. Rodin, V. Girdauskas, Efficient two stage transient stimulated Raman chirped pulse amplification in KGW with compression to <160 fs. *Conference on Advanced Solid State Lasers*, online (2020). (oral)

**C2** **A. Petrulėnas**, P. Mackonis, A. M. Rodin, V. Girdauskas, IR-supercontinuum seeded efficient two-stage transient stimulated Raman amplification in KGW with pulse compression. *SPIE Photonics West. LASE 2021*, online (2021). (oral)

**C3** **A. Petrulėnas**, P. Mackonis, A. M. Rodin, V. Girdauskas, Spectrum synthesizer based on two-stage transient stimulated Raman chirped pulse amplification in KGW crystal. *2021 Conference on Lasers and Electro-Optics Europe*, online (2021). (oral)

**C4** **A. Petrulėnas**, P. Mackonis, A. M. Rodin, 1800 – 2400 nm OPCPA based on BiBO with signal-to-idler conversion by transient stimulated Raman chirped pulse amplification. *SPIE Security and Defense*, online (2021). (oral)

**C5** **A. Petrulėnas**, P. Mackonis, A. M. Rodin, Amplification of a broadband 1800 – 2100 nm supercontinuum seed in a three-stage OPCPA based on BiBO crystals. *4th International Conference on Optics, Photonics and Lasers (OPAL '2021)*, Corfu, Greece (2021). (oral)

**C6** **A. Petrulėnas**, P. Mackonis, A. M. Rodin, A. Černekytė, Cost-effective femtosecond laser source at 1800 – 3400 nm wavelengths based on multistage nonlinear conversion. *SPIE Defense and Commercial Sensing*, Orlando, USA (2022). (oral)



- C7** **A. Petrulėnas**, P. Mackonis, A. M. Rodin, Generation of femtosecond pulses up to 3  $\mu\text{m}$  by combining OPCPA with transient stimulated Raman amplification. *5th International Conference on Optics, Photonics and Lasers (OPAL'2022)*, Tenerife, Spain (2022). (oral)
- C8** **A. Petrulėnas**, A. Butkutė, P. Mackonis, A. Rodin, Multi-mJ SWIR OPCPA pumped and seeded with 1.2 ps Yb:YAG laser, *10th EPS-QEOD Europhoton Conference*. Hannover, Germany (2022). (oral)
- C9** **A. Petrulėnas**, P. Mackonis, A. M. Rodin, High-efficiency BiBO-based OPCPA at 2000 – 2300 nm with 2 mJ output pulses compressed to 38 fs. *Optica Advanced Photonics Congress 2022*, Barcelona, Spain (2022). (oral)
- C10** **A. Petrulėnas**, P. Mackonis, A. M. Rodin, High-energy few-optical-cycle multispectral NIR–SWIR–MIR laser based on OPCPA and stimulated Raman scattering, *6th International Conference on Optics, Photonics and Lasers (OPAL'2023)*. Madeira, Portugal (2023). (invited)
- C11** **A. Petrulėnas**, P. Mackonis, A. M. Rodin, A new approach to OPCPA idler pulse energy build-up at 2.3  $\mu\text{m}$  by transient stimulated Raman chirped-pulse amplification. *2023 Conference on Lasers and Electro-Optics Europe*, Munich, Germany (2023). (poster)
- C12** **A. Petrulėnas**, A. Černekytė, P. Mackonis, and A. M. Rodin, High-efficiency BiBO-Based OPCPA with  $\sim 2.2$  mJ output pulses at  $\sim 2.2$   $\mu\text{m}$  compressed to 25 fs. *High-Brightness Sources and Light-Driven Interactions Congress 2024*, Vienna, Austria (2024). (oral)
- C13** **A. Petrulėnas**, P. Mackonis, A. Černekytė, A. M. Rodin, Recent advances in the development of few-cycle mid-IR laser based on OPCPA and SRRS. *7th International Conference on Optics, Photonics and Lasers (OPAL'2024)*, Palma de Mallorca, Spain (2024). (invited)

**Other international conferences:**

- C14** A. M. Rodin, P. Mackonis, **A. Petrulėnas**, Ultrafast NIR–SWIR lasers with transient stimulated Raman chirped pulse amplification for advanced LIDARs. *SPIE Future Sensing Technologies*, online (2020).

- C15** P. Mackonis, **A. Petrulėnas**, A. M. Rodin, V. Girdauskas, VIS-to-NIR multiple output sub-TW class modular laser based on OPCPA and TSRCPA. *SPIE Photonics West. LASE 2021*, online (2021).
- C16** V. Girdauskas, P. Mackonis, **A. Petrulėnas**, A. M. Rodin, Towards 50 fs SWIR pulses by transient stimulated Raman chirped-pulse amplification with spectrum synthesis. *64th International Conference for Students of Physics and Natural Sciences "Open Readings'2021"*, Vilnius, Lithuania (2021).
- C17** A. M. Rodin, P. Mackonis, **A. Petrulėnas**, Transient stimulated Raman chirped-pulse amplification (TSRCPA) as an alternative or complementary to OPCPA. *23rd Photonics North conference*, online (2021).
- C18** P. Mackonis, **A. Petrulėnas**, A. M. Rodin, Signal-to-idler energy conversion from 1.9 to 2.3  $\mu\text{m}$  by transient stimulated Raman chirped-pulse amplification. *Optica Advanced Photonics Congress 2022*, Barcelona, Spain (2022).
- C19** J. Gradauskas, S. Ašmontas, I. Zharchenko, O. Masalskyi, A. Sužiedėlis, A. Šilėnas, A. Čerškus, A. Rodin, **A. Petrulėnas**, Low and high photon energy induced photoresponse in single junction solar cells. *International Conference Advanced Properties and Processes in Optoelectronic Materials and Systems „Apropos 16“*, Vilnius, Lithuania (2022).
- C20** A. Černeckytė, **A. Petrulėnas**, P. Mackonis, A. M. Rodin, Excitation of cascaded stimulated rotational Raman scattering by single-picosecond laser pulses. *44th Lithuanian National Physics Conference*, Vilnius (2023).
- C21** P. Mackonis, **A. Petrulėnas**, A. Černeckytė, and A. M. Rodin, Amplification of supercontinuum seed pulses at 1.1 – 1.4  $\mu\text{m}$  by cascade rotational SRS in compressed hydrogen. *Optica High-Brightness Sources and Light-Driven Interactions Congress 2024*, Vienna, Austria (2024).
- C22** A. Černeckytė, **A. Petrulėnas**, P. Mackonis, A. M. Rodin, High-efficiency mid-IR OPCPA with  $\sim 2.5$  mJ 25 fs output pulses. *67th International Conference for Students of Physics and Natural Sciences "Open Readings'2024"*, Vilnius, Lithuania (2024).

**C23** A. Černeckytė, **A. Petrulėnas**, P. Mackonis, A. M. Rodin, Excitation of a stimulated rotational Raman scattering comb in a hydrogen cell. *7th International Conference on Optics, Photonics and Lasers (OPAL '2024)*, Palma de Mallorca, Spain (2024).

**C24** P. Mackonis, A. Černeckytė, **A. Petrulėnas**, A. M. Rodin, D. Klumbys, High-energy dual-channel four-pass phase-conjugated Nd:YAG amplifier with SBS pulse compression for interference patterning. *7th International Conference on Optics, Photonics and Lasers (OPAL '2024)*, Palma de Mallorca, Spain (2024).

**C25** A. M. Rodin, **A. Petrulėnas**, P. Mackonis, A. Černeckytė, Economic aspects and technologies in the development of advanced cost-effective few-cycle sub-TW class mid-IR lasers. *7th International Conference on Optics, Photonics and Lasers (OPAL '2024)*, Palma de Mallorca, Spain (2024).

#### AUTHOR'S CONTRIBUTION

The author of the PhD thesis performed all experiments and calculations described here, analyzed the results and formulated conclusions and hypotheses. He also actively participated in the preparation of all publications, presented the latest results at international conferences, and prepared A1–A5 manuscripts.

#### CO-AUTHOR'S CONTRIBUTION

**Dr. A. M. Rodin** – supervisor of the entire study, determined its directions, put forward scientific concepts, formulated specific tasks and the methodology for their implementation, consulted on scientific issues, participated in the interpretation of results, and also made a significant contribution to the preparation of publications A1–A4.

**Dr. P. Mackonis** – made a great contribution to improving the methodology of studying SWIR OPCPA and transient SRS phenomena, actively participated in the analysis of results and the formulation of new tasks, and also made a significant contribution to the preparation of publications A1–A4.

**A. Černeckytė** – actively participated in experiments with transient SRRS in compressed hydrogen in the NIR and SWIR ranges, and also contributed to the preparation of manuscripts A4 .

# 1. LITERATURE OVERVIEW

## 1.1. Methods for generating ultrashort SWIR pulses

Several approaches to generating intense ultrashort laser pulses in the wavelength range of about 2  $\mu\text{m}$  have been explored. First of all, significant progress has been made in recent years in the development of ultrafast lasers based on thulium and holmium ions operating near a wavelength of  $\sim 2 \mu\text{m}$ . In particular, lasers with  $\text{Tm}^{3+}$  and  $\text{Ho}^{3+}$  doped garnets, perovskites, vanadates, fluorides, tungstates, rare earth sesquioxides and other host materials have been demonstrated [29]. Among them, Tm-based mode-locked oscillators provide pulses shorter than 50 fs due to the inherently large bandwidth of the emission cross section [30,31]. However, narrowing the bandwidth in CPA results in output pulses of only sub-ps order. For example,  $\sim 0.36$  ps mJ-level pulses were obtained from Tm:YAP CPA at  $\sim 1.94 \mu\text{m}$  [32].

Sub-ps pulse generation with Ho-doped active medium is even more challenging due to the limited emission bandwidth. The first broadband OPA-seeded Ho:YAG CPA delivered 0.53 ps pulses with  $\sim 3$  mJ energy at  $\sim 2 \mu\text{m}$  [33]. Meanwhile, with an increase in the CPA output energy from 1 to 100 mJ, the pulse width rises from several to tens of picoseconds [34,35]. Such energy levels are achieved using sophisticated Ho:YLF regenerative amplifiers pumped with over 100 W of Tm-doped fiber lasers power.

Despite the high energy level obtained with  $\text{Ho}^{3+}$  and  $\text{Tm}^{3+}$  CPAs, the orders of magnitude longer pulse compared to OPCPA are not suitable for driving HHG-based attosecond sources. On the other hand, the development of room temperature Ho-doped CPAs pumped by a Tm-doped fiber laser demonstrated scalable picosecond pulses with energies of several mJ at repetition rates of several kHz, suitable for pumping and seeding femtosecond MWIR (3 – 7  $\mu\text{m}$ ) OPAs [34,36].

Moreover, post-compression techniques could be explored with such solid-state lasers to generate few-cycle pulses. In particular, nonlinear spectral broadening setups in gas-filled hollow-core fiber (HCF) [37], hollow-core photonic crystal fiber (HC-PCF) [38,39], or multi-pass cell [40] allow obtaining few-cycle pulses. For instance, high-power, few-cycle 2  $\mu\text{m}$  output pulses were obtained by post-compressing the coherently combined output from a Tm-doped fiber laser in a multi-pass compression stage [40]. Furthermore, two-stage nonlinear spectral broadening in Kagome-type HC-PCF allows multiple picosecond  $\sim 2 \mu\text{m}$  pulses from a Ho:YLF amplifier to be compressed to less than 50 fs at a repetition rate of 1 kHz [39].

Recent studies of  $\text{Cr}^{2+}:\text{ZnSe}$  CPA have shown a way to achieve ultrashort SWIR pulses of  $\sim 3\text{--}4$  optical cycles due to the broad ( $2\text{--}3.3\ \mu\text{m}$ ) vibronic emission spectrum. In most cases,  $\text{Cr}:\text{ZnSe}$  oscillators are pumped by Er-doped fiber lasers at  $1.56\ \mu\text{m}$ , Tm-doped fiber lasers at  $1.9\ \mu\text{m}$ , or laser diodes at  $1.65\ \mu\text{m}$  [41]. However, the upper state lifetime of the order of microseconds in  $\text{Cr}:\text{ZnSe}$  requires synchronization of the nanosecond pump and seed lasers. The unavailability of suitable pump lasers slowed the progress of  $\text{Cr}:\text{ZnSe}$  CPA research until 2011, when the first setup was pumped by a Q-switched Ho:YLF laser [42]. This scheme, consisting of a  $\text{Cr}:\text{ZnSe}$  mode-locked oscillator, stretcher, regenerative amplifier and compressor, provided 138 fs pulses with an energy of 1.5 mJ at 1 kHz [43].

In addition to mode-locked oscillators,  $\text{Cr}:\text{ZnSe}$  CPAs can be seeded with Ti:Sa laser-pumped OPAs or DFGs. The available  $\mu\text{J}$  level energy from an OPA or DFG [44] is two to three orders of magnitude higher than from an oscillator [45]. Therefore, the effects of gain narrowing and amplified spontaneous emission (ASE) can be suppressed. In particular, the DFG seed was boosted to  $\sim 4$  mJ in  $\text{Cr}:\text{ZnSe}$  CPA at 1 kHz, pumped from both ends by 25 mJ, 50 ns Ho:YAG laser pulses with compression to  $\sim 44$  fs [46]. Another example is OPA-seeded  $\text{Cr}:\text{ZnSe}$ , which produced 6.2 mJ,  $\sim 39$  fs pulses at 1 kHz after nonlinear compression in a series of  $\text{CaF}_2$  lenses and a YAG plate [47].

Despite advances in solid-state laser technology, OPCPA [48] remains the most common and straightforward method for constructing SWIR lasers. In fact, OPCPA combines the advantages of CPA and OPA, offering high gain, low thermal effects, great wavelength flexibility and wide bandwidth, beyond the capabilities of modern solid-state laser amplifiers [49–51]. The wavelength range and achievable pulse width of solid-state lasers in comparison with OPCPA in the SWIR range are shown in Fig. 1.1.

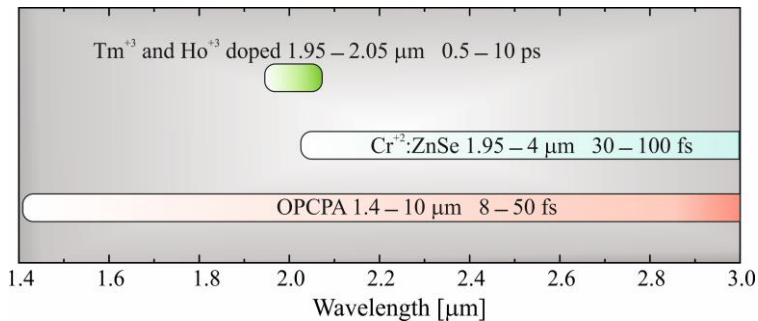


**Fig. 1.1.** Overview of high-energy ultrashort pulse laser sources operating in the SWIR range.

Over the past two decades, OPCPA has evolved into a mature technology applicable to both compact benchtop setups [52,53] and facility-deployed laser sources [54]. Tabletop OPCPA are robust high peak power laser sources that deliver a few cycle pulses, with carrier wavelengths covering a considerable part of the optical spectrum. Recently, significant efforts have been directed towards the development of few optical cycle OPCPA setups operating in the SWIR–MWIR spectral ranges, which are difficult to access for ultrafast solid-state lasers. The next section will discuss the designs options as well as the advantages and drawbacks of SWIR OPCPA.

## 1.2. Overview of OPCPA setups operating in the SWIR range

This section provides an overview of ultrashort pulse SWIR OPCPA setups in terms of pump pulse width, operating repetition rate, used nonlinear crystals and seed delivery options.

Broadband SWIR OPCPAs typically operate near the degeneracy wavelength corresponding to laser pumping at  $\sim 1.6 \mu\text{m}$  for Ti:Sa [55],  $\sim 2 \mu\text{m}$  for neodymium (Nd) [56] and ytterbium (Yb) [24] in various nonlinear crystals, such as  $\text{BaB}_2\text{O}_4$  (BBO) [57],  $\text{BiB}_3\text{O}_6$  (BiBO) [58],  $\text{YCa}_4\text{O}(\text{BO}_3)_3$  (YCOB) [24], as well as periodically poled Lithium Niobate  $\text{LiNbO}_3$  (PPLN) [25] and periodically poled stoichiometric Lithium Tantalate  $\text{LiTaO}_3$  (MgO:PPLT) [26]. In this case, placing signal and idler pulses in the same spectral range significantly reduces the group velocity mismatch and facilitates the generation of few-cycle laser pulses.

The pump pulse width plays a crucial role in determining the stretching factor of the seed pulse, thereby affecting the dispersion control and the overall stretching-compression configuration. While in CPA pulse stretching primarily allows for intensity reduction, in OPCPA it ensures equal width of chirped seed and pump pulses. The use of sub-ns pump pulses facilitates pulse amplification especially in benchtop TW-class OPCPAs [59]. In contrast, mJ energy levels from the OPCPA setup can be achieved with pump pulses of 1 – 5 ps [60]. Notably, single-picosecond pump pulses exhibit high temporal contrast of the amplified pulses after compression, since OPCPA maintains gain only for the duration of the pump pulse. In this case, OPCPA crystals are pumped at much higher intensities [61–63], which provides high gain even in thin crystals, thereby maintaining a wider bandwidth. Moreover, since the third-order dispersion (TOD) accumulated in sub-ns pumped OPCPA can exceed  $10^6 \text{fs}^3$ , its compensation using prism or grating compressors, especially in the SWIR range [64], becomes challenging but critical for achieve high-contrast output pulses. Mainly for this reason, the most

expensive part of few-cycle OPCPAs becomes the AOPDF, which is capable to compensate for the accumulated TOD and even fourth-order dispersion (FOD). However, commercially available TeO<sub>2</sub>-based AOPDF may be ineffective at repetition rates greater than ~100 kHz. In this case, a lithium niobate (LiNbO<sub>3</sub>) based AOPDF was developed to operate in the SWIR range [65]. Thus, although the OPCPA configuration with single-picosecond pumping is more sensitive to the relative timing of the seed and pump pulses, it benefits from easier spectral phase control.

Previously, SWIR OPCPA setups have primarily used Ti:Sa lasers with pump and seed pulse width of tens of picoseconds. The shortest pulses of 9 fs, corresponding to 1.7 optical cycle at 1.6  $\mu\text{m}$ , were achieved in a two-stage Ti:Sa-pumped BiBO OPCPA [66]. Meanwhile, in a three-stage BiBO-based OPCPA, pulses of 10.4 fs with an energy of 3 mJ were obtained at 1.7  $\mu\text{m}$  [55]. In both cases, DFG was used to seed OPCPA, which favors passive CEP stabilization [67]. However, the maximum pump-to-signal efficiency for Ti:Sa-pumped OPCPA did not exceed 22.6% [68].

Modern lasers based on Yb-doped active elements represent a better alternative for pumping high peak and average power OPCPA setups. Advances in Yb laser technology have made it possible to generate ultrashort high-energy pulses at repetition rates from 1 Hz to hundreds of kHz [69–71] with superior beam quality, beam pointing and energy stability. The rapid development of high-power picosecond Yb lasers at ~1  $\mu\text{m}$  has also paved the way for significant progress in the field of SWIR–MWIR OPCPA. Operation of OPCPA at 2  $\mu\text{m}$  when pumped by such lasers is more efficient due to degeneracy and lower group velocity mismatch between the pump photon wavelength and gain bandwidth when compared to SWIR OPCPA based on Ti:Sa laser systems, where ~1.3  $\mu\text{m}$  signal and ~2  $\mu\text{m}$  idler pulses are generating [72].

Currently, high repetition rate OPCPA setups are pumped using Innoslab or Yb:YAG disk CPAs, while broadband seed pulses are delivered from DFG. For example, BiBO-based OPCPA produced 15.4 fs pulses at 2  $\mu\text{m}$  with an average power of ~2.6 W at 200 kHz [73], but the output energy was limited to less than 100  $\mu\text{J}$ . Periodically poled nonlinear crystals perform well in high repetition rate SWIR OPCPA due to their large nonlinear coefficient, providing high gain in thin plates, octave-spanning phase-matching bandwidth, and low absorption. In particular, using MgO:PPLN-based OPCPA operating at 100 kHz, 16.5 fs pulses with an average power of 25 W were obtained at 2.2  $\mu\text{m}$  [16]. As another example, the shortest pulses of 10.5 fs were achieved using MgO:PPLN-based OPCPA at 2.1  $\mu\text{m}$  [25]. However, periodically poled nonlinear crystals are not suitable for multi-mJ

OPCPA due to their rather limited thickness at large aperture. Thus, the best average power of 50 W at 2  $\mu\text{m}$  was achieved from a BBO-based OPCPA, delivering 38 fs pulses with  $\sim 1$  mJ energy [74].

To obtain few-cycle optical pulses, ultra-broadband OPCPA phase-matching is critical. This is achieved in the SWIR range by matching the group velocities of the signal and the idler [49] for type-I phase matching under degeneracy, or in non-collinear optical parametric amplifier (NOPA), where the idler group velocity is projected along the signal propagation direction. Although, as mentioned earlier, wide gain bandwidth is inherent in periodically poled nonlinear crystals, there are alternative methods to expand the OPCPA bandwidth. In particular, the dual-color pumping approach uses two pump pulses at different wavelengths [75,76]. By amplifying different parts of the signal spectrum, a composite bandwidth is obtained. Then the second and third harmonics of the pump source amplify the long and short-wavelength ranges of the seed in separate OPA stages. This provides an exceptionally wide bandwidth of 0.45 – 1.3  $\mu\text{m}$ , corresponding to nearly single-cycle pulses of less than 3 fs [75]. In the SWIR range, the OPCPA bandwidth can be expanded to several octaves by using different nonlinear crystals or their orientation in successive OPCPA stages [77,78]. This has been demonstrated in a dual-chirped Ti:Sa-pumped OPA (DC-OPA) using BiBO and MgO-doped lithium niobate, which delivered single-cycle  $\sim 8.6$  fs MWIR pulses with 53 mJ energy at wavelengths from 1.4 to 3.1  $\mu\text{m}$  [77]. This is the highest pulse energy and peak power achieved in the MWIR OPCPA. Such DC-OPA setups use both chirped pump and signal pulses to achieve high conversion efficiency without damaging nonlinear crystals [79–81].

Another approach to expand the bandwidth is to amplify different parts of the incident broadband seed spectrum in parallel OPCPA stages, where the pulses follow independent optical paths before being combined by dichroic mirrors, allowing individual control of gain, dispersion, and beam shape. Due to the separate routes taken for each pulse, such setups are sensitive to environmental and mechanical instability. It is therefore critical to synchronize their arrival times and relative phase at the synthesis point with sub-cycle accuracy, and similar precision is required for CEP-locking. Then, spectral range coverage is ensured using different nonlinear crystals, beam transport optics and dispersion control for each of the parallel channels. Thus, by combining the visible, NIR and SWIR ranges, pulses shorter than 5 fs can be obtained [82–84]. However, the scalability of the output energy, limited by the complexity of such laser setups, has not reached even mJ.

Besides the choice of pump source, another challenge is to ensure a sufficiently broadband seed to cover the entire OPCPA spectral range. Several



approaches have been proposed to obtain a broadband SWIR seed. One option is to generate visible SC in solids [24] or gases [25] followed by DFG between the SC and Yb laser radiation. Another technique uses DFG from short-wave and long-wave components of Ti:Sa radiation [56]. The complexity of both approaches is due to the need for periodically poled DFG crystals. On the other hand, these methods have the advantage of passive CEP stabilization [51], which is the key to obtaining isolated attosecond pulses [85,86]. Finally, for extreme signal bandwidth of 0.5 – 2.4  $\mu\text{m}$ , DFG, OPO and SC can be used in series [87] as the front-end for a multi-octave laser system.

Thus, typical SWIR OPCPA setups [88] include DFG stages to obtain a seed in the desired spectral range with expensive AOPDF to control group delay dispersion (GDD) and TOD in mJ-level systems, and hard-to-find periodically poled nonlinear crystals to support extreme bandwidth (Fig. 1.2). There are a number of challenges when translating the DFG and OPCPA concepts into the SWIR range. Efficient conversion requires broadband phase matching with temporal overlap of all involved spectral components. The complexity of the developed SWIR OPCPAs operating near 2  $\mu\text{m}$  limits their application in areas where CEP stability is not critical, such as remote sensing, nonlinear microscopy, selective X-ray spectroscopy, biological or nanoscale imaging, laser medicine, metrology, and material processing [22,89]. This calls for exploration of alternative simple and cost-effective OPCPA setups.

The direct use of a broadband SC seed in the SWIR range allows to simplify the SWIR OPCPA configuration (Fig. 1.2) by eliminating the need for active synchronization between the seed and pump lasers. However, the extension of the SC spectrum to  $\sim 2.2 \mu\text{m}$  is a challenge when using femtosecond laser pulses [90], while for picosecond pulses it is fraught with intra-volume damage. Nevertheless, stable and long-lasting broadband SC reaching  $\sim 2.5 \mu\text{m}$  has been convincingly demonstrated [91–93] using single-picosecond pulses at 1030 nm. In addition to eliminating the DFG stage, the SC seed operating in the SWIR range also reduces the overall TOD accumulated in the OPCPA setup. Moreover, low TOD in turn maintains monotonous chirp, which simplifies pulse compression even without AOPDF. The compressibility of amplified SWIR SC seed pulses in 3 mm thick MgO:LN in the wavelength range of 1.6 – 2.2  $\mu\text{m}$  was first demonstrated in 2021 [91], simultaneously with the continuation of our experiments. The accumulated GDD of only 500 fs<sup>2</sup> was compensated by four bounces in the chirped mirrors, providing  $\sim 25$  fs pulses after compression. Furthermore, particularly broadband SC seed is a good candidate for wavelength-tunable OPCPA [94,95].

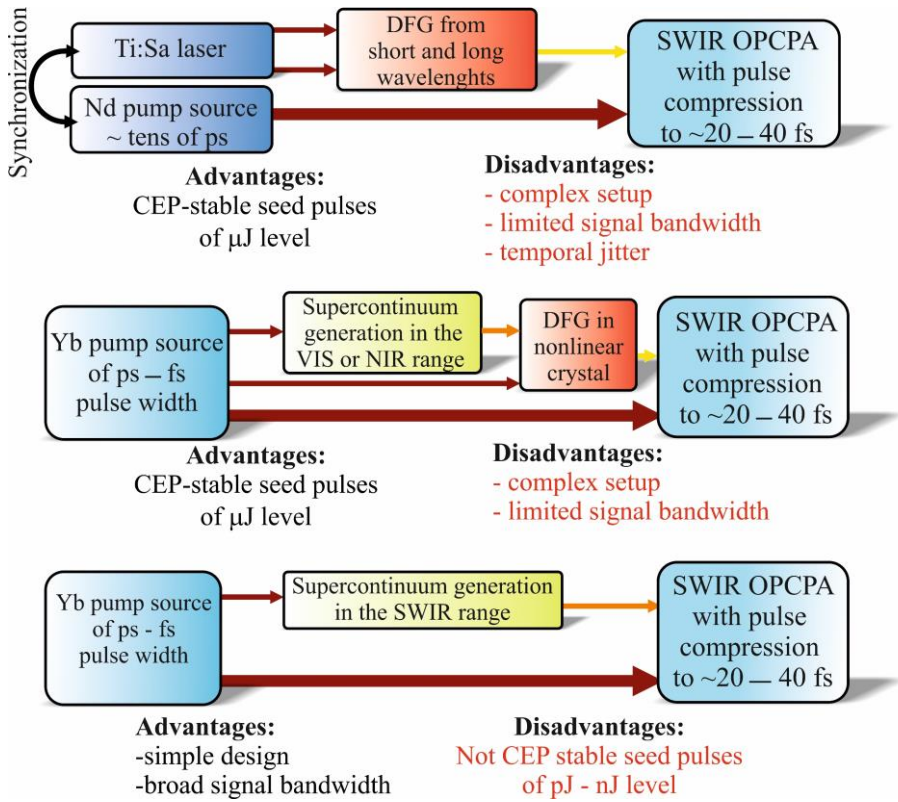


**Fig. 1.2.** Methods for generating broadband SWIR seed pulses for use in OPCPA.

In summary, although current SWIR OPCPA development efforts cover a variety of architectures, many of them are either complex, expensive, and unreliable, or do not reach even hundreds of  $\mu\text{J}$  of energy. Among them, OPCPA with single-picosecond pump sources offer a number of advantages, such as the inherent synchronization between the pump and the broadband SC seed, the possibility of using shorter nonlinear crystals with a wider spectral bandwidth and lower cumulative GDD and TOD, which eliminates the need for AOPDF. However, the OPCPA setups reported so far with single-picosecond pumping and direct seeding with broadband SWIR SC pulses have not yet reached mJ output levels.

Therefore, the investigation of high-intensity, compact and cost-effective SWIR OPCPA with few-cycle output pulses is of great scientific and practical significance. The goal of this study was to explore alternative high-energy OPCPA configurations using SWIR SC seed pulses and to conduct a comparative analysis of this approach.

### 1.3. Fundamentals of optical parametric amplification

In the OPA process, a low-intensity beam known as the “signal” at a lower frequency  $\omega_s$ , is amplified in a suitable nonlinear crystal in the field of a high-intensity pump beam at a higher frequency  $\omega_p$  while simultaneously generating a third low-intensity beam, called the “idler” at the lowest frequency  $\omega_i$ , providing the relation:  $\omega_i < \omega_s < \omega_p$ . For an efficient OPA it is necessary to satisfy the phase-matching condition:

$$\hbar k_p = \hbar k_s + \hbar k_i, \quad k_{j=p,s,i} = \frac{n_j \omega_j}{c}, \quad (1.1)$$

where  $k_p, k_s, k_i$  are the pump, signal, and idler wave vectors, respectively,  $\hbar$  denotes Planck’s constant,  $n_p, n_s, n_i$  correspond to the refractive indices of nonlinear media at the pump, signal and idler wavelengths respectively, and  $c$  is the speed of light in vacuum. The signal frequency intended for amplification can theoretically be in the range from  $\omega_p/2$  (the so-called degeneracy condition) to  $\omega_p$ , and, accordingly, the idler frequency varies from  $\omega_p/2$  at degeneracy, when the signal and the idler coincide in frequency. Hence, to provide flexibility in frequency amplification, the OPA process must satisfy the following condition:

$$\Delta k = \frac{1}{c} (n_p \omega_p - n_s \omega_s - n_i \omega_i) = 0, \quad (1.2)$$

where  $\Delta k$  is the phase mismatch. This condition can be satisfied in anisotropic media, where two distinct modes can propagate, namely ordinary ( $o$ ) and extraordinary ( $e$ ) waves. These two modes exhibit different refractive indexes, for extraordinary waves depending on the direction of propagation relative to the optical axis of the crystal:

$$\frac{1}{n_e^2(\theta)} = \frac{\sin^2 \theta}{n_e^2} + \frac{\cos^2 \theta}{n_o^2}, \quad (1.3)$$

where  $\theta$  is the angle between the wave vector  $k$  and the optical axis,  $n_e$  is the refractive index of the extraordinary wave at  $\theta = 90^\circ$  and  $n_o$  is the refractive index of the ordinary wave. Thus, the tunability and optical characteristics of OPOs are mainly determined by the optical properties of nonlinear crystals.

The transmission of the most popular nonlinear crystals for high-energy SWIR OPCPA is shown in Fig. 1.3. Among these crystals, YCOB and Mg:PPLN exhibit the lowest absorption near  $2 \mu\text{m}$ .

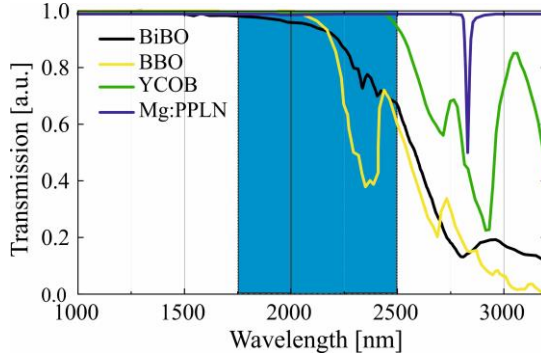


**Fig. 1.3** Transmission through 10 mm samples for different nonlinear crystals [96–99]. The filled area corresponds to the spectral range of the amplified signal pulses at degeneracy.

However, PPLN crystals are susceptible to photorefractive damage, which may compromise their long-term performance in high-power lasers. Moreover, PPLN crystals have limitations in damage threshold when exposed to high-intensity laser pulses. Therefore, power and energy scaling requires larger crystal apertures, which are currently not available. On the other hand, BBO, BiBO, and YCOB crystals have significantly higher optical damage thresholds ( $\sim 100 \text{ GW/cm}^2$  at  $\sim 1 \text{ ps}$ ), making them most suitable for multi-mJ OPCPA. Moreover, these crystals are available with apertures up to  $20 \times 20 \text{ mm}^2$ , opening up prospect for energy scaling of OPCPA in the  $2 \mu\text{m}$  range. The main difference between these nonlinear crystals is their effective nonlinear coefficient  $d_{eff}$ , which determines the strength of the nonlinear interaction and, therefore, the achievable output energy and conversion efficiency. The magnitude of this coefficient depends on both the material properties and the polarization properties of the interacting beams. Optical properties such as  $d_{eff}$ , transmission range and damage threshold intensity for the main nonlinear crystals suitable for OPCPA at  $2 \mu\text{m}$  are given in Table 1.1.

**Table 1.1.** Optical properties of nonlinear crystals relevant for high-energy SWIR OPCPA pumped by picosecond pulses.  $I_{th}$  – damage threshold intensity at 10 ns pulse width.

Nonlinear crystal	Interaction	$d_{eff}$ , [pm/V]	Transmission range, [ $\mu\text{m}$ ]	$I_{th}$ , [ $\text{GW/cm}^2$ ]
BBO	I type oo-e	1.88	0.189–3.2	1.3
BiBO	I type oo-e	2.6	0.3–3.4	0.9
	I type ee-o	-1.4		
YCOB	I type oo-e	-0.7	1-3	0.8
Mg:PPLN	I type oo-e	-3.98	0.4-4	0.1

A detailed analysis of the optimal crystal selection for a multi-mJ OPCPA setup operating in the SWIR range will be continued in Section 2.3.

#### 1.4. Transient stimulated Raman scattering in the NIR–SWIR ranges

An alternative method for extending the spectral range of laser radiation towards longer wavelengths is stimulated Raman scattering (SRS), a third-order nonlinear effect discovered in 1962 during a study of Q-switching of a ruby laser using a nitrobenzene Kerr cell [27]. Since then, SRS has found applications in scientific and practical areas, such as the enhancement of conventional Raman spectroscopy [100,101], the conversion of pump laser radiation into new spectral ranges with the ability to control the duration and temporal shape, spectral composition and linewidth, as well as the energy and directionality [102–106] of laser pulses. Finally, SRS is even used for cooling atoms [107] and wavefront conjugation [108]. As soon as lasers with pulse width comparable to or shorter than the relaxation time of Raman vibrations became available, transient SRS became actively studied [28,109–112]. Despite the long history of research in the field of nonlinear optics, interest in SRS does not fade due to the complex physics underlying the interaction processes and new applications.

While the OPCPA remains the predominant technique for down converting ultrashort pulses, its efficiency is often limited to ~15% and its spectral range is limited by phase matching [113]. Maintaining bandwidth much beyond ~1.1  $\mu\text{m}$  becomes particularly challenging due to the lack of suitable broadband gain media or requires operating near the damage threshold of many nonlinear crystals [114]. In contrast, SRS has advantages in wavelength conversion, pulse compression, and beam clean-up [115,116] due to its inherent phase-matching, which is not susceptible to thermal dephasing. Moreover, the particularly broad spectral bandwidth of cascade SRS opens up a promising path for the synthesis of sub-cycle coherent light pulses covering the range from UV to NIR [117,118]. SRS can also complement OPCPA in converting SWIR pulses into the MWIR range, eliminating the need for nonlinear phase-matched crystals.

In the next section, the features of SRS in solids and gases using ultrashort pulses as a pump source will be discussed.

##### 1.4.1. Fundamentals of stimulated Raman scattering

When a photon interacts with a crystal lattice or molecule, it can undergo inelastic scattering, producing spectral components at frequencies below and

above the frequency of the incident light. This phenomenon, called spontaneous Raman scattering [119,120] occurs in gases, solids, liquids and plasmas. The transfer of energy to the crystal lattice creates a quantum of vibration known as a phonon. Raman scattering in crystals can also give rise to paramagnetic ions, surface and spin waves [121]. Components shifted towards lower frequencies are called Stokes components, and those shifted towards higher frequencies are called anti-Stokes components. In energy terms, the scattering process can be expressed as follows:

$$\begin{aligned}\hbar\omega_s &= \hbar\omega_p - \hbar\Omega_R, \\ \hbar\omega_a &= \hbar\omega_p + \hbar\Omega_R,\end{aligned}\tag{1.4}$$

where  $\omega_p, \omega_s, \omega_a$  are the frequencies of the incident pump, Stokes and anti-Stokes photons,  $\Omega_R$  – the frequency of the Raman phonon or molecular vibration (rotation). Spontaneous Raman scattering, as shown in Fig. 1.4a, is the isotropic scattering of an incident light wave by molecules or the crystal lattice of a solid containing a frequency range different from the frequency of the excitation source. Furthermore, Raman scattering can be represented using an energy level diagram, as shown in Fig. 1.4b.

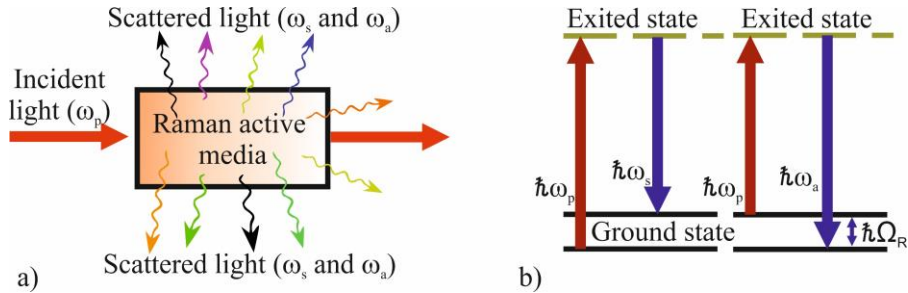


**Fig. 1.4** a) Spontaneous Raman scattering involves the isotropic scattering of an incident laser beam by molecules or a crystal lattice of a solid containing a series of rotational-vibrational Stokes and anti-Stokes modes. b) transitions between the vibrational eigenstates of the material.

Stokes scattering involves a transition from the ground state to the final state via a virtual intermediate level associated with the excited state. In contrast, anti-Stokes Raman scattering corresponds to a transition from the final Stokes level to the ground state level, with the excited state acting as an intermediate level. Anti-Stokes lines are usually much weaker than Stokes lines due to the lower population of the final Stokes level compared to the ground state level in thermal equilibrium.

According to classical theory, any scattered light arises from an oscillating dipole. The electric field of the incident light produces an induced dipole moment  $\mu$ , which is determined by:

$$\mu = \alpha E = \alpha E_0 \cos(2\pi\omega\tau), \quad (1.5)$$

where  $\alpha$  is the polarizability of the molecule and  $E$  is the electric field of radiation with frequency  $\omega$ . Hence, the induced dipole oscillates at a frequency  $\omega$  if the polarizability  $\alpha$  of the molecule changes during vibrational and rotational motion. In all diatomic molecules, the interaction between electrons and nuclei changes as the molecule undergoes vibration, leading to a variation in polarizability. Consequently, all diatomic molecules, both homonuclear or heteronuclear, exhibit vibrational Raman activity. On the other hand, linear molecules are characterized by anisotropic polarizability, which leads to a rotational Raman spectrum. This phenomenon occurs even in molecules such as  $O_2$ ,  $N_2$ ,  $H_2$  and others, which lack a pure rotational spectrum. In such cases, rotational motion around the bond axis does not affect the polarizability; only end-over-end rotations contributes to the observed Raman spectra (Fig. 1.5).

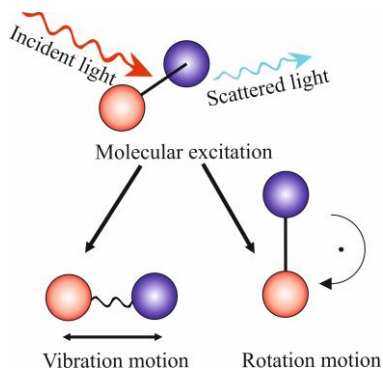


**Fig. 1.5** Illustration of the Raman scattering process in a diatomic molecule. Raman scattering can occur simultaneously with a change in the vibrational or rotational energy of the molecule.

The vibrational Raman effect arises as a result of the change in  $\alpha$  with the vibrational coordinate  $q$ . An essential condition for the Raman effect is that the optical polarizability of the dipole is not constant, but depends on the displacement. Thus, expanding the polarizability into Taylor series in terms of the displacement  $q$  and substituting it into Eq. 1.5 we obtain:

$$\mu = \alpha_0 E_0 \cos(2\pi\omega\tau) + \frac{1}{2} \frac{\beta}{A} q_0 E_0 [\cos(2\pi(\omega - \Omega_R)\tau) + \cos(2\pi(\omega + \Omega_R)\tau)], \quad (1.6)$$

where  $\beta = \frac{\partial\alpha}{\partial q}$ ,  $A$  – vibration amplitude. The last equation provides the classical explanation of the Raman effect. It is obvious that in Eq. 1.6 the first, second and third terms give rise to the Rayleigh, Stokes and anti-Stokes lines respectively. Thus, the dipole oscillates not only at the incident frequency  $\omega$ , but also at the Stokes frequency  $\omega_s$  and the anti-Stokes frequency  $\omega_a$ .

For the rotational Raman effect to occur, an essential condition is that the molecule must be anisotropic, and its polarizability changes depending on the direction or orientation of the molecule (i.e. the molecule must not be spherically symmetric). In this case, the polarizability changes, since when the molecule rotates, its orientation relative to the electric field  $E$  of the incident light changes. For a diatomic molecule, if the rotational frequency is  $\Omega_R$ , the time dependent polarizability is given by:

$$\alpha = \alpha_0 \cos(2\pi(2\Omega_R)\tau). \quad (1.7)$$

The rotation of the molecule leads to a periodic modulation of the dipole moment induced by the laser electric field, and, in turn, to a modulation of the scattered radiation frequency (with  $2\Omega_R$ ). In this case, the factor  $2\Omega_R$  arises because during a complete rotation (by  $2\pi$ ) the molecule takes the same orientation twice (when rotating by  $\pi$  and  $2\pi$ ). Then the induced dipole moment for rotational Raman scattering can be written as follows:

$$\mu = \alpha_0 E_0 \cos(2\pi\omega\tau) + \frac{1}{2} \frac{\beta}{A} q_0 E_0 [\cos(2\pi(\omega - 2\Omega_R)\tau) + \cos(2\pi(\omega + 2\Omega_R)\tau)]. \quad (1.8)$$

Additional lines accompanying the Rayleigh signal appear at intervals corresponding to twice the rotational frequency.

However, the spontaneous Raman scattering mechanism discussed above is typically characterized as a relatively weak process. Even in solid matter, the scattering cross section per unit volume for Raman scattering is  $\sim 10^{-6} \text{ cm}^{-1}$ . In this case, only about 1 part of  $10^6$  incident radiation is scattered at the Stokes frequency over a 1 cm length of the Raman active medium. On the contrary, when excited by an intense laser beam, highly efficient scattering can occur through the stimulated Raman scattering process. SRS is known for its high energy conversion efficiency of incident laser radiation into Stokes, often exceeding 10% [122,123]. Another difference between spontaneous and



stimulated Raman scattering is the spatial distribution of Stokes radiation. The spontaneous process results in emission along a dipole radiation pattern, whereas the stimulated process leads to emission in a narrow cone in both the forward and backward directions. The relationship between spontaneous and stimulated Raman scattering can be understood by considering the process in terms of photon occupation numbers for different field modes [123]. In the quantum mechanical approach, the laser and Stokes fields are described by the laser and Stokes photon numbers  $m_L$  and  $m_S$ , respectively. The generation of a Stokes photon is given by the relation [124]:

$$\frac{dm_S}{dt} = \frac{c}{n} \frac{dm_S}{dz} \propto m_L(m_S + 1), \quad (1.9)$$

where  $\frac{c}{n}$  is the speed of light in media. The vacuum state is characterized by  $m_S = 0$ , and the unit in Eq. 1.9 gives spontaneous Raman scattering. Thus, the spontaneous scattering regime is characterized by  $m_L \ll 1$  and  $m_L \cong$  constant over distances small compared to  $(\sigma_R N^{-1})$ , where  $\sigma_R$  is the Raman scattering cross section for incident light photons scattered into all Raman modes, and  $N$  is molecular density. This means that the Stokes intensity increases proportionally to the length of the Raman medium and, hence, to the total number of molecules contained in the interaction region. Also, the number of photons can be experimentally related to the optical power. The measured Stokes power emitted in a small solid angle  $\Delta\Omega$  is given by:

$$\delta P_S = N \frac{d\sigma}{d\Omega}(\theta, \Phi) \Delta\Omega \delta z P_L, \quad (1.10)$$

where the angles  $\theta, \Phi$  represent the scattering direction from the material volume element of length  $\delta z$ , and  $P_L$  is the power of the incident light. In this context, the integral scattering cross section is denoted as  $\frac{d\sigma}{d\Omega}$ . When the Raman scattering is aligned parallel to the incident laser beam, the integral scattering cross-section can be defined as [125]:

$$\frac{d\sigma}{d\Omega} = \beta^2 \frac{\omega_s^4 n_s \hbar}{c^4 n_L 2m\omega_p}, \quad (1.11)$$

where  $n_s$  and  $n_L$  are the refractive indices of the Raman-active medium for Stokes and incident radiation, respectively, and  $m$  is the reduced mass. Thus, the probability of Raman scattering in the active medium decreases with increasing wavelength of the incident light.

In the opposite scenario, when there are numerous photons in the Stokes mode ( $m_s \gg 1$ ), the unity term in Eq. 1.9 becomes negligible. Consequently, when the number of laser photons remains relatively constant, the Stokes mode experiences exponential amplification, leading to SRS. In this scenario, the Stokes intensity increases exponentially as the radiation propagates through the medium, often resulting in substantial Stokes intensity observed at the output of the interaction region. In other words, SRS is a process of amplification of radiation with the Stokes frequency:

$$I_s(z) = I_s(0) \exp[G_{SS}], \quad G_{SS} = g_R I_p z, \quad (1.12)$$

where  $G_{SS}$  is the steady state Raman gain and  $g_R$  is the Raman gain coefficient. In this scenario, two waves of light interact with a dipole (or solid): a high-intensity laser beam at a certain frequency and a second beam at the Stokes frequency (Fig. 1.6).

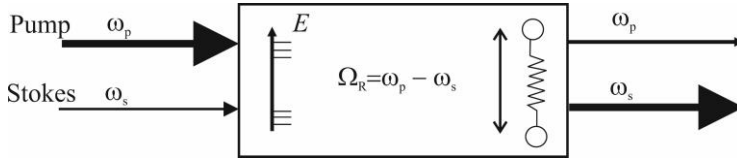


**Fig. 1.6** Schematic illustration of SRS [124].

In principle, this configuration reflects the conditions of spontaneous Raman scattering, except that both the initial laser beam and the Stokes wave are incident on the medium [126]. The Raman gain coefficient per unit length per unit pump intensity is given by [127]:

$$g_R = \frac{2\pi\lambda_s^2 N}{\hbar\omega_s \Gamma} \left( \frac{d\sigma}{d\Omega} \right), \quad (1.13)$$

here  $\Gamma = \frac{1}{T_2}$  is the half width at half maximum of the Raman line, where  $T_2$  is the vibration or phonon dephasing time. If  $I_s$  is small, then  $I_p$  is constant, and the Stokes wave experiences exponential small-signal gain as it propagates. The Raman gain increases linearly with increasing Stokes shift, and it becomes obvious that the Raman gain diminishes markedly with increasing excitation wavelength. Typically, the SRS generation at the first Stokes wavelength becomes noticeable when the exponent in Eq. 1.12 reaches the value of  $g_R I_p z \approx 25 - 30$ , which corresponds to a conversion efficiency of  $\sim 1\%$ . The excitation intensity that provides such an efficiency value is taken as the steady-state SRS threshold pumping level.

Hence, the SRS process depends on the spontaneous Raman scattering cross section, the spectral linewidth, the length of the interaction path of the light field with the matter, the input intensity and optical feedback (light generation) at the Stokes frequency. The properties of the most common SRS-active media are presented in Table 1.2. It is evident that vibrational Raman shifts are larger in gases compared to solids. However, the gain is noticeably reduced in gases due to their lower density. Nevertheless, gases can be used in large volumes, making them suitable for high-power applications requiring large beam diameters, unlike single crystals with limited aperture.

**Table 1.2** The properties of the most common Raman-active media. FWHM – full-width at half-maximum.

Raman-active media	Raman shift, [cm <sup>-1</sup> ]	Linewidth, [cm <sup>-1</sup> ] at FWHM	Gain coefficient [cm/GW]
H <sub>2</sub>	4155 (vibr.)	0.03 at 100 bar [131]	0.2 at 532 nm [132]
	358 (rot.)	-	2×10 <sup>-5</sup> at 10 μm [133]
	587 (rot.)	0.15 at 100 bar [131]	-
	814 (rot.)	-	-
N <sub>2</sub>	2326 (vibr.)	-	1×10 <sup>-5</sup> at 1 μm [134]
	~60 (rot)	-	2×10 <sup>-6</sup> at 1 μm [135]
SF <sub>6</sub>	~774 (vibr.)	-	0.83 at 532 nm [136]
Nitrobenzene	1345	6.6 [124]	1 at 1 μm [124]
KGW	901	17 [137]	3 at 1 μm [137]
	768	20 [137]	4.4 at 1 μm [137]
Ba(NO <sub>3</sub> ) <sub>2</sub>	1047	1.3 [137]	10 at 1 μm [137]
Diamond	1332.5	1.5 [138]	10 – 16 at 1 μm [138]

SRS occurs predominantly in the forward and/or backward directions relative to the incident laser pulse. Forward scattering is favored for incident pulses with durations shorter than or comparable to the characteristic dephasing time of the material ( $T_2$ ), whereas backward scattering is favored for long laser pulses. This is explained by the increase in the interaction length of the Stokes pulse when propagating in the same direction as the short pump

pulse, from which it draws energy. Conversely, the Stokes wave can draw energy by counter-propagating to long pump pulses [128].

The described process does not impose any special requirements on the pump laser wavelength. Thus, SRS in high-pressure gases emerged in the 1960–1970s as a highly efficient method for wavelength conversion of nanosecond laser pulses [129], thereby paving the way to discrete wavelengths tuning in a wide spectral range from 0.7 to 7  $\mu\text{m}$  [130]. With the advancement of laser technologies, the reduction of laser pulse widths to picoseconds or femtoseconds led to transient scattering regime. The use of pump pulse widths shorter than the dephasing time of the molecules or phonons of the material ( $T_2$ ) has become a new trend in SRS research, allowing for a deeper understanding of the interaction between laser pulses and molecular vibrations.

#### 1.4.2. Transient stimulated Raman scattering and amplification

Depending on the response time of materials to electromagnetic radiation, two SRS regimes are distinguished. In the steady-state regime, the pump pulse width significantly exceeds the medium dephasing time. In contrast, the transient regime covers two specific cases: when the pump pulse width closely matches  $T_2$  and when the pulses are shorter than  $T_2$ . In this context, the evolution of the Stokes wave exhibits distinct dynamics, involving inertial delays, pulse compression, and other related phenomena. In addition to short pump pulses, transient SRS can be achieved in the case of high gain, then the transition between the steady-state and transient regimes has the form [139]:

$$\left. \begin{array}{l} \textit{Steady - state} \\ \textit{Transient} \end{array} \right\} \begin{array}{l} \tau_p > G_{ss}T_2 \\ \tau_p < G_{ss}T_2 \end{array} \} G_{ss} \gg 1. \quad (1.14)$$

Since in the experiment  $G_{ss}$  can easily exceed 30, the transient regime can extend to situations where the laser pulse width even greatly exceeds the molecular or phonon dephasing time. However, when the pulses are shorter than  $T_2$ , the Stokes power gain at its peak is [139]:

$$G_\tau = \sqrt{\frac{4G_{ss}\tau_p}{T_2}}. \quad (1.15)$$

The transient gain depends on the square root of both the laser intensity and the interaction length, whereas in the steady-state case the gain depends linearly on these two parameters.

Studies of Raman-active gases pumped with picosecond pulses have shown that a reduction in pulse width leads to an increase in the SRS excitation threshold and a decrease in the conversion efficiency [140,141]. In the transient SRS regime, the SRS threshold becomes energy rather than intensity-dependent, and, consequently, the threshold pump intensity increases drastically compared to the steady-state case [28]. Furthermore, other nonlinear phenomena such as multiphoton ionization, SC generation, beam self-focusing or self-phase modulation (SPM) may compete with SRS [105], thereby affecting the SRS conversion efficiency. Despite the potential reduction in the efficiency of SRS, these phenomena contribute to the expansion of the spectrum of scattered radiation from 2 to 10 times [142–145]. Consequently, when studying SRS of ultrashort pulses, the correlation between the efficiency and the broadened spectrum of the scattered radiation becomes essential.

Due to the highly transient nature of the regime in gaseous media, the SRS conversion efficiency of femtosecond pulses reaches only ~6% at a wavelength of 1  $\mu\text{m}$  and ~18% at 390 nm [103,141,146]. It is noteworthy that in crystals the efficiency remains similar, despite the dephasing time being tens of times shorter [147–149]. While efforts to keep the laser intensity below the critical self-focusing power can mitigate some nonlinear effects, SPM is challenging to eliminate because, like the Raman gain per unit length, it depends on the laser intensity and the length of the active medium [150]. Moreover, L. L. Losev et al. [151] experimentally observed a sharp decrease in the SRS conversion efficiency with broadening of the pump spectrum. A. V. Konyashchenko et al. determined the minimum laser pulse width at which SRS will still dominate over SPM [152]:

$$\tau_{min} \sim n_2 \left( \frac{d\sigma}{d\Omega} \right)^{-1} \left| \frac{1}{\lambda_p} - \frac{2}{\lambda_s} \right|, \quad (1.16)$$

where  $n_2$  is the nonlinear refractive index of the Raman medium, and  $\lambda_p, \lambda_s$  are the pump and Stokes wavelengths, respectively. In this case, the shortest pump pulses of ~0.5 ps, can be converted using SRS in hydrogen. This was confirmed by an experiment in a capillary filled with hydrogen, when the pump pulse width varied from 0.5 to 4 ps at a wavelength of 0.8  $\mu\text{m}$ . However, under dual-frequency excitation, where two femtosecond pulses of similar intensity with a Stokes frequency offset are used, the minimum pump pulse width can be further reduced. This reduction is facilitated by the lower requirements for SRS increment compared to single-frequency excitation [153]. In addition, due to the fact that the nonlinear refractive index decreases

with increasing wavelength [154], a decrease in the minimum pulse width was observed during SRS generation with increasing pump wavelength, [145,152]. The use of chirped pump pulses allows suppressing nonlinear phenomena and improving the efficiency of transient SRS by up to 20% in gases and solids [105,155].

The Stokes radiation generated from the quantum noise level [156] undergoes significant amplification, which leads to a narrowing of its spectrum compared to the pump pulse, and, in turn, to a broadening of the Stokes pulse after compression. To bring the efficiency of transient SRS to the level of steady-state regime, generator–amplifier setups are used. In this case, the seed spectrum obtained from the SRS-generator does not narrow after the second stage amplification due to the reduction in gain [122]. Then, an SRS conversion efficiency of up to 47% was achieved in compressed methane when pumped with 1 ps pulses [157]. The Stokes pulse during transient SRS is amplified only at the trailing end of the pump pulse, since a finite time is required for the resonant mode to build-up in the medium [110]. Therefore, proper selection of the delay between the pump and seed pulses is crucial to improving the conversion efficiency. In this configuration, Stokes pulses gather competing nonlinear phenomena that affect their duration, as well as temporal and spatial propagation. To mitigate the influence of nonlinear effects in potassium gadolinium tungstate (KGW) crystals, V. A. Orlovich et al. used a Bessel pump beam [106], which provided a SRS conversion efficiency of 50%. Another approach to improve the transient SRS efficiency involves the use of SC seed pulses [158,159]. This also allows for improved the spatial beam distribution. However, the main advantage of using a SC seeding is the expansion of the Stokes pulse bandwidth with the possibility of further compression. Accordingly, the two-stage TSRCPA based on KGW crystals studied in our group ensured a conversion efficiency of 55% [160] with amplification of SC seed pulses at a wavelength of 1135 nm to ~0.6 mJ and compression to ~145 fs, which was an order of magnitude shorter than pump pulses. Thus, this approach results in an increase in both the SRS efficiency and the intensity of compressed Stokes pulses.

However, transient SRS in the SWIR range has not been sufficiently studied. The cross sections and SRS gain in this range are significantly inferior to the NIR range (Eq. 1.8 and Eq. 1.10). Hence, using commercially available fs – ps laser pump sources at a wavelength of 1  $\mu\text{m}$ , SRS in the SWIR range can be realized only in gaseous media. In particular, a deuterium-filled revolver fiber provided two-stage SRS-conversion of 1.03→1.49→2.68  $\mu\text{m}$  when pumped with chirped femtosecond pulses, but with a conversion efficiency of only <10% [161]. Meanwhile, the hydrogen-filled photonic

crystal HCF made it possible to generate <40 fs Stokes pulses at  $\sim 1.8 \mu\text{m}$  wavelength with SRS conversion efficiency of  $\sim 30\%$  by properly choosing the chirp [162]. However, as the energy of the incident pump pulses increases, the use of traditional high-pressure gas cells becomes preferable. For instance, high-energy femtosecond Stokes pulses can be obtained from a hydrogen cell using several temporally spaced pump pulses [102]. In this case, the leading pump pulse excites coherent molecular vibrations, and the delayed one undergoes highly efficient SRS-conversion. This made it possible to obtain  $\sim 40$  fs Stokes pulses with an energy of 0.26 mJ at a conversion efficiency of 22% at a wavelength of  $\sim 1.2 \mu\text{m}$  [163]. Also, the efficiency of transient SRS can be improved by suppressing nonlinear and parametric effects in mixtures of Raman-active and noble gases, such as Kr and He [164].

Meanwhile, the development of crystalline SWIR SRS sources, due to the much smaller Raman shift compared to gases, requires the use of a pump laser in a similar spectral range. In particular, to obtain Stokes wavelengths of 3–4  $\mu\text{m}$ , Group IV materials, such as silicon and diamond are used due to their exceptional thermal conductivity, high damage thresholds, high Raman gain and low absorption. In such setups, nanosecond optical parametric oscillators are used as a pump source [165,166]. The development of actively Q-switched Tm:YLF or Ho:YAG solid-state lasers operating at  $\sim 2 \mu\text{m}$  wavelength has provided the opportunity for SRS-conversion into the SWIR range with 10 – 50% efficiency in YVO<sub>4</sub>, BaWO<sub>4</sub> or KGW crystals [167–170]. Although crystals have short dephasing times that favor transient SRS, such studies in the SWIR range are relatively few. On the other hand, the OPCPA as a pump source provides flexibility in tuning the signal and idler wavelengths. Moreover, this allows the signal wave to be used as a pump and the idler wave as a seed in TSRCPA. Thus, our previous results in the NIR range [165,166], are also promising when transferred into the SWIR.

In summary, methods to mitigate competing nonlinear effects are vital in transient SRS with ultrashort pump pulses, especially due to the inherent low efficiency in the SWIR–MWIR ranges.

#### 1.4.3. Transient SRS bandwidth expansion

It is generally accepted that the main disadvantage of SRS is its limited gain bandwidth compared to OPCPA. The spectral bandwidth of the SRS radiation is determined primarily by the spectral width of the pump, which necessitates the use of an ultra-broadband pump source to generate ultrashort Stokes pulses. However, during amplification, the Stokes spectral bandwidth inevitably narrows compared to the pump spectrum. On the other hand, the

accompanying SRS competitive SPM contributes to the expansion of the spectral bandwidth. Whether the SPM has a positive or destructive effect in transient SRS depends on the properties of the pump radiation, the configuration of the SRS-converter, and the characteristics of the Raman-active medium. SPM is a nonlinear optical effect where a high-intensity laser beam, when passing through a medium, causes a phase modulation proportional to its own intensity profile. The propagation of an ultrashort laser pulse causes a dynamic change in the refractive index of the medium, which is ascribed by the optical Kerr effect. This change in the refractive index leads to a corresponding adjustment of the pulse phase, and in turn, to a change in the frequency spectrum. As a result, the SPM expands the pulse spectrum (Fig. 1.7) due to frequency modulation, while the spectral components are red-shifted at the front and blue-shifted at its tail.

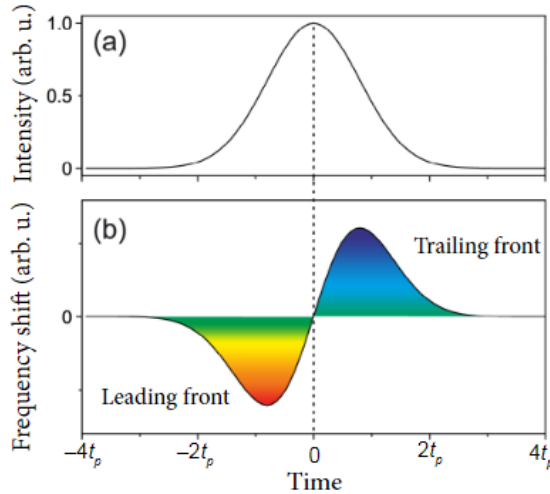


**Fig. 1.7** SPM of a Gaussian pulse (a), causing a change in instantaneous frequency (b) [171].

The combination of SRS and SPM in a BaWO<sub>4</sub> crystal provided spectral expansion up to 100 nm with a SRS conversion efficiency of up to 20% using 0.3 ps pump pulses at 515 nm [149]. In this case, the spectral broadening of the pump pulse was proportional to the energy with a dominant red shift. High SRS-conversion efficiency reduces SPM-broadening [172], and the change in the pulse spectrum with increasing intensity is similar to the soliton self-frequency shift in optical fibers, despite normal dispersion [173].

At high pump intensity, it also becomes possible to broaden the SRS bandwidth by sequentially exciting several vibrational Stokes modes in the crystal [174,175]. In particular, our previous studies demonstrated the



simultaneous generation of vibrational modes at 768 and 901  $\text{cm}^{-1}$  in a KGW crystal with a spectral bandwidth of  $\sim 25$  nm, which corresponds to a transform-limited pulse of 80 fs [160]. However, since the short- and long-wave edges of the spectrum, corresponding to different Stokes shifts, had orthogonal polarizations, pulse compression with a composite spectrum was not considered.

Another way to obtain broadband Stokes pulses is the cascade generation of SRS comb of frequencies separated by the molecular transition energy [176]. In recent decades, molecular modulation has become a key technique for generating extremely short optical pulses at femtosecond and attosecond scales [118,177,178]. Gas-based SRS-converters, compared to solid-state ones, cover a wider wavelengths range, have a higher damage threshold, and operate at repetition rates up to 20 kHz [179]. Raman-active gases such as hydrogen, deuterium, and nitrogen recover even after ionization by high-intensity laser pulses. Moreover, the optical transmission of Raman-active gases spans from vacuum ultraviolet to far infrared radiation. Adiabatic excitation of the  $\text{D}_2$  molecule has been demonstrated to generate a pulse train with a nearly single-cycle waveforms. Similarly, sub-4 fs pulses have been obtained in HCF filled with a Raman-active gas under impulsive preexcitation [180], or octave-spanning Raman combs have been obtained using single-frequency lasers in parahydrogen [181]. SRRS facilitates broadband cascade Stokes generation due to much smaller frequency shifts compared to vibrational SRS. In this case, together with the SPM, the generation of broadband Stokes pulses is ensured, with subsequent compression to a pulse width significantly shorter than those of the pump pulses. Currently, the prevailing technique for generating ultrabroadband Stokes pulses is based on the use of HCFs filled with gases. When pumped with femtosecond Yb laser pulses, this provides a spectrum broadening to 1.3  $\mu\text{m}$  in  $\text{N}_2$  [182,183] and to 2  $\mu\text{m}$  in  $\text{N}_2\text{O}$  [184]. However, this expensive and bulky technique is inferior to more convenient traditional high-pressure gas cells. The molecular modulation technique was also applied to diamond and  $\text{PbWO}_4$  [185–187]. Femtosecond laser pulses can induce coherent Raman sidebands in crystals with small Stokes shifts, offering isolated single-cycle pulses in the visible range. However, the spread of output angles of these sidebands encourages the search for methods of combining them to synthesize ultrashort pulses [187–189].

Thus, although transient SRS allows to expand the bandwidth of incident laser pulses, the induced competing nonlinear effects reduce its efficiency. Therefore, understanding the physics underlying transient SRS opens up opportunities for optimizing its excitation parameters.

## 2. HIGH-ENERGY OPCPA OPERATING IN THE SWIR RANGE

As follows from the literature overview, to generate pulses of tens of femtoseconds from a SWIR OPCPA setup, seed pulses with a sufficiently wide spectral bandwidth and a nonlinear crystal with appropriate broadband phase matching, as well as a high-intensity pump source, are required. In all experiments described below, a previously developed high-energy single-picosecond hybrid fiber / solid-state laser [71] was used both for SC excitation and as a pump source for OPCPA and SRS after being upgraded for better gain and beam stability.

### 2.1. High-energy single-picosecond pump source

The OPCPA pump source (Fig. 2.1) consisted of four main modules: a fiber front-end for seed pulse generation with two protective Faraday isolators (FI) and a pulse picker (I), a two-stage, double-pass CPA based on square Yb:YAG rods (II and III), and a four-pass grating compressor (IV).

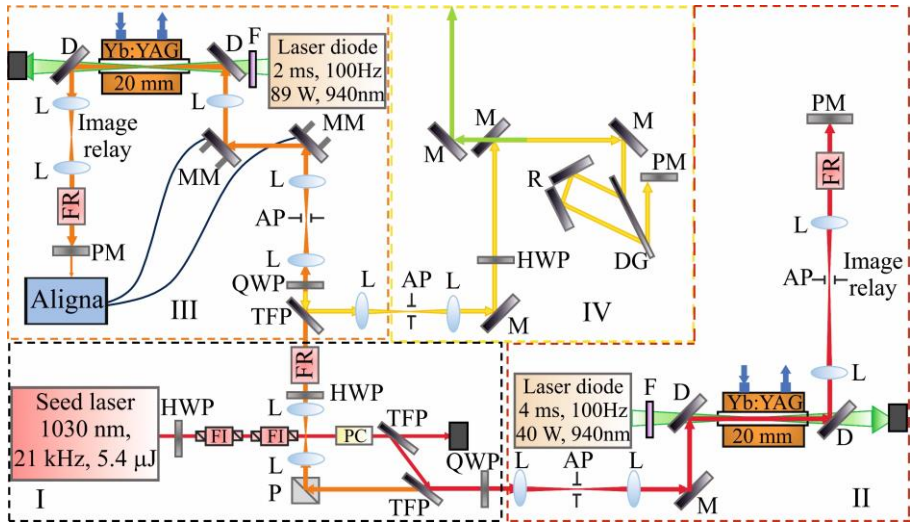


**Fig. 2.1** Hybrid fiber – solid-state pump source: HWP – half-wave retardation plate, FI – Faraday isolators, FR – Faraday rotator, PC – BBO Pockels cell of pulse picker, TFP – thin-film polarizers, M – 45°-plane mirror with high reflectivity at 1030 nm, D – dichroic mirror with high reflectivity at 1030 nm and high transmission at 940 nm, F – protective interference filters, L – lenses, PM – plane mirror with high reflectivity at 1030 nm, P – polarizing cube, AP – aperture, QWP – quarter-wave retardation plates, MM – motorized plane mirrors with high reflectivity at 1030 nm, Aligna – beam position and tilt sensor for autoalignment system, DG – transmission diffraction grating, R – retroreflector.

An all-in-fiber, passively mode-locked front-end [190] delivered spectrally broadened to 3.6 nm FWHM and temporally stretched to  $\sim 0.32$  ns FWHM seed pulses at a central wavelength of 1030 nm. The seed energy was limited to  $\sim 2.4$   $\mu$ J at a pulse repetition rate of 21 kHz, to maintain the energy density on the CPA optical coatings below the laser induced damage threshold (LIDT) of  $\sim 2$  J/cm<sup>2</sup>. These pulses were directed to the CPA at a repetition rate reduced to 100 Hz by using a double BBO-based Pockels cell (PC) with thin-film polarizers (TFP). Accordingly, pulsed diode pumping further reduced the thermal load in 20 mm long Yb:YAG rods.

In the first stage, a  $2 \times 2 \times 20$  mm<sup>3</sup> Yb:YAG rod with a doping level of 2% at. was bonded to a water-cooled copper heatsinks set at 14°C. The heatsink consisted of two copper plates which assembled, formed a square hole for the Yb:YAG rod with an internal water channel surrounding it. The ends of the rod protruded beyond the holder by 0.5 mm. The gap between the crystal and the holder was filled with a layer of indium  $\sim 0.1$  mm thick melted in a furnace. To improve the pump source performance and reduce the output beam drift compared to the original setup [71], a number of modifications were made. First, replacing the nLIGHT pump diode in the first CPA stage with a wavelength-locked model at  $940 \pm 1$  nm ensured a stable emission spectrum over a wide range of operating currents. Then replacing the power supply with a Delta-Elektronika SM 35-45-P211 provided steeper rise and fall fronts of electrical pulses. This made it possible to reduce the duty cycle from 7 ms to 4 ms and, accordingly, the average output power of the pump diode to  $\sim 40$  W. All this reduced the thermal load and relaxed the cooling requirements of the pump diode and Yb:YAG rod, ensuring an increase in the output energy. The output beam of the laser diode was imaged by a collimator to a diameter of 0.56 mm at a depth of  $\sim 5$  mm in the laser rod. The plane mirror (PM) reflected the amplified beam for the second pass, while the induced thermal lens was compensated for by adjusting the distance between the lenses in the relay telescope. To suppress induced depolarization, a Faraday rotator (FR) was used in combination with a quarter-wave retardation plate (QWP). The output pulses, amplified to  $\sim 1.6$  mJ after a double pass of the first CPA stage, were directed to the second, while unwanted cross-coupling between stages was suppressed by a Faraday rotator (FR), polarization cube (P) and a half-wave retardation plate (HWP). To reduce the energy density on the second stage laser crystal, the input signal beam was expanded to  $\sim 2$  mm and focused inside the Yb:YAG rod, for better overlap with the pump beam. Here, a larger cross-section Yb:YAG rod of  $5 \times 5 \times 20$  mm<sup>3</sup> with the same doping level was glued to the heatsink to avoid residual stresses due to non-uniform solidification of indium. The combined output of seven laser diodes produced 2 ms FWHM

pulses with a total average power of 89 W at a repetition rate of 100 Hz (nLIGHT fiber coupled laser diodes with a CW output power of 70 W at a wavelength of 940 nm, a fiber core diameter of 105  $\mu\text{m}$  and  $\text{NA} = 0.22$ ). A Lightcomm beam combiner with a 400  $\mu\text{m}$  output fiber diameter mounted on a water-cooled heatsink provided power loss of less than 5%. The relative arrangement of the laser diodes on a common heatsink in accordance with the radiation wavelength ensured an integral spectral bandwidth of only  $\sim 5$  nm. The output beam from the beam combiner was imaged by a collimator to a diameter of 1.45 mm at a depth of  $\sim 5$  mm in the laser rod. After upgrading the pump source, the same output pulse energy was achieved using only a fraction of the seed pulse energy (Fig. 2.2a). To avoid premature wear and damage to optical coatings, the energy of the amplified pulses was always maintained below 20 mJ. Finally, the output pulses were compressed to  $\sim 1.3$  ps (Fig. 2.2 b) in 4-pass through a 1842 groove/mm transmission grating from Gitterwerk GmbH with a diffraction efficiency of  $\sim 97\%$ .

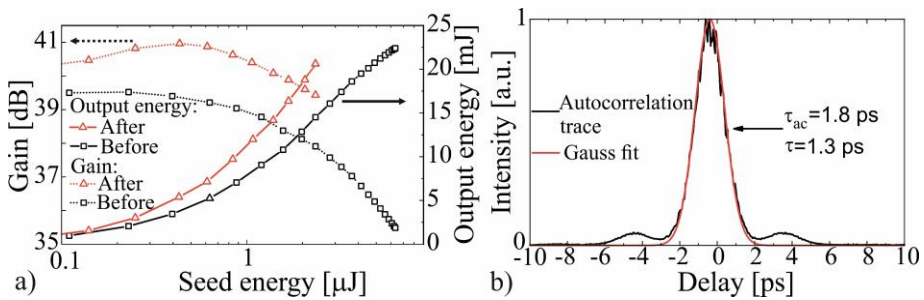


**Fig. 2.2** a) The output energy after the second stage of Yb:YAG CPA (solid lines – right axis) and gain (dotted lines – left axis) as a function of seed energy. b) Autocorrelation trace of compressed CPA output pulses (black line) with Gaussian fit (red line).

Due to the  $\sim 3$  dB gain improvement after the upgrade, the compressed pulses were slightly widened from  $\sim 1.2$  ps to  $\sim 1.3$  ps (Fig. 2.2 b). Undesirable output beam slow drift, accompanied by a decay in output energy and associated primarily with the second CPA stage, was suppressed after the integration of the “Aligna” autoalignment setup from TEM Messtechnik. It was formed by a combined angle and position sensor, as well as two motorized mirrors (MM), forming an electronically controlled feedback loop. A weak leaky beam passing through the return plane mirror (PM) in the second CPA stage was used as a reference. Thus, the thermal drift caused by heating of the adjustable mirror mounts is partially compensated by aligning the two motorized mirrors using the beam offset and tilt data obtained from the sensor.

## 2.2. Generation of supercontinuum seed in the SWIR range

SC seed pulses at wavelengths up to  $\sim 2.5 \mu\text{m}$  were generated in 15 or 130 mm long yttrium aluminum garnet (YAG) crystals using a small  $\sim 100 \mu\text{J}$  portion split off from the pump pulse. The incident pulse energy, focal length and beam waist position were optimized [191] to achieve a continuous SC spectral envelope with the best energy stability. The long-wavelength wing of the SC spectrum was selected by a Thorlabs FELH1200 long-pass filter and collimated by a Thorlabs MPD127165-90-P01 parabolic mirror. For spectral measurements, an Ocean Optics NIRQuest512-2.5 spectrometer with an integration time of 100 ms was used. The SC beam profiles were measured using a Xeva XC-130 profilometer with an operating wavelength range from 900 nm to 1700 nm. The SWIR SC spectrum under optimal conditions is shown in Fig. 2.3. The daily repeatability of the SC operation was not disturbed by small changes in the width or energy of the incident pulses.

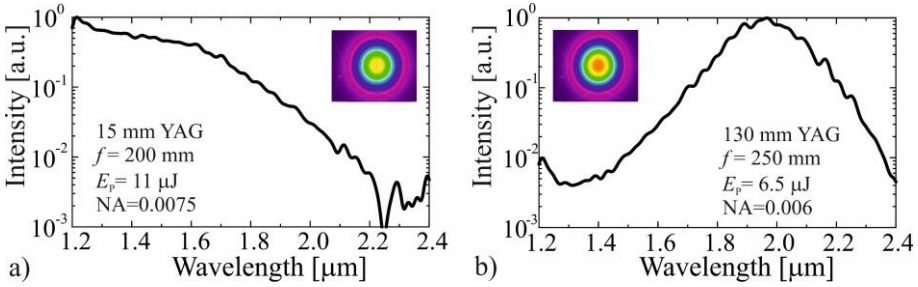


**Fig. 2.3** SWIR SC spectra under optimal conditions in YAG crystals a) 15 mm and b) 130 mm long. The insets show the corresponding beam profiles.  $f$  – focal length,  $E_p$  – pump energy, NA – numerical aperture ( $d/2f$ ), where  $d$  is the beam diameter at the focus ( $1/e^2$  level).

The SWIR SC spectral envelope in the short YAG gradually decayed to  $\sim 1\%$  intensity level at  $\sim 2.1 \mu\text{m}$  (Fig. 2.3 a), whereas in the longer crystal it continued to  $\sim 2.4 \mu\text{m}$  (Fig. 2.3 b) well matching the OPCPA bandwidth at a pump wavelength of  $\sim 1 \mu\text{m}$  [91]. Estimation of the energy of the SC spectral components at wavelengths greater than 1700 nm gives values of  $\sim 5 \text{ nJ}$  and  $\sim 11 \text{ nJ}$  for short and long YAG crystals, respectively. On the other hand, despite the lower SC intensity from the short YAG crystal, the lower accumulated GDD facilitates its sign reversal in materials with positive dispersion in the SWIR range, such as ZnSe, GaAs, CdSe, etc., which is suitable for low-cost compressors. This choice of SC seeds excited by single-picosecond pulses allows to use of either an intense SC seed at  $\sim 1.8\text{--}2.5 \mu\text{m}$  with negative GDD from a longer YAG crystal, or a weak seed with low GDD

from a short crystal. The design of compressors can be varied while maintaining compactness and simplicity.

### 2.3. Analysis of optimal OPCPA configuration in the SWIR range

Since BiBO leads in terms of the highest damage threshold intensity ( $I_{th}$ ) and effective nonlinear coefficient  $d_{eff}$  (Table 1.1), it was chosen to obtain the best gain and conversion efficiency. BiBO, also known as bismuth triborate, is classified as a biaxial crystal due to the distinct refractive indices ( $n_x$ ,  $n_y$ ,  $n_z$ ) along each of its three axes ( $x$ ,  $y$ ,  $z$ ). The phase matching requirements for collinear SWIR OPCPA can be satisfied in the X-Z plane at a pump wavelength of 1.03  $\mu\text{m}$ . In this case, for the phase matching condition, there are two types of signal, idler and pump interactions:  $n_p^e(\theta)\omega_p = n_s^o\omega_s + n_i^o\omega_i$  (oo-e) and  $n_p^o\omega_p = n_s^e(\theta)\omega_s + n_i^e(\theta)\omega_i$  (ee-o). Knowing the phase matching conditions from Equation 1.2, it is possible to determine the angle ( $\theta$ ) between the crystal optical axis and the pump at  $\Delta k = 0$ . The phase matching curves for the ee-o and oo-e interaction types are shown in Fig. 2.4. Although the ee-o curve is wider at degeneracy, the effective nonlinear coefficient  $d_{eff}$  is lower in this case (Table 1.1). Therefore, for maximum pump-to-signal conversion efficiency in SWIR OPCPA, it is more appropriate to use the oo-e phase matching.

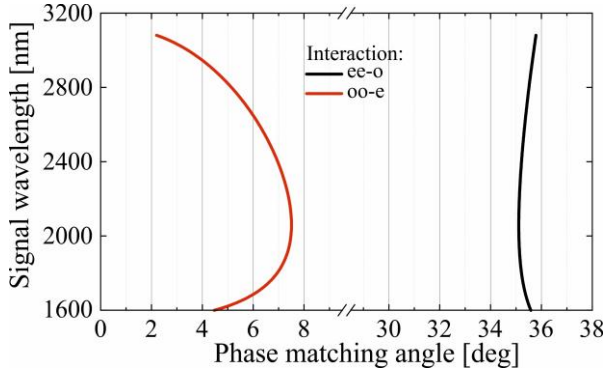


**Fig. 2.4** BiBO crystal phase matching curves for different interactions in a collinear configuration pumped at 1.03  $\mu\text{m}$ .

However, the phase matching curve is not the only factor that determines the OPA gain bandwidth. It is more correct to calculate the dependence of the amplified signal intensity on the wavelength:

$$I_s = I_s(0) \left[ 1 + \frac{\Gamma^2}{g^2} \sinh^2(gz) \right] = I_s(0)G, \quad (2.1)$$

where:

$$\Gamma^2 = \frac{2d_{eff}^2 I_p}{\epsilon_0 c n_p n_s n_i \lambda_s \lambda_i} \text{ and } g = \sqrt{\Gamma^2 - \left(\frac{\Delta k}{2}\right)^2}. \quad (2.2)$$

Here  $z$  is the crystal length,  $I_s(0)$  – the initial signal intensity,  $I_p$  – the pump intensity,  $G$  – the OPA gain,  $\epsilon_0$  – the vacuum permittivity,  $c$  – the speed of light,  $\lambda_s, \lambda_i$  – the signal and idler wavelengths [192]. As can be seen, the signal gain grows exponentially with the crystal length  $z$  and the nonlinear coefficient  $\Gamma$ . Also, the parametric gain can be simplified to  $\sim \sinh^2(gz)$  assuming exact phase matching ( $\Delta k = 0$ ). From this expression, one can derive the relationship between the pump intensity and the crystal length. In this case,  $G$  retains the same value if  $gz$  is constant and can be related to  $\sqrt{I_p z}$ , therefore, a 10-fold reduction in pump intensity to achieve the same gain can be compensated for by increasing the length of the nonlinear crystal by a factor of  $\sim 3.2$ .

Moreover, the OPA gain bandwidth is highly dependent on the phase matching condition. From Fig. 2.5 a) it is evident that changing the angle between the pump wave and the optical axis of the BiBO crystal has a noticeable effect on the signal spectrum.

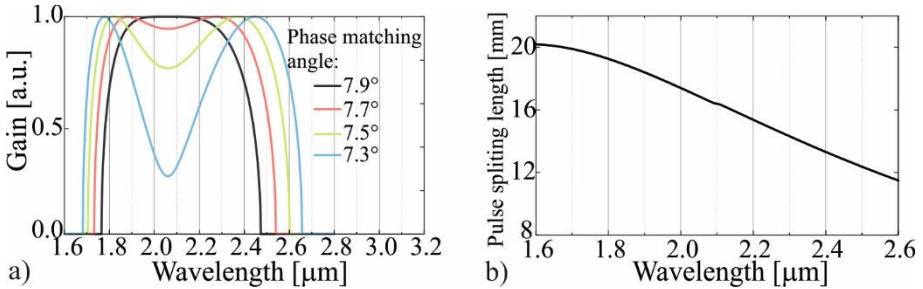


**Fig. 2.5** a) Normalized signal gain for different phase matching angles in a 2 mm thick BiBO crystal at a pump intensity of 100 GW/cm<sup>2</sup>. b) Dependence of the pulse splitting length (Eq. 2.3) on the signal wavelength in a BiBO crystal with a pump pulse width of 1.3 ps (FWHM).

Decreasing this angle results in a significant broadening of the spectrum, whereas decreasing the gain at the degeneracy wavelength leads to a more modulated spectrum at a smaller phase matching angle. Moreover, even a slight deviation in angle can result in a significant change of the signal bandwidth. Therefore, to maintain pulse width stability over several optical cycles, it is necessary to ensure spatial stability of both the pump and the signal in the OPCPA scheme.

It is also important to consider the possible lengths of nonlinear crystal when designing ultrashort pulse pumped OPCPA. The useful coupling length for parametric interaction is quantified by the pulse splitting length, which is defined as the propagation distance over which the signal (or idler) pulse is separated from the pump pulse in the absence of gain, and is expressed as:

$$L = \frac{\tau_p}{\frac{1}{v_{gj}} - \frac{1}{v_{gp}}}, j = s, i, \quad (2.3)$$

where  $\tau_p$  is the pump pulse width and  $\frac{1}{v_{gj}} - \frac{1}{v_{gp}}$  – group velocity mismatch (GVM) between the pump and the signal or idler [49]. Thus, the pulse splitting length usually determines the maximum effective gain length in short-pulse OPAs. Meanwhile, GVM depends on the crystal type, pump wavelength, and phase matching type. The dependence of the splitting length for the picosecond pump pulse on the signal wavelength in the BiBO crystal is shown in Fig. 2.5b. It can be seen that in the entire spectral range of the signal (from 1.6 to 2.6  $\mu\text{m}$ )  $L$  varies from 20 to  $\sim 12$  mm.

Additionally, when determining the optimal crystal length for specific OPCPA setups, it is crucial to consider other factors such as the temporal course of pump depletion and the impact of GDD or TOD on the signal waveform. For instance, excessive crystal length in the final OPCPA stage may prevent the use of entire pump energy, since the pump pulse will initially undergo significant depletion, leading to the onset of back-conversion. However, designing the discussed collinear SWIR OPCPA in a multistage configuration precisely at the degeneracy point does not seem to be possible. In this case, the separation of the signal pulse from the idler at the output becomes unattainable, which leads to interference and instability of the amplified pulses. Hence, OPA must operate near degeneracy, where the signal and idler pulses are spectrally separated. Further analysis of this topic will be presented in Chapter 4. Consequently, to address this issue, a non-collinear configuration is needed that provides spatial separation of the idler and signal beams. Then, in a non-collinear configuration (Fig. 2.6 a), vectorial Eq. 1.1 for the phase matching condition leads to the following two scalar equations:

$$\frac{n_p}{\lambda_p} \cos(\alpha_p) = \frac{n_s}{\lambda_s} + \frac{n_i}{\lambda_i} \cos(\alpha_i), \quad \frac{n_p}{\lambda_p} \sin(\alpha_p) = \frac{n_i}{\lambda_i} \sin(\alpha_i), \quad (2.4)$$

where  $\alpha_p$  is the angle between the signal and pump waves, and  $\alpha_i$  is the angle between the pump and idler waves [193]. In this case, the angle  $\alpha_p$  also



becomes important for the spectral bandwidth of the amplified signal. It is noteworthy that a small angle from 0 to 2° between the pump and signal waves does not lead to a significant change in the amplified signal bandwidth when  $\theta$  also changes (Fig. 2.6 b). In principle, it is possible to amplify the same signal bandwidth as in a collinear configuration.

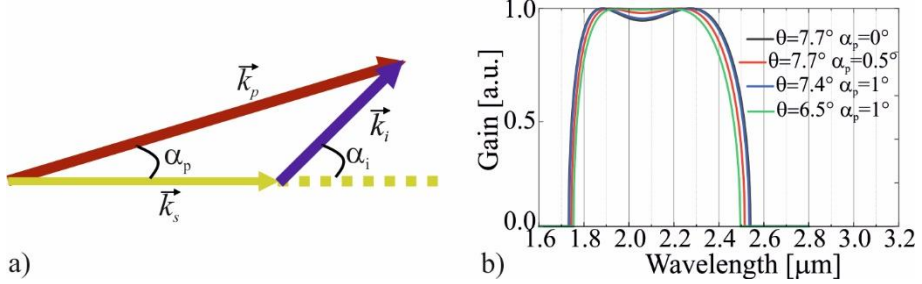


**Fig. 2.6** a) Wave vector configurations and corresponding angles of phase-matched noncollinear three-wave parametric interactions. b) Normalized signal gain at different phase matching angles and angles between the signal and pump waves in a 2 mm thick BiBO crystal at a pump intensity of 100 GW/cm<sup>2</sup>.

#### 2.4. Control of signal pulses in the SWIR OPCPA

Controlling the temporal shape and phase of seed pulses plays a critical role in OPCPA. The output energy and spectrum of OPCPA depend significantly on the signal and pump pulse width. The optimal seed-to-pump pulse width ratio  $\frac{\Delta\tau_s}{\Delta\tau_p}$  for the best OPCPA conversion efficiency also depends on the gain  $G$  and varies from  $\sim 0.4$  to  $\sim 1$  as  $G$  varies from 10 to  $10^7$  [194]. At high gain, spontaneous parametric generation can cause noise at the signal wavelengths with pulse width much shorter than the pump. This noise, known as superfluorescence, can suppress the signal amplification, resulting in a noticeable reduction in both the energy and stability of amplified pulses, as well as appearance of a temporal pedestal after compression.

The pulse width can be controlled using different stretching and compression schemes depending on the OPCPA output power. In high-power OPCPAs, with pump pulse width of tens or hundreds of picoseconds, signal stretching and compression is usually performed by a prism or gratings [195,196]. In contrast, dispersive transparent media and chirped mirrors are typically used to control the signal phase under single-picosecond pumping due to their low loss and compactness [16,24,197]. In particular, precise phase control plays a key role in the generation of ultrashort pulses, where the amplified signal bandwidth matches the bandwidth of the transform-limited pulses approaching few optical cycles. However, when conventional phase

control methods prove insufficient, active phase control is used. This is especially true for TOD, which consistently shows positive values in transparent materials. To counteract this, one can use a prism compressor, chirped mirrors, or an expensive alternative such as an AOPDF.

The main objective of this work was to develop a relatively simple setup where the signal phase in transparent materials is easier to control due to the small amount of GVD and TOD. Dielectric materials exhibit a frequency-dependent refractive index, which results in pulse broadening during propagation, because different frequencies accumulate distinct phases. The phase of a pulse centered at a certain frequency ( $\omega_0$ ) can be determined by estimating the refractive index derivative at  $\omega_0$ . The wave vector  $k$  (Eq. 1.1) can be written as a Taylor expansion of the wave vector at the center frequency:

$$k(\omega) = k(\omega_0) + \left. \frac{\partial k}{\partial \omega} \right|_{\omega_0} (\omega - \omega_0) + \frac{1}{2!} \left. \frac{\partial^2 k}{\partial \omega^2} \right|_{\omega_0} (\omega - \omega_0)^2 + \frac{1}{3!} \left. \frac{\partial^3 k}{\partial \omega^3} \right|_{\omega_0} (\omega - \omega_0)^3 + \dots, \quad (2.5)$$

where  $k(\omega_0)$  denotes the inverse phase velocity, and the first-order derivative denotes the inverse group velocity. Meanwhile, the second and third order derivatives are, respectively, group velocity dispersion (GVD) or group delay dispersion per unit length and TOD per unit length:

$$GVD = \frac{\partial^2 k}{\partial \omega^2}, \quad TOD = \frac{\partial^3 k}{\partial \omega^3}. \quad (2.6)$$

Phase velocity solely alters the phase with a consistent change across all frequencies, while group velocity merely displaces the pulse temporally with a linear phase adjustment. These phase components do not affect the pulse width. In contrast, dispersion characteristics such as GVD and TOD introduce additional second- or third-order phase changes into each spectral component, leading to pulse elongation. In the ultrashort pulse range, control of GVD and TOD is essential to achieve transform-limited pulses.

In our case, seed pulses were generated in a YAG crystal (section 2.2), which exhibits negative GVD in the SWIR range (Fig. 2.7a, the black curve almost merges with the green one). This can be compensated by materials with positive GVD, such as ZnSe (Fig. 2.7a, red line), GaAs, CdSe or Si. However, since these materials have a large nonlinear refractive index  $n_2$ , mJ-level ultrashort pulse compressors cannot maintain peak power below the threshold of competing nonlinear effects. To avoid this, the pulses are compressed in

fused silica (FS) with  $n_2$  about two orders of magnitude lower than of the materials mentioned above. Since the GVD of FS is negative in the SWIR range (Fig. 2.7a, blue line), and the seed pulses are generated in the YAG crystal, the chirp has to be inverted using ZnSe. However, all these materials accumulate positive TOD (Fig. 2.7b), which affects the temporal shape of the amplified pulses after compression.

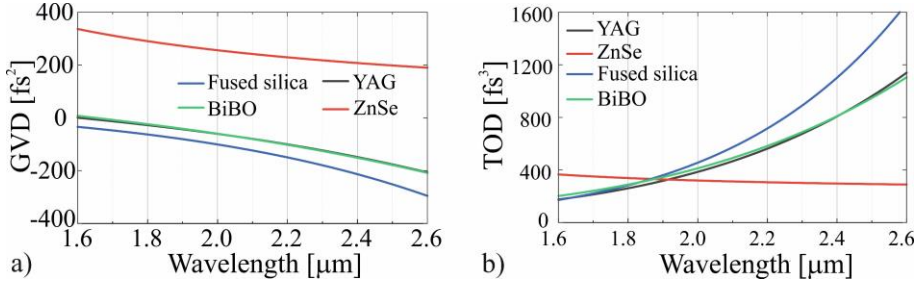


**Fig. 2.7** Theoretical calculations of a) GVD and b) TOD as a function of wavelength in SWIR OPCPA media.

Therefore, for ultimate compression in OPCPA, it is essential to align both the stretcher and compressor for minimum GDD and to reduce TOD as much as possible without sacrificing conversion efficiency.

## 2.5. Experimental setup of three-stage SWIR OPCPA

Based on the above analysis, an experimental setup of a three-stage OPCPA operating in the SWIR range was built (Fig. 2.8). The long-wavelength wing of the SC pulses (Fig. 2.3) was amplified in a three-stage noncollinear OPCPA based on BiBO crystals (type-I, phase matching angle  $\theta = 8^\circ$ ) AR-coated in the range of 1750 – 2500 nm. Most of the  $\sim 11$  mJ output energy of the Yb:YAG laser was used to pump the OPCPA. The BiBO crystal lengths in the three stages were selected to achieve the best conversion efficiency with a negligible spectral narrowing:  $4 \times 4 \times 6$  mm<sup>3</sup>,  $10 \times 10 \times 4$  mm<sup>3</sup>, and  $15 \times 15 \times 4$  mm<sup>3</sup>, respectively. When generating a SC in a 15 mm long YAG crystal, to change the GDD sign, the seed pulse was additionally chirped in an AR-coated ZnSe plate. The OPCPA-amplified signal pulses were compressed in either ZnSe plates or Suprasil 300 glass plates, depending on the sign of the chirp.

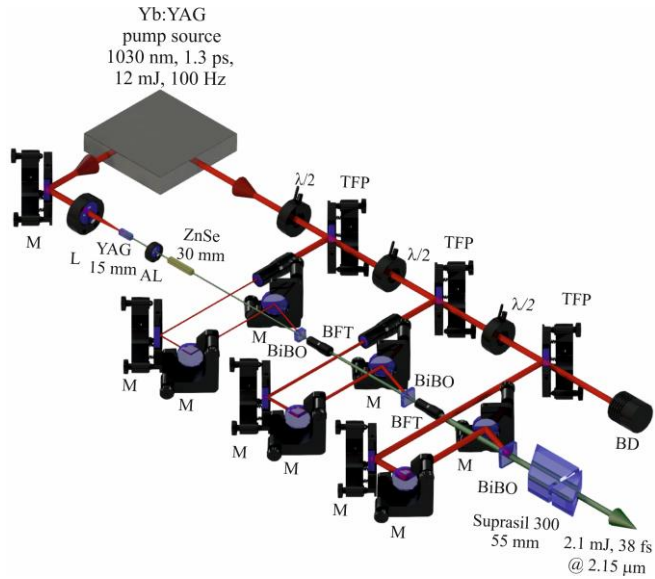


**Fig. 2.8** Experimental setup of mJ-level SWIR OPCPA: Yb:YAG – two-stage Yb:YAG CPA with  $\sim 1.3$  ps output pulses at 1030 nm for OPCPA pumping and SC seed generation, TFP – thin-film polarizers,  $\lambda/2$  – half-wave retardation plates, L – focusing lens, YAG – crystal for SC generation, AL – achromatic lens, ZnSe – AR-coated ZnSe plate, M – HR1030 nm mirrors, BFT – beam forming telescopes, BiBO – nonlinear crystals, Suprasil 300 – a pair of glass prisms for pulse compression.

The compressed pulses were then fed to a second-harmonic frequency-resolved optical gating (SHG-FROG) setup. It was assembled using a thin calcium fluoride beamsplitter with a reflectivity of  $50 \pm 5\%$  in the  $1 - 6 \mu\text{m}$  wavelength range, a  $10 \mu\text{m}$  thick barium borate (BBO) type-I crystal, and an Ocean Optics NIRQuest-512-2.5 spectrometer. The next section details the optimization of the stretcher-compressor for ultimate compression at best conversion efficiency by controlling the GDD and TOD.

## 2.6. Optimization of seed pulse width and OPCPA gain bandwidth

The primary goal was to compress the OPCPA amplified pulses to below 30 fs. For this reason, pulse propagation calculations were performed with a 25 fs transform-limited pulse at a central wavelength of 2060 nm. Hence, as stated above, to mitigate superfluorescence, the ratio  $\frac{\Delta\tau_s}{\Delta\tau_p}$  should be greater than 0.4. According to calculations, the initial signal pulse, after passing through YAG crystals of 15 and 130 mm length, had a duration of  $\sim 100$  and  $\sim 780$  fs (FWHM), respectively (Fig. 2.9a, red solid and purple dashed lines). It was assumed that the SC seed pulse occurs in the waist of the pump beam at a distance of  $\sim 2$  and  $\sim 40$  mm from the input face in the short and long YAG

crystals, respectively. Thus, the calculations took into account the GDD and TOD accumulated by the signal pulse at YAG lengths of  $\sim 13$  and  $\sim 90$  mm. However, the exact location of the spectral broadening into the SWIR range was unknown. Hence, the ratio  $\frac{\Delta\tau_s}{\Delta\tau_p}$  in the long and short crystal was  $\sim 0.6$  and  $\sim 0.07$ , respectively. To improve the OPCPA conversion efficiency with a shorter YAG crystal, it was necessary to either introduce an additional negative GDD into the SC seed pulse or perform chirp reversal using materials with normal dispersion in the SWIR range. As shown in Fig. 2.7, the anomalous dispersion materials exhibit much higher TOD/GVD ratios compared to ZnSe. Therefore, to minimize TOD, it was more practical to lengthen the signal pulse at the output of a short YAG crystal in a 19 mm long ZnSe plate with chirp reversal (Fig. 2.9a, brown dashed line). Although the temporal shape of the pulse in this case turned out to be different due to the TOD being 3 times lower.

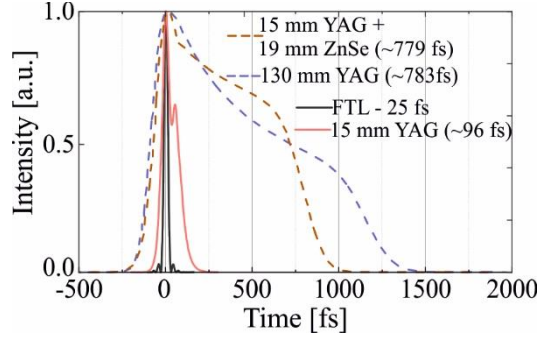


**Fig. 2.9** The transform-limited pulse shape of (black solid line) and the calculated temporal shapes of the signal pulses after propagation in a 15 mm (red solid line) and 130 mm (purple dashed line) YAG crystal, as well as in a 15 mm YAG crystal with an additional 19 mm ZnSe (brown dashed line).

Accordingly, two different single-stage OPCPA configurations were first studied at low pump energy (Fig. 2.10). In both cases, the angle between the pump and SC seed was maintained  $< 2^\circ$  inside the BiBO crystal, and the phase-matching bandwidth was optimized by tuning the pump incidence angle relative to the optical axis of the crystal. The signal spectrum at the output of a single-stage OPCPA is shown in Fig. 2.11a. Regardless of the YAG crystal length (130 mm or 15 mm), used to generate SC seed, the output spectrum spanned from  $\sim 1.9 \mu\text{m}$  to  $\sim 2.5 \mu\text{m}$  with a bandwidth of  $\sim 460$  nm (FWHM), corresponding to a 25 fs transform-limited pulse (Fig. 2.11a, inset), i.e.,  $\sim 3.4$  optical cycles at  $2.2 \mu\text{m}$ . At a pump intensity of  $52 \text{ GW}/\text{cm}^2$ , a maximum

signal energy of  $\sim 14 \mu\text{J}$  and a conversion efficiency of  $\sim 5.1\%$  (Fig. 2.11b, solid line) were achieved in a single OPCPA stage using a long YAG crystal.

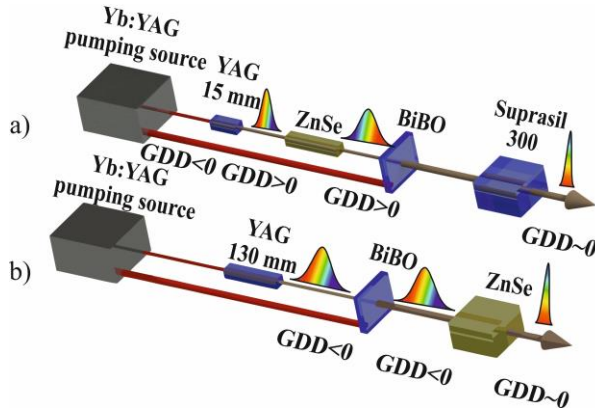


**Fig. 2.10** OPCPA configurations with a) short and b) long YAG crystals.

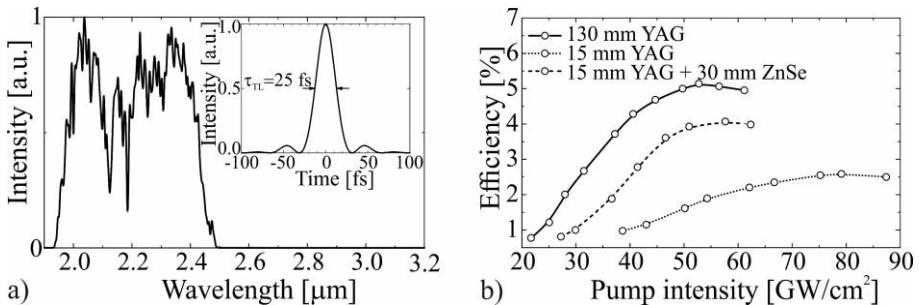


**Fig. 2.11** Performance of the first OPCPA stage. a) Amplified signal spectrum using a 130 mm long YAG crystal to generate the SC seed (inset – transform-limited pulse shape calculated from the spectrum). b) Pump-to-signal conversion efficiency using a 130 mm long YAG (solid line), a 15 mm long YAG (dotted line), and an additional chirp in a 30 mm long ZnSe plate (dashed line).

Further increase of the pump energy above the saturation level led to distortion of the spatiotemporal profiles of the signal pulse. The amplified signal for SC generated in a long YAG crystal was stretched to  $\sim 500$  fs due to the accumulation of GDD in the relatively long YAG and BiBO crystals. The deviation from the theoretical pulse width is apparently explained by displacement of the excitation point of the SC seed from the pump beam waist. For the SC seed obtained from a short YAG crystal, the signal pulse was stretched to only  $\sim 100$  fs, and the pump-to-signal conversion efficiency was only  $\sim 2.6\%$ , saturating at a much higher pump intensity of  $\sim 80 \text{ GW/cm}^2$  (Fig. 2.11b, dotted line) with a maximum output energy of  $\sim 9 \mu\text{J}$ . To improve the conversion efficiency to  $\sim 4\%$  (Fig. 2.11b, dashed line), the SC seed was

additionally chirped to  $\sim 500$  fs in a 30 mm long ZnSe plate (Fig. 2.10a). The length of the ZnSe plate exceeded the previously estimated one, since the BBO crystal, like the YAG crystal, has a negative GDD. No significant narrowing of the spectrum of the amplified signal was observed. Despite similar signal pulse widths, using a longer YAG crystal resulted in  $\sim 20\%$  greater efficiency and output energy, most likely due to the higher SC spectral intensity and different pulse shapes (Fig. 2.9).

The ability to apply positive or negative signal chirp simplifies the selection of the optimal compressor configuration in high-energy OPCPA. Propagating over a length of 90 mm in YAG and over a length of 6 mm in BiBO, the signal pulse accumulates a negative GDD, which is then compensated by a 26 mm long ZnSe plate. Meanwhile, propagating over a length of 15 mm in YAG and 6 mm in BiBO, the signal pulse acquired a negative GDD, then expanded in 30 mm long ZnSe with a positive GDD, and finally compressed in a 58 mm long fused silica. The total accumulated GDD and TOD in both cases are presented Table 2.2. For the short YAG crystal, the overall GDD and TOD are marginally reduced, but the accumulated TOD in both cases remains large enough to affect the temporal profile of the  $<30$  fs compressed high-energy pulse.

**Table 2.1** Calculated GDD and TOD for the amplified signal from the first OPCPA stage at a central wavelength of 2060 nm and the output pulse width (FWHM) compared to Fourier transform limit (FTL) using either a glass compressor or a ZnSe plate with a SC seed obtained in 15 or 130 mm long YAG crystals.

YAG length	FTL pulse width [fs]	Output GDD [fs <sup>2</sup> ]	Acquired TOD [fs <sup>3</sup> ]	Compressor GDD [fs <sup>2</sup> ]	Output pulse width [fs]
15 mm	25	$\sim 0$	49000	$-6600$	$\sim 47$
130 mm	25	$\sim 0$	52000	7000	$\sim 48$

The calculated temporal shape of the amplified signal pulses after compression in a ZnSe plate using a SC seed obtained in a long YAG crystal is shown in Fig. 2.12a. Since the residual TOD is similar in both cases, the temporal pulse shape will also be similar. The pulse width of  $\sim 47$  fs (FWHM) is  $\sim 1.9$  times higher than FTL due to uncompensated TOD. Hence, with single-picosecond pumping, it is impossible to obtain  $<30$  fs high-energy pulses in the SWIR range only by controlling the higher order dispersion of the medium. Thus, to achieve high-contrast, high-energy, few-cycle pulses in the SWIR range, even at TOD much lower than those in setups pumped with tens or hundreds of picoseconds pulses [64], higher-order dispersion compensation becomes important. In this case, specially designed chirped

mirrors with both GDD and TOD compensation are used. Moreover, more expensive setups use AOPDF as a stretcher and bulk material or chirped mirrors as a compressor.

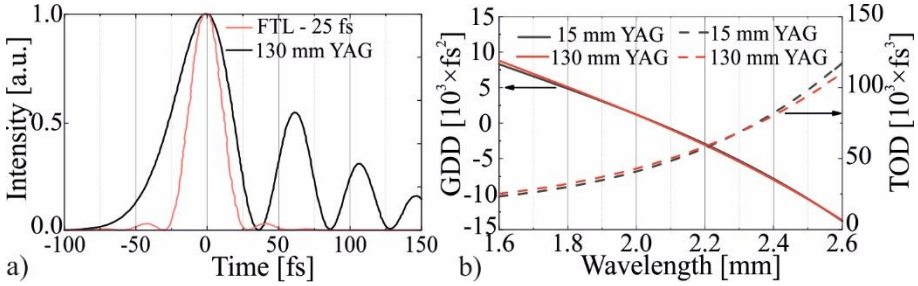


**Fig 2.12** a) Calculated temporal shape of the amplified signal pulses after compression in ZnSe plate (solid black line) using a SC seed obtained in 130 mm YAG crystal compared to FTL (red line). b) Acquired GDD (solid lines – left axis) and TOD (dashed lines – right axis) of the signal after single-stage OPCPA as a function of wavelength using a SC seed obtained in 15 and 130 mm long YAG crystals.

For the above calculation of the temporal pulse shape, only the dispersion at the central degeneracy wavelength of 2060 nm was taken into account. However, over a wide spectral bandwidth, components at distinct wavelengths acquire different GDD and TOD. In particular, for the wavelength range of 1.8 – 2.4  $\mu\text{m}$ , the TOD varied by more than  $\sim 5 \times 10^4 \text{ fs}^3$ , while the GDD varied by more than  $\sim 1.25 \times 10^4 \text{ fs}^2$  (Fig. 2.12b). This means that different spectral components required different lengths of the dispersive medium to fully compensate for the accumulated GDD. Hence, experimental results may differ from calculations, but the general trends are similar.

As mentioned above, although ZnSe has zero dispersion at  $\sim 4800 \text{ nm}$ , it exhibits a very high nonlinear refractive index  $n_2$ . Therefore, the maximum aperture of commercially available ZnSe plates is insufficient to maintain peak power below the threshold of competing nonlinear effects in ultrashort pulse mJ-level compressors. This is why it is typically used as a pulse stretcher before OPCPA stages or as a compressor in high average but low peak power setups [73]. Based on this, it was decided to compress positively chirped pulses in Suprasil 300 glass with  $n_2$  two orders of magnitude lower than that of ZnSe and a transmission of  $>90\%$  in the range of 0.5 – 2.5  $\mu\text{m}$ . According to calculations (Fig. 2.12a), the amplified signal pulses with a spectral bandwidth corresponding to the FTL pulse width of  $\sim 25 \text{ fs}$  were compressed in a 55 mm long Suprasil 300 plates to  $\sim 47 \text{ fs}$  (FWHM), while the tail (Fig. 2.13a) did not exceed  $\sim 35\%$  of the total pulse energy. Given these preliminary results, a trade-off was made in the design of a cost-effective high-



energy SWIR OPCPA: reduce the bandwidth and explore compression only with GDD compensation in mind. Then the total TOD accumulated in OPCPA had less influence on the output pulse shape (Fig. 2.13b). By gradually limiting the spectral bandwidth according to the FTL pulse width from 20 to 40 fs, the temporal contrast can be improved by  $\sim 30\%$  with shorter output pulses. Based on these estimations, the influence of higher-order dispersion on the temporal shape of the compressed pulse was suppressed by narrowing the spectral bandwidth of the amplified signal to match the FTL pulse width of 35 fs.

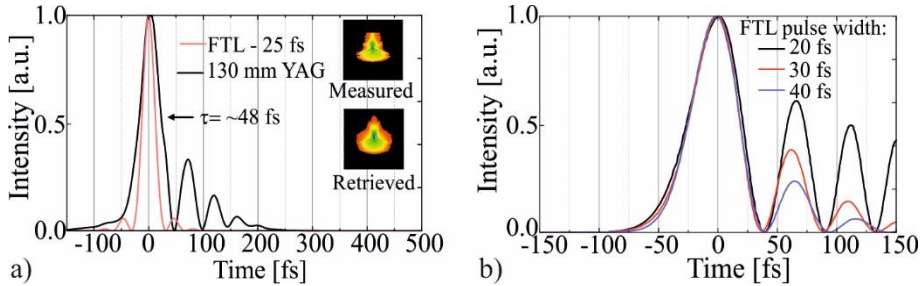


**Fig. 2.13** a) SHG-FROG retrieved temporal profile (black line) of the amplified signal pulse after compression in Suprasil 300 plates with a SC seed obtained in a 15 mm YAG crystal, compared to the FTL pulse calculated from the measured spectrum (red line). Insets – measured (top) and reconstructed (bottom) FROG traces with an error of 0.9% and a  $512 \times 512$  grid. b) Temporal pulse shape calculated after a single OPCPA stage with different bandwidths at a central wavelength of 2060 nm.

## 2.7. High-energy three-stage OPCPA operating in the SWIR range

To narrow the gain bandwidth in the high-energy OPCPA (Fig. 2.8), we detuned the phase matching in all three stages. The amplified pulse spectrum then spanned the range from  $\sim 1.95 \mu\text{m}$  to  $\sim 2.4 \mu\text{m}$  (Fig. 2.14a) with a bandwidth corresponding to the FTL pulses of  $\sim 35$  fs (Fig. 2.14a, inset), which is  $\sim 4.9$  optical cycles at a central wavelength of  $2.15 \mu\text{m}$ . After the second OPCPA stage, the signal pulses were amplified up to  $250 \mu\text{J}$  with a pump-to-signal efficiency of 14%, reaching a saturation at a pump power intensity of  $\sim 35 \text{ GW}/\text{cm}^2$ . Superfluorescence was not observed until the pump pulse energy exceeded the saturation level in the first and second stages. In the final OPCPA stage, the highest pump pulse energy of  $\sim 9 \text{ mJ}$  was used. Due to the high energy of the incident signal, the pump intensity was reduced to  $\sim 30 \text{ GW}/\text{cm}^2$ , which was close to the saturation level. As a result, the energy of the amplified signal reached  $\sim 2.25 \text{ mJ}$  (Fig. 2.14b) with a pump-to-signal conversion efficiency of  $\sim 25\%$ .

It should be noted that the noncollinear degenerate OPCPA also provides angularly dispersed idler pulses at  $\sim 2.1 \mu\text{m}$  wavelength, that have the same pulse energy, polarization, and spectral bandwidth as the amplified signal pulses. These pulses have the opposite chirp sign to the signal pulses and can be separately compressed using Si/ZnSe blocks. Thus, the total energy available at  $2.15 \mu\text{m}$  wavelength from signal and idler pulses reached  $\sim 4.5 \text{ mJ}$  with an overall conversion efficiency of  $\sim 50\%$ .

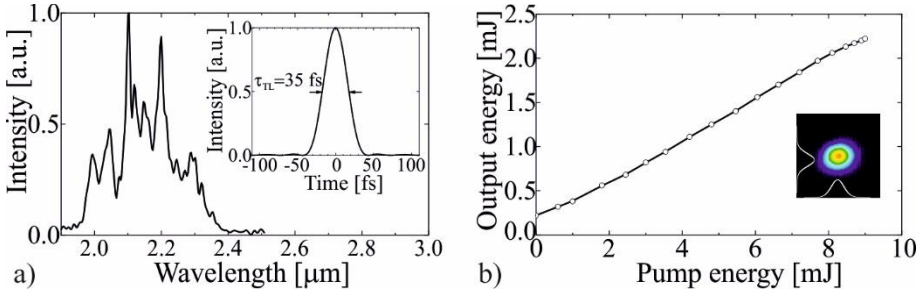


**Fig. 2.14** a) Output spectrum of a three-stage OPCPA (inset – FTL pulse shape calculated from the measured spectrum). b) Output energy versus pump pulse energy in the final OPCPA stage (inset – far-field beam profile at  $2.15 \mu\text{m}$  wavelength with maximum output energy).

The far-field amplified signal beam profile was measured by two-photon excitation using a Si-CMOS camera (WinCamD-LCM, DataRay) at the  $750 \text{ mm}$  focus of a  $\text{CaF}_2$  lens. At maximum output energy, the intensity distribution was close to Gaussian, indicating the absence of back conversion (Fig. 2.14b, inset).

Although there was still about  $10 \text{ mJ}$  of unused pump energy left, we did not increase the pump pulse energy in the last OPCPA stage due to saturation in the BiBO crystal with the maximum aperture available at the time of the experiments. Thus, further increase of the output energy can be achieved either by using nonlinear crystals with a larger aperture or by forming a top-hat intensity profile of the pump beam. Although BiBO crystals with apertures up to  $20 \times 20 \text{ mm}^2$  are becoming available,  $20 \times 20 \text{ mm}^2$  YCOB crystal can also be used in the last OPCPA stage [24], albeit with lower conversion efficiency (Tab. 1.1). To utilize all available pump energy, a shorter BiBO crystal can also be used in the last OPCPA stage or an additional stage.

After three OPCPA stages, a chirped signal pulse width of  $\sim 420 \text{ fs}$  (FWHM) was observed. To compress the amplified pulses, two Suprasil 300 glass blocks were used, the input and output faces of which were cut at the Brewster angle for the first and second, respectively (Fig. 2.15a). In this setup, the most distant spectral components of the signal (at  $\sim 1.8$  and  $\sim 2.4 \mu\text{m}$ ) will

be separated by  $\sim 0.2$  mm. Since this discrepancy is  $\sim 40$  times smaller than the beam size, spatial dispersion can be neglected. By adjusting the propagation length in glass blocks, a GDD value of  $-5100$  fs<sup>2</sup> was obtained. Due to reflection losses on the glass surface, the output energy was reduced to  $\sim 2.1$  mJ ( $\sim 90\%$  transmission).

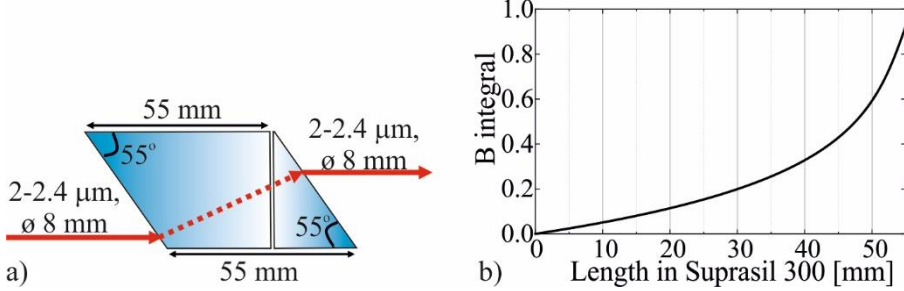


**Fig. 2.15** a) Diagram of a Suprasil 300 glass block cut at Brewster angle. b) Increase in B-integral as the pulse propagates through the compressor.

At the ultimate compression of mJ-level laser pulses in a glass volume, it becomes important to estimate the nonlinear phase shift. At radiation intensities reaching tens of GW/cm<sup>2</sup>, self-focusing and self-modulation phenomena may occur. The B-integral parameter is used to estimate the maximum phase shift due to nonlinearity accumulated over the entire length of the dispersive medium:

$$B = \frac{2\pi}{\lambda} \int n_2 I(z) dz, \quad (2.7)$$

where  $I(z)$  is the optical intensity along the beam axis,  $z$  is the position in the beam direction, and  $n_2$  is the nonlinear refractive index of the medium. When the B-integral value is less than 1, such phase distortions do not affect the shape of the pulse envelope. At values above  $\approx 3-5$  there is a risk of self-focusing, spectrum broadening, pulse breakup or deterioration of beam quality. In our case, a beam with diameter of 8 mm (at the level of  $1/e^2$ ) propagates over a length of 55 mm in Suprasil 300 glass with  $n_2 = \sim 2.74 \times 10^{-16}$  cm<sup>2</sup> [198]. Accordingly, the accumulated B-integral in the compressor reached  $\sim 0.9$  at maximum output energy (Fig. 2.15 b).

The retrieved temporal phase of the pulses compressed to  $\sim 38$  fs was almost flat (Fig. 2.16b). This pulse width corresponds to  $\sim 5$  optical cycles at a wavelength of  $2.15$   $\mu$ m. However, the uncompensated TOD resulted in a  $\sim 10\%$  pedestal of the main pulse. The measured pulse width differed from the FTL by less than 8%, and  $\sim 80\%$  of the pulse energy contained within a  $\pm 50$  fs

window. The calculated peak power of the compressed pulse was  $\sim 47$  GW. The stability of the output energy StDev  $\pm 4\%$  (Fig. 2.16a) was observed during 30 min of operation without a protective casing in air flows from the filters. Thus, without jitter compensation, the energy stability was 2 times worse than that of the pump laser.

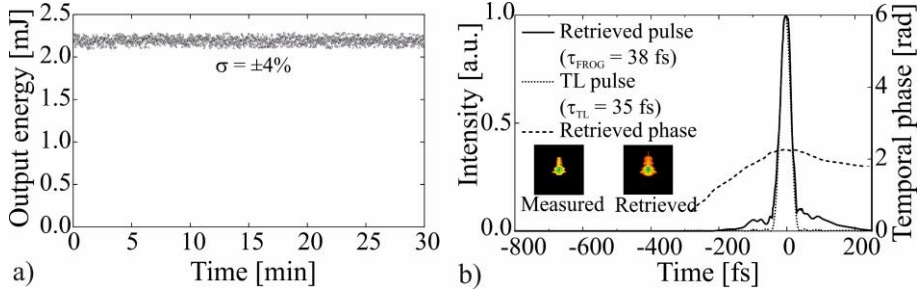


**Fig. 2.16** a) Energy stability of OPCPA output pulses during 30 min of operation. b) SHG-FROG retrieved temporal profile (solid line) and temporal phase (dashed line) of the compressed signal pulse at maximum output energy compared to the FTL pulse, calculated from the measured spectrum (dotted line). Insets – the measured (left) and retrieved (right) FROG traces with an error of 1.1% using a 512×512 grid.

The possibility of compressing amplified pulses to  $<30$  fs with further increase in peak power to  $>80$  GW using adaptive phase control will be discussed further.

## 2.8. OPCPA with integrated AOPDF operating in the SWIR range

To overcome the SWIR pulse compression challenges due to the acquired TOD, an AOPDF were used. Developed by P. Tournois, the AOPDF is an acousto-optical collinear beam modulator capable of controlling the spectral phase and amplitude of ultrashort laser pulses [199]. The operating principle of AOPDF resembles that of a Bragg grating, where the grating is generated by inducing a programmable acoustic wave in a highly birefringent crystal, such as tellurium dioxide ( $\text{TeO}_2$ ) [200]. This acoustic wave, whose frequency varies with time, is spatially replicated within the crystal as it advances along the z-direction, as shown in Fig. 2.17. The anisotropic interaction of waves ensures diffraction of the incident optical wave from the ordinary to the extraordinary axis of the crystal. Diffraction occurs only when a certain phase matching between acoustic and optical waves is met. By manipulating the frequencies within an acoustic wave, each optical frequency  $\omega$  travels a certain distance before it encounters a phase-matched spatial frequency in the acoustic grating, acquiring unique group delays due to the difference in refractive index

between the ordinary and extraordinary axes. Thus, the pulse emerging from the device at extraordinary polarization has only those spectral components that were diffracted at different positions. In addition, the amplitude of the diffracted spectral component is controlled by the acoustic intensity at the location of its diffraction, which allows AOPDF to perform both amplitude and phase modifications.

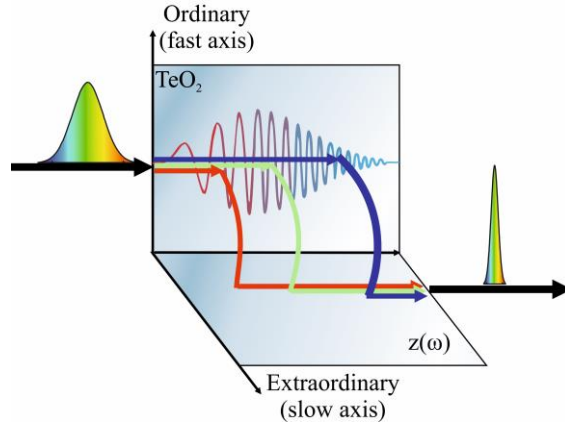


**Fig. 2.17** Diagram of the operating principle of AOPDF [200].

One of the limitations of AOPDF concerns its efficiency. Optimum efficiency is achieved when the acoustic wave propagates longitudinally throughout the crystal under the influence of the applied GDD. Efficiencies of up to 50% can be achieved using powerful radio frequency amplifiers. However, in an OPCPA setup with single-picosecond pumping, even a moderate efficiency of  $\sim 20\text{--}30\%$  is considered sufficient. Another disadvantage is the induced spatial chirp of the diffracted pulse, since the spectral components are diffracted at different locations in the crystal, leading to walk-off due to the birefringence. To prevent any spatiotemporal issues in OPCPA, the spatial chirp can be eliminated before amplification by using a pair of prisms or by implementing a double pass through the AOPDF. Despite these limitations, AOPDFs play a key role in high-energy few-cycle OPCPA setups.

Thus, to compensate for higher order dispersion, we integrated an AOPDF (Dazzler WB45-1450-3000 from Fastlite) with a wavelength tuning range of  $1.45\text{--}3\ \mu\text{m}$  before the first OPCPA stage (Fig. 2.18). The radio frequency and optical signals were synchronized using a digital delay generator. In this case, chirped mirrors can be used to mitigate nonlinear effects in the pulse compressor. To compare the OPCPA efficiency, seeds were obtained in YAG crystals of 15 and 130 mm length. However, the impact of Dazzler on the compressed pulse width was only assessed after amplifying the SC seed

obtained from a 130 mm long YAG crystal in a 6 mm long BiBO crystal of the first OPCPA stage.

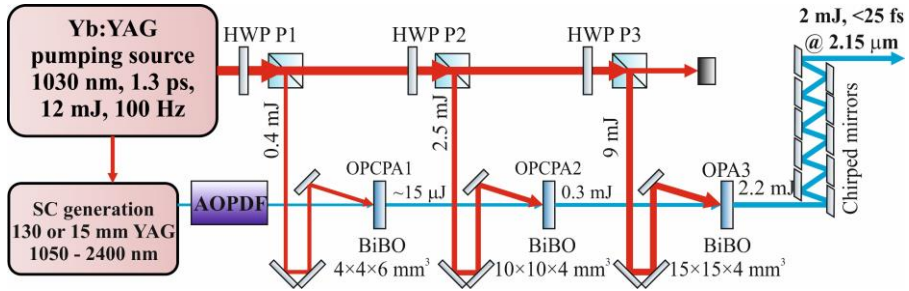


**Fig. 2.18** Experimental setup of a three-stage OPCPA based on BiBO with AOPDF. HWP – half-wave retardation plates, P1-P3 – polarization cubes

The widest bandwidth was achieved by optimizing the angles between the seed and pump beams, as well as between the pump and the crystal optical axis. This provided an output spectrum in the range of  $\sim 1.8 - 2.4 \mu\text{m}$  (Fig. 2.19a), with a bandwidth corresponding to a FTL pulse width of  $\sim 20$  fs.

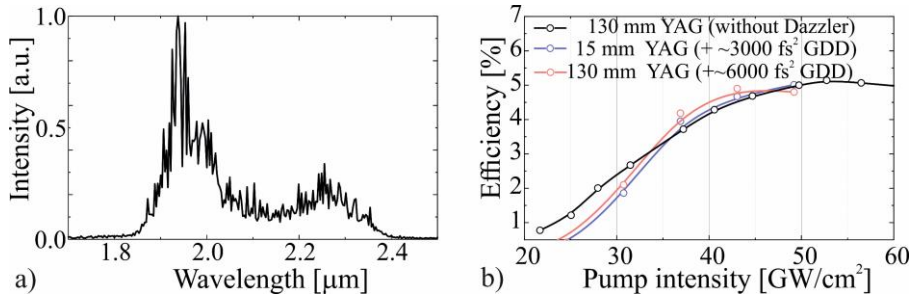


**Fig. 2.19** a) Spectrum of amplified pulses after the first OPCPA stage. b) Pump-to-signal conversion efficiency in the first OPCPA stage seeded with a SC obtained in a 130 mm long YAG crystal without Dazzler (black line) compared to that using Dazzler with 15 mm (blue line) or 130 mm (red line) long YAG crystals.

The conversion efficiency of  $\sim 5\%$  obtained in the first OPCPA stage (Fig. 2.19b) using SC seeds obtained in short and long YAG crystals was similar to that without Dazzler. To achieve maximum efficiency, the signal was further chirped with a GDD of  $\sim 3000$  or  $\sim 6000 \text{ fs}^2$  to a pulse width of  $\sim 550$  fs for short and long YAG crystals, respectively. Hence, given the similar efficiency at almost the same signal pulse width, it follows that the SWIR SC seed pulses are excited over a length of  $\sim 80$  mm in a long YAG crystal. However, positively chirped pulses are not suitable, since with a small amount of GDD accumulated over the total length of 14 mm BiBO crystals in

a three-stage OPCPA, the amplified pulses only reach  $\sim 140$  fs (Fig. 2.20a, black line) after higher-order dispersion compensation. Moreover, the conversion efficiency in second and third OPCPA stage will be reduced compared to the configuration without Dazzler. Conversely, at negative GDD, a signal pulse width of  $\sim 1$  ps (Fig. 2.20a, red line) after OPCPA is optimal for the best conversion efficiency in the final stage.

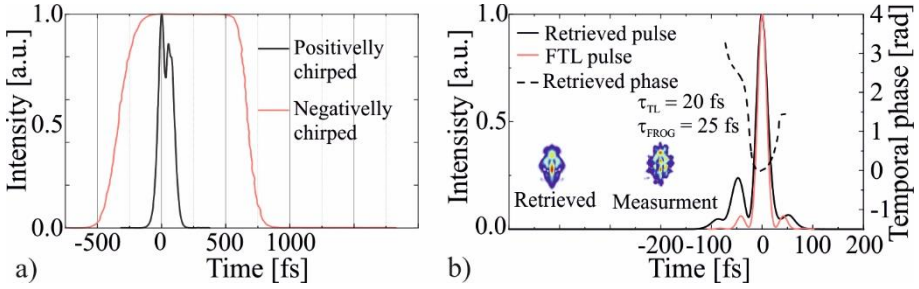


**Fig. 2.20** a) Calculated temporal shape of the signal pulse after three OPCPA stages with positive (black line) or negative (red line) chirps. b) The temporal profile (black solid line) of the amplified pulse after compression retrieved from the SHG-FROG measurement, compared to the transform-limited pulse (red) and the retrieved temporal phase (dashed black line). Insets are measured and retrieved FROG traces with  $\sim 1\%$  error using a  $512 \times 512$  grid.

In the OPCPA setup with a long YAG crystal and integrated AOPDF, the GDD, TOD, and FOD values were carefully tuned to ensure that the amplified pulse width after the first stage was close to the FTL of 20 fs. By compensating for the dispersion in a long YAG crystal, a 45 mm long  $\text{TeO}_2$  crystal, and a 6 mm long BiBO crystal, which corresponded to a cumulative dispersion of  $\sim 3800$  fs<sup>2</sup> GDD,  $\sim 32000$  fs<sup>3</sup> TOD and  $\sim 170000$  fs<sup>4</sup> FOD,  $\sim 25$  fs pulses were achieved (Fig. 2.20b). However, FROG still exhibited residual dispersion, requiring even more fine tuning of the AOPDF. Given the significant wavelength dependence of GDD and TOD in YAG and BiBO crystals (Fig. 2.7), it is important to optimize the spectral phase settings in Dazzler to provide distinct GDD and TOD values for different wavelengths.

As mentioned earlier, in the OPCPA configuration with AOPDF, using positive GDD CMs to compress the amplified pulses to a few mJ is the most effective approach to mitigating nonlinear effects in the pulse compressor. However, the negative GDD CMs were sourced from "Ultrafast Innovation" long before the feasibility of integrating AOPDF into the OPCPA setup became apparent. It was expected that this choice would reduce the TOD accumulated in the compressor glass block and thus increase the

temporal contrast of the compressed pulses. However, these CMs with a GDD of  $-500 \text{ fs}^2$  in the spectral range from 1.9 to  $2.4 \mu\text{m}$  (Fig. 2.21) were not tested in the OPCPA setup.

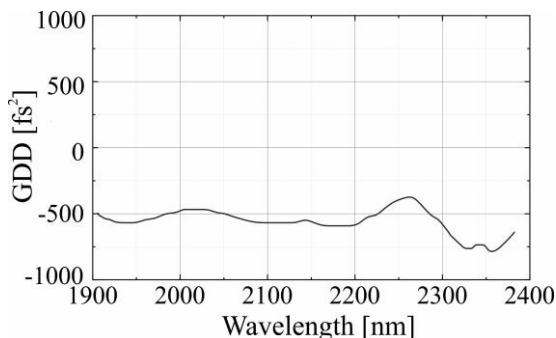


**Fig. 2.21** Measured GDD for custom-made CMs in the 1.9– $2.4 \mu\text{m}$  wavelength range.

On the other hand, when AOPDF is integrated into the setup more appropriate is to use negative chirped pulses. In this case, using a positive GDD CMs of  $+500 \text{ fs}^2$  will require only eight bounces to reach FTL, when the optimal pulse width incident on the OPCPA is 550 fs. Thus, in this configuration, a peak power of  $\sim 80 \text{ GW}$  is achievable after compression, sufficient for filamentation in the ambient air. However, even at lower peak powers, the exploration of gas sensing capabilities is of interest and the relevant feasibility studies are described below.

## 2.9. Excitation of supercontinuum in the MWIR range for gas sensing

Further experiments were carried out to extend the SC spectrum into the MWIR range. Such laser radiation is relevant both for SRS seeding and for remote sensing of volatile substances. Timely remote detection of airborne hazardous chemicals during emergencies is critical to ensuring the safety of facilities, infrastructure, personnel and civilians. Broadband SWIR–MWIR pulses, covering multiple molecular vibrations of molecules such as  $\text{H}_2\text{O}$ ,  $\text{CO}_2$ ,  $\text{CO}$ , and  $\text{NH}_4$ , can be used in remote sensing LIDARs to detect biochemicals and air pollutants [201]. In this case, the transition into the MWIR wavelength range is achieved by filamentation of high-intensity laser pulses in air or transparent media. Compared to traditional LIDARs using nanosecond laser pulses, the airborne filamentation overcomes the diffraction limit over long propagation distances, providing directional backscattered light [202]. However, due to the limited intensity of SWIR pulses, the MWIR



SC generation tests were carried out under conditions of anomalous and normal dispersion in 10 mm long YAG and 30 mm long ZnSe crystals.

A wide transmission range with a high damage threshold and zero-dispersion wavelength at 1.6  $\mu\text{m}$ , make YAG suitable for filamentation in the MWIR range [203–205]. Moreover, its dispersion curve remains relatively flat up to the visible range. The dispersion of ZnSe is also relatively flat in the wavelength range of  $\sim 1.5 - 5.5 \mu\text{m}$ . The split portion of the OPCPA output pulses with an energy of  $\sim 100 \mu\text{J}$  was attenuated by neutral density filters (Fig. 2.22) and suppressed after SC excitation using an Edmunds Optics FELH2400 long-pass filter. The SC beam collimated by a parabolic mirror was fed into the input fiber of the Avesta ASP-IR-3.5 spectrometer, covering the spectral range 1200 – 3450 nm.

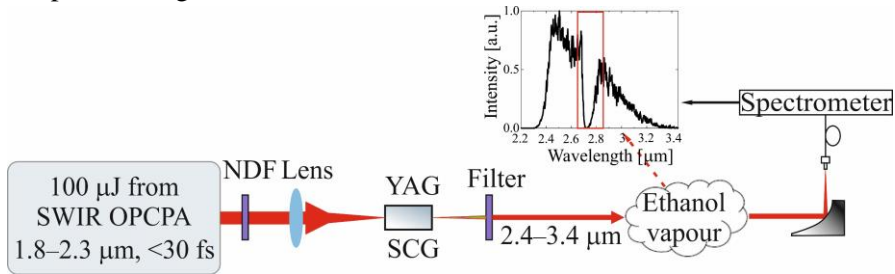


**Fig. 2.22** Experimental setup for gas sensing. NDF – neutral density filter, SCG – supercontinuum generation.

Particular attention was paid to the stability of the energy and spectral envelop of SC pulses at wavelengths above 3  $\mu\text{m}$  by optimizing the incident pulse energy, focal length, and beam waist position. The optimal incident pulse energies of 10  $\mu\text{J}$  and 15  $\mu\text{J}$  were determined for YAG and ZnSe crystals, respectively, with a  $\text{CaF}_2$  lens of 250 mm focal length. The obtained SC spectrum extended to  $\sim 3 \mu\text{m}$  and  $\sim 3.5 \mu\text{m}$  in ZnSe and YAG, respectively (Fig. 2.23 a). At higher energies, the formation of multiple filaments was observed.

Due to its higher MWIR SC spectral intensity, the YAG crystal was chosen for probing illumination in gas detection tests (Fig. 2.23 a). A collimated SC beam was directed over an open-necked cell filled with ethanol ( $\text{C}_2\text{H}_6\text{O}$ ). A well-defined absorption line was detected at  $\sim 2730 \text{ nm}$  (Fig. 2.23 b, dashed line), coinciding with the reference line of ethanol vapor at  $3670 \text{ cm}^{-1}$  from the NIST database (Fig. 2.23 b, red line). Thus, it was shown that the obtained SC MWIR radiation is suitable for detecting volatiles in laboratory conditions, while remote sensing of gas in backscattered light was beyond the scope of this work.

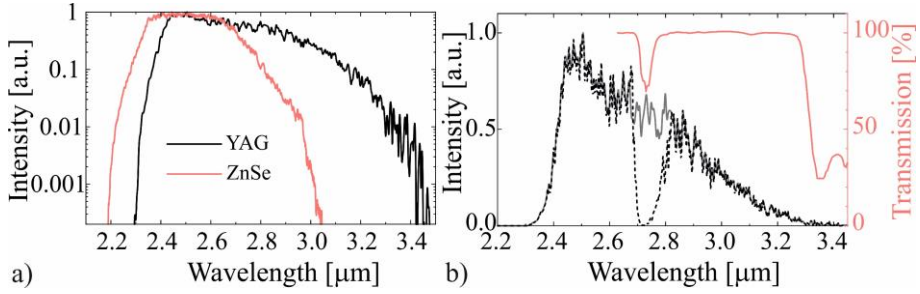


**Fig. 2.23** a) MWIR SC spectra obtained in YAG (black line) and ZnSe (red line) crystals under optimal conditions. b) Spectra of incident (black solid line – left axis) and transmitted (black dashed line – left axis) laser radiation through ethanol vapor in comparison with NIST data (red line – right axis).

## 2.10. Summary of the results

We compared several SWIR OPCPA configurations pumped by a single-picosecond Yb:YAG laser and different compression methods to achieve few-cycle multi-mJ output pulses in the SWIR range. In these setups, the SWIR wing of SC pulses obtained with the same pump laser in 15 mm and 130 mm long YAG crystals was used as a seed. The SWIR SC pulses were first amplified in a single-stage OPCPA. Due to the higher SC seed intensity obtained from the longer YAG crystal, better pump-to-signal conversion efficiency and higher output energy were achieved. Regardless of the YAG crystal length, the amplified pulse spectrum corresponded to  $\sim 25$  fs ( $< 4$  cycles) FTL pulses at a central wavelength of  $\sim 2.2$   $\mu\text{m}$ . However, residual dispersion after compression in the bulk material limited the pulse width to  $\sim 47$  fs. Next, a three-stage SWIR OPCPA setup was developed with an output energy of  $\sim 2.1$  mJ and a signal-to-pump conversion efficiency of up to 25% in the last stage. The amplified pulses were compressed in a glass block to  $\sim 38$  fs, resulting in a peak power of  $\sim 47$  GW. Further integration of AOPDF allowed pulse compression to  $\sim 25$  fs after the first OPCPA stage. Thus, proper selection of the signal pulse width and fine tuning of the GDD make it possible to achieve pulses  $< 30$  fs with a peak power of  $\sim 80$  GW. However, the integration of AOPDF significantly increases the cost [16,24,206]. Further optimization of Dazzler is required to achieve maximum compression to  $< 25$  fs.

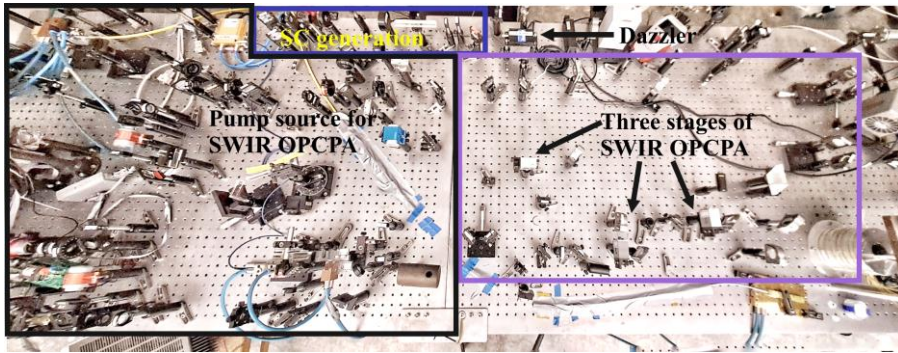


**Fig. 2.23** Photo of the developed SWIR OPCPA setup with Yb:YAG CPA.

In the developed OPCPA setup (Fig. 2.23), SC seed pulses in the SWIR range were amplified directly to the mJ level for the first time. The achieved conversion efficiency in the last stage approached the limit [24,25,55,56]. The repetition rate of the described OPCPA of 100 Hz is limited by the used self-made Yb:YAG CPA pump source. Although the lack of CEP stability compared to DFG is a drawback, the suitability of such a laser source for the detection of volatiles has been verified. Also, since the developed setup provides intensities of  $\sim 10^{13} - 10^{15} \text{ W/cm}^2$  at the focus, it can be used to generate soft X-rays in the water window [16]. Moreover, the passively CEP-stable idler pulse after the first OPCPA stage can be used for amplification in the second and third stages. Then the angular dispersion of the idler pulse can be compensated using prisms or wedges. This opens up the possibility of developing compact cost effective mJ-level CEP-stable SWIR lasers with a pulse width of less than 25 fs.

### 3. TRANSIENT SRS IN THE NEAR IR RANGE

One of the goals of this study was to further extend the SWIR OPCPA output pulse spectrum to longer wavelengths using a transient SRS. But this is initially easier to implement in the near IR range using 1.3 ps pump pulses at 1030 nm. In addition, femtosecond pulse radiation sources in the wavelength range of  $\sim 1 - 1.3 \mu\text{m}$  are of great importance for two-photon imaging of living tissues [207]. It has recently been shown that excitation at wavelengths of  $\sim 1050 - 1700 \text{ nm}$  provides  $\sim 50-100\%$  greater imaging depth compared to 800 nm [208, 209]. Moreover, increasing the wavelength of driving femtosecond pulses allows generating attosecond X-ray pulses with higher photon energy [210] and increasing the efficiency of THz radiation [6]. In particular, sources of intense THz radiation are based on optical rectification of femtosecond pulses in highly nonlinear organic crystals. These applications require intense lasers at relatively difficult-to-reach wavelengths of  $\sim 1.1 - 1.5 \mu\text{m}$ . In this spectral range, optical rectification ensures the best phase-matching conditions, ideal for studying ultrafast processes in atoms and molecules [211]. Although, OPCPA remains the dominant frequency conversion method here, SRS may also be an alternative.

The most well-known Raman-active medium is hydrogen, combining the largest vibrational shift of  $4155 \text{ cm}^{-1}$  with a high gain. However, in the NIR range, rotational shifts of  $587 \text{ cm}^{-1}$  and  $342 \text{ cm}^{-1}$  [212–214] in ortho- and para-hydrogen are more attractive for generating optical frequency combs and ultrashort pulses [215]. In this case, orthohydrogen has a higher gain. However, most studies have focused on the excitation of steady-state vibrational SRS, albeit with impressive conversion efficiencies of up to 68% [216]. Despite the observation of SRRS with nanosecond pump pulses as early as 1966 [217], the issue of achieving maximum energy and efficiency in the transient regime remains unresolved. A discrete SRRS spectrum at  $\text{H}_2$  pressures up to 120 atm was obtained with 30 ps pump pulses at 1064 nm [218]. Meanwhile, more than 40 mainly anti-Stokes lines were observed in the 239 – 993 nm range [219] at 10 atm using a high-energy 80 fs Ti:Sa laser. Another possibility for expanding the Stokes bandwidth in the NIR range is the superposition of two vibrational modes in KGW crystals [160,191]. This concept led to the study of the spectrum synthesized in two successive KGW stages tuned to vibrational modes at  $767$  and  $901 \text{ cm}^{-1}$ , respectively.

This chapter discusses two methods for generating mJ-level femtosecond pulses in the NIR range (Fig. 3.1): cascaded transient SRRS in compressed hydrogen covering  $\sim 1.1 - 1.4 \mu\text{m}$ , and transient SRS at  $\sim 1.1 - 1.2 \mu\text{m}$  formed by a tailored spectrum from two consecutive KGW stages. These experiments

laid the foundation for the transition into the SWIR–MWIR range by replacing the Yb:YAG pump laser with a SWIR OPCPA setup, as described in Chapter 4.

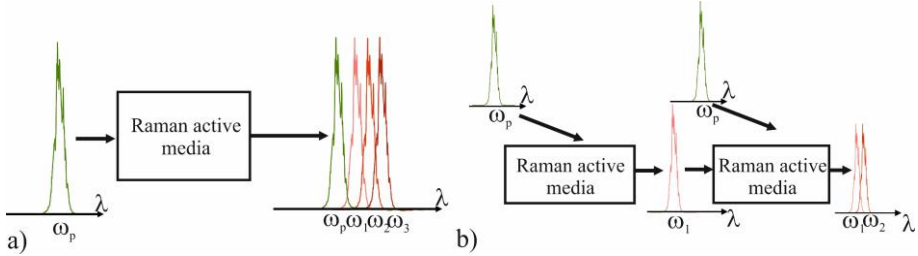


**Fig. 3.1** Broadband pulse generation using transient SRS: a) cascaded SRS and b) spectrum tailored by several Stokes orders.

### 3.1. Setup for cascade transient SRRS in compressed hydrogen

Particular attention in the experiments was paid to reducing the SRRS threshold, as well as expanding the spectral bandwidth of the rotational mode comb. The influence of focusing conditions, energy and polarization of pump pulses, as well as H<sub>2</sub> pressure on the conversion efficiency and evolution of the spectral envelope of SRRS and SRS was studied. To further reduce the SRRS threshold, SC seed radiation was used. The experimental setup for the investigation of cascade SRRS is shown in Fig 3.2. A Yb:YAG [71] laser was used for both SC seed excitation and SRRS pumping.

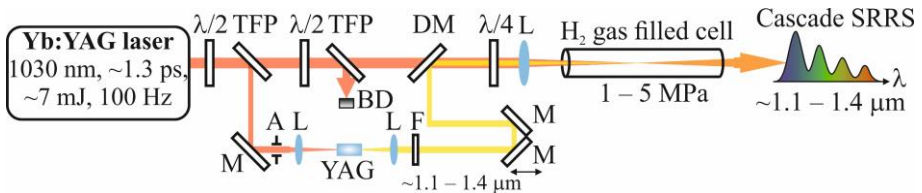


**Fig. 3.2** Experimental setup for studying cascade SRRS in compressed hydrogen:  $\lambda/2$  – half-wave retardation plates,  $\lambda/4$  – quarter-wave retardation plate, TFP – thin-film polarizers, A – iris aperture, DM – dichroic mirror, L – focusing lenses, F – long-pass interference filter, BD – beam dump, M – 45 deg mirrors.

A small portion ( $\sim 100 \mu\text{J}$ ) of the laser pulse energy was used to obtain SC in a 10 mm long YAG rod. The first thin-film polarizer (TFP), together with a half-wave retardation plate ( $\lambda/2$ ), formed an attenuator of the incident pulse energy, and the iris aperture (A) selected the central part of the beam with an initial diameter of 6.4 mm. A focusing lens (L) with a focal length of 100 mm was chosen to obtain stable SC spanning to  $\sim 1.4 \mu\text{m}$ . The long-wavelength

spectrum of the SC radiation was selected with a long-pass filter FELH1050 (F) (Thorlabs Inc.) and collimated using another lens with a focal length of 400 mm. Collinear propagation of the SC seed and pump beams was provided by a custom-made dichroic mirror (DM) transmitting at 1030 nm and reflecting in the 1100 – 1400 nm wavelength range, while precise temporal overlap was ensured by two plane silver mirrors in the delay line. To vary the pump energy supplied to the gas cell, a second attenuator was used. A quarter-wave retardation plate ( $\lambda/4$ ) provided circular polarization of the pump to suppress vibrational SRS. The SC seed and pump beams were focused by a lens with a focal length of 750 mm into the center of the high-pressure gas cell. Both SRS and SRRS occurred in this 1 m long cell with 5 mm thick  $\text{MgF}_2$  windows, filled with compressed hydrogen at variable pressure from 1 MPa to 5 MPa. Spectral measurements were carried out using an Ocean Optics NIRQuest512-2.5 spectrometer with an integration time of 10 pulses. In this case, a small portion of the Stokes beam was split by a fused silica wedge and directed onto a diffuser in front of the spectrometer's multimode input fiber to ensure uniform spatial distribution. Beam intensity profiles were measured with a CMOS profiler (WinCamDLCM-C, DataRay Inc.). Pulse energy was measured using a LabMax-TOP console with energy sensors (J-10MB-HE, Coherent Corp.). The combined energy of the SRS and SRRS was separated from the pump radiation by a long-pass filter FELH1050, while the SRS alone was selected by a long-pass filter FELH1350 (Thorlabs Inc.).

The main challenges in designing a high-pressure gas cell were related to the convenience of its extension over a wide range, sufficient strength at pressures above 5 MPa, minimal induced depolarization in the windows, and limited transverse dimensions for fitting into a dense scheme (Fig. 3.3).

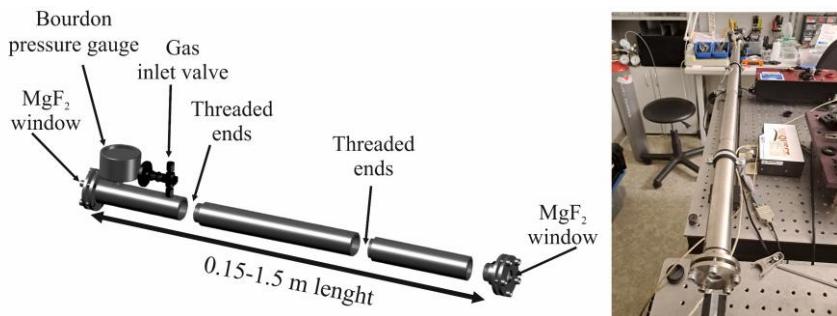


**Fig. 3.3** 3D drawing and photo of high-pressure gas cell.

The gas cell consists of custom machined stainless-steel tubes with threaded ends for easy extension, and external flanges with windows installed

through rubber O-rings. The cell is equipped with a Bourdon pressure gauge and a gas inlet valve. The half-inch window diameter was selected due to the wide choice of optical materials available. MgF<sub>2</sub> windows are superior due to their ~95% transmission in the ~200 nm to ~6 μm range [220], mechanical strength, resistance to cleaning solvents, and high LIDT. To minimize birefringence [221], the windows were cut with the optical axis parallel to the c-axis of the crystal and aligned to eliminate any influence on the polarization of the pump or Stokes radiation.

### 3.2. Performance of SRRS in hydrogen on the pump beam polarization

In the steady-state SRS regime, the conversion efficiency to high-order Stokes pulses increases with the elongated focusing of the pump beam [222]. In the transient SRS regime, when the pump pulse width is comparable to the rotational dephasing time in hydrogen ~1 ps [223], the threshold intensity increases drastically [28], while the effects of SPM, self-focusing, and SC generation become predominant. Then the insufficient pump intensity caused by loose beam focusing is compensated by a longer interaction length. Therefore, a loose focus with a long interaction length is suitable for exciting cascade SRRS by ultrashort laser pulses. However, since loose beam focusing entails low peak power density, the tradeoff is to exceed the SRS threshold while remaining below the SPM and self-focusing thresholds. Thus, focusing conditions and pump energy should be optimized to excite more Stokes orders in SRRS while mitigating competing nonlinear effects.

Initially, SC seeds were not used in experiments. According to the above assumption, the focal length was varied from 500 to 1500 mm at a constant pump energy of ~2 mJ and an H<sub>2</sub> pressure of 3 MPa. Under these conditions, when the SRRS threshold was exceeded, no SC was observed from the cell. As a result, a convenient focal length of 750 mm was chosen, although no significant differences in SRS conversion efficiency or spectrum envelope were observed.

Although in the steady-state hydrogen exhibits the best gain at 4155 cm<sup>-1</sup>, in these experiments the rotational shift at 587 cm<sup>-1</sup> was particularly expected. Moreover, the SRRS can dominate in the highly transient regime. The axis of the quarter-wave retardation plate was first set to ensure the linear polarization of the laser beam, and the incident energy was limited to 7 mJ to avoid damage to the MgF<sub>2</sub> cell windows. The dependence of the SRRS conversion efficiency on the pump energy for different polarizations of the pump beam at a hydrogen pressure of 3 MPa is shown in Fig. 3.4a.

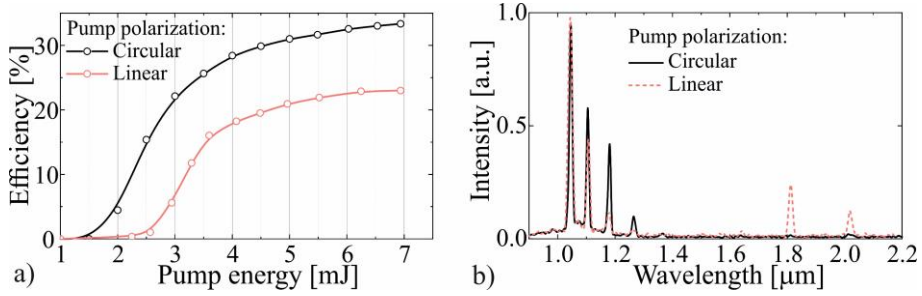


**Fig. 3.4** a) The dependence of the SRRS conversion efficiency on the pump energy for circular (black line) and linear (red line) polarizations of the incident pump beam at a hydrogen pressure of 3 MPa. b) Overall SRS spectra for circular (black line) and linear (red dashed line) polarizations of the pump beam at a pulse energy of 7 mJ.

Under the linear polarization of the pump beam, the SRRS threshold (defined at an SRRS efficiency of 1%) was reached at an energy of  $\sim 2.5$  mJ (Fig. 3.4a, red line). With the increase of pump energy, the SRRS conversion efficiency rose sharply to 16%. However, due to the occurrence of anti-Stokes components, upon reaching a pump energy of  $\sim 4.5$  mJ, the SRRS conversion efficiency gradually saturated to a maximum value of  $\sim 23\%$ . The observed spectrum was formed by several peaks at  $\sim 1094$  nm,  $\sim 1166$  nm, and  $\sim 1251$  nm (Fig. 3.4b, red dashed line) with gradually decreasing intensity, within the measurement error corresponding to the first, second, and third Stokes orders of the cascade SRRS in hydrogen (spaced apart by a rotational Raman shift of  $587\text{ cm}^{-1}$ ). The first of the peaks in Fig. 3.4b is at the 1030 nm pump wavelength of the Yb:YAG laser. Hence, with linear polarization of the pump beam, vibrational SRS could not be sufficiently suppressed. Therefore, in addition, two more lines were observed, related to the measurement error accuracy with the vibrational Raman shift at  $\sim 1790$  nm and to the rotational Stokes from this line at  $\sim 1993$  nm.

Although it is generally accepted that SRRS cannot be excited by a linearly polarized pump beam due to the parametric Stokes–anti-Stokes coupling (SAC) [224], it is noteworthy that rotational Stokes components have been detected. In other words, SAC can elevate the SRRS threshold for linearly polarized pump beam while leaving the threshold for circularly polarized beam unchanged [134]. Experiments revealed a strong dependence of the SRRS threshold on the polarization of nanosecond pump pulses [225], in particular, its threshold was not overcome even with a quadrupling of the linearly polarized pump energy. However, in our investigation SRRS was reliably observed when the dichroic mirror and the quarter-wave retardation plate were removed, and even when an additional thin-film polarizer was placed to ensure a strictly linear polarization of the pump beam. The windows



in the cell were also carefully inspected for both the absence of depolarization and cross-polarized wave generation. Finally, after installing a Glan prism after the cell, it was shown that the opposite output polarization appeared only when the SRS threshold was exceeded. Although the accompanying SC due to the SPM from the pump pulse can serve as a seed for SRRS via four-wave Raman mixing, only the first vibrational Stokes is expected at the SRS threshold. Thus, the consistently observed SRRS when using linear pump polarization was not associated with the inaccurate experimental design, but has not yet found a comprehensive explanation.

Apparently, with circular polarization of the driving pulses, two units of angular momentum are transferred to the hydrogen, which promotes SRRS [219]. Circularly polarized in opposite directions, the pump and Stokes waves interfere to yield a linear polarization that rotates at the same rate as the molecules. Then the rotational energy is efficiently transferred to the molecules, resulting in SRRS [226]. Indeed, changing the pump beam polarization to circular led to the suppression of vibrational Stokes (Fig. 3.4b, black line) with a decrease in the SRRS threshold to  $\sim 1.5$  mJ (Fig. 3.4a, black line) and a conversion efficiency of 33%. Thus, it was confirmed that circular polarization of the pump beam enhances the transient SRRS.

### 3.3. Dependence of SRRS on pump energy and hydrogen pressure

The evolution of the transient SRRS spectra on the pump pulse energy at a hydrogen pressure of 3 MPa is shown in Fig. 3.5a. In the spectrum above the threshold at  $\sim 3$  mJ, only the first rotational Stokes line was observed. When the pump energy was increased to  $\sim 5$  mJ, the saturated first Stokes, in turn, served as a pump for excitation of the second-order Stokes. Finally, at the maximum pump energy of 7 mJ, a third-order Stokes line was also observed. Thus, the choice of optimal excitation conditions in compressed hydrogen ensures cascade generation of equidistant rotational Stokes lines.

Since the Raman gain is proportional to the density of the medium [219], the conversion efficiency of transient SRRS was strongly dependent on the hydrogen pressure. Therefore, the pressure was also optimized to ensure efficient generation of higher-order rotational Stokes components. Although the SRS linewidth broadens with increasing gas pressure [28], in our experiments this effect was negligible because the pump laser linewidth exceeded the SRRS linewidth [227]. The evolution of the SRS spectra as a function of hydrogen pressure at a pump pulse energy of 7 mJ is shown in Fig. 3.5b. Due to the low Raman gain, only the first rotational Stokes line was observed at 1 MPa, while the number and intensity of higher-order Stokes

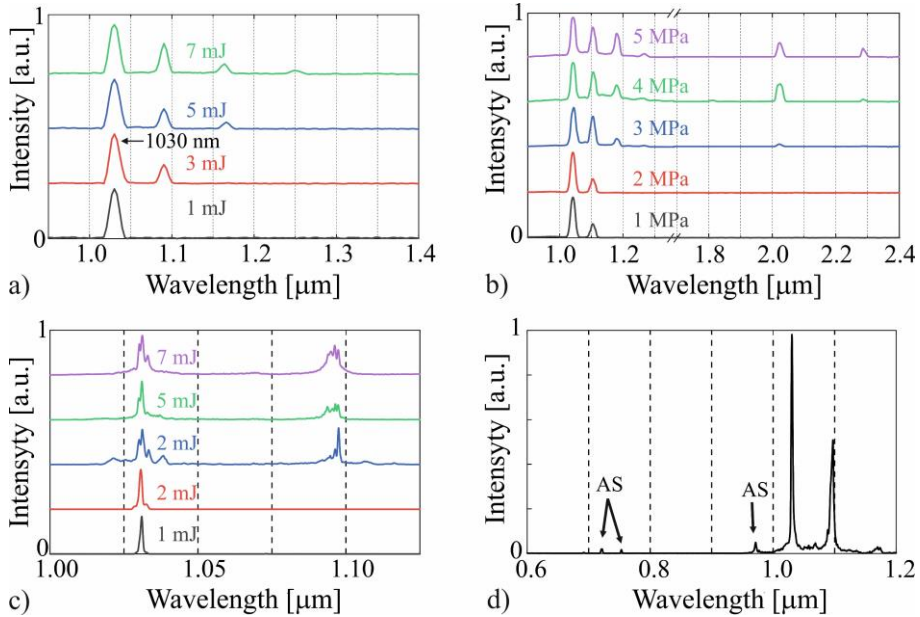


**Fig. 3.5** a) The evolution of SRRS spectra with pump pulse energy at H<sub>2</sub> pressure of 3 MPa and b) with H<sub>2</sub> pressure at a pump pulse energy of 7 mJ. c) The evolution of the envelope of the pump and first rotational Stokes spectra with the pump pulse energy at 5 MPa. d) SRRS spectrum envelope with Stokes and anti-Stokes lines (AS) at 3 MPa and 7 mJ pump pulse energy. Spectra c) and d) were measured using an Ando AQ-6315A spectrum analyzer with a resolution of 0.5 nm.

components increased at higher pressures. It is noteworthy that although the circular polarization of the pump beam made it possible to suppress the generation of vibrational SRS directly (Fig. 3.4b, black line), at pressures above 3 MPa the first rotational Stokes pulse in turn became a pump source for vibrational SRS at  $\sim 2012$  nm (Fig. 3.5b, blue line). When the hydrogen pressure reached 4 MPa, the cascade generation of vibrational SRS from second-order rotational Stokes was also observed at  $\sim 2074$  nm (Fig. 3.5b, green line). Thus, at elevated hydrogen pressure, two vibrational Stokes lines were observed at once (Fig. 3.5b, purple line), corresponding to a Raman shift of  $4155$   $\text{cm}^{-1}$  from the first- and second-order rotational Stokes, respectively.

The increase in the nonlinear refractive index  $n_2$  with hydrogen pressure [228] led to the rise of the spectral pedestal between the rotational Stokes lines in the wavelength range of  $\sim 1 - 1.4$   $\mu\text{m}$  due the SPM. The evolution of the bandwidth of the pump and first rotational Stokes spectra as a function of the pump pulse energy at 5 MPa is shown in Fig. 3.5c. To improve the spectral resolution to  $\sim 0.5$  nm, an Ando AQ-6315A spectrum analyzer was used for these measurements. It can be seen that the pump spectrum is slightly

broadened by SPM even before reaching the SRRS threshold (Fig. 3.5c, red line). With further increase of energy, new satellite peaks appeared in the pump spectrum around the central wavelength, and one of these peaks was even replicated in the Stokes spectrum (Fig. 3.5c, blue line). At the highest energies, cascade generation of the SRRS comb was launched with an even greater broadening of the Stokes band than the pump and suppression of the satellite peaks on the pump envelope (Fig. 3.5c, green and purple line). In addition, in the short-wavelength range at 3 MPa and a pump energy of 7 mJ, relatively weak first rotational anti-Stokes at  $\sim 972$  nm with a first vibrational anti-Stokes at  $\sim 721$  nm was observed, and from the latter also a rotational Stokes at  $\sim 752$  nm (Fig. 3.5d). Under these experimental conditions, the SC was not observed at the output of the gas cell.

The high pump pulse energy at elevated hydrogen pressure not only facilitated the cascade generation of higher-order rotational Stokes, but also improved the SRRS conversion efficiency and reduced its threshold from  $\sim 5$  mJ to  $\sim 0.95$  mJ with an increase in pressure from 1 MPa to 5 MPa (Fig. 3.6a,c). This dependence corresponded to the reciprocal function  $4.9/p$ , where  $p$  is the  $H_2$  pressure (Fig. 3.6c, red dashed line).

The best SRRS conversion efficiency in saturation increased rapidly with pressure from  $\sim 1.5\%$  to  $\sim 42\%$  (Fig. 3.6c, black solid line). However, with further increase in gas pressure and pump pulse energy,  $n_2$  increases, which leads to competing phenomena of SPM, multiphoton ionization, harmonic generation, etc. A weak conversion to vibrational SRS was observed at hydrogen pressures above 3 MPa (Fig. 3.6b) through cascade energy transfer from rotational Stokes. This was also evident from the change in the slope of the SRRS efficiency curve (Fig. 3.6c). The highest conversion efficiency of the pump pulse energy into vibrational Stokes was  $\sim 3.2\%$ . It is noteworthy that even at the maximum pump energy of 7 mJ and hydrogen pressure of 5 MPa, the beam after the spatial filter remained smooth (Fig. 3.6d,e) at a repetition rate of 100 Hz.

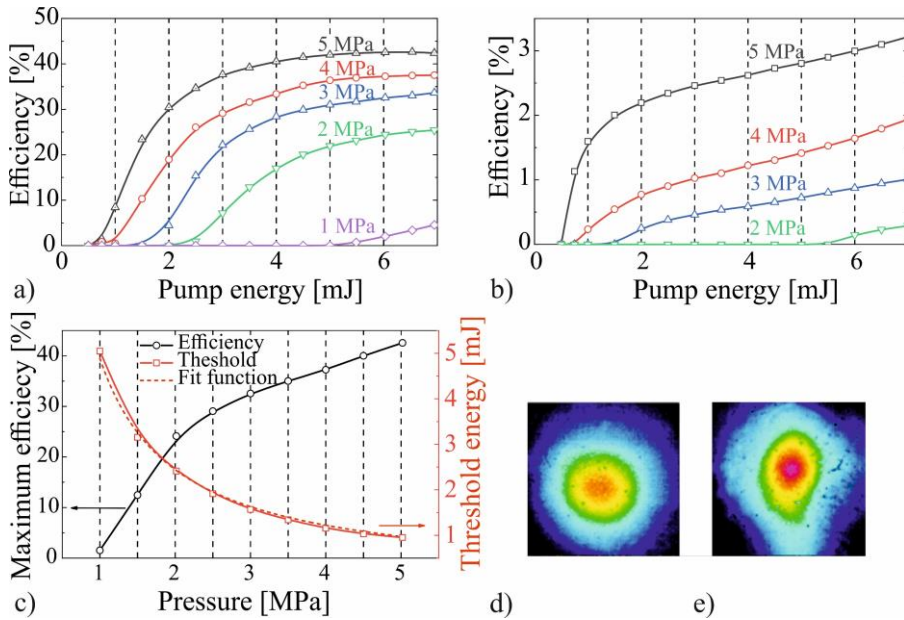


**Fig. 3.6** Conversion efficiency of a) SRRS and b) vibrational SRS at different H<sub>2</sub> pressures. c) Dependence of the maximum SRRS conversion efficiency (black line) and threshold energy (red solid line) on H<sub>2</sub> pressure; SRRS beam profile at 5 MPa: d) with pump energy of 1 mJ and e) with pump energy of 7 mJ.

### 3.4. Transient SRRS amplification of SC seed in compressed hydrogen

Since SRS usually originates from a very low level of spontaneous Raman scattering, using a higher intensity coherent seed at Stokes excitation wavelengths can greatly facilitate the process. Accordingly, the SRRS in the high-pressure hydrogen cell was seeded with broadband SC pulses obtained in a YAG crystal sharing the same Yb:YAG pump source. Indeed, by covering a wide range of high-order Stokes modes with a broadband SC seed pulse, one can expect a lower threshold, higher conversion efficiency, and a wider comb spectrum [160]. The spectral envelope evolution of SC-seeded SRRS as a function of H<sub>2</sub> pressure at a pump pulse energy of 7 mJ is shown in Fig. 3.7a.

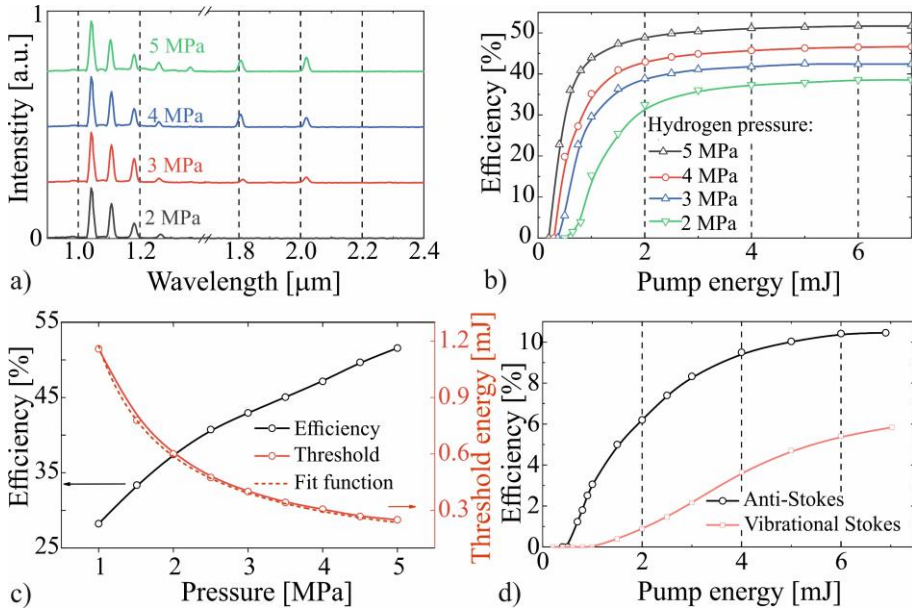


**Fig. 3.7** a) The spectral envelope evolution of SC-seeded SRRS as a function of  $\text{H}_2$  pressure at a pump pulse energy of 7 mJ. b) SC-seeded SRRS conversion efficiency at different  $\text{H}_2$  pressures. c) Dependence of the maximum SC-seeded SRRS conversion efficiency (black line) and minimum onset energy (red solid line) on  $\text{H}_2$  pressure. d) Conversion efficiency into anti-Stokes and vibrational Stokes at 5 MPa.

In contrast to the case for SRRS without SC seed pulses (Fig. 3.5 b), at a hydrogen pressure of 5 MPa, rotational Stokes generation was observed up to the fourth order at  $\sim 1351$  nm. The spectra also contain a vibrational Stokes line at  $\sim 1795$  nm and the first rotational Stokes line from it at  $\sim 2007$  nm. Thus, despite the low intensity of the SC radiation near  $\sim 1.8$   $\mu\text{m}$ , it is quite sufficient to excite the first vibrational Stokes directly from the pump wavelength. The use of SC seed also dramatically reduced the minimum pump energy for SRRS onset to  $\sim 1.15$  mJ at 1 MPa and  $\sim 0.25$  mJ at 5 MPa (Fig. 3.7c, red solid line), which is  $\sim 4$  times lower than without seeding (Fig. 3.6c, red solid line). This dependence corresponded to the reciprocal function  $1.15/p$ , where  $p$  is the  $\text{H}_2$  pressure (Fig. 3.7c, red dashed line). The use of the SC seed allowed earlier SRRS results to be surpassed at all hydrogen pressures tested. With increasing pump energy, the conversion efficiency of SRRS using the SC seed increased sharply (Fig. 3.7b). However, due to the contribution of anti-Stokes and vibrational Stokes which arise at pump pulse energies exceeding  $\sim 0.5$  mJ and  $\sim 1$  mJ (Fig. 3.7d), respectively, the SRRS conversion efficiency began to saturate. Thus, at a pump pulse energy of 7 mJ and a  $\text{H}_2$  pressure of 5 MPa, the conversion efficiency into anti-Stokes and vibrational Stokes reached

~10.4% and ~5.8%, respectively. The best SRRS conversion efficiencies of ~28% to ~52% were achieved at pressures from 1 MPa to 5 MPa, with the maximum Stokes pulse energy exceeding 3 mJ.

The widest SRRS comb spectrum was obtained at 5 MPa and 7 mJ pump energy (Fig. 3.8a). The positions of the observed peaks are given in Table 3.1.

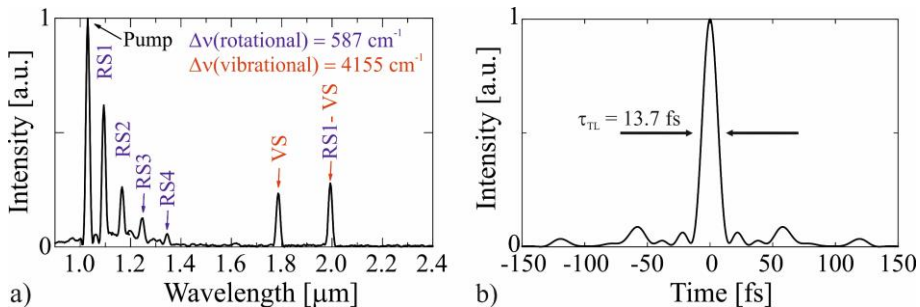


**Fig. 3.8** a) SC-seeded SRRS spectrum at 5 MPa H<sub>2</sub> pressure and 7 mJ pump pulse energy. b) FTL temporal shape calculated from the measured SRRS spectrum in the wavelength range 1 – 1.4 μm.

Accordingly, the spectral peaks detected at wavelengths of ~1096 nm, ~1166 nm, ~1252 nm, and ~1351 nm (designated as “RS1–4”) were assigned to the 1<sup>st</sup> – 4<sup>th</sup> rotational Stokes orders, which corresponds to a Raman shift of 587 cm<sup>-1</sup> in hydrogen pumped at 1030 nm. The spectrum also contained two long-wavelength peaks at ~1795 nm and ~1997 nm. The first was assigned to the vibrational Stokes excited by the pump radiation (designated as “VS”), and the second – to the vibrational Stokes excited from the first rotational Stokes component “RS1” (designated as “RS1-VS”). In accordance with the pump beam, the SRRS output was circularly polarized, and its spectrum corresponded to a FTL pulse width of ~14 fs at a central wavelength of 1.2 μm (Fig. 3.8b).

**Table 3.1** Positions of SRRS spectrum peaks and corresponding wavelength shifts.

Peak position, nm	Raman shift, cm <sup>-1</sup>	Mode assignment	Designation
1096	587	Rotational first-order Stokes	RS1
1166	1174	Rotational second-order Stokes	RS2
1252	1761	Rotational third-order Stokes	RS3
1351	2348	Rotational fourth-order Stokes	RS4
1795	4155	Vibrational Stokes from a pump pulse	VS
1997	4742	Vibrational Stokes from rotational first-order Stokes	RS1-VS

### 3.5. Compression of SRRS pulses amplified in a hydrogen cell

Further experiments were aimed at exploring the possibilities of compressing SRRS pulses amplified in a hydrogen cell. Stokes pulse compression tests were performed using two SF11 glass prisms with an apex angle of  $59^\circ$ . A Glan-Taylor prism sampled  $p$ -polarized SRRS radiation into the SHG-FROG setup. With an optimal prism spacing of 80 cm, the first-order rotational Stokes pulses were compressed to  $\sim 152$  fs, which was almost 9 times shorter than the pump pulse (Fig. 3.9).

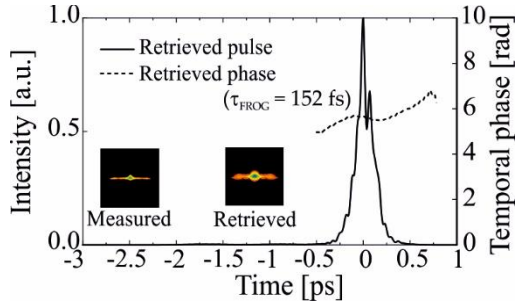


**Fig. 3.9** Temporal profile (solid line) of the first-order rotational Stokes pulses after compression, retrieved from the SHG-FROG measurement, and the retrieved temporal phase (dashed line). Insets are measured and retrieved FROG traces with  $\sim 1.5\%$  error using a  $512 \times 512$  grid.

However, in the case of multiple higher-order rotational Stokes, linear compression methods proved insufficient, because precise phase control of several molecular modulation sidebands was required. One way to achieve this is to use transparent plates between the prisms, specific to each rotational Stokes component, with adjustable thickness and position, thereby providing spectral control over the sideband generation process [229]. In addition, the relative phases can be controlled using a spatial light modulator [215] or a spatial phase controller [230]. In particular, this could be a programmable liquid crystal spatial light modulator containing tens of pixels with computer control of the refractive index of each [215]. Furthermore, compression into a 14-fs pulse train has been demonstrated using phase-controlled multiphoton ionization in xenon [231]. Thus, together with appropriate compression methods, the multi-wavelength SRRS radiation source can be used not only for broadband sensing, but also for generating few-cycle optical pulses in the difficult-to-reach spectral range of  $1.1 - 1.4 \mu\text{m}$ .

### 3.6. Setup for studying broadband TSRCPA in KGW crystals

The expansion of the TSRCPA bandwidth can be achieved by combining the spectra of sufficiently close SRS modes in separate stages. This method involves the SPM-induced overlap of discrete Stokes shifts in the transient SRS regime. Solid-state materials such as KGW are particularly susceptible to SPM broadening due to their high nonlinear refractive index  $n_2$ . The composite bandwidth can be synthesized in two successive TSRCPA stages tuned to adjacent vibrational modes at 767 and 901  $\text{cm}^{-1}$  of the KGW crystal, followed by evaluation of the compressibility of the amplified Stokes pulses.

The widely used KGW crystal has a monoclinic lattice structure (space group –  $C2/c$ ), which leads to anisotropic optical and thermophysical properties [232]. This crystal possesses a high third-order nonlinear susceptibility and exhibits several intense spontaneous Raman vibrations, which depend on the direction and polarization of the pump beam with respect to the crystal indicatrix axes. The crystallographic  $b$ -axis, also known as the second-order symmetry axis, coincides with the optical indicatrix axis  $N_p$ , while the  $N_m$  and  $N_g$  axes are located under 14 and 20° angles with the  $a$ - and  $c$ -axes, respectively, as shown in Fig. 3.10a. Edge-sharing  $[\text{WO}_6]$  octahedra form molecular groups in the KGW crystal that have complex polarized Raman spectra. The most intense Stokes lines appear at 767  $\text{cm}^{-1}$  ( $N_g$ ) and 901  $\text{cm}^{-1}$  ( $N_m$ ) with line widths of 7.8 and 5.9  $\text{cm}^{-1}$  (FWHM), respectively, observed in the polarized SRS spectra of the  $N_p$ -cut KGW crystal. Much richer spectral lines can be obtained for other excitation configurations. The short KGW dephasing time of several picoseconds (1.6 – 5.6 ps according to [232,233]) makes this material a promising candidate for SRS-conversion of fs–ps pulses. Finally, the steady-state Raman gain in KGW decreases from 4.4 at 1  $\mu\text{m}$  to  $\sim 1$   $\text{cm}/\text{GW}$  at  $\sim 2$   $\mu\text{m}$  [170,234].

As before, the Yb:YAG laser described in Chapter 2 was used as the pump source (Fig. 3.10). A small portion ( $\sim 12$   $\mu\text{J}$ ) of the laser pulse energy was directed onto a 15 mm long YAG rod to obtain stable SC pulses in the wavelength range from  $\sim 1050$  to  $\sim 2400$  nm. These SC pulses were used to seed the two TSRCPA stages. Laser pulses with energies up to 2.5 mJ after passing through optical delay lines were used to pump two successive TSRCPA stages based on 30 mm and 15 mm long  $N_p$ -cut KGW crystals, tuned to vibrational modes at 901 and 767  $\text{cm}^{-1}$ , respectively. Both TSRCPA stages were aligned in a non-collinear configuration with a 2° angle between the signal and pump beams to easily separate the unwanted SRS generated directly by the pump pulses. Such parasitic SRS radiation has a frequency-



independent spectral phase [105], unlike the linearly chirped amplified signal [160], which can prevent further pulse compression.

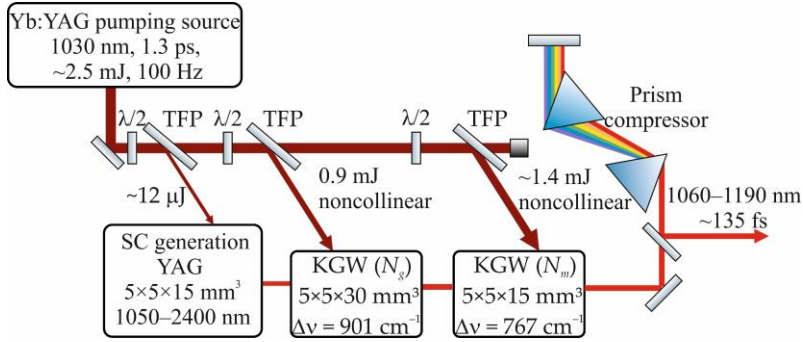


**Fig. 3.10** Experimental setup for investigation of transient stimulated Raman chirped-pulse amplification (TSRCPA):  $\lambda/2$  – half-wave retardation plate; TFP – thin-film polarizers.

The spectra of the amplified Stokes pulses were measured using an Anritsu MS9740B spectrum analyzer. The possibility of compressing the amplified Stokes pulses was tested using SF11 glass prisms with an apex angle of  $59^\circ$  to compensate for the positive dispersion in the YAG and KGW crystals. The distance between the two prisms was varied to achieve the shortest pulse width.

### 3.7. Spectral synthesis in a two-stage TSRCPA based on KGW crystals

The first TSRCPA stage was tuned to excite the vibrational mode in the KGW crystal at  $901\text{ cm}^{-1}$  (Fig. 3.11a, black line). Although it was also possible to obtain another vibrational mode at  $767\text{ cm}^{-1}$  (Fig. 3.11a, red line). Then the spectral bandwidth of the amplified Stokes pulses (Fig. 3.11b) after the first stage was  $\sim 13\text{ nm}$  (FWHM) at a pump pulse energy of  $0.9\text{ mJ}$ , which corresponds to a FTL pulse width of  $130\text{ fs}$ . It is noteworthy that both the greatest spectral broadening and the best gain were achieved with the optimal delay between the SC seed and pump pulses. As the pump energy increased, the amplified Stokes pulse was predominantly broadened towards shorter wavelengths. This is explained by the fact that in transient SRS the Stokes pulse is formed at the trailing edge of the pump pulse [235]. Due to SPM, the leading and trailing edges of the pump pulse exhibit red- and blue-shifted frequency components, so that the amplified Stokes pulse basically replicates the frequency and phase structure of the trailing edge of the pump pulse. As a result, a more significant spectral broadening into the short-wavelength range was observed. Such asymmetric broadening is convenient for spectral

synthesis in the second TSRCPA stage, where the spectrum from the first stage should overlap with the Stokes component at  $767\text{ cm}^{-1}$ .

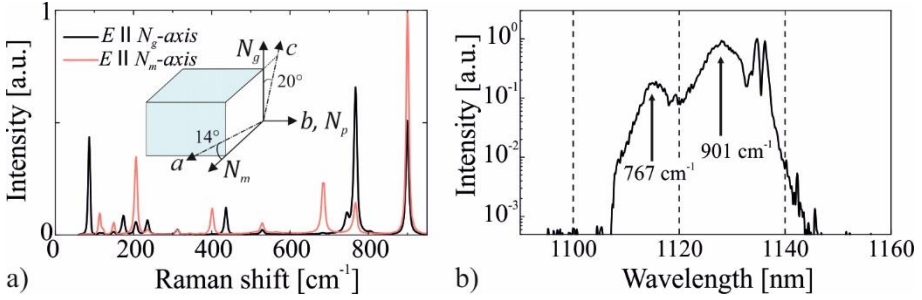


**Fig. 3.11** a) Spontaneous Raman spectra of a KGW crystal in orthogonal orientations. Inset: positions of the crystallographic axes  $a$ ,  $b$ , and  $c$  relative to the optical indicatrix axes  $N_m$ ,  $N_g$ , and  $N_p$  [160,191]. b) Spectrum after the first TSRCPA stage, tuned to vibrational modes at  $901\text{ cm}^{-1}$  and  $767\text{ cm}^{-1}$  of the KGW crystal.

The second TSRCPA stage was tuned to the adjacent vibrational mode of the KGW crystal at  $767\text{ cm}^{-1}$ , which allowed the synthesis of a  $\sim 38\text{ nm}$  tailored spectral bandwidth (Fig. 3.12a), corresponding to the FTL pulse width of  $50\text{ fs}$  (Fig. 3.13b, black solid line) at a central wavelength of  $1120\text{ nm}$ .

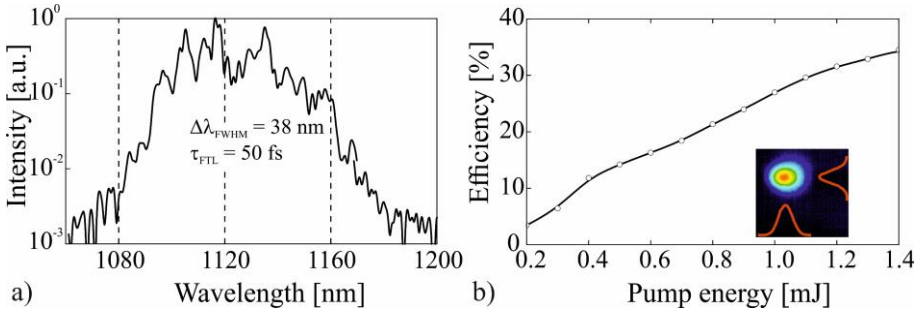


**Fig. 3.12** a) Synthesized spectra after two TSRCPA stages tuned to vibrational modes at  $901\text{ cm}^{-1}$  and  $767\text{ cm}^{-1}$  of the KGW crystal. b) Conversion efficiency of the second TSRCPA stage as a function of pump pulse energy and (inset) the amplified beam profile at a pump energy of  $1.4\text{ mJ}$ .

The spectrum of the amplified Stokes after the second TSRCPA stage has been broadened towards longer wavelength. It is noteworthy that in this case the short-wavelength and long-wavelength wings of the amplified Stokes spectrum are in the same polarization, in contrast to the simultaneous excitation of several vibrational modes in a single KGW crystal [160]. A conversion efficiency of  $\sim 35\%$  was achieved (Fig. 3.12b) at a pump pulse energy of  $1.4\text{ mJ}$ , which corresponded to an intensity of  $30\text{ GW/cm}^2$ . It is obvious that due to the large mismatch between the central wavelengths,

adjacent wings of the tailored spectrum were amplified independently. As a result, the conversion efficiency was lower compared to the amplification of a single Stokes component in two successive TSRCPA stages [160]. Indeed, additional amplification stages or multi-pass cell can be used to further improve the conversion efficiency [236]. The measured composite spectrum, the FROG-retrieved spectrum, and its phase for the amplified Stokes pulses are shown in Fig. 3.13a).

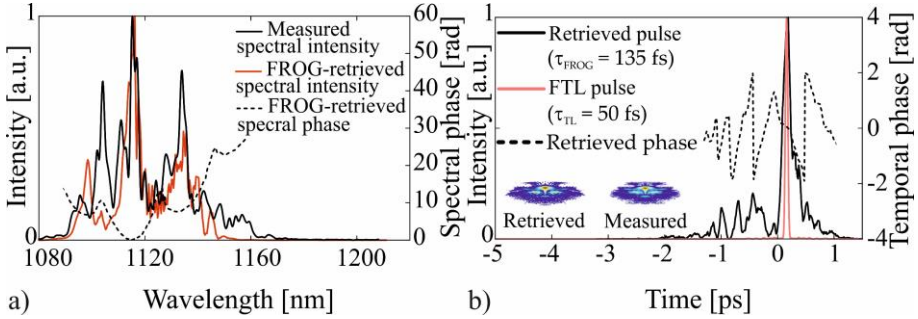


**Fig. 3.13** a) The composite spectrum after two TSRCPA stages (solid black line), FROG-retrieved spectral intensity profile (red line), and its spectral phase (dashed line) before compression. b) Temporal profile (solid black line) of the amplified Stokes pulses after compression retrieved from the SHG-FROG measurement compared to the FTL pulse calculated from the measured spectrum (red line) and the retrieved temporal phase (dashed line).

It can be seen that the synthesized pulse has a positive chirp imprinted from the SC pulses, which is accompanied by significant spectral phase modulations (Fig. 3.13a, dashed line). Although it is difficult to clearly determine what exactly caused the phase modulations. We assume that the SPM-induced phase distortions of the pump pulse were transferred to the amplified Stokes pulses. The B-integral of the pump pulses accumulated in the first TSRCPA stage exceeded 9, which certainly affected the phase structure of the amplified Stokes. Meanwhile, in the second stage, the B-integral did not exceed 3, therefore the SPM-induced spectral phase structures of adjacent Stokes modes were different. In addition, the SPM of Stokes pulses during amplification can also affect spectral phase distortions. Amplified Stokes pulses of  $\sim 1$  ps were observed at the output of the two-stage TSRCPA. The delay in the second stage was then optimized to obtain the best temporal contrast after compression. With an optimal prism spacing of  $\sim 2.1$  m, partly compressed pulses to  $\sim 135$  fs (FWHM) were achieved (Fig. 3.13b, solid black line), which is almost 10 times shorter than the pump. Although due to phase modulation (Fig. 3.13b, dashed line) these pulses contained a pedestal and

sub-pulses on the side, therefore for the best result it is necessary to use active phase control, i.e. AOPDF.

### 3.8. Summary of the results

The use of a circularly polarized pump beam and broadband SC seed pulses provides cascaded rotational Stokes up to the fourth order at 5 MPa hydrogen pressure in the difficult-to-reach wavelength range of  $\sim 1.1 - 1.4 \mu\text{m}$  with an output energy of  $\sim 3 \text{ mJ}$  and a conversion efficiency of 52%. The bandwidth of the resulting SRRS comb was sufficient to generate FTL pulses compressed to  $\sim 14 \text{ fs}$  at a central wavelength of  $\sim 1.2 \mu\text{m}$ . Although this would require complex techniques, SF11 prisms made it possible to compress first-order rotational Stokes pulses to  $\sim 150 \text{ fs}$ , which is  $\sim 9$  times shorter than the pump pulses.

Coupling adjacent vibrational modes in successive TSRCPA stages based on KGW crystals ensured a 23-fold increase in the composite bandwidth of amplified Stokes pulses compared to pump pulses with a conversion efficiency of  $\sim 35\%$ . The achieved spectral bandwidth of  $\sim 38 \text{ nm}$  at a central wavelength of  $1120 \text{ nm}$  made it possible to compress the amplified Stokes pulses to  $135 \text{ fs}$ , which is  $\sim 10$  times shorter than the pump pulses. The explored concept can be extended to different SRS-active media to obtain even wider bandwidth.

Thus, spectral expansion of amplified Stokes pulses under transient SRRS in compressed hydrogen or by TSRCPA bandwidth synthesis in KGW crystals paves the way for the generation of intense femtosecond pulses in the NIR range. Moreover, the research approaches can be transferred to the SWIR–MWIR ranges, as shown in Chapter 4.

However, experimental difficulties have been noted in the compression of amplified Stokes pulses. Excitation of the SRRS in hydrogen by pulses shorter than  $50 \text{ fs}$  in the so-called “impulsive” regime can lead to the emergence of a coherent standing Stokes wave [237–239]. Compression of such pulses can be achieved without using spectral phase control methods.

## 4. COLLINEAR SWIR OPCPA COMBINED WITH TSRCPA

As discussed above, intense laser pulses in the SWIR–MIR range are in demand for generating attosecond pulses [5], THz radiation [6], and even PHz optoelectronics [240]. Tabletop attosecond sources rely on the HHG where few-cycle laser pulse interacts with noble gases in a vacuum. Despite the widespread use of Ti:Sa lasers providing pulses in the tens of eV range via HHG, scaling photon energies beyond 100 eV requires intense few-cycle lasers at longer wavelengths. While the maximum photon energy achievable by HHG scales as  $\lambda^2$ , the efficiency falls off as  $\lambda^{-5} - \lambda^{-6}$  [15,241]. Hence, a wavelength of  $\sim 2 \mu\text{m}$  is most suitable for generating soft X-rays up to 540 eV [16,17]. This shows the importance of developing cost-effective few-cycle lasers operating in the SWIR range and preferably with CEP stability. Since the idler pulses from OPCPA are passively CEP-stable, their energy needs to be scaled up [67]. The collinear OPCPA configuration provides a simple way to obtain CEP-stable idler pulses without angular chirp and spectrally separated from the signal [242]. However, this approach suffers from a narrow bandwidth. Therefore, the idler pulses are used only to obtain a broadband CEP-stable SC seed [243].

Transient SRS-conversion in the SWIR range was not considered as an alternative or complementary to OPCPA method for amplifying idler pulses. In this case, the signal pulses can be used as a source for SRS pumping, and the idler pulses will provide a seed at the Stokes wavelength. Apparently, the output OPCPA pulses with a single-picosecond pumping will be of the sub-ps order, which leads to low SRS-conversion efficiency in the transient regime, especially in the SWIR range. This chapter discusses signal-to-idler energy transfer via TSRCPA in both the KGW crystal and the compressed hydrogen coupled with a collinear SWIR OPCPA.

### 4.1. Setup for TSRCPA combined with SWIR OPCPA in KGW crystal

The experimental setup for studying the signal energy conversion into idler pulse using TSRCPA in KGW crystal is shown in Fig. 4.1. Although the same pump source was used again, the OPCPA was set to a collinear configuration. The broadband SC seed pulse was obtained in a 15 mm long YAG crystal and amplified in a two-stage collinear OPCPA based on BiBO crystals (type-I, phase-matching angle  $\theta = 8^\circ$ ) AR-coated at wavelengths of 1750 – 2500 nm. In the first and second OPCPA stages, BiBO crystals of 6 mm and 4 mm length were used. Collinear propagation of the signal and pump beams was ensured by dichroic mirrors DM (HR@1800–2400 nm, HT@1030 nm). The

signal pulse was reflected along the path from the mirrors to avoid accumulation of GDD and especially TOD in the case of its propagation through the substrates. Pump pulses with energy up to 4 mJ were divided by a beam splitter (BS) into two parts of 0.4 mJ and 3.6 mJ for the first and second OPCPA stage, respectively.

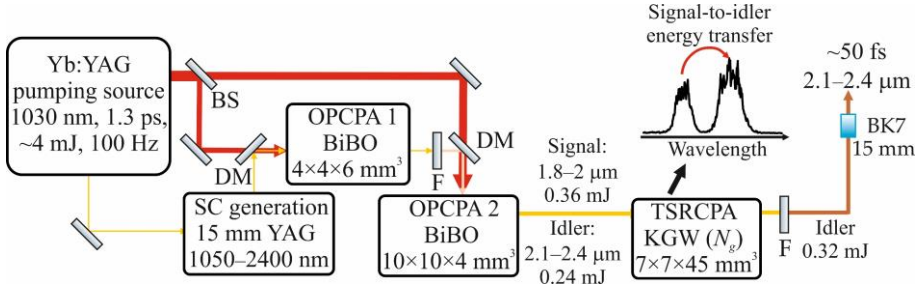


**Fig. 4.1** Experimental setup of signal-to-idler energy converter using TSRCPA in KGW crystal: OPCPA 1,2 – the first and second stages of the OPCPA, BS – beam splitter, DM – dichroic mirrors, F – broadband filters,.

Then the amplified signal and idler beams were directed to the TSRCPA stage based on  $N_p$ -cut KGW crystal with dimensions of  $7 \times 7 \times 30 \text{ mm}^3$  or  $7 \times 7 \times 45 \text{ mm}^3$ . To attenuate the pulse energy incident into the KGW, neutral density filters with an optical density of 0.1 to 0.7 were used. Finally, the idler pulses amplified in the TSRCPA stage were compressed in 15 mm long BK7 glass by compensating for the dispersion accumulated in the YAG, BiBO and KGW crystals. The principle of idler pulse amplification in the KGW crystal is shown in Fig. 4.2.

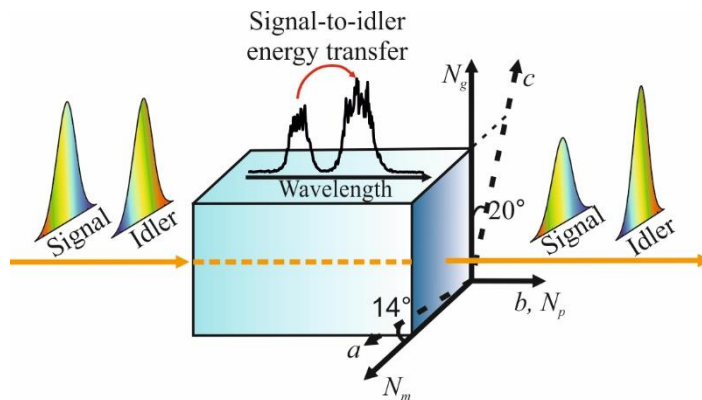


**Fig. 4.2** The principle of signal-to-idler energy conversion using TSRCPA in KGW crystal. The signal and idler waves, with a wavelength difference corresponding to the Stokes shift, propagate collinearly. The positions of the crystallographic axes  $a$ ,  $b$  and  $c$  of the KGW crystal are given relative to the optical indicatrix axes  $N_p$ ,  $N_m$  and  $N_g$ .

The idler wave is amplified as it propagates in the Raman-active crystal with the signal wave serving as a pump, and the wavelengths difference corresponding to the Stokes shift. The phase-matching angle of the BiBO crystals in both OPCPA stages was aligned to facilitate separation of the idler spectrum from the signal. However, wider bandwidth and better gain are achieved at degeneracy, where signal and idler wavelengths are similar (Chapter 2.3). Therefore, the smallest Stokes shift at  $767 \text{ cm}^{-1}$  was chosen to amplify the idler in TSRCPA. The idler wavelength (in nm) can be expressed in terms of the Stokes shift  $\Omega_R$  (in  $\text{cm}^{-1}$ ) and the wavelength of the signal pulse:

$$\lambda_i = \frac{1}{\frac{1}{\lambda_s} - \frac{\Omega_R}{10^7}}, \quad (4.1)$$

Substituting this expression into Eq 1.2, we can calculate the signal wavelength when the idler pulse can serve as a seed for TSRCPA:

$$\lambda_s = \frac{2\lambda_p}{10^7 + \Omega_R\lambda_p} 10^7. \quad (4.2)$$

Hence, with a pump laser wavelength of 1030 nm and a Stokes shift of  $767 \text{ cm}^{-1}$ , the required signal wavelength will be  $\sim 1900 \text{ nm}$ . Accordingly, for the best signal-to-idler conversion efficiency using TSRCPA in the KGW crystal, OPCPA operates in the wavelength range  $\sim 1800 - 2000 \text{ nm}$  for signal and  $\sim 2100 - 2400 \text{ nm}$  for idler. In the first OPCPA stage, a maximum signal energy of  $\sim 16 \mu\text{J}$  and a conversion efficiency of  $\sim 3\%$  were achieved. In the second OPCPA stage, the signal was amplified to  $0.36 \text{ mJ}$  with a conversion efficiency of  $10\%$  at a pump intensity of  $\sim 45 \text{ GW/cm}^2$ . The maximum idler pulse energy of  $\sim 0.24 \text{ mJ}$  was obtained after signal suppression with a bandpass filter FB2250-500 (Thorlabs Inc.), although with a loss of  $20\%$  of the idler energy. To eliminate the interference pattern in the idler beam, a broadband filter FB1900-200 (Thorlabs Inc.) was also placed between the stages, blocking the incident idler radiation.

#### 4.2. Investigation of SWIR TSRCPA in the KGW crystal

Since the zero dispersion in the KGW crystal is at  $2.2 \mu\text{m}$ , the signal wave from the OPCPA falls within the normal dispersion range, while the idler experiences both anomalous and normal dispersion. As a result, the OPCPA signal wave propagates in the KGW crystal faster than the idler wave. This mismatch between the pump and Stokes pulses leads to their temporal

separation. Such a violation of phase coherence between the pump and Stokes radiation in a dispersive medium lead to the reduction in the Stokes gain. In this case, the signal pulse leaving the two OPCPA stages acquires a negative chirp due to the accumulated GDD in the YAG and BiBO crystals, and the  $\sim 175$  fs idler pulse is chirped positively. Thus, an estimate of the group velocity mismatch (Eq. 2.3) between the idler and signal waves in a KGW crystal yields a length limitation of  $\sim 60$  mm. Moreover, the opposite chirp of the idler and signal pulses propagating in the KGW crystal results in a reduction in the signal pulse width, while the Stokes pulse width remains virtually unchanged. For this reason, in the experimental setup we chose KGW crystals that were shorter than 60 mm. At the output of the TSRCPA stage, an amplified idler pulse at the Stokes wavelength and a depleted signal (i.e. pump for TSRCPA) pulse were observed using a 45 mm long KGW crystal. Although, the central wavelength of the idler slightly shifted to  $\sim 2250$  nm (Fig. 4.3, black line), to match the Stokes vibrational mode at  $767\text{ cm}^{-1}$  (indicated by the arrow). Apparently, the OPCPA signal in this case acts as a TSRCPA pump, while the idler serves as a high-energy Stokes seed. No narrowing of the Stokes spectrum was observed, it corresponded to a FTL pulse of  $\sim 50$  fs (inset in Fig. 4.3).

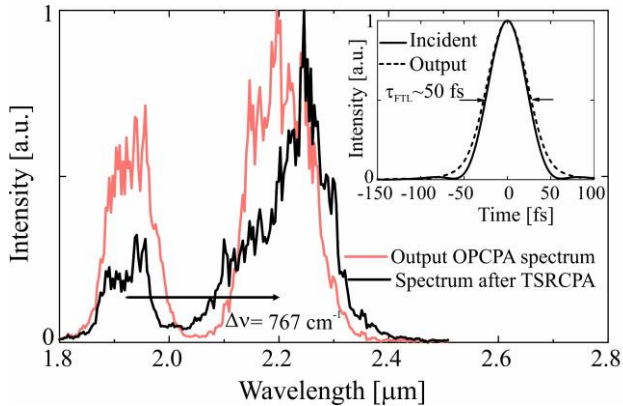


**Fig. 4.3** Normalized output spectra of the OPCPA (dashed line) and TSRCPA (solid line) stages. The arrow indicates the vibrational Stokes shift in the KGW crystal at  $767\text{ cm}^{-1}$ . Inset – FTL temporal shapes calculated from the measured spectra of the TSRCPA incident idler (solid line) and amplified Stokes pulses (dashed line).

The energy conversion from the signal to the idler pulse at the Stokes wavelength occurs even at low incident signal (i.e. pump for TSRCPA) energy and increases linearly (Fig. 4.4a). In the entire measurements range, the energies of the incident signal (i.e. pump for TSRCPA) and idler (seed) pulses were attenuated before the TSRCPA stage in the same ratio (Fig. 4.4a, black



line). At a maximum incident signal energy of 0.36 mJ (18 GW/cm<sup>2</sup>), the idler pulses at the Stokes wavelength leaving the TSRCPA stage reached energies of 0.3 mJ and 0.32 mJ for 30 mm and 45 mm long KGW crystals, respectively (Fig. 4.4a, blue and red lines). The spatial distributions of the incident idler and amplified Stokes beams measured by the Si-CMOS camera under two-photon excitation are shown in the insets of Fig. 4.4a. Hence, the energy build-up in the idler pulse at the Stokes wavelength using TSRCPA is a threshold-free phenomenon [160], in contrast to the generation of SRS. Accordingly, sufficient energy in the seed (idler) pulse at the Stokes wavelength of ~2250 nm allows achieving high conversion efficiency even in a single TSRCPA stage.

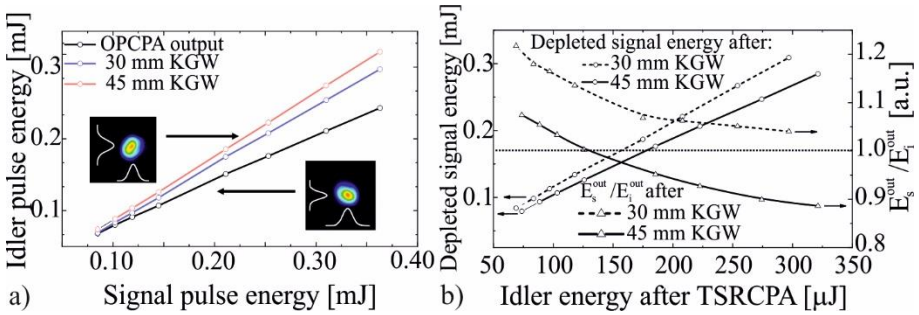


**Fig. 4.4** a) The energies incident on the TSRCPA stage of the idler pulse (black line) and the amplified Stokes in KGW crystals 30 mm (blue line) and 45 mm long (red line) as a function of the incident signal energy. b) Depleted signal (i.e. pump for TSRCPA) energy leaving the TSRCPA stage (left axis) and the ratio of depleted signal (i.e. pump for TSRCPA) to amplified Stokes energy (right axis) as a function of amplified Stokes energy in 30 mm and 45 mm long KGW crystals.

The signal (i.e. pump for TSRCPA) pulse was significantly depleted after propagation in the KGW crystal, and these losses were converted into amplified Stokes energy (Fig. 3.4b, left axis). Thus, the OPCA signal pulse serves as a pump in the TSRCPA process.  $F$  (Fig. 4.4b, right axis). This is related to the TSRCPA occurrence at the long-wavelength edge of the idler spectrum. Due to the relatively low initial intensity in this spectral range, the overall pulse energy at Stokes wavelengths including the transmitted idler energy after the TSRCPA stage can exceed the signal (i.e. pump for TSRCPA) energy. In other words, although the overall idler and amplified Stokes energy after the KGW crystal exceed the signal energy, the amplified section of the spectrum is still lower in intensity than the pump for TSRCPA.

At the maximum energy level, the amplified Stokes beam was close to Gaussian (inset in Fig. 4.4a) with an accumulated B-integral value (according to Eq. 2.7) of ~3.1 in a 45 mm long KGW crystal. This estimate only took into

account the maximum energy level, although the energy gradually increased during the amplification process. However, when the OPCPA signal (i.e. pump for TSRCPA) intensity reached 18 GW/cm<sup>2</sup>, no adverse nonlinear effects were observed that could interfere with TSRCPA, such as SPM, self-focusing, or SC generation. In contrast, reducing the diameters of the OPCPA signal (i.e. pump for TSRCPA) and idler beams to ~1.8 mm (at a peak intensity of 45 GW/cm<sup>2</sup>), resulted in a red shift of the TSRCPA output spectrum to ~2.5 μm (Fig. 4.5a) in a 30 mm long KGW crystal. This rise of the long-wavelength wing is probably caused by SPM with an increase in the incident pulse intensities by ~2.5 times. Furthermore, the TSRCPA efficiency was likely reduced by unwanted direct SRS-generation that overlapped spatially and spectrally with amplified Stokes.

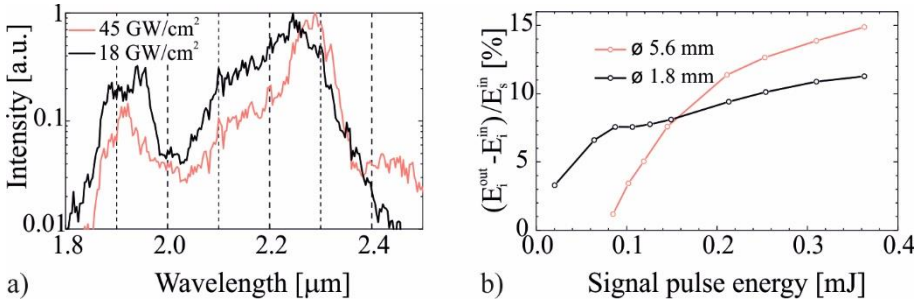


**Fig. 4.5** a) Normalized TSRCPA output spectra for a 45 mm KGW crystal at an incident signal intensity of 18 GW/cm<sup>2</sup> (black) and after a 30 mm KGW crystal at an incident signal intensity of 45 GW/cm<sup>2</sup> (red line). b) TSRCPA efficiency as a function of incident signal energy in a 30 mm long KGW crystal with both incident beam diameters of 5.6 mm (red line) and 1.8 mm (black line), where  $E_s^{\text{in}}$  – incident signal pulse energy;  $E_i^{\text{in}}$  – incident idler pulse energy.

At higher pump and seed intensities, the TSRCPA conversion efficiency approached saturation at signal energies as low as ~80 μJ and reached ~11% in a 30 mm long KGW crystal (Fig. 4.5b, black line). This is probably due to the SPM of the amplified Stokes. In contrast, at lower intensities of both the incident signal and idler, when nonlinear effects were not observed, saturation was not achieved even with a conversion efficiency reaching ~15% (Fig. 4.5b, red line). However, it was difficult to determine whether the intensity of the OPCPA signal (i.e., TSRCPA pump) or the idler (i.e., TSRCPA seed) has a greater impact on the TSRCPA conversion efficiency and the occurrence of nonlinear effects in the KGW crystal. In the experiment, the diameters of the signal and idler beams incident on the TSRCPA stage were adjusted simultaneously, although the use of dichroic mirrors to separate them would shed light on the impact of changing the intensity of only one of the pulses.

Thus, the maximum TRSCPA efficiency reached  $\sim 15\%$  and  $\sim 22\%$  in 30 mm and 45 mm long KGW crystals, respectively, at a peak incident pump intensity of  $\sim 18 \text{ GW/cm}^2$  (Fig. 4.6). Meanwhile, the maximum idler energy buildup due to conversion to Stokes reached 22% and 33% in KGW crystals with a length of 30 mm and 45 mm, respectively. It is obvious that with the used pump energies and KGW crystal lengths, TRSCPA is still far from saturation (Fig. 4.6).

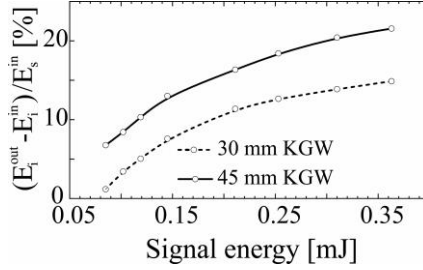


**Fig. 4.6** Dependence of the TRSCPA conversion efficiency on the incident signal energy (i.e. pump for TRSCPA) in 30 mm (dashed line) and 45 mm (solid line) KGW crystals, where  $E_s^{in}$  – incident signal pulse energy;  $E_i^{in}$  – incident idler pulse energy.

Since improving the efficiency of OPCPA is of great importance [51], even a relatively small increase in the pump-to-idler conversion efficiency for the described two-stage OPCPA of  $\sim 3\%$  is beneficial. Moreover, the additional OPCPA stage will provide an efficiency improvement of  $\sim 6\%$  when using a larger KGW crystal aperture. The TRSCPA efficiency can also be improved by delaying the idler pulse relative to the signal, since the Stokes pulse is formed on the trailing edge of the pump pulse [244]. It is also more justified to use crystals with a smaller Stokes shift of  $\sim 650 \text{ cm}^{-1}$ , such as  $\text{TeO}_2$  [245], for more accurate matching of the central wavelengths of the Stokes and idler pulses. Another option is the use  $\text{SF}_6$  gas cells with a Stokes shift of  $765 \text{ cm}^{-1}$  [246], which can provide energy scaling while limiting competing nonlinear effects.

It is important that the high TRSCPA efficiency is achieved even before the SRS self-excitation threshold, which is achieved at an incident OPCPA signal (i.e., TRSCPA pump) pulse intensity of  $\sim 25 \text{ GW/cm}^2$ . When this threshold is exceeded, the unwanted Stokes pulse replicates the chirp of the TRSCPA pump pulse, opposite to the idler one, preventing pulse compression. Otherwise, a noncollinear TRSCPA configuration should be used to spatially separate this beam [160].

The signal leaving the OPCPA exhibited a negative chirp, while the idler pulse exhibited a positive chirp. This phenomenon arises due to the phase

matching condition, where shorter signal wavelengths result in longer idler wavelengths, and vice versa. Therefore, the idler pulses could be compressed in the glass block with negative dispersion in the SWIR range. Thus, the signal leaving the OPCPA accumulated GDD of  $\sim -1800 \text{ fs}^2$  in the YAG and BiBO crystals, while the idler GDD was  $\sim 1800 \text{ fs}^2$ . Given that the idler bandwidth falls within the zero-dispersion range of the KGW crystal, the GDD acquired in it can be neglected when determining the required glass length for compression. Furthermore, TOD at this idler bandwidth had minimal impact on compression and could also be ignored. Thus, the pulses amplified in TSRCPA were compressed in the BK7 glass plate. It was estimated that a plate length of  $\sim 13 \text{ mm}$  was suitable for GDD compensation (Fig. 4.7a). Experimentally, the optimal pulse compression was achieved with a  $\sim 15 \text{ mm}$  long BK7 glass plate. Finally, pulses amplified in a  $45 \text{ mm}$  long KGW crystal were compressed to  $\sim 53 \text{ fs}$ , which is close to the value calculated from the measured spectrum at a central wavelength of  $2250 \text{ nm}$  (Fig. 4.7b). However, it is preferable to use another type of glass, since the transmission of a  $10 \text{ mm}$  long BK7 plate is less than  $80\%$  at wavelengths greater than  $2 \mu\text{m}$  [247].

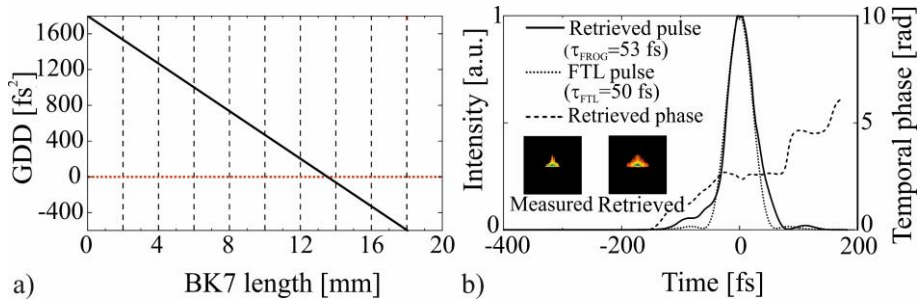


**Fig. 4.7** a) Estimated GDD of the idler pulse depending on length of the BK7 glass plate. b) SHG-FROG retrieved temporal profile (solid line) and temporal phase (dashed line) of the amplified in TSRCPA pulses after compression, compared to a FTL pulse calculated from the measured spectrum at  $2250 \text{ nm}$  (dotted line).

#### 4.3. Setup for investigation of SWIR SRRS in compressed hydrogen

To extend the OPCPA coverage further into the SWIR and even MWIR ranges, the high-order rotational Stokes excitation can be used. However, even at the highest output energy levels of noncollinear OPCPA, rotational Stokes in compressed hydrogen were not observed. Therefore, collinear OPCPA configuration was chosen to provide a seed pulse at the Stokes wavelength. Thus, the results of previous investigations were used to explore a transient SRRS coupled to a collinear OPCPA operating at central wavelengths of  $\sim 1.9 \mu\text{m}$  for the signal and  $\sim 2.2 \mu\text{m}$  for the idler. The goal of this study was to

achieve cascade generation of high-order rotational Stokes pulses in compressed hydrogen by optimizing the pressure, cell length, spectral mismatch between the signal and idler pulses, and the chirp induced in the SC pulses.

The experimental setup for studying transient SRRS in compressed hydrogen is shown in Fig. 4.8. Broadband SC seed pulses obtained in a 130 mm long YAG crystal were amplified in a three-stage collinear OPCPA, and then both the signal and idler pulses were focused into a hydrogen cell.

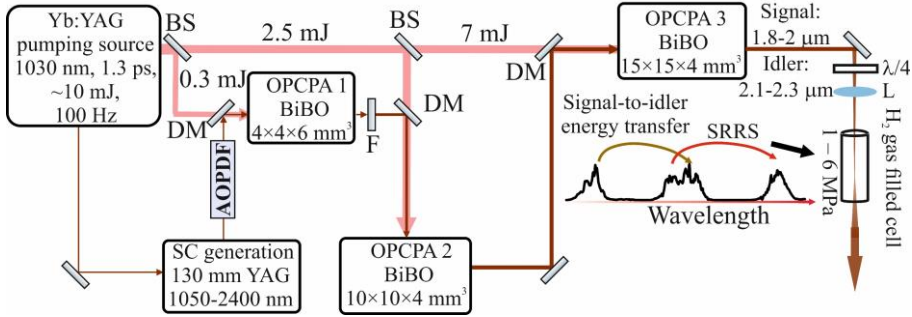


**Fig. 4.8** Experimental setup for investigation of transient SRRS in compressed hydrogen: DM – dichroic mirrors; BS – beam splitters;  $\lambda/4$  – quarter-wave retardation plate; L – focusing lens; AOPDF – acousto-optic programmable dispersive filter.

The OPCPA operated in the wavelength range of 1800 – 2050 nm for the signal and 2100 – 2300 nm for the idler, with both bandwidths corresponding to  $\sim 90$  fs FTL pulses. After the third OPCPA stage, the signal and idler pulses were focused by  $\text{CaF}_2$  lenses with a focal length of 500 mm or 750 mm into cells 45, 65 or 110 cm long, filled with hydrogen under a pressure of up to 6 MPa. The previously used  $\text{MgF}_2$  windows were replaced with uncoated 5 mm thick  $\text{CaF}_2$  windows. An achromatic quarter-wave retardation plate ( $\lambda/4$ ) with an operating wavelength range of 2000 – 2600 nm was placed in front of the cell. Spectral measurements were carried out using an ASP-IR-3.5 spectrometer (Avesta Ltd.) with an integration time corresponding to 10 pulses. To ensure uniform spatial distribution, a diffuser was placed in front of the  $\text{Ø}450 \mu\text{m}$  core ZBLAN multimode fiber (MZ41L1, Thorlabs Inc.) connected to the spectrometer. Pulse energy was measured using a LabMax-TOP console with J-25MB-LE energy sensors (Coherent Corp.). The energies of the signal, idler, and Stokes pulses were selected using broadband filters FB1900-200, FB2250-500 (Thorlabs Inc.) and a  $2.4 \mu\text{m}$  long-pass filter (Edmund Optics Inc.), respectively.

#### 4.4. Investigation of transient SWIR SRRS in compressed hydrogen

Substituting the value of the rotational Raman shift in hydrogen at  $587\text{ cm}^{-1}$  into Eq. 4.2, the signal wavelength was determined to be  $\sim 1.94\ \mu\text{m}$ , and the idler wavelength was  $\sim 2190\text{ nm}$ . To achieve sufficient separation of the idler and signal spectra, the phase-matching angles of the BiBO crystals in the three OPCPA stages were adjusted from  $0$  to  $0.12^\circ$  ( $0^\circ$  corresponds to a BiBO crystal phase-matching angle of  $7.8^\circ$ ). The dependence of the central wavelength of the signal and idler spectra for collinear OPCPA on the BiBO crystal adjustment angle is shown in Fig. 4.9a. It should be noted that each time the phase matching angle was adjusted, the delay between the signal and pump in OPCPA stages was also optimized for best Stokes generation efficiency at wavelengths of  $\sim 2.4 - 2.6\ \mu\text{m}$ . For this reason, the signal and idler spectra were not symmetrical and were narrower near degeneracy. At the initial crystal angle ( $0^\circ$ ), when there is no interference between the signal and the idler pulse, the signal pulses are at a central wavelength of  $\sim 2\ \mu\text{m}$ , while the idler pulses are at  $\sim 2.15\ \mu\text{m}$ . By fine-tuning this angle, the central wavelength of the signal pulse is shifted towards shorter wavelengths, while that of the idler pulse is shifted towards longer wavelengths.

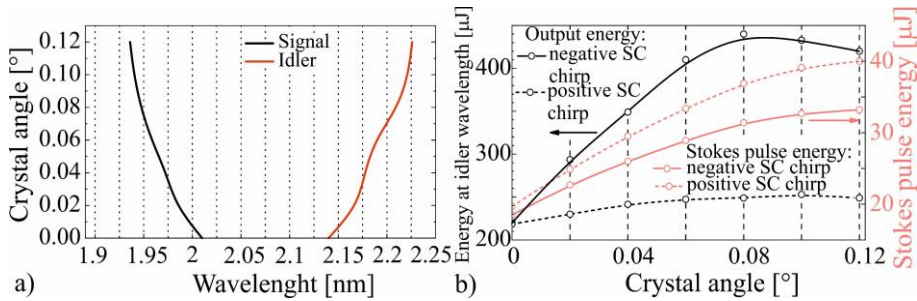


**Fig. 4.9** a) Signal and idler spectrum center wavelength of collinear OPCPA dependence on the BiBO crystal adjustment angle. b) The pulse energies at the output of the hydrogen cell at the idler (black lines – right axis) and the Stokes wavelengths from it (red lines – left axis) depending on the BiBO crystal adjustment angle with negative (solid lines) and positive (dashed lines) GDD induced in the SC seed at a pressure of 6 MPa.

Then, the signal and idler pulses, amplified in three stages of the OPCPA, passed through a broadband quarter-wave retardation plate to impart circular polarization and were focused into a cell with compressed hydrogen. The pulse energies at the output of the cell at the idler (black lines) and the Stokes wavelength from it (red lines) depending on the BiBO crystal angle are shown in Fig. 4.9b at a hydrogen pressure of 6 MPa. This pressure was chosen based

on the lowest SRRS threshold, since it is roughly inversely proportional to pressure [158]. Signal pulses of  $\sim 0.9$  ps duration were chirped either positively (dashed lines) or negatively (solid lines) by inducing a GDD of  $4 \times 10^4$  fs<sup>2</sup> or  $-4 \times 10^4$  fs<sup>2</sup> in the SC seed using AOPDF. These results reveal that with negative chirp, the output pulse energy at the idler wavelength reached  $\sim 440$   $\mu$ J, whereas with a positive chirp it reduced to  $\sim 250$   $\mu$ J at the same total incident energy of the signal and idler pulses of  $\sim 1.5$  mJ.

Hence, proper phase matching in OPCPA is critical to maintain sufficient separation between the signal and idler wavelengths, which in turn increases the pulse energy at the idler wavelength after SRRS. To maximize the energy transfer from the signal to the idler in SRRS, an optimal spectral separation was experimentally determined corresponding to a crystal adjustment angle of  $0.08^\circ$  (Fig. 4.9a), which is consistent with that calculated from (Eq. 4.2). In contrast, the Stokes pulse generated by the idler reached its maximum energy of  $\sim 40$   $\mu$ J with a positive chirp induced in the OPCPA signal, whereas with a negative chirp it was only  $\sim 33$   $\mu$ J. These results for SRRS in hydrogen suggest a trade-off between the output energies at idler and Stokes wavelengths depending on the sign of the signal pulse chirp. Higher SRS-conversion efficiency was observed with negatively chirped signal pulse than with positively chirped one [248–250] due to compensation of GVD and positive chirp caused by SPM, cross-phase modulation. Therefore, for scaling up the idler pulse after SRRS, it is preferable to use a negatively chirped OPCPA signal. On the other hand, positive chirp contributed to the generation of Stokes pulses. It should also be noted that the Stokes pulse was not observed when either the incident idler or the signal wavelength range were suppressed by the filter. This may be due to the energy transfer from the OPCPA signal to the idler and from latter to Stokes with the steepening of the depleted pulses during the transient SRRS, which contributes to SPM with the appearance of spectral components favorable for Stokes generation. For further investigation, the output idler pulse cross-correlation technique may be useful here [251].

The relationship between spectral separation (Fig. 4.9a) and energy redistribution between the output idler and Stokes pulses (Fig. 4.9b) depends on optimal phase matching by adjusting the BiBO angle. Therefore, a balance is required between maximizing the idler energy (which benefits from a negative chirp) and enhancing Stokes generation (which favors a positive chirp). These findings highlight the subtle interplay between the OPCPA spectral tuning and the energy distribution across different spectral components in the SRRS output. Managing this balance is critical for

applications where either amplified idler or Stokes pulses are important depending on the desired outcome.

The normalized spectra of the incident radiation into the hydrogen cell and the output radiation are shown in Fig. 4.10 for the negative (Fig. 4.10a) and positive GDD (Fig. 4.10b) applied to in the SC seed pulse. Hence, the influence of chirp on the spectral redistribution of the signal, idler, and Stokes components is obvious. In the case of negative GDD (Fig. 4.10a), the energy transfer from the signal at  $\sim 1.94 \mu\text{m}$  to the idler pulse at  $\sim 2.22 \mu\text{m}$  is more significant, since the peak at the idler wavelength is more pronounced. This result is consistent with previous findings that negative chirp promotes earlier energy transfer to the idler, thereby weakening Stokes generation.

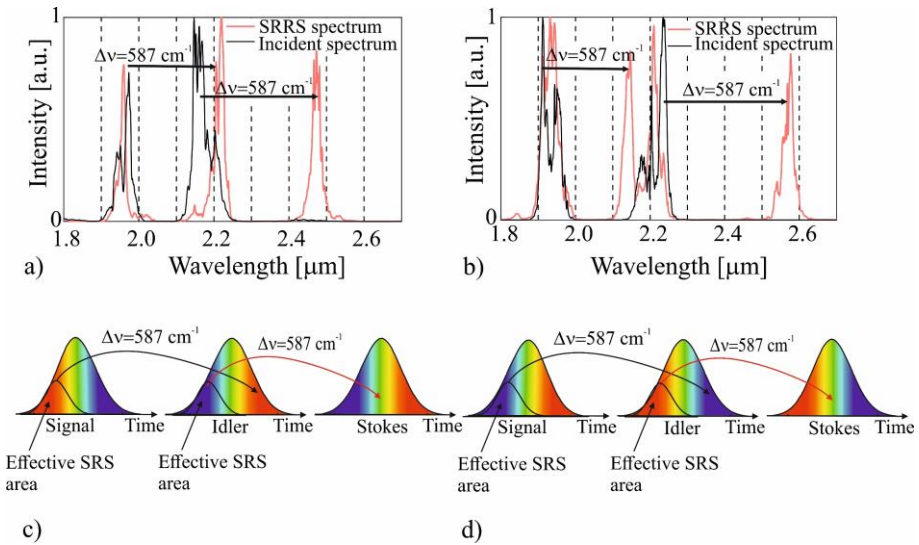


**Fig. 4.10** The normalized output spectra before (black lines) and after (red lines) a hydrogen cell with negative a) and positive b) GDD induced in the SC seed pulse. Arrows show the signal-to-idler (orange lines) and idler-to-Stokes (red lines) energy transfer, both corresponding to a rotational Stokes shift at  $587 \text{ cm}^{-1}$ . Illustration of signal and idler chirps and effective SRS amplification and Stokes generation when the signal has a negative c) or positive d) chirp.

Furthermore, with a positive (reverse) chirp of the idler pulse, Stokes radiation is generated at a central wavelength of  $\sim 2.47 \mu\text{m}$ , which corresponds to a rotational Raman shift of  $587 \text{ cm}^{-1}$  from the trailing edge of the incident idler pulse (Fig. 4.10 c). In contrast, a positive GDD (Fig. 4.10b) results in a more efficient energy transfer to the Stokes radiation, whose spectrum is shifted towards longer wavelength at  $\sim 2.57 \mu\text{m}$ . These observations can be explained by the fact that for negatively chirped pulses the radiation



frequencies in the pulse tail are shifted to the red, while for positively chirped pulses – to the blue range (Fig. 4.10 c and d). Therefore, the observed SRRS shift does not correspond to the central frequency of the pump pulse, but it is shifted toward a longer wavelength for negatively chirped pulses and a shorter wavelength for positively chirped ones. Thus, these findings highlight the influence of chirp on the spectral output of the OPCPA coupled to SRRS, since the timing and GDD of the SC seed pulse affect the efficiency of energy redistribution between different spectral components. The interplay between chirp, timing, and spectral distribution plays a critical role in determining the energy transfer efficiency in SRRS chirped-pulse amplification.

The evolution of the SRRS output spectra and total pulse output energy as a function of hydrogen pressure are shown in Fig. 4.11 at a positive GDD induced in the SC seed pulse. The spectra in Fig. 4.11a were measured with a total incident energy of the signal and idler pulses of 1.5 mJ. As the hydrogen pressure increases to 6 MPa, the spectral peaks corresponding to the signal-to-idler and idler-to-Stokes shifts become more pronounced.

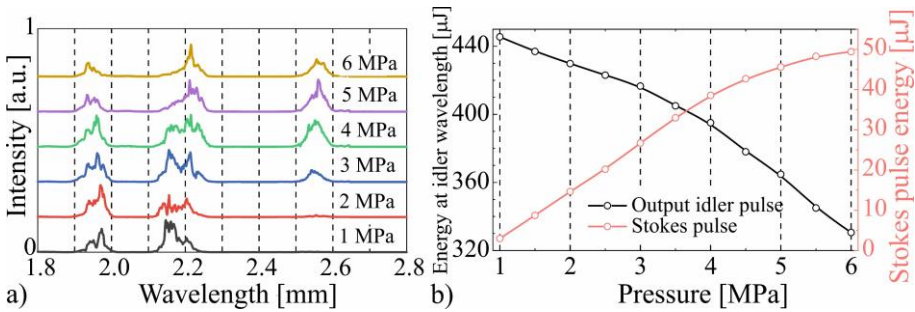


**Fig. 4.11** a) The evolution of the SRRS output spectra at a total incident energy of 1.5 mJ. b) The output energy at the idler (black line – left axis) and Stokes wavelength (red line – right axis) as a function of hydrogen pressure with a positive GDD induced in the SC seed pulse

The dependence of the output energy at the idler wavelength (black line, left axis in Fig. 4.11b) on the hydrogen pressure shows the steadily decay from  $\sim 445 \mu\text{J}$  to  $\sim 330 \mu\text{J}$ . In contrast, the Stokes pulse energy (red line – right axis in Fig. 4.11b) shows a continuous increase, reaching a value of  $\sim 50 \mu\text{J}$  at 6 MPa. It is clear that increasing the Raman gain with hydrogen pressure provides better energy transfer to Stokes pulses, although saturation was observed from  $\sim 4.5$  MPa, apparently due to SPM and other nonlinear effects.

Further improvements in SRRS conversion efficiency were expected for an even longer hydrogen cell. The dependence of the Stokes pulse energy on the incident idler pulse energy is shown in Fig. 4.12a using different length: 65 cm or 110 cm, as well as a composite double cell of 65 cm each. The double

cell outperformed all others, delivering a Stokes energy of  $\sim 70 \mu\text{J}$ , while the output of the single 110 cm long cell barely reached  $\sim 10 \mu\text{J}$  (Fig. 4.12a). This can be explained by the suppression of accompanying nonlinear effects in the composite cell, such as SPM, self-focusing and a smaller contribution of vibrational SRS at wavelengths longer than  $10 \mu\text{m}$ , outside the transparency range of  $\text{CaF}_2$  windows. In the two-cell configuration, the signal and idler beams were focused in the first cell by a 500 mm focal length lens and then refocused in the second cell by a 250 mm focal length lens. Better overlap of interacting beams provides increased SRS efficiency.

The transmission of signal and idler pulses with a total energy of 1.5 mJ in the wavelength range of  $\sim 1.9 - 2.25 \mu\text{m}$  was measured as a function of hydrogen pressure for 65 cm and 110 cm long cells (Fig. 4.12b). The significant decrease in transmission, especially in the long cell, is most likely explained by collision-induced absorption [252] and the contribution of vibrational Stokes at pressures above 2 MPa.

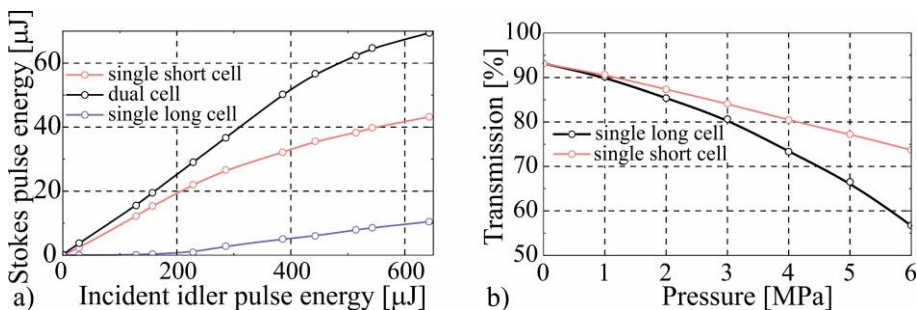


**Fig. 4.12** a) The dependence of the Stokes pulse energy on the incident idler pulse energy using 65 cm (blue line), 110 cm (red line), and a double cell of 65 cm each (black line). b) The transmission of cells 65 cm and 110 cm long depending on the hydrogen pressure.

Finally, an even shorter cell of 43 cm length with a 250 mm focusing length provided the highest order rotational Stokes. With a total energy contained in the incident signal and idler pulses of 1.5 mJ and a hydrogen pressure of 6 MPa, a third-order rotational Stokes pulse was observed at a wavelength of  $\sim 3 \mu\text{m}$  (Fig. 4.13 – black line). In this case, the output signal and the idler pulses were filtered with  $2.4 \mu\text{m}$  long-pass filter due to the high intensity during the measurement.

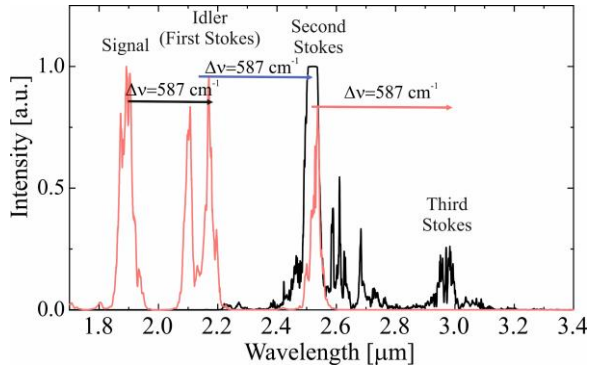


**Fig. 4.13** Normalized output spectra from a 63 cm (red line) and 43 cm (black line) cell at 6 MPa hydrogen pressure. Arrows indicate the Stokes shift at  $587\text{ cm}^{-1}$ .

These results highlight the importance of careful selection of gas cell lengths to minimize losses in the SWIR and MWIR range. Hence, to improve the efficiency of the transient SRRS and expand the SWIR pulse bandwidth, it is best to use few passes in a short cell, possibly in a Herriot configuration [253,254]. Seeding with SC can be useful for reducing the cascade SRRS threshold, but requires custom-made dichroic separators in this wavelength range.

#### 4.5. Summary of the results

The combination of TSRCPA with OPCPA operating in the SWIR range provides a significant build-up in the idler pulse energy at the Stokes wavelength. Using a single KGW crystal-based TSRCPA stage, the energy conversion from a signal pulse at  $\sim 1950\text{ nm}$  into an idler pulse at the Stokes wavelength of  $\sim 2250\text{ nm}$  was demonstrated with an efficiency of  $\sim 33\%$  and further compression to  $\sim 53\text{ fs}$ . Using a larger aperture KGW crystal or even replacing it with a gas cell filled with  $\text{SF}_6$  could pave the way to scaling the output energy to multi-mJ levels.

The transient cascade SRRS in compressed hydrogen provides a Stokes pulse energy of  $\sim 70\text{ }\mu\text{J}$  at  $\sim 2.6\text{ }\mu\text{m}$  with a conversion efficiency of  $\sim 11\%$  after optimization of the signal and idler spectra, the chirp induced in the signal pulses, and the cell length. The possibility of generating third-order Stokes at a wavelength of  $\sim 3\text{ }\mu\text{m}$  was also demonstrated, although to improve the SRRS conversion efficiency it is necessary to use a SC seed covering the range of  $\sim 2.5 - 3.5\text{ }\mu\text{m}$ .

The prospects for using the OPCPA/TSRCPA hybrid configuration are not limited to the SWIR range, but can also be extended to the MWIR or even

LWIR ranges. Progress in developing ultrafast, high-intensity laser sources in the LWIR range spanning 8 – 20  $\mu\text{m}$  will facilitate applications such as direct laser acceleration [255], high-energy particle and nuclear physics, dipole approximation limit studies [256], remote sensing [257,258], and advanced molecular spectroscopy [259]. Typically, broadband LWIR pulses were obtained by nonlinear down-conversion in DFG or OPA [260–262], with OPCPA serving to upscale their energy [263,264]. In this case, the TSRCPA stage based on a hydrogen-filled cell can replace the OPCPA stage. When using pump pulses at a wavelength of  $\sim 1.8 - 2 \mu\text{m}$ , the first vibrational Stokes pulse in hydrogen will be at a wavelength of  $\sim 7.1 - 11.8 \mu\text{m}$  (Fig. 4.14). These ultrashort output pulses in the LWIR range can be used to seed TW-class  $\text{CO}_2$  amplifiers [265]. Then TSRCPA seed pulses can be obtained by DFG between the signal at  $\sim 1.9 \mu\text{m}$  and the idler at  $\sim 2.25 \mu\text{m}$  in a variety of nonlinear crystals: silver gallium sulfide ( $\text{AgGaS}_2$  or AGS) [266], lanthanum gallium silicate ( $\text{LiGaS}_2$  or LGS) [267], gallium selenide ( $\text{GaSe}$  or GS) [261,263], zinc germanium phosphide ( $\text{ZnGeP}_2$  or ZGP) [268]. However, in this case type II BiBO or BBO crystals should be used due to the differing polarization of the signal and idler waves.

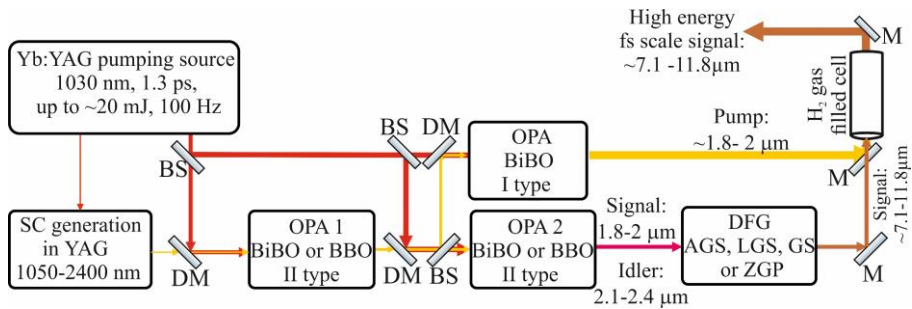


**Fig. 4.14** Hybrid OPCPA/TSRCPA configuration for generation of high-energy femtosecond LWIR pulses: OPA 1, OPA 2 – optical parametrical amplifiers, BS – beam splitter, DM – dichroic mirror, M – mirrors, DFG – difference frequency generation.

Thus, the demonstrated OPCPA/TSRCPA hybrid approach paves the way for efficient generation of high-energy femtosecond pulses in SWIR, MWIR and even LWIR spectral ranges.

## MAIN RESULTS AND CONCLUSIONS

1. The high-energy SWIR OPCPA setup based on BiBO crystals achieved an output energy of  $\sim 2.1$  mJ with an outstanding pump-to-signal conversion efficiency of up to 25% in the last stage. Driven by single-picosecond pump pulses, the low stretch-compression ratio ensured compression to  $\sim 38$  fs in a glass block with a peak power of  $\sim 47$  GW. Adaptive spectral phase control enables pulse compression to below 25 fs with peak powers exceeding 80 GW, thus validating the broadband SWIR SC seed generated by a single-picosecond 1030 nm pump laser.
2. The use of  $\sim 1.3$  ps circularly polarized pump pulses in the NIR range made it possible to suppress the vibrational SRS modes and achieve efficient cascade generation of high-order rotational Stokes components in compressed hydrogen with a conversion efficiency of  $\sim 42\%$  at 5 MPa.
3. The use of broadband NIR supercontinuum seed allowed generation of rotational Stokes up to the fourth order in the difficult-to-reach wavelength range of  $\sim 1.1 - 1.4$   $\mu\text{m}$  with an increase in conversion efficiency up to 52%. The maximum output pulse energy within the rotational Stokes comb exceeded 3 mJ, while the spectral bandwidth was sufficient to generate transform-limited pulses of  $\sim 14$  fs at a central wavelength of 1.2  $\mu\text{m}$ .
4. Synthesis of adjacent vibrational Stokes modes in successive TSRCPA stages based on KGW ensured a 23-fold expansion in the composite bandwidth compared to the pump pulses, supporting  $\sim 50$  fs transform-limited pulses at 1120 nm. Despite the modulated spectral phase, the amplified Stokes pulses were partially compressed to 135 fs.
5. The collinear SWIR OPCPA setup combined with TSRCPA enabled efficient signal-to-idler energy conversion in the KGW crystal. Meanwhile, the third-order rotational Stokes generation in compressed hydrogen ensured spectral extension beyond 3  $\mu\text{m}$  after optimization of the signal and idler spectra, the chirp induced in the signal pulse, the cell length and gas pressure.

# SANTRAUKA

## Įvadas

Nuo pat lazerių atsiradimo 1960 m., [1] sparčiau jų plėtrą lėmė taikomieji mokslo, medicinos ir pramonės sričių poreikiai [2]. Nobelio premijos laureatų D. Strickland ir G. Mourou 1985 m. pademonstruotas metodas – čirpuotų impulsų stiprinimas (CPA) tapo kertiniu atradimu, kuriant ultrasparčiuosius lazerius. Šis metodas leido pasiekti TW eilės smailinę impulsų galią [3], o tai atvėrė kelią daugeliui stipraus lauko fizikos taikymų [2], tokių kaip izoliuotų atosekundinių impulsų generavimas, elektronų ir jonų greitinimas, bei bangos paketų dinamikos atomuose ir molekulėse tyrimai. Šiandien mokslinėse laboratorijose naudojamos lazerinės sistemos, kurių impulsų trukmė siekia dešimtis femtosekundžių, o jų taikymo sritys nuolat plečiasi.

Šiuolaikiniai lazeriai apima platų elektromagnetinių bangų spektrą – nuo ultravioletinių iki ilgųjų infraraudonųjų spindulių (LWIR). Pastaraisiais metais ypač susidomėta 2  $\mu\text{m}$  – terahercų (THz) bangų spektro sritimi. Ši spektro sritis taikoma molekulėms identifikuoti cheminės analizės metu, stebint aplinką, atliekant medicininę diagnostiką, procesų valdymą, taip pat pritaikoma ir saugumo ir gynybos srityse [4]. Šiuo metu didelis dėmesys skiriamas femtosekundiniams lazeriams, veikiantiems trumpųjų ir vidutinių infraraudonųjų bangų diapazone (SWIR-MWIR), apimančiame 1.4–3  $\mu\text{m}$  ir 3–8  $\mu\text{m}$  bangos ilgius. Šio spektro didelio intensyvumo lazeriai gali būti naudojami ne tik molekuliniais jutikliams, bet ir stipraus lauko fizikos eksperimentams, užtikrinant efektyvesnę atosekundinių impulsų generaciją [5], didesnę THz generavimo efektyvumą [6] ir geresnę tuneliavimo bei daugiafotoninių procesų atskyrimą [7]. Šiuolaikiniai didelės smailinės galios lazeriniai šaltiniai, veikiantys SWIR-MWIR bangų ilgių ruože, pastaruoju metu plačiai taikomi molekulinės struktūros atvaizdavimui [8] ir medžiagų apdirbimui [9]. Atosekundžių impulsų lazerinių šaltinių kūrimas grindžiamas aukštųjų harmonikų generacijos (HHG) principu, kai kelių optinių ciklų impulsai, pasižymintys didele smailine galia, sąveikauja su inertinėmis dujomis. Tokie lazeriniai šaltiniai yra ypač vertingi tiesioginiams biologinių molekulių tyrimams vandeniniuose tirpaluose [10], taip pat elektroninės, vibracinės, rotacinės [11] ir magnetizmo [12] dinamikos stebėjimui realiuoju laiku. Nors didžiausia fotonų energija, pasiekama naudojant HHG, [13] kaip ir fotoemituojamų elektronų energijos riba [14] priklauso nuo  $\lambda^2$ , bendras keitimo efektyvumas mažėja [15], tad kiekvienam generuojamam spektriniam diapazonui būtina parinkti optimalų kaupinimo bangos ilgį. Atsižvelgiant į tai

kompromisinis sprendimas yra naudoti SWIR bangos ilgio lazerinius šaltinius koherentinės minkštosios rentgeno spinduliuotės generacijai 284–543 eV diapazone [16, 17]. Be to, ultratrumpi SWIR-MWIR impulsai palengvina išsamius atomų ir molekulių dinamikos tyrimus [18,19] leidžiančius vizualizuoti molekulinę struktūrą [20].

Siekiant generuoti ultratrumpuosius impulsus SWIR-MWIR diapazone, dažniausiai naudojami netiesiniai metodai, kurių kaupinimui pasitelkiami femtosekundiniai ir pikosekundiniai Nd arba Yb lazeriniai šaltiniai su  $\sim 1 \mu\text{m}$  spinduliuotės bangos ilgiu [24–26]. Šiuo atveju ypač didelės energijos, kelių optinių ciklų trukmės SWIR lazerių kūrimui pagrinde naudojama išsigimusios konfigūracijos OPCPA, ties  $\sim 2 \mu\text{m}$ . Tačiau dauguma iki šiol sukurtų SWIR OPCPA koncepcijų yra sudėtingos ir salyginai brangios, nes reikalauja aktyvaus fazės valdymo su AOPDF ir skirtingų užkrato ir kaupinimo lazerių sinchronizavimo, o tai mažina sistemos stabilumą [25]. Taigi, siekiant didinti SWIR femtosekundinių lazerių prieinamumą ir patikimumą, svarbu ištirti ir sukurti alternatyvias, paprastesnes ir pigesnes OPCPA architektūras.

Kitas metodas, galintis išplėsti komerciškai prieinamų lazerių spektrinį diapazoną iki SWIR-MWIR srities, yra priverstinė Ramano sklaida (SRS), kuri plačiai ištirta su nanosekundiniais kaupinimo impulsais [27]. Šiuo atveju, skirtingai nuo keturbangio maišymo, skirtuminio dažnio generavimo (DFG) ar optinio parametrinio stiprinimo (OPA), SRS neriboja fazinis sinchronizmas. Vis dėl to, SRS efektyvumas nenuostovijame režime ženkliai sumažėja [28], todėl būtina ieškoti efektyvių ultratrumpųjų SWIR impulsų generacijos būdų panaudojant SRS.

Šiame tyrime nagrinėjama didelės smailinės galios SWIR OPCPA lazerinė sistema, kaupinama dviejų pakopų Yb:YAG CPA, kurio išvadinių impulsų trukmė  $\sim 1.3$  ps. Pagrindinis tikslas kuriant šią OPCPA sistemą, kurios užkrato šaltinis yra plačiajuostis superkontinuumas (SC), buvo pasiekti didžiausią keitimo efektyvumą, išlaikant sistemos paprastumą ir kompaktiškumą. Šių tyrimų rezultatas – lengvai atkuriami kelių mJ išvadinės impulsų energijos OPCPA sistema, veikianti SWIR diapazone ir pasižyminti išskirtiniu efektyvumu.

Tyrime taip pat buvo nagrinėjami metodai, skirti padidinti SRS efektyvumą nenuostovijame režime, išplečiant spektrinį diapazoną NIR ir SWIR srityse. Tyrimo metu ištirtas dviejų pakopų priverstinės Ramano sklaidos stiprintuvas, kuriame skirtingi gretimi Stokso komponentai stiprinami nuosekiose pakopose. Be to, parodyta, kad nenuostovijame režime SRS kartu su SWIR OPCPA leidžia padidinti šaltinės bangos intensyvumą. Apibendrinant galima teigti, kad šiame darbe nagrinėjama

įvairių netiesinių efektų sinergija, siekiant efektyviai generuoti SWIR femtosekundinius impulsus.

### Disertacijos tikslas ir uždaviniai

Disertacijos tikslas – ištirti ir sukurti femtosekundinės trukmės lazerines sistemas, veikiančias SWIR diapazone ir paremtas superkontinuumo, OPCPA bei nenuostoviosios SRS aukšto slėgio dujose ir kristaluose netiesiniais procesais.

Disertacijos tikslui pasiekti buvo išskirti šie darbo uždaviniai:

1. Ištirti ir sukurti kelių optinių ciklų, kelių mJ išvadinės impulso energijos OPCPA, veikiančią SWIR diapazone ties  $\sim 2 \mu\text{m}$ , kaupinimui naudojant  $\sim 1.3 \text{ ps}$  trukmės Yb:YAG CPA išvadinius impulsus, o užkratui plačiajuostę SC spinduliuotę.
2. Ištirti pakopinės priverstinės rotacinės Ramano sklaidos (SRRS) aukšto slėgio vandenilio kiuvetėje galimybes, siekiant išplėsti  $\sim 1.3 \text{ ps}$  trukmės ir 1030 nm centrinio bangos ilgio kaupinimo impulsų spektrinę juostą į SWIR diapazoną panaudojus plačiajuostę SC ir įvertinti Stokso impulsų spūdą.
3. Ištirti gretimų vibracinių Stokso modų sintezę taikant nenuostoviąją SRS KGW kristaluose, kaupinimui naudojant  $\sim 1.3 \text{ ps}$  trukmės impulsus ties 1030 nm ir SC kaip užkrato šaltinį, bei įvertinti sustiprintų NIR srities impulsų spūdą.
4. Ištirti kolinearios konfigūracijos SWIR OPCPA kartu su nenuostoviaja vibracine SRS KGW kristale ir SRRS suslėgtime vandenilyje, siekiant išplėsti išvadinių impulsų spektrinę juostą ir užtikrinti energijos pernašą į SWIR ir MWIR spektro sritis.

### Mokslinis tyrimų naujumas

1. Optimizuotoje kelių mJ BiBO kristalo pagrindo SWIR OPCPA sistemoje, veikiančioje  $\sim 2 \mu\text{m}$  bangos ilgio diapazone, paskutinėje pakopoje buvo pasiektas išskirtinis – iki  $\sim 25\%$  kaupinimo į signalą keitimo efektyvumas, o impulsai, be aktyvaus spektro fazės valdymo,



buvo suspausti iki ~38 fs trukmės. Šie rezultatai pirmą kartą pasiekti naudojant SWIR SC impulsus, kurie generuojami su pikosekundės trukmės 1030 nm bangos ilgio impulsais, kaip užkrato šaltinį kelių mJ OPCPA.

2. Pirmą kartą pademonstruota 52% keitimo efektyvumo nenuostovioji pakopinė SRRS suslėgtame vandenilyje ir sugeneruoti kelių mJ energijos išvadiniai impulsai, apimantys sunkiai pasiekiamą ~1.1–1.4  $\mu\text{m}$  bangos ilgių spektro ruožą, kaupinimui naudojant ~1.3 ps trukmės ir 1030 nm centrinio bangos ilgio impulsus.
3. Pirmą kartą pademonstruota gretimų vibracinių Stokso modų spektro sintezė KGW kristaluose, dėl kurios sustiprintų SC impulsų spektrinės juostos plotis padidėjo ~23 kartus, palyginti su kaupinimo impulsais, o keitimo efektyvumas siekė ~35%.
4. Apjungiant SWIR OPCPA su nenuostovioju priverstinės Ramano sklaidos čirpuotų impulsų stiprinimu (TSRCPA) KGW kristaluose, pirmą kartą pademonstruota energijos pernaša į šalutinės bangos impulsą, pasiekiant ~25% signalo į šalutinę bangą keitimo efektyvumą.
5. Hibridinės SWIR OPCPA ir TSRCPA suslėgto vandenilio dujose sistemos tyrimai parodė, kad teigiamai čirpuoti plačiajuosčiai SC impulsai leidžia išplėsti SRRS spektrinę juostą link tolimesniųjų bangų ilgių, palyginti su neigiamai čirpuotais impulsais.

### Praktinė nauda

Doktorantūros studijų metu buvo sukurta kelių optinių ciklų, kelių mJ OPCPA, veikiantis SWIR diapazone ties ~2  $\mu\text{m}$ . Lazerinę sistemą sudaro Yb:YAG kaupinimo lazeris, plačiajuosčio SC generacija, AOPDF, trys BiBO kristalų pagrindo OPCPA pakopos ir impulsų spūda stikle. Ekonomiškai efektyvus šios sistemos įgyvendinimas be AOPDF leidžia pasiekti panašius išvadinius parametrus, tik su kiek ilgesne impulsų trukme. Sukurta didelės galios SWIR lazerinė sistema, gali būti pritaikyta nuotolinio stebėjimo LIDAR'ams, skirtiems atmosferos teršalams, biocheminėms medžiagoms ir pavojingoms dujoms aptikti. Tuo tarpu, ypač intensyvių SWIR-MWIR impulsų filamentacija sudaro sąlygas aptikti dideliu atstumu tokias molekules kaip  $\text{H}_2\text{O}$ ,  $\text{CO}_2$ ,  $\text{CO}$  ir  $\text{NH}_4$ . Padidinus sukurtos lazerinės sistemos impulsų

pasikartojimo dažnį, būtų galima pritaikyti sistemą palydoviniam ryšiui palaikyti atmosferos skaidrumo srityje.

Pritaikius SRRS metodą aukšto slėgio vandenilio dujose, pademonstruotas paprastas ir efektyvus būdas generuoti kelių mJ energijos,  $<150$  fs ar net  $15$  fs trukmės impulsus,  $\sim 1.1 - 1.4$   $\mu\text{m}$  spektro ruože. Šie impulsai gali būti pritaikyti įvairiose srityse, įskaitant netiesinę mikroskopiją.

Šiame darbe taip pat nagrinėjama kolinearios konfigūracijos OPCPA kombinacija su TSRCPA dujose ar kristaluose gali būti efektyvus būdas padidinti šalutinės bangos impulso energiją. Kadangi nešlio fazės gaubtinės (CEP) stabilumas yra esminis HHG, atosekundinių impulsų generavimui ir kitiems stipraus lauko fizikos eksperimentams, šis metodas gali prisidėti prie paprastų, tačiau aukšto efektyvumo kelių optinių ciklų lazerinių šaltinių kūrimo, veikiančių SWIR-MWIR diapazone. Galiausiai, sujungus SWIR OPCPA su nenuostoviąja SRRS suslėgtame vandenilyje, išvadinio impulso spektrinė juosta išplinta iki  $\sim 3$   $\mu\text{m}$ . Tokie lazeriniai šaltiniai yra ypač naudingi spektroskopijai, nuotoliniam aptikimui ir medicinos diagnostikai. Be to, ši metodą galima pritaikyti generuoti LWIR bangos ilgių ruožo impulsus, skirtus molekulinei spektroskopijai, atmosferos nuotoliniam stebėjimui ir TW klasės  $\text{CO}_2$  stiprintuvų užkratui.

### Ginamieji teiginiai

1. Plačiajuosčio SWIR SC užkrato impulsai, generuojami  $1030$  nm bangos ilgio vienetinių pikosekundžių kaupinimo impulsais, tinka pasyviai sinchronizuotai trijų pakopų BiBO OPCPA sistemai. Tokia OPCPA konfigūracija leidžia generuoti kelių mJ SWIR impulsus, suspaustus stiklo bloke iki kelių optinių ciklų trukmės.
2. Naudojant plačiajuosį superkontinuumo užkrato šaltinį, apskritiminės poliarizacijos vienetinių pikosekundžių trukmės  $1030$  nm kaupinimo impulsus ir didelį vandenilio slėgį dujų kiuvetėje, efektyviai generuojama pakopinė SRRS sunkiai pasiekiamame  $\sim 1.1-1.4$   $\mu\text{m}$  bangos ilgių diapazone bei slopinama vibracinė SRS.
3. NIR TSRCPA spektrinės juostos plotis išplečiamas daugiau nei  $20$  kartų, naudojant gretimų vibracinių Ramano modų spektrinę sintezę stiprintuvo pakopose su KGW kristalais, lyginant su vienetinių pikosekundžių kaupinimo impulsais, o išvadiniai impulsai yra dalinai spūdūs.

4. Kolinearios konfigūracijos SWIR OPCPA kombinacija su TSRCPA užtikrina efektyvų energijos pernešimą iš signalo į šalutinės bangos impulsą KGW kristale, o kombinacija su nenuostoviaja SRRS aukšto slėgio vandenilio dujų kiuvetėje, naudojant teigiamo čirpo superkontinuumo impulsus, išplečia išvadinės spinduliuotės spektrą virš  $\sim 3 \mu\text{m}$ , generuojant aukštesnės eilės rotacinius Stoksus.

## Aprobacija

### **Publikacijos susijusios su disertacijos tema:**

- A1.** A. Petrulėnas, P. Mackonis and A. M. Rodin, Synthesis of Adjacent Stokes Spectra in a Two-Stage Transient Stimulated Raman Chirped-Pulse Amplifier, *Crystals* **12** (7), 888 (2022).
- A2.** A. Petrulėnas, P. Mackonis and A. M. Rodin, Signal-to-idler energy conversion from 1.9 to 2.3  $\mu\text{m}$  by transient stimulated Raman chirped-pulse amplification, *Optics Letters* **48** (7), 1598-1601 (2023).
- A3.** A. Petrulėnas, P. Mackonis and A. M. Rodin, High-efficiency bismuth borate-based optical parametric chirped pulse amplifier with  $\sim 2.1$  mJ, 38 fs output pulses at  $\sim 2150$  nm, *High Power Laser Science and Engineering*, **11**, e27 (2023).
- A4.** A. Petrulėnas, P. Mackonis, A. Černeckytė and A. M. Rodin, Amplification of Supercontinuum Seed Pulses at  $\sim 1078$ – $1355$  nm by Cascade Rotational SRS in Compressed Hydrogen. *Applied Science*, **13** (24), 13087 (2023).

## Autoriaus indėlis

Disertacijos autorius atliko visus čia aprašytus eksperimentus ir skaičiavimus, analizavo rezultatus ir suformulavo išvadas bei hipotezes. Jis taip pat aktyviai dalyvavo rengiant visas publikacijas, pristatė naujausius rezultatus tarptautinėse konferencijose ir parengė A1–A5 rankraščius.

## Bendraautorių indėlis

**Dr. A. M. Rodin** vadovavo visam tiriamojo darbo procesui, nustatė jo kryptį, teikė mokslines koncepcijas, suformulavo konkrečias užduotis ir jų įgyvendinimo metodiką, konsultavo moksliniais klausimais, dalyvavo diskusijose interpretuojant rezultatus bei reikšmingai prisidėjo prie publikacijų A1–A4 parengimo.

**Dr. P. Mackonis** reikšmingai prisidėjo prie SWIR OPCPA ir nenuostoviosios SRS tyrimų metodologijos tobulinimo, aktyviai dalyvavo rezultatų analizėje ir naujų užduočių formulavime bei ženkliai prisidėjo prie publikacijų A1–A4 parengimo.

**A. Černeckytė** aktyviai dalyvavo atliekant nenuostoviosios SRRS eksperimentus aukšto slėgio vandenilio dujų kiuvetėje NIR ir SWIR diapazonuose bei prisidėjo prie A4 rankraščio parengimo.

## Literatūros apžvalga

Pirmajame šios disertacijos skyriuje aprašomi ultratrumpųjų impulsų generavimo metodai SWIR spektriniame ruože, daugiausia dėmesio skiriant OPCPA ir SRS. Šios technologijos yra ypač reikšmingos generuojant didelės energijos ultratrumpus impulsus, kurie naudojami įvairiose srityse – nuo fundamentaliųjų tyrimų iki pramonės ir medicinos taikymų.

Skyrius (1.1 poskyris) pradedamas nuo ultratrumpų SWIR impulsų generavimo metodų apžvalgos, kurioje aptariamos įvairios technologijos, tokios kaip kieto kūno lazeriniai šaltiniai kurių aktyvioji terpė yra tuliu, holmiu ar chromu legiruoti granatai, perovskitai, vanadatai, fluoridai, volframidai ar retųjų žemių seskvioksidai [29]. Šie lazeriniai šaltiniai gali generuoti nuo fs [43,46,47] iki kelių ps [35] trukmės ir iki keliasdešimt mJ energiją [34] turinčius lazerio impulsus.

Kitoje skyriaus dalyje (1.1.1 poskyris) aptariama dabartinė pažanga siekiant išplėsti OPCPA stiprinimo juostą [82–84], padidinti išvadinių impulsų energiją [79–81] bei pateikiami galimi sprendimai norint padaryti sistemas kompaktiškesnes ir lengviau atkuriamas. Taip pat pateikiama nuodugni OPCPA sistemų, veikiančių 1.4–3  $\mu\text{m}$  bangos ilgių diapazone, apžvalga, kurioje akcentuojami pagrindiniai techniniai iššūkiai ir naujausi technologiniai sprendimai. Aptariama, kaip kaupinimo impulsų trukmė daro įtaką sistemos efektyvumui [59,60]. Šiuo atveju, kaupinimo impulsų trukmė yra svarbi nustatant pradinio signalinio impulso plėtimo koeficientą, daro

įtaką jo dispersijos kontrolei ir bendrai impulso plėtimo ir suspaudimo konfigūracijai [64,65]. Įprastai didelės energijos ultratrumpųjų impulsų lazerinės sistemos šiame diapazone yra sudėtingos ir brangios, kai jose yra naudojamas aktyvus fazės valdymas [88]. Kadangi SWIR spektriniame diapazone veikiančių lazerinių sistemų išvadinių impulsų spektrinė juosta yra labai plati, kritiškai svarbu tinkamai valdyti GDD ir TOD. Esant didelei kaupinimo impulso energijai ir plačiai spektrinei juostai, dispersijos valdymas tampa dar sudėtingesnis. Tokiose sistemose, norint pasiekti impulsų trukmę artimą FTL trukmei, dažnai naudojamas AOPDF, kuris leidžia tiksliai kompensuoti GDD ir TOD. Galiausiai taip pat aptariami naujaisi pokyčiai, susiję su kompaktiškesnių ir efektyvesnių OPCPA sistemų kūrimu, įskaitant superkontinuumo naudojimą, kaip OPCPA užkrato šaltinį [90–93]. Šiuo atveju superkontinuumo spinduliuotė, generuojama plačiame spektriniame diapazone, leidžia eliminuoti poreikį naudoti papildomas dažnio keitimo pakopas, tokias kaip DFG ar OPG [87].

Trečioje skyriaus dalyje (1.2 poskyris) išsamiai aptariama priverstinė Ramano sklaidos taikymas lazerinėse sistemose. Šis metodas yra netiesinis optinis procesas, leidžiantis efektyviai konvertuoti lazerinės spinduliuotės bangos ilgį link ilgesnių, naudojant Ramano aktyvias medžiagas [27]. Vienas iš pagrindinių SRS privalumų – nėra fazinio sinchronizmo sąlygos, todėl ji yra itin lanksti ir gali būti naudojama plačiame spektriniame ruože su skirtingomis Ramano aktyviomis terpėmis. Skyriuje (1.2.1 poskyris) pirmiausia pateikiami SRS pagrindai – nusakoma kuo SRS skiriasi nuo spontaniškos Ramano sklaidos, aprašomas sklaidos mechanizmas, esant tiek rotacinei tiek vibracinei sklaidai bei pateikiami svarbiausi SRS aprašantys dydžiai, tokie kaip sklaidos skerspjūvis, stiprinimo koeficientas, bei medžiagos Ramano poslinkis [119,124].

Taip pat yra nagrinėjama nenuostovioji priverstinė Ramano sklaida (1.2.2 poskyris), kai lazerio impulsų trukmė yra trumpesnė nei Ramano aktyviosios terpės molekulių arba fononų relaksacijos trukmė. Šiuo atveju kartu su SRS, kai kaupinimo trukmė yra tarp 0.1-2 ps, atsiranda ir kiti netiesiniai procesai kaip SPM, superkontinuumo generacija ir panašiai, kurie mažina SRS generacijos efektyvumą [140,141]. Tad šiuo atveju reikia ieškoti būdų kaip efektyviai keisti ultratrumpų impulsų lazerinę spinduliuotę link tolimesnių bangos ilgių [105,155].

Skyriaus pabaigoje pateikiama tyrimų apžvalga, susijusi su ultratrumpų impulsų generavimu SWIR bangos ilgių ruože, tam naudojant SRS tiek dujinėse [161–163] tiek kieto kūno terpėse [167–170], aprašomi metodai kaip galima padidinti Stokso spektrinė juosta esant nenuostoviajai SRS. Šiuo atveju galima apjungti SPM su SRS [149] arba panaudoti daugiapakopinę

SRS [176]. Visgi šiuo metu vyraujantis ultratrumpųjų Stokso impulsų generavimo metodas yra pagrįstas tuščiaidurių skaidulų užpildytų dujomis, panaudojimu [182–184]. Tačiau šis brangus ir nekompaktiškas metodas nėra toks patrauklus kaip aukšto slėgio dujų kiuvetės.

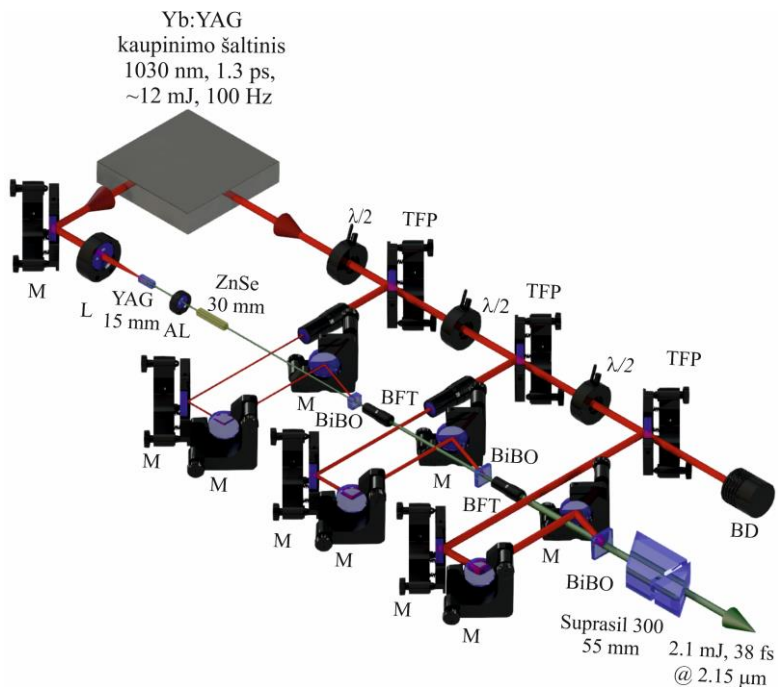
## Rezultatai

Tyrimų rezultatai disertacijoje išdėstyti trijuose skyriuose. Pirmajame pateikti rezultatai apie mJ eilės SWIR OPCPA sistemą. Antrajame rotacinės ir vibracinės SRS NIR spektro ruože tyrimai, naudojant 1.3 ps trukmės kaupinimo impulsus. Trečiajame aprašomas SRS ir SWIR OPCPA apjungimas siekiant išplėsti išvadinių impulsų spektrinę juostą.

### Didelės energijos OPCPA sistema veikianti SWIR diapazone

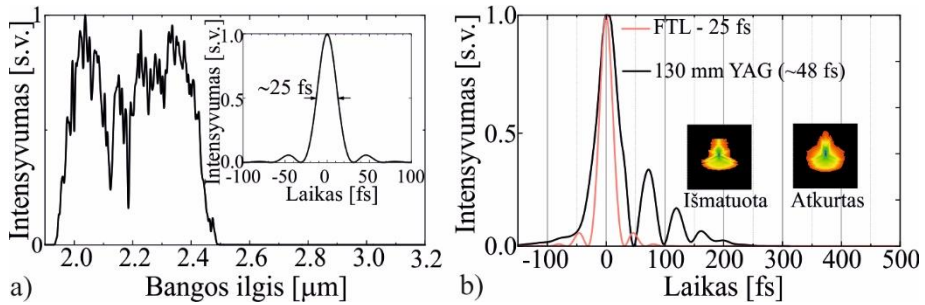
Antrame disertacijos skyriuje aprašoma efektyvi ir kompaktiška mJ eilės SWIR OPCPA sistema. Ją sudaro lengvai atkuriami moduliai: Yb:YAG CPA, SC generacija YAG kristale, trijų pakopų OPCPA su BiBO kristalais, ir impulsų spūda Suprasil 300 stiklo prizmėse (1 Pav). Šios dalies lazerinės sistemos schema telpa ant  $1 \times 3 \text{ m}^2$  dydžio optinio stalo, o projektuojant kompaktiškesnę prototipą schemą galima sumažinti dar bent du kartus. Ypatingas dėmesys buvo skiriamas optimizuoti sukauptą TOD, plačios pastiprinto signalo dažnių juostos išlaikymą bei galimą mažiausią sustiprintų impulsų trukmę naudojant tik GDD kompensuojantį kompresorių

Taigi SC impulsai sugeneruoti 15 mm ilgio YAG kristale ties  $\sim 2.15 \mu\text{m}$  buvo stiprinami trijuose nekolinearios konfigūracijos OPCPA pakopose kurias sudarė  $4 \times 4 \times 6 \text{ mm}^2$ ,  $10 \times 10 \times 4 \text{ mm}^2$  ir  $15 \times 15 \times 4 \text{ mm}^2$  dydžio BiBO kristalai (I tipo, fazinio sinchronizmo kampas  $\theta = 8^\circ$ ), su AR danga 1700 – 2500 nm spektriniame diapazone (1 Pav.) ir galiausiai suspausti 55 mm ilgio Suprasil 300 stikle.



**1 Pav.** mJ-eilės SWIR OPCPA eksperimentinė schema: Yb:YAG – 1030 nm bangos ilgio dviejų pakopų čirpuotų impulsų stiprintuvas OPCPA kaupinimui ir SC generacijai, kurio išvadinių impulse trukmė yra 1.3 ps, TFP – plonasluoksnis poliarizatorius,  $\lambda/2$  – pusės bangos ilgio fazinė plokštelė, L – fokusuojantis lęšis, YAG – itrio aliuminio granatas skirtas SC generacijai, AL – achromatinis lęšis, ZnSe – cinko selenido strypas skirtas OPCPA signalo GDD valdymui, M – HR1030 nm veidrodžiai, PFT – pluošto formavimo teleskopas, BiBO – netiesinis kristalas, Suprasil 300 – prizmių pora skirta išvadinių impulsų spūdai.

Kuriant šią sistemą, pirmiausia buvo ištirta keletas skirtingų vienos pakopos OPCPA konfigūracijų: SC generuojamas 15 mm ir 130 mm ilgio YAG kristaluose, o sustiprinti impulsai atitinkamai spaudžiami priešingo ženklo GDD medžiagose – Suprasil 300 ir ZnSe. Šiuo atveju kai SC generuojamas trumpesniam YAG kristale, čirpas buvo apverčiamas 30 mm ZnSe prieš OPCPA pakopą. Taigi naudojant ilgesnį YAG kristalą SC generuoti, dėl didesnio spektrinio intensyvumo SWIR srityje pastebėtas geresnis efektyvumas iš kaupinimo į signalą keitimo ir ~20% didesnė išvadinė energija. Nepriklausomai nuo YAG kristalo ilgio, sustiprintų impulsų spektrinė juosta (FWHM lygyje) atitiko ~25 fs (<4 optinių ciklų) spektriškai ribotą impulsų trukmę, ties ~2.2  $\mu\text{m}$  centriniu bangos ilgiu (2 Pav. a) dalis). Visgi dėl likutinės trečios eilės dispersijos po spūdos abiem atvejais impulsų trukmė buvo apie ~47 fs (2 pav. b) dalis).

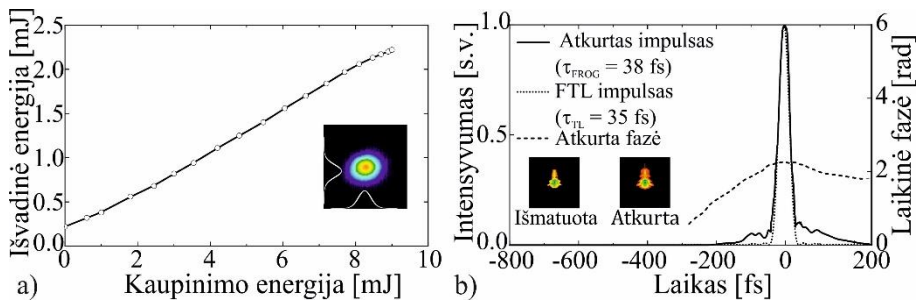


**2 Pav.** a) Išvadinis sustiprinto signalo spektras po vienos OPCPA pakopos, kai SC generuojamas 130 mm YAG kristale (intarpe – pagal išmatuotą spektrą apskaičiuota spektriškai ribota impulso trukmė). b) Išmatuotas su SHG-FROG sustiprinto signalo impulso laikinis profilis (juoda kreivė), kai SC generuojamas 15 mm ilgio YAG kristale ir palygintas su spektriškai ribotu impulsu apskaičiuotu pagal išmatuotą spektrą (raudona kreivė). Intarpai – išmatuoti (kairėje) ir atkurti (dešinėje) FROG pėdsakai su 1.3 % paklaida 512×512 pikselių tinklelyje.

Atsižvelgiant į šiuos preliminarius rezultatus, siekiant sukurti efektyvią didelės energijos OPCPA sistemą, buvo nuspręsta sumažinti stiprinimo juostos plotį. Šiuo atveju tuomet OPCPA sukaupta bendra TOD turi mažesnę įtaką išvadinių impulsų formai bei kontrastui. Palaipsniui ribojant stiprinimo juostos plotį taip, kad ji atitiktų 20–40 fs spektriškai ribotų impulsų plotį, galima daugiau kaip 30 % pagerinti laikinį kontrastą ir generuoti trumpesnius išvadinius impulsus.

Taigi, didelės energijos OPCPA sistemoje (1 Pav), siekiant susiaurinti stiprinimo dažnių juostos plotį, buvo išderintas fazinis sinchronizmas visose trijose OPCPA pakopose. Atitinkamai sustiprintas spektras apėmė diapazoną nuo  $\sim 1.95 \mu\text{m}$  iki  $\sim 2.4 \mu\text{m}$ , o juostos plotis atitiko 35 fs spektro ribotą impulso trukmę ir  $< 5$  optinius ciklus, ties centriniu  $2.15 \mu\text{m}$  bangos ilgiu. Remiantis mūsų skaičiavimais ir mažos energijos OPCPA tyrimu, spektrinės juostos plotis buvo pakankamai siauras, kad likutinės aukštesnės eilės dispersijos įtaka suspausto impulso laikinei formai būtų ženkliai mažesnė. Šiuo atveju trečioje OPCPA pakopoje panaudojus 9 mJ kaupinimo impulsų energijos, keitimo efektyvumas siekė iki  $\sim 23\%$ , o išvadinė signalo impulso energija iki 2.25 mJ (3 pav. a) dalis). Galiausiai sustiprinti impulsai Suprasil 300 stiklo bloke buvo suspausti iki 38 fs, o smailinė galia siekė  $\sim 47 \text{ GW}$  (3 pav. b) dalis).

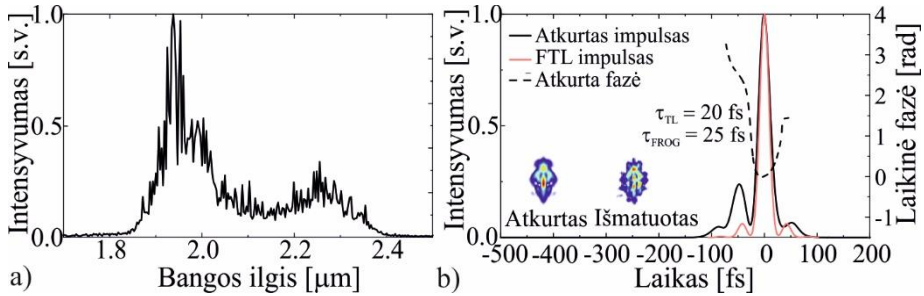




**3 Pav.** a) Išvadinės impulso energijos priklausomybė nuo kaupinimo impulso energijos paskutinėje OPCPA pakopoje (intarpe pavaizduotas tolimojo lauko pluošto profilis esant centriniam  $2.15 \mu\text{m}$  bangos ilgiui ties maksimalia išvadinė signalo energija). b) Atkurtas po SHG-FROG matavimo signalo impulsas po spūdos, esant maksimaliai išvadinėi energijai, laikinis profilis (ištinė linija) ir laikinė fazė (brūkšninė linija) palyginus su spektriškai ribojamu impulsu (punktyrinė linija).  $\tau_{\text{TL}}$  - spektriškai ribojamas impulso plotis. Intarpai - išmatuoti (kairėje) ir atkurti (dešinėje) FROG pėdsakai su 1.1 % paklaida  $512 \times 512$  pikselių tinklelyje.

Paskutinėje skyriaus dalyje aprašomi rezultatai integravus į OPCPA sistemą AOPDF (Dazzler WB45-1450-3000, Fastlite, Prancūzija). Tai leido pagerinti sustiprintų ir suspaustų impulsų laikinį kontrastą ir pasiekti trumpesnius impulsus, kompensuojant likutinę aukštesnės eilės dispersiją. Didžiausia OPCPA stiprinimo juosta nuo  $1.8$  iki  $2.4 \mu\text{m}$  nekolinarinioje konfigūracijoje (4 pav. a) dalis), buvo pasiekta optimizavus kampą tarp SC užkrato ir kaupinimo spinduliuočių, bei suderinus BiBO kristalų fazinio sinchronizmo kampą.

Trečios (TOD) ir ketvirtos (FOD) eilės, taip pat grupinių greičių dispersijos buvo preciziškai suderintos naudojant AOPDF, kad būtų pasiekta maksimali sustiprintų impulsų spūda pirmosios OPCPA pakopos išėjime. Atitinkamai, buvo kompensuojama bendrai sukaupta dispersija  $130 \text{ mm}$  YAG,  $45 \text{ mm}$   $\text{TeO}_2$  (AOPDF) ir  $6 \text{ mm}$  BiBO kristaluose:  $\sim 3.8 \times 10^3 \text{ fs}^2$  GDD,  $\sim 3.2 \times 10^4 \text{ fs}^3$  TOD ir  $\sim 1.7 \times 10^5 \text{ fs}^4$  FOD. Tai leido impulsus suspausti iki  $\sim 25 \text{ fs}$  (4 pav. – juoda linija) trukmės artimos spektro ribotai  $20 \text{ fs}$  trukmei (10 pav. – taškinė linija), atitinkančiai mažiau nei tris optinius ciklus ties  $2.1 \mu\text{m}$  centriniu bangos ilgiu. Tiesa, atsižvelgiant į platų impulsų spektrinės juostos plotį, galutinis impulsų suspaudimas labai priklauso nuo GDD ir TOD priklausomybės nuo bangos ilgio YAG ir BiBO kristaluose. Todėl norint pasiekti ribinę impulsų spūdą, būtinas dar tikslesnis spektrinės fazės aprašymas dispersiniame filtre.



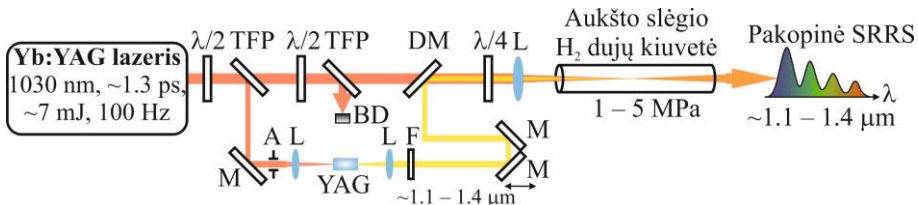
**4 Pav.** a) Sustiprinto signalo spektras po pirmosios OPCPA pakopos, kai yra į sistemą integruotas AOPDF. b) Atkurtas po SHG-FROG matavimo signalo impulsas po spūdos laikinis profilis (iššinė linija) ir laikinė fazė (brūkšninė linija) palyginus su spektriškai ribojamu impulsu (punktūrinė linija).  $\tau_{TL}$  - spektriškai ribojamas impulso plotis. Intarpai - išmatuoti (dešinėje) ir atkurti (kairėje) FROG pėdsakai su 1% paklaida 512×512 pikselių tinklelyje.

Apibendrinus, pademonstruotoje OPCPA pirmą kartą SC impulsai SWIR diapazone buvo sustiprinti tiesiogiai iki mJ lygio, o pasiektas paskutinės OPCPA pakopos keitimo efektyvumas artėja prie ribinės vertės. Šios OPCPA pagrindinis trūkumas yra 100 Hz pasikartojimo dažnis, kurį riboja Yb:YAG CPA kaupinimo šaltinis. Be to, suspausti impulsai nepasiekė ribinės trukmės dėl likutinės aukštesnių eilių dispersijos. Galiausiai šiam OPCPA trūksta CEP fazės stabilumo, palyginus su sistemomis kur naudojama DFG pakopa. Nepaisant to, sukurta OPCPA įrodė, kad ji tinka lakiosioms medžiagoms aptikti. Be to, po pirmos OPCPA pakopos pasyviai CEP stabilus šaltutinės bangos impulsas gali būti stiprinami antroje ir trečioje OPCPA pakopoje. Šiuo atveju spinduliuotės kampinę dispersiją galima kompensuoti prizmėmis arba pleištais. Tai atveria galimybę sukurti CEP stabilių mJ lygio impulsų SWIR lazerinę sistemą, kurios išvadinių impulsų plotis mažesnis nei 25 fs.

### Nenuostovioji priverstinė Ramano sklaida NIR spektriniame diapazone

Trečiame disertacijos skyriuje yra aprašomi keli metodai, leidžiantys išplėsti nenuostovios priverstinės Ramano sklaidos spektrinę juostą NIR spektriniame diapazone. Pirmiausia pateikiami spektro sintezės rezultatai žadinant pakopinę rotacinę priverstinę Ramano sklaidą vandenilio dujose, kaupinimui naudojant vienetinių ps trukmės Yb:YAG lazerio impulsus. Šiuo atveju, ypatingas dėmesys buvo skiriamas SRRS slenksčio sumažinimui, taip pat rotacinių Stokso modų spektrinės juostos išplėtimui. Ištirta kaupinimo spinduliuotės polarizacijos ir fokusavimo sąlygų, taip pat H<sub>2</sub> slėgio įtaka SRRS ir SVRS konversijos efektyvumui bei spektro gaubtinės kitimui.

Apskritiminė kaupinimo poliarizacija ir superkontinuumas kaip užkrato šaltinis ženkliai sumažino vibracinių Stokso modų generaciją, kai tuo tarpu didelis H<sub>2</sub> slėgis užtikrino pakopinį aukštesnių eilių rotacinių Stokso, atitinkančių 587 cm<sup>-1</sup> Ramano poslinkį, generavimą.

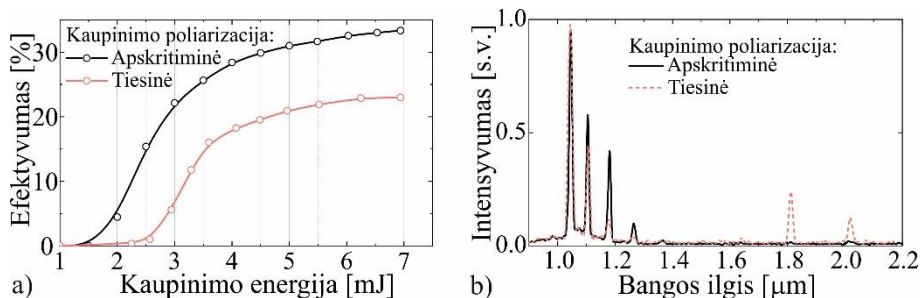


**5 Pav.** Pakopinės priverstinės Ramano sklaidos suslėgtame vandenilyje tyrimo schema:  $\lambda/2$  – pusės bangos ilgio fazinės plokštelės,  $\lambda/4$  – ketvirčio bangos ilgio fazinės plokštelė, TFP – plonasluksniai poliarizatoriai, A – apertūra, DM – dichroinis veidrodis, L – fokusuojantys lęšiai, F – spektrinis filtras, M – 45° plokštieji veidrodžiai.

Dalis kaupinimo lazerio energijos (~100 μJ) buvo panaudota generuoti superkontinuumą YAG kristale (5 pav.). Pirmasis plonasluksnis poliarizatorius (TFP) kartu su pusės bangos ilgio fazine plokšte ( $\lambda/2$ ) sudarė kaupinimo impulso energijos atenuatorių, o diafragmos skersmuisi parinktas apriboti centrinę įvadinio pluošto dalį iki 6.4 mm skersmens. Siekiant sugeneruoti stabilų SC, išplitusį iki ~1.4 μm pasirinktas 10 mm kristalo ilgis ir lęšis. Sugeneruoto SC spektras filtruojamas interferenciniu filtru (F) FELH1050 (Thorlabs Inc.) ir kolimuojamas 400 mm židinio nuotolio lęšiu. Kolinearus SC užkrato ir kaupinimo spinduliuočių sklaidimas realizuojamas dichroiniu veidrodžiu (DM), praleidžiančiu 1030 nm ir atspindinčiu 1100–1400 nm bangos ilgių spinduliuotes, o tiksli laikinė impulsų sanklota valdoma vėlinimo linija. Antrasis atenuatorius, sudarytas iš plonasluksnio poliarizatoriaus (TFP) ir pusės bangos ilgio fazinės plokštelės ( $\lambda/2$ ), buvo naudojamas valdyti kaupinimo impulso energiją. Ketvirčio bangos ilgio fazinė plokštelė ( $\lambda/4$ ) užtikrino apskritiminę kaupinimo spinduliuotės poliarizaciją, SVRS slopinimui. SC užkrato ir kaupinimo spinduliuotės fokusuojamos į SRS-kiuvertės centrą 750 mm židinio nuotolio lęšiu. Tiek SVRS, tiek SRRS buvo generuojama 1 m ilgio aukšto slėgio dujų kiuvetėje su 5 mm storio MgF<sub>2</sub> optiniais langeliais pripildytoje suslėgto (1 MPa – 5 MPa) vandenilio dujų.

Pradinių tyrimų etape, SC užkratas SRS eksperimentuose nebuvo naudojamas. Kadangi SRS keitimo efektyvumas ar Stokso spinduliuotės spektro gautinė nepriklausė nuo naudojamo lęšio, todėl 750 mm židinio nuotolis pasirinktas kaip optimalus. Nors labiausiai ištirtas 4155 cm<sup>-1</sup> vandenilio vibracinis Ramano poslinkis ir dominuoja nenuostovijame SRS

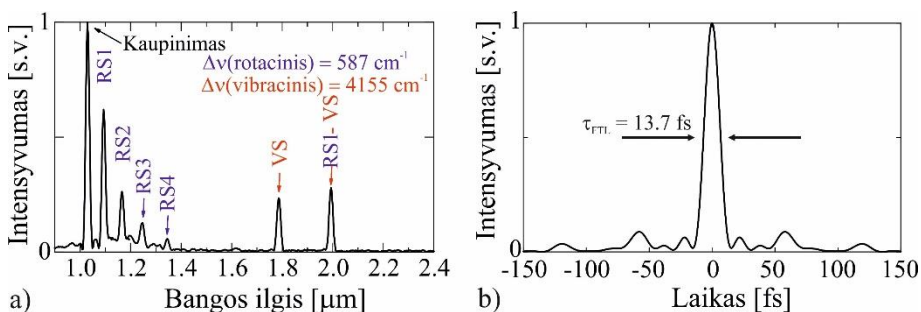
režime, tačiau eksperimentuose buvo tikėtasi stebėti ir rotacinį  $587\text{ cm}^{-1}$  Ramano poslinkį, kurio stiprinimą galima ženkliai padidinti naudojant apskritiminę kaupinimo spinduliuotės poliarizaciją. SRRS keitimo efektyvumo priklausomybė nuo kaupinimo impulso energijos esant skirtingoms spinduliuotės poliarizacijoms, kai vandens slėgis yra 3 MPa, pateikta 6 paveikslu a) dalyje.



**6 Pav.** a) SRRS keitimo efektyvumo priklausomybė nuo kaupinimo impulso energijos, esant apskritiminei (raudona išštinė linija) ir tiesinei (juoda brūkšninė linija) spinduliuotės poliarizacijai, kai vandens slėgis 3 MPa; b) SRS spektro gaubtinės, esant apskritiminei (raudona išštinė linija) ir tiesinei (juoda brūkšninė linija) lazerio poliarizacijai, kai impulso energija 7 mJ.

Ketvirčio bangos ilgio fazinės plokštelės ( $\lambda/4$ , 5 pav.) ašis pirmiausiai buvo nustatyta  $0^\circ$  kampų, kad būtų užtikrinta tiesinė lazerio spinduliuotės poliarizacija. Kaupinimo impulso energija buvo apribota iki 7 mJ, siekiant išvengti  $\text{MgF}_2$  langelių optinės pažaidos. Su tiesine kaupinimo spinduliuotės poliarizacija, SRRS keitimo efektyvumas palaipsniui įsisotina iki didžiausios 23% vertės. Tuo tarpu sugeneruotą Stokso bangos spektrą sudarė keletas palaipsniui mažėjančio intensyvumo spektrinių smailių ties  $\sim 1094\text{ nm}$ ,  $\sim 1166\text{ nm}$  ir  $\sim 1251\text{ nm}$  (6 b) pav., juoda brūkšninė linija), atitinkančių pakopinės SRRS vandenilyje pirmosios, antrosios ir trečiosios eilės Stokso bangos ( $587\text{ cm}^{-1}$  rotacinis Ramano poslinkis). Be to, spektruose stebimos ir dar dvi linijos, kurios siejamos su SVRS ties  $\sim 1790\text{ nm}$  bangos ilgiu ( $4155\text{ cm}^{-1}$  vibracinis Ramano poslinkis) ir šios spinduliuotės rotacinio Stokso banga ties  $\sim 1993\text{ nm}$  bangos ilgiu. Pakeitus kaupinimo spinduliuotės poliarizaciją iš tiesinės į apskritiminę, stebėtas aiškus 33% SRRS keitimo efektyvumo maksimumas bei vibracinio Stokso modų slopinimas (6 b) pav., raudona išštinė linija). Taigi nustatyta, kad apskritiminė kaupinimo poliarizacija ženkliai pagerina SRRS generaciją, todėl ją nuspręsta naudoti ir tolimesniuose eksperimentuose, kas leido pasiekti SRRS keitimo efektyvumą iki 42% esant 5 MPa vandens slėgio kiuvetėje.

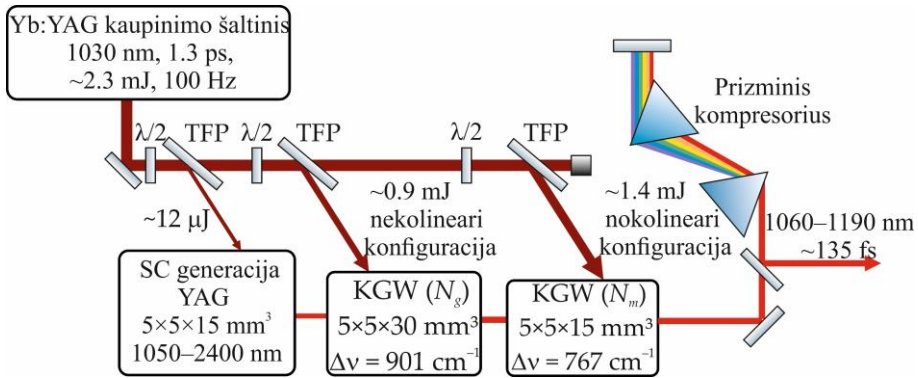
Tuo tarpu, naudojant SC kaip užkratą buvo galima generuoti rotacinio Stokso modas iki ketvirtos eilės plačiame  $\sim 1.1-1.4$   $\mu\text{m}$  bangos ilgio diapazone ir keturis kartus sumažinti SRS slenkstį, o keitimo efektyvumą padidinti iki 52%. Plačiausias SRRA spektras buvo gautas esant 5 MPa vandenilio slėgiui ir 7 mJ kaupinimo impulso energijai (7 pav a) dalis). Spektro smailių padėtys ties 1096 nm, 1164 nm, 1252 nm ir 1351 nm centriniais bangos ilgiais (pažymėtos kaip „RS1-4“) buvo priskirtos atitinkamai pirmos, antros, trečios ir ketvirtos eilės rotacinio Stokso modoms, atitinkančioms  $587\text{ cm}^{-1}$  Ramano poslinkį vandenilyje. Spektre matomos ir dvi smailės ilgesnių bangų srityje ties 1795 nm ir 1997 nm. Pirmoji smailė priskiriama vibracinio Stokso modai, sužadintai kaupinimo spinduliuote, ir žymima „VS“, o antroji – vibracinio Stokso modai, sužadintai pirmos eilės rotacinio Stokso modos („RS1“), ir žymima „RS1-VS“.



**7 Pav.** a) Išvadinis SRRA spektras esant 5 MPa vandenilio slėgiui ir 7 mJ kaupinimo impulso energijai; b) apskaičiuota spektro riboto impulso laikinė gaubtinė pagal išmatuotą SRRA spektrą 1-1.4  $\mu\text{m}$  bangos ilgių ruože.

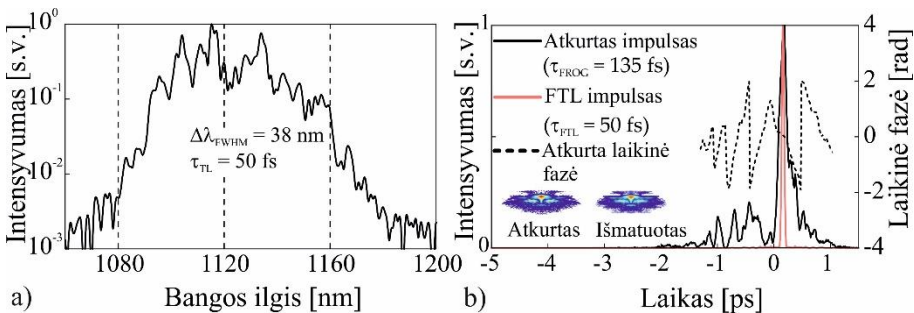
Kaip ir kaupinimo spinduliuotė, išvadiniai SRRA impulsai buvo apskritiminės poliarizacijos. Susintezuotas SRRA spektras (jo plotis) atitiko  $\sim 14$  fs spektro ribotų impulsų trukmę, ties 1.2  $\mu\text{m}$  centriniu bangos ilgiu (7 pav b) dalis). Nors tokie ekstremaliai spūdiniai reikėtų sudėtingesnių metodų, naudojant SF11 prizmių porą, pirmosios eilės rotaciniai Stokso impulsai buvo suspausti iki 152 fs, t. y. maždaug aštuonis kartus trumpiau nei kaupinimo impulsai. Taigi, galime teigti, kad pakopinė SRRA turi nemažą potencialą generuojant didelės energijos femtosekundinius impulsus sunkiai realizuojamoje 1.1-1.4  $\mu\text{m}$  spektrinėje srityje.

Antroje skyriaus dalyje pristatomi rezultatai susiję su dviejų pakopų TSRCPA kurio pagrindą sudaro KGW kristalai, kurie buvo orientuoti taip, kad būtų sužadinti skirtingose pakopose gretimi Stoksoi (8 Pav)



**8 Pav.** Principinė priverstinės Ramano sklaidos stiprintuvo schema.  $\lambda/2$  – pusės bangos ilgio fazinė plokštelė, TFP – plonasluoksnis poliarizatorius.

Gretimų Stokso linijų žadinimui pirmoji TSRCPA pakopa buvo suderinta KGW kristalo  $901 \text{ cm}^{-1}$  vibracinei modai, o pirmoji –  $768 \text{ cm}^{-1}$  modai, kas leido suformuoti itin plačią  $\sim 38 \text{ nm}$  spektrinę juostą (9 Pav. a) dalis), atitinkančią 50 fs trukmės spektro ribotą impulsą (4.12 pav. b) – punktyrinė linija), ties 1120 nm centru bangos ilgiu. Šiuo atveju pasiektas aukštas 35% keitimo efektyvumas, su 1.4 mJ kaupinimo impulso energija, atitinkančia  $30 \text{ GW/cm}^2$  smailinės galios tankį.



**9 Pav.** a) Plačiausias suformuotas spektras po dviejų TSRCPA pakopų. b) Sustiprinto ir suspausto impulso laikinis profilis (ištininė linija) ir jo laikinė fazė (punktyrinė) atkurta iš SHG-FROG matavimų. Apskaičiuotas spektro riboto impulso laikinis profilis (raudona linija).

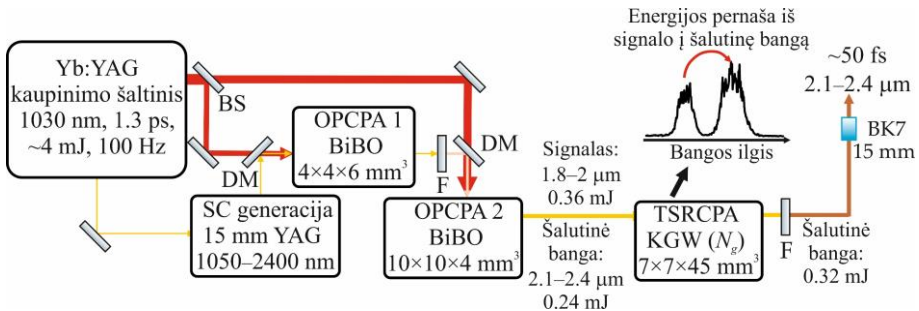
Sustiprinti impulsai po TSRCPA buvo spaudžiami prizminiame kompresoriuje naudojant SF11 prizmes (8 pav). Šiuo atveju optimalus ilgis tarp prizmių buvo nustatytas eksperimentiškai esant trumpiausiai sustiprintų impulsų trukmei. Taigi, atlikus FROG matavimus ir atkūrus sustiprinto Stokso impulso spektrą ir jo fazę, pastebėta, kad suformuotas impulsas turi teigiamą čirpą, sąlygotą superkontinuumo impulsų, kurių lydi reikšmingos spektrinės fazės moduliacijos. Deja, sunku tiksliai pasakyti, kas sąlygojo ryškias fazės

moduliacijas, tačiau galima daryti prielaidą, kad SPM sukelti kaupinimo impulso fazės iškraipymai yra perduodami signalui stiprinimo metu. Tuo tarpu, ir pačio Stokso impulso savaiminė fazės moduliacija stiprinimo metu galėjo turėti tam tikrą poveikį sustiprinto signalo spektrinės fazės iškraipymams. Nepaisant to, kad suformuotas impulsas turi nehomogenišką spektrinę fazę, jis vis tiek yra spūdis (9 Pav. b) dalis).

Apibendrinus nenuostoviosios SRRS ir gretimų Stokso modų sintezės rezultatai sudaro sąlygas generuoti ultratrumpuosius impulsus NIR bangos ilgio diapazone. Be to, abu metodai gali būti pritaikyti ir SWIR-MIR diapazone. Naudojant SWIR OPCPA kaip kaupinimo šaltinį galim išplėsti impulsų spektrą virš 3  $\mu\text{m}$ , sužadinant antrosios eilės rotacinį Stoksą aukšto slėgio vandenilio kiuvetėje.

### Kolinearios konfigūracijos SWIR diapazono OPCPA kombinacija su TSRCPA

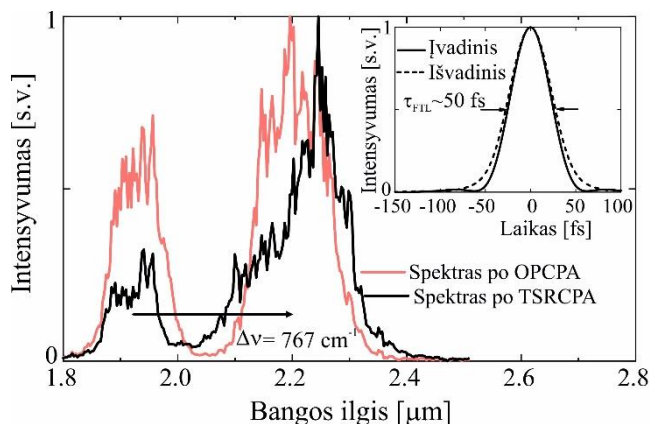
Ketvirtame disertacijos skyriuje pristatomas naujas metodas efektyviai signalo energijos pernašai į šalutinės bangos spinduliuotę naudojant TSRCPA KGW ir vandenilyje.



**10 Pav.** Eksperimentinė schema, skirta energijos pernašai iš signalo į šalutinės bangos spinduliuotę naudojant nenuostovųjį priverstinės Ramano sklaidos čirpuotų impulsų stiprinimą (TSRCPA): BS – pluošto daliklis, DM – dichroiniai veidrodžiai, F – plačiajuosčiai filtrai.

Pirmiausia skyriuje pristatomi rezultatai kuomet TSRCPA pakopoje buvo naudojamas KGW kristalas. 10 paveiksle pateikta eksperimentinė schema signalo energijos pernašos į šalutinę bangą, naudojant nenuostovųjį priverstinės Ramano sklaidos čirpuotų impulsų stiprinimą. Šiuo atveju taip pat tiek SC generacijai, tiek OPCPA kaupimui naudojamas jau anksčiau minėtas Yb:YAG lazeris. Pradiniai SC impulsai generuojami 15 mm ilgio YAG kristale ir stiprinami kolinearios konfigūracijos dviejų pakopų OPCPA.

Kolinearus signalo ir šalutinės bangos spinduliuočių sklidimas užtikrinamas dichroiniais veidrodžiais (HR@1800-2400 nm, HT@1030 nm). Signalo spinduliuotę buvo pasirinkta atspindėti nuo veidrodžių, kad būtų išvengta papildomos grupinės vėlinimo dispersijos ir ypatingai trečiosios eilės dispersijos spinduliuotei sklindant stiklu. Abi sustiprintos signalo ir šalutinės bangos spinduliuotės toliau nukreipiamos į TSRCPA pakopą, pagrįstą neskaidrintu  $N_p$ -ašies pjovimo  $7 \times 7 \times 30$  mm<sup>3</sup> arba  $7 \times 7 \times 45$  mm<sup>3</sup> dydžio KGW kristalu. Įvadinių impulsų energija buvo keičiama neutralaus optinio tankio (ND) filtrais (Thorlabs), kurių optinis tankis keičiamas nuo 0.1 iki 0.7. Signalo ir šalutinės bangos spinduliuotės buvo orientuotos sklisti išilgai kristalo  $N_p$  optinės ašies, o jų poliarizacijos ir elektrinio lauko vektoriai  $E$  lygiagretūs kristalo  $N_g$  ašiai, atitinkančiai  $767$  cm<sup>-1</sup> Stokso poslinkį. Po TSRCPA pakopos signalo ir šalutinės bangos spinduliuotės spektriškai atskiriamos plačiajuosčiais filtrais (Thorlabs FB2250-500 ir FB1900-200). Sustiprintas šalutinės bangos impulsas spaudžiamas BK7 stiklo bloke, kompensuojant teigiamą dispersiją, lygią neigiamai dispersijai, susikaupusiai spinduliuotei sklindant YAG ir BiBO kristalais. Sustiprinti ir suspausti Stokso impulsai buvo charakterizuojami SHG-FROG matavimo prietaisu.



**11 Pav.** Išvardiniai spektrai po dviejų OPCPA pakopų (raudona linija) ir po signalo energijos pernašos į šalutinę bangą 45 mm ilgio KGW kristale (juoda linija). Intarpas - apskaičiuoti spektro ribotų impulsų laikiniai profiliai ties 2250 nm centru bangos ilgiu prieš (punktyrinė linija) ir po (ištininė linija) KGW kristalo. Rodyklė nurodo  $767$  cm<sup>-1</sup> Stokso poslinkį.

Abiejų OPCPA pakopų fazinis sinchronizmas buvo suderintas taip, kad šalutinės bangos ir signalo impulsų spektrai būtų pakankamai atskirti. Atitinkamai OPCPA veikė bangos ilgių srityje nuo  $\sim 1800$  nm iki  $\sim 2000$  nm signalui ir nuo  $\sim 2100$  nm iki  $\sim 2400$  nm šalutinei bangai (11 pav. - punktyrinė linija), o spektrų juostos pločiai atitiko  $\sim 50$  fs spektro ribotas impulsų trukmes.

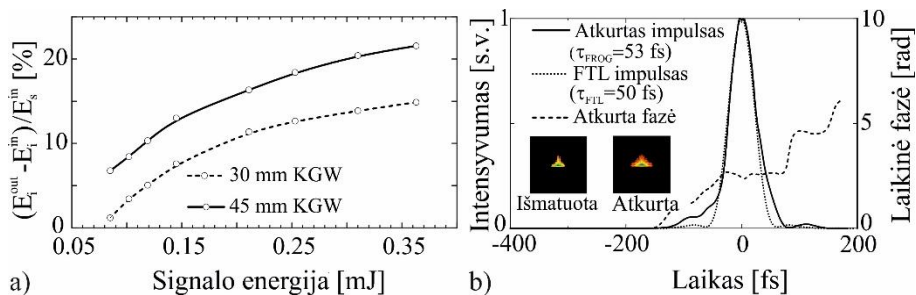


Po dviejų OPCPA pakopų šalutinės bangos impulso energija buvo 240  $\mu\text{m}$  ir 175 fs trukmės su neigiamu čirpu.

Po TSRCPA pakopos stebėtas ženklus šalutinės bangos impulso spektrinio intensyvumo padidėjimas ir signalo impulso nuskurdimas. Šalutinės bangos impulso centrinis bangos ilgis šiek tiek pasislinko į 2250 nm (11 Pav. – juoda linija), kas atitiko  $767\text{ cm}^{-1}$  dažnio Stokso poslinkį (11 Pav., pažymėta rodykle). Šiuo atveju OPCPA signalas veikė kaip kaupinimas priverstinės Ramano sklaidos stiprinimo procese, o šalutinės bangos impulsas kaip didelės energijos Stokso impulsas. TSRCPA procesas neturėjo reikšmingos įtakos šalutinės bangos impulso spektrinės juostos pločiui, todėl po KGW kristalo ženklaus spektro susiaurėjimo nepastebėta. Sustiprintas šalutinės bangos impulsas išlaikė dažnių juostos plotį, atitinkantį  $\sim 50$  fs spektro riboto impulso trukmę, kaip ir OPCPA išvade (11 Pav., intarpas).

Po TSRCPA pakopos, esant maksimaliai 0.36 mJ ( $18\text{ GW/cm}^2$ ) signalo energijai, buvo pasiektos 0.3 mJ ir 0.32 mJ šalutinės bangos impulso energijos, atitinkamai 30 mm ir 45 mm ilgio KGW kristaluose. Dėl pakankamos pradinės užkrato (šalutinės bangos) impulso energijos Stokso spinduliuotės bangos ilgyje ties  $\sim 2250$  nm, energijos pernaša į šalutinės bangos spinduliuotę naudojant TSRCPA yra slenksčio neturintis reiškinys, priešingai nei SRS procesas. Net ir vienoje TSRCPA pakopoje galima pasiekti didelį keitimo efektyvumą.

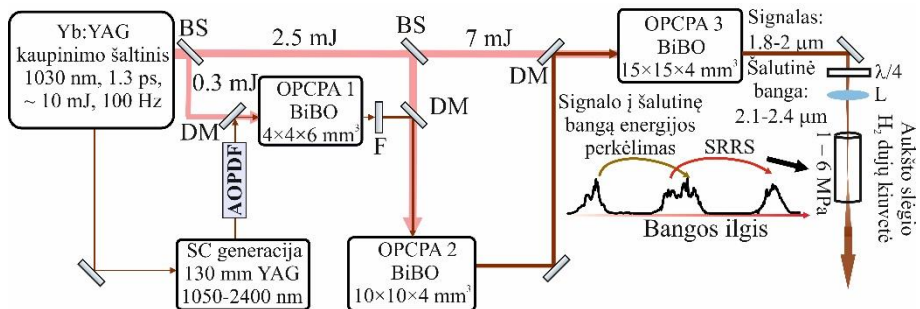
Visgi, norint pasiekti didelį kaupinimo (signalų) impulso nuskurdimą ir efektyvią energijos pernašą į šalutinę bangą, svarbu, kad Ramano terpė būtų pakankamo ilgio. Todėl didžiausias TRSCPA efektyvumas buvo pasiektas 14% ir 24%, atitinkamai 30 mm ir 45 mm ilgio KGW kristaluose, kai didžiausias įvadinio kaupinimo (signalų) smailinės galios tankis buvo  $\sim 18\text{ GW/cm}^2$  (12 Pav. a) dalis). Tuo tarpu, didžiausias Stokso (šalutinės bangos) impulso energijos prieaugis 30 mm ir 45 mm ilgio KGW kristaluose atitinkamai 22% ir 33%. Nors aprašytos dviejų pakopų OPCPA bendras kaupinimo į šalutinę bangą keitimo efektyvumas padidėjo tik 3%, tačiau naudojant papildomą OPCPA pakopą, bei užtikrinant mJ eilės išvadinę energiją, daugiau kaip 6% efektyvumo padidėjimas įmanomas panaudojant didesnės apertūros KGW kristalą. TSRCPA pakopos efektyvumą taip pat galima padidinti vėlinant šalutinės bangos impulsą signalo atžvilgiu, nes Stokso impulsas generuojasi galiniame kaupinimo impulso fronte.



**12 Pav.** a) TSRCPA efektyvumo priklausomybė nuo įvadinės signalo impulso energijos 30 mm (brūkšninė linija) ir 45 mm (išsistinė linija) ilgio KGW kristaluose. b) SHG-FROG atkurtas sustiprinto ir suspausto šalutinės bangos impulso laikinis profilis (išsistinė) ir laikinė fazė (punktūrinė). Apskaičiuotas spektro riboto impulso laikinis profilis (taškinė linija) ties 2250 nm centriniu bangos ilgiu.

Svarbu, kad dėl didelės pradinės užkrato (šalutinės bangos) impulso energijos, didelis TSRCPA efektyvumas pasiekiamas dar iki nepageidaujamos spektriškai persidengiančios SRS spinduliuotės sužadavimo slenksčio, kuri atsiranda tik tada, kai kaupinimo (signalų) impulso smailinės galios tankis viršija  $\sim 20$  GW/cm<sup>2</sup>. Nepageidaujamas Stokso impulsas, pasiekęs SRS slenkstį, atkartoja kaupinimo (signalų) impulso čirpą, kuris yra priešingas šalutinės bangos impulsui, o tai trukdo tolesnei impulso spūdai. Kitu atveju, norint erdviškai atskirti SRS spinduliuotę nuo sustiprinto šalutinės bangos impulso, reikėtų naudoti nekolinearią TSRCPA konfigūraciją. Taigi, optimaliose sąlygose, jokių reikšmingų šalutinės bangos impulso čirpo iškraipymų po energijos pernašos 45 mm KGW kristale nepastebėta. Impulsai 15 mm storio BK7 stikle suspausti iki 53 fs trukmės, artimos spektro ribotai trukmei ties 2250 nm centriniu bangos ilgiu (12 Pav. b) dalis). Taigi šis metodas atveria kelią didelio našumo hibridinėms OPCPA/TSRCPA sistemoms, skirtoms efektyviai generuoti didelės energijos CEP stabilūs femtosekundinius impulsus SWIR spektro ruože.

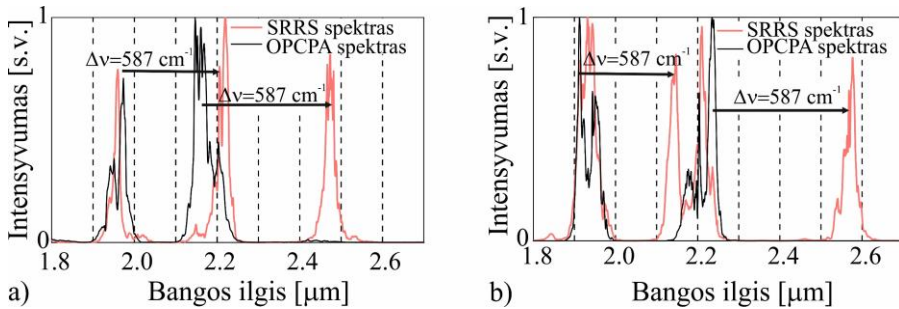
Taip pat priverstinės Ramano sklaidos tyrimai SWIR srityje kuomet kaupinimui naudojami kolinearios konfigūracijos OPCPA išvardiniai impulsai buvo atlikti aukšto slėgio vandenilio dujų kiuvetėje (13 Pav.).



**13 Pav.** Eksperimentinė SRRS suslėgtame vandenilyje tyrimo schema: DM – dichroiniai veidrodžiai; BS – spektro dalikliai;  $\lambda/4$  – ketvirčio bangos ilgio fazinė plokštelė; F – fokusuojanti s lęšis; AOPDF – akustoptinis programuojamasis dispersinis filtras.

Šiuo atveju, SC užkrato impulsai buvo generuojami 130 mm ilgio YAG kristale, kurie paskui stiprinami trijų pakopų kolinearos konfigūracijos OPCPA su BiBO kristalais. Po trečiosios OPCPA pakopos signalo ir šalutinės bangos impulsai buvo fokusuojami 500 mm arba 750 mm židinio nuotolio  $\text{CaF}_2$  lęšiais atitinkamai į 43 cm, 65 cm arba 110 cm ilgio kiuvetes, pripildytas vandenilio, kuriose slėgis siekė 6 MPa. Kiuvetėse buvo naudojami 1 colio skersmens ir 5 mm storio  $\text{CaF}_2$  optiniai langeliai. Siekiant pagerinti SRRS efektyvumą, prieš kameras buvo sumontuota achromatinė ketvirčio bangos ilgio ( $\lambda/4$ ) fazinė plokštelė (HT@2000-2600 nm). Kad būtų pasiektas pakankamas šalutinės bangos ir signalo impulsų spektrų atskyrimas, trijų OPCPA pakopų BiBO kristalų fazinio sinchronizmo kampai buvo derinami 0 iki  $0.12^\circ$  diapazone ( $0^\circ$  atitinka  $7.8^\circ$  BiBO kristalų fazinio sinchronizmo kampą). Priciziškai derinant BiBO kristalų kampą, centrinis signalo impulso bangos ilgis pasislenka trumpesnių bangų link, o šalutinės bangos - ilgesnių bangų link.

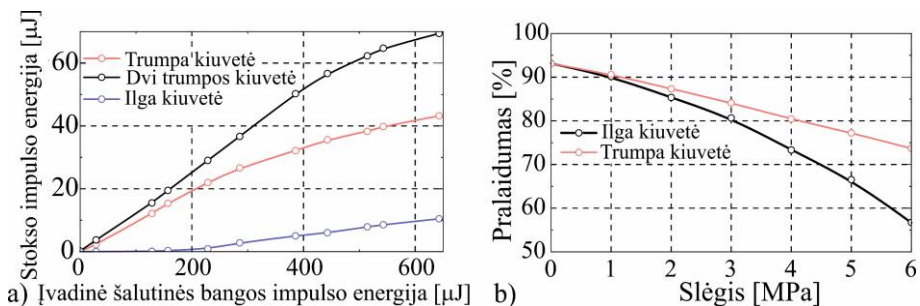
Tyrimo metu signalo impulsai, kurių trukmė  $\sim 0.9$  ps, buvo čirpuojami teigiamai arba neigiamai, priklausomai nuo parenkamo GDD kiekio SC impulsui AOPDF, atitinkamai  $4 \times 10^4 \text{ fs}^2$  arba  $-4 \times 10^4 \text{ fs}^2$ . Esant optimaliam spektro atskyrimui su neigiamu čirpu, išvadinė impulso energija, ties šalutinės bangos ilgiais siekė  $\sim 440 \mu\text{J}$ , kai tuo tarpu su teigiamu čirpu, ji sumažėjo iki  $\sim 250 \mu\text{J}$ , kai bendra įvadinė signalo ir šalutinės bangos impulsų energija buvo  $\sim 1.5 \text{ mJ}$ . Tuo tarpu Stokso impulsas, generuojamas nuo šalutinės bangos, pasiekė maksimalią  $\sim 40 \mu\text{J}$  impulso energiją, kai OPCPA signalui buvo pritaikytas teigiamas čirpas, o esant neigiamam čirpui, energija sumažėjo iki  $\sim 33 \mu\text{J}$ . Verta pažymėti, jog Stokso impulsai nebuvo stebimi, kai įvadinėje spinduliuotėje į kiuvetę spektriškai nufiltruojama signalo arba šalutinės bangos spinduliuotė.



**14 Pav.** Normuoti išvadiniai spektrai prieš (juodos linijos) ir po (raudonos linijos) vandenilio kiuvetės su neigiamu a) ir teigiamu b) SC čirpu. Rodyklėmis parodytos signalo–šalutinės bangos ir šalutinės bangos-Stokso energijos pernašos, atitinkančios  $587 \text{ cm}^{-1}$  rotacinį Stokso poslinkį.

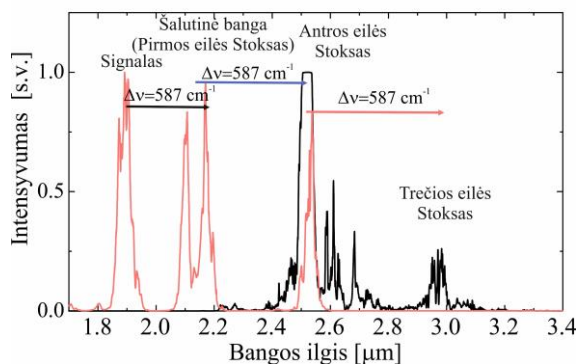
14 paveiksle pateikti normuoti spektrai spinduliuotės, krintančios ir išeinančios iš vandenilio kiuvetės su neigiamu (14 a) Pav.) ir teigiamu (14 b) Pav.) SC čirpu. Aiškiai matoma, kaip čirpas ženkliai įtakoja ir spektrinį signalo, šalutinės bangos ir Stokso komponentų pasiskirstymą. Neigiamo čirpo atveju (14 a) Pav.) energijos pernaša iš signalo,  $\sim 1.94 \mu\text{m}$  centriniu bangos ilgiu, į šalutinės bangos impulsą –  $\sim 2.22 \mu\text{m}$ , yra žymiai ryškesnė, nei teigiamo čirpo atveju. Tuo tarpu, teigiamo (atvirkštinio signalui) šalutinės bangos impulso čirpo atveju, Stokso spinduliuotė generuojama ties centriniu  $\sim 2.47 \mu\text{m}$  bangos ilgiu. Priešingai, esant teigiamam čirpui (14 a) Pav.), energija efektyviau perduodama Stokso spinduliuotei, kurios spektras pasislenka į ilgesnių bangos ilgių sritį ( $\sim 2.57 \mu\text{m}$ ). Taigi čirpas, laikinis ir spektrinis pasiskirstymas impulse yra esminiai veiksniai, lemiantys energijos pernašos efektyvumą SRRS čirpuotų impulsų stiprinimo metu.

Galiausiai buvo tikėtasi, kad SRRS keitimo efektyvumą dar labiau pavyks padidinti panaudojus ilgesnę dujų kiuvetę. 15 a) paveiksle pateikta Stokso impulso energijos priklausomybė nuo įvadinės šalutinės bangos impulso energijos, kai SRRS generuojamas skirtingo ilgio vandenilio kiuvetėse: 65 cm, 110 cm, taip pat dvi nuoseklios 65 cm ilgio kiuvetės.



**15 Pav.** a) Stokso impulso energijos priklausomybė nuo įvadinės šalutinės bangos impulso energijos, kai SRRS generuojamas 65 cm (raudona linija), 110 cm (mėlyna linija) ir dvejose 65 cm ilgio kiuvetėse (juoda linija). b) 65 cm ir 110 cm ilgio kiuvėčių optinio pralaidumo priklausomybės nuo vandenilio slėgio.

Nors visų išbandytų kiuvėčių energijų priklausomybių kreivės rodo kylančią tendenciją, dviguba kiuvetė pranoko kitas, pasiekiant  $\sim 70 \mu\text{J}$  Stokso impulso energiją. Verta pažymėti, kad nepaisant panašaus sąveikos ilgio, vienos 110 cm ilgio kiuvetės atveju Stokso impulso energija vos siekė  $\sim 10 \mu\text{J}$ . Šį skirtumą galima paaiškinti tuo, kad sudėtinėje kiuvetėje galimai pavyksta efektyviau nuslopinti gretutinius netiesinius reiškinius kaip SPM, savifokusacija ar vibracinė SRS, kurios Stokso bangos ilgis šiuo atveju viršija  $10 \mu\text{m}$ , t. y. už  $\text{CaF}_2$  optinių langų skaidrumo ribos. Išmatuotos 65 cm ir 110 cm ilgio kiuvėčių optinio pralaidumo priklausomybės nuo vandenilio slėgio (15 b) pav.), kai įvadinė bendra signalo ir šalutinės bangos impulsų ( $1.9\text{--}2.25 \mu\text{m}$  bangos ilgių ruožas) energija siekė 1.5 mJ. Stebimas žymus pralaidumo sumažėjimas (15 b) Pav. – ištisinė linija), ypač ilgoje kiuvetėje, tikėtina, dėl sugerties sukeltos vandenilio molekulių susidūrimų [11], bei vibracinio Stokso indėlio, kai slėgis viršija 2 MPa. Taip pat, siekiant pakopinės SRRS modų generacijos, buvo išbandyta techniškai trumpiausia įmanoma  $\sim 40$  cm ilgio vandenilio kiuvetė. SRRS žadinimui buvo panaudota maksimali 1.5 mJ bendra impulsų energija bei 6 MPa vandenilio slėgis. Tokiu būdu pavyko sugeneruoti ir trečios eilės rotacinę Stokso spinduliuotę kurios centrinis bangos ilgis  $\sim 3 \mu\text{m}$  (16 pav.).



**16 Pav.** Normuoti išvadinės spinduliuotės spektrai po 63 cm (raudona kreivė) ir 40 cm (juoda kreivė) ilgio vandenilio 6 MPa slėgio kiuvetės. Linijos nurodo rotacinį Ramano poslinkį ties  $587\text{ cm}^{-1}$ .

### Pagrindiniai rezultatai ir išvados

1. Sukurta didelės energijos SWIR OPCPA sistema, pagrįsta BiBO kristalais, kurios paskutinėje pakopoje pasiektas išskirtinis – 25% kaupinimo į signalą keitimo efektyvumas ir 2.1 mJ išvadinė energija. Dėl santykinai mažo plėtros-spūdos santykio, naudojant vienetinių pikosekundžių trukmės kaupinimo impulsus, sustiprintas signalas suspaustas stikle iki ~38 fs trukmės, pasiekiant 47 GW smailinę galią. Tuo tarpu aktyvus spektro fazės valdymas leidžia spausti impulsus iki mažiau nei 25 fs, viršijant 80 GW smailinę galią, kas parodo kad plačiajuostis SWIR superkontinuumas yra tinkamas užkratas tokio tipo sistemoje.
2. Apskritiminės poliarizacijos, NIR diapazono, 1,3 ps trukmės kaupinimo impulsų panaudojimas leido slopinti vibracinę SRS ir su ~42% keitimo efektyvumu generuoti keletą eilių rotacinius Stoksus 5 MPa slėgio vandenilio dujų kiuvetėje.
3. Plačiajuosčio NIR superkontinuumo užkrato panaudojimas leido generuoti keturių eilių rotacinio Stokso spinduliuotę, sunkiai realizuojamame ~1.1–1.4 μm bangos ilgių diapazone, ir padidinti SRRS keitimo efektyvumą iki 52%. Tuo tarpu maksimali rotacinių Stoksų spinduliuotės impulso energija viršijo 3 mJ, o spektrinis plotis

yra pakankamas generuoti ~14 fs spektriškai ribotos trukmės impulsus ties 1.2  $\mu\text{m}$  centriniu bangos ilgiu.

4. Gretimų vibracinių Stokso modų sintezė dviejų pakopų TSRCPA, KGW kristalų pagrindu, užtikrino 23 kartus platesnę, nei kaupinimo impulsų, spektrinę juostą, pakankamą generuoti ~50 fs spektriškai ribotus impulsus ties 1120 nm. Nepaisant spektro fazės moduliacijos, sustiprinti Stokso impulsai suspausti iki 135 fs trukmės.
5. Kolinearios konfigūracijos SWIR OPCPA kombinacija su TSRCPA užtikrina efektyvų signalo energijos keitimą į šalutinę bangą KGW kristale. Tuo tarpu trečios eilės Stokso generacija leidžia išplėsti išvadinės spinduliuotės spektrinę juostą virš 3  $\mu\text{m}$ . optimizavus signalo ir šalutinės bangos spektrą, signalo impulso čirpą, vandenilio dujų slėgį ir kiuvetės ilgį.

## BIBLIOGRAPHY

- [1] T. H. Maiman, Stimulated Optical Radiation in Ruby, *Nat.* **187**(4736), 493–494 (1960).
- [2] J. Hecht, Short history of laser development, *Opt. Eng.* **49**(9), 091002 (2010).
- [3] D. Strickland and G. Mourou, Compression of amplified chirped optical pulses, *Opt. Commun.* **55**(6), 447–449 (1985).
- [4] H. Pires, M. Baudisch, D. Sanchez, M. Hemmer, and J. Biegert, Ultrashort pulse generation in the mid-IR, *Prog. Quantum Electron.* **43**, 1–30 (2015).
- [5] P. Agostini and L. F. DiMauro, The physics of attosecond light pulses, *Rep. Prog. Phys.* **67**(6), 813–855 (2004).
- [6] M. Clerici, M. Peccianti, B. E. Schmidt, L. Caspani, M. Shalaby, M. Giguère, A. Lotti, A. Couairon, F. Légaré, T. Ozaki, D. Faccio, and R. Morandotti, Wavelength scaling of terahertz generation by gas ionization, *Phys. Rev. Lett.* **110**(25), 252003 (2013).
- [7] W. Li, X. Zhou, R. Lock, S. Patchkovskii, A. Stolow, H. C. Kapteyn, and M. M. Murnane, Time-Resolved Dynamics in N<sub>2</sub>O<sub>4</sub> Probed Using High Harmonic Generation, *Science* **322**(5905), 1207–1211 (2008).
- [8] M. G. Pullen, B. Wolter, A. T. Le, M. Baudisch, M. Hemmer, A. Senftleben, C. D. Schröter, J. Ullrich, R. Moshhammer, C. D. Lin, and J. Biegert, Imaging an aligned polyatomic molecule with laser-induced electron diffraction, *Nat. Commun.* **6**(1), (2015).
- [9] R. A. Richter, N. Tolstik, S. Rigaud, P. D. Valle, A. Erbe, P. Ebbinghaus, I. Astrauskas, V. Kalashnikov, E. Sorokin, and I. T. Sorokina, Sub-surface modifications in silicon with ultra-short pulsed lasers above 2  $\mu\text{m}$ , *J. Opt. Soc. Am. B* **37**(9), 2543–2556 (2020).
- [10] I. Jordan, M. Huppert, M. A. Brown, J. A. van Bokhoven, and H. J. Wörner, Photoelectron spectrometer for attosecond spectroscopy of liquids and gases, *Rev. Sci. Instrum.* **86**(12), 123905 (2015).
- [11] N. Saito, H. Sannohe, N. Ishii, T. Kanai, N. Kosugi, Y. Wu, A. Chew, S. Han, Z. Chang, and J. Itatani, Real-time observation of electronic, vibrational, and rotational dynamics in nitric oxide with attosecond soft x-ray pulses at 400 eV, *Optica* **6**(12), 1542–1546 (2019).
- [12] B. Vodungbo, J. Gautier, G. Lambert, A. B. Sardinha, M. Lozano, S. Sebban, M. Ducouso, W. Boutu, K. Li, B. Tudu, M. Tortarolo, R. Hawaldar, R. Delaunay, V. López-Flores, J. Arabski, C. Boeglin, H. Merdji, P. Zeitoun, and J. Lüning, Laser-induced ultrafast



- demagnetization in the presence of a nanoscale magnetic domain network, *Nat. Commun.* **3**(1), 999 (2012).
- [13] T. Popmintchev, M.-C. Chen, D. Popmintchev, P. Arpin, S. Brown, S. Ališauskas, G. Andriukaitis, T. Balčiunas, O. D. Mücke, A. Pugzlys, A. Baltuška, B. Shim, S. E. Schrauth, A. Gaeta, C. Hernández-García, L. Plaja, A. Becker, A. Jaron-Becker, M. M. Murnane, and H. C. Kapteyn, Bright Coherent Ultrahigh Harmonics in the keV X-ray Regime from Mid-Infrared Femtosecond Lasers, *Science* **336**(6086), 1287–1291 (2012).
- [14] G. Herink, D. R. Solli, M. Gulde, and C. Ropers, Field-driven photoemission from nanostructures quenches the quiver motion, *Nat.* **483**(7388), 190–193 (2012).
- [15] P. B. Corkum and F. Krausz, Attosecond science, *Nat. Phys.* **3**(6), 381–387 (2007).
- [16] J. Pupeikis, P.-A. Chevreuril, N. Bigler, L. Gallmann, C. R. Phillips, and U. Keller, Water window soft x-ray source enabled by a 25 W few-cycle 2.2  $\mu\text{m}$  OPCPA at 100 kHz, *Optica* **7**(2), 168–171 (2020).
- [17] C. Schmidt, Y. Pertot, T. Balciunas, K. Zinchenko, M. Matthews, H. J. Wörner, and J.-P. Wolf, High-order harmonic source spanning up to the oxygen K-edge based on filamentation pulse compression, *Opt. Express* **26**(9), 11834–11842 (2018).
- [18] J. Dura, N. Camus, A. Thai, A. Britz, M. Hemmer, M. Baudisch, A. Senftleben, C. D. Schröter, J. Ullrich, R. Moshhammer, and J. Biegert, Ionization with low-frequency fields in the tunneling regime, *Sci. Rep.* **3**(1), 2675 (2013).
- [19] B. Wolter, C. Lemell, M. Baudisch, M. G. Pullen, X. M. Tong, M. Hemmer, A. Senftleben, C. D. Schröter, J. Ullrich, R. Moshhammer, J. Biegert, and J. Burgdörfer, Formation of very-low-energy states crossing the ionization threshold of argon atoms in strong mid-infrared fields, *Phys. Rev. A* **90**(6), 063424 (2014).
- [20] C. I. Blaga, J. Xu, A. D. Dichiaro, E. Sistrunk, K. Zhang, P. Agostini, T. A. Miller, L. F. Dimauro, and C. D. Lin, Imaging ultrafast molecular dynamics with laser-induced electron diffraction, *Nat.* **483**(7388), 194–197 (2012).
- [21] Y. Xiao, M. Guo, K. Parker, and M. S. Hutson, Wavelength-dependent collagen fragmentation during Mid-IR laser ablation, *Biophys. J.* **91**(4), 1424–1432 (2006).
- [22] I. Mingareev, F. Weirauch, A. Olowinsky, L. Shah, P. Kadwani, and M. Richardson, Welding of polymers using a 2  $\mu\text{m}$  thulium fiber laser, *Opt. Laser Technol.* **44**(7), 2095–2099 (2012).

- [23] T. W. Bae, B. I. Kim, Y. C. Kim, and S. H. Ahn, Jamming effect analysis of infrared reticle seeker for directed infrared countermeasures, *Infrared Phys. Technol.* **55**(5), 431–441 (2012).
- [24] T. Feng, A. Heilmann, M. Bock, L. Ehrentraut, T. Witting, H. Yu, H. Stiel, S. Eisebitt, and M. Schnürer, 27 W 2.1  $\mu\text{m}$  OPCPA system for coherent soft X-ray generation operating at 10 kHz, *Opt. Express* **28**(6), 8724–8733 (2020).
- [25] Y. Deng, A. Schwarz, H. Fattahi, M. Ueffing, X. Gu, M. Ossiander, T. Metzger, V. Pervak, H. Ishizuki, T. Taira, T. Kobayashi, G. Marcus, F. Krausz, R. Kienberger, and N. Karpowicz, Carrier-envelope-phase-stable, 1.2 mJ, 1.5 cycle laser pulses at 2.1  $\mu\text{m}$ , *Opt. Lett.* **37**(23), 4973–4975 (2012).
- [26] K.-H. Hong, C. J. Lai, J. P. Siqueira, P. Krogen, J. Moses, C. L. Chang, G. J. Stein, L. E. Zapata, and F. X. Kärtner, Multi-mJ, kHz, 2.1  $\mu\text{m}$  optical parametric chirped-pulse amplifier and high-flux soft X-ray high-harmonic generation, *Opt. Lett.* **39**(11), 3145–3148 (2014).
- [27] G. Eckhardt, R. W. Hellwarth, F. J. McClung, S. E. Schwarz, D. Weiner, and E. J. Woodbury, Stimulated Raman Scattering From Organic Liquids, *Phys. Rev. Lett.* **9**(11), 455–457 (1962).
- [28] G. Hilfer and C. R. Menyuk, Stimulated Raman scattering in the transient limit, *J. Opt. Soc. Am. B* **7**(5), 739–749 (1990).
- [29] S. Li, Q. Fang, Y. Zhang, S. Tao, J. Zhang, C. Quan, D. Sun, C. Zhao, and Y. Hang, 2  $\mu\text{m}$  Ultrabroad spectra and laser operation of Tm:GdScO<sub>3</sub> crystal, *Opt. Laser Technol.* **143**, 107345 (2021).
- [30] N. Zhang, Q. Song, J. Zhou, J. Liu, S. Liu, H. Zhang, X. Xu, Y. Xue, J. Xu, W. Chen, Y. Zhao, U. Griebner, and V. Petrov, 44-fs pulse generation at 2.05  $\mu\text{m}$  from a SESAM mode-locked Tm:GdScO<sub>3</sub> laser, *Opt. Lett.* **48**(2), 510–513 (2023).
- [31] A. Suzuki, C. Kränkel, and M. Tokurakawa, Sub-6 optical-cycle Kerr-lens mode-locked Tm:Lu<sub>2</sub>O<sub>3</sub> and Tm:Sc<sub>2</sub>O<sub>3</sub> combined gain media laser at 2.1  $\mu\text{m}$ , *Opt. Express* **29**(13), 19465–19471 (2021).
- [32] S. A. Rezvani, M. Suzuki, P. Malevich, C. Livache, J. V. de Montgolfier, Y. Nomura, N. Tsurumachi, A. Baltuška, and T. Fuji, Millijoule femtosecond pulses at 1937 nm from a diode-pumped ring cavity Tm:YAP regenerative amplifier, *Opt. Express* **26**(22), 29460–29470 (2018).
- [33] P. Malevich, G. Andriukaitis, T. Flöry, A. J. Verhoef, A. Fernández, S. Ališauskas, A. Pugžlys, A. Baltuška, L. H. Tan, C. F. Chua, and P. B. Phua, High energy and average power femtosecond laser for

- driving mid-infrared optical parametric amplifiers, *Opt. Lett.* **38**(15), 2746–2749 (2013).
- [34] U. Elu, T. Steinle, D. Sanchez, L. Maidment, K. Zawilski, P. Schunemann, U. Zeitner, C. Simon-Boisson, and J. Biegert, Table-top high-energy 7  $\mu\text{m}$  OPCPA and 260 mJ Ho:YLF pump laser, *Opt. Lett.* **44**(13), 3194–3197 (2019).
- [35] L. von Grafenstein, M. Bock, D. Ueberschaer, A. Koç, U. Griebner, and T. Elsaesser, 2.05  $\mu\text{m}$  chirped pulse amplification system at a 1 kHz repetition rate—2.4 ps pulses with 17 GW peak power, *Opt. Lett.* **45**(14), 3836–3839 (2020).
- [36] L. von Grafenstein, M. Bock, D. Ueberschaer, E. Escoto, A. Koç, K. Zawilski, P. Schunemann, U. Griebner, and T. Elsaesser, Multi-millijoule, few-cycle 5  $\mu\text{m}$  OPCPA at 1 kHz repetition rate, *Opt. Lett.* **45**(21), 5998–6001 (2020).
- [37] V. Cardin, N. Thiré, S. Beaulieu, V. Wanie, F. Légaré, and B. E. Schmidt, 0.42 TW 2-cycle pulses at 1.8  $\mu\text{m}$  via hollow-core fiber compression, *Appl. Phys. Lett.* **107**(18), 181101 (2015).
- [38] T. Balciunas, C. Fourcade-Dutin, G. Fan, T. Witting, A. A. Voronin, A. M. Zheltikov, F. Gerome, G. G. Paulus, A. Baltuska, and F. Benabid, A strong-field driver in the single-cycle regime based on self-compression in a kagome fibre, *Nat. Commun.* **6**(1), 6117 (2015).
- [39] K. Murari, G. Cirimi, H. Cankaya, G. J. Stein, B. Debord, F. Gérôme, F. Ritzkosky, F. Benabid, O. Muecke, and F. X. Kärtner, Sub-50 fs pulses at 2050 nm from a picosecond Ho:YLF laser using a two-stage Kagome-fiber-based compressor, *Photonics Res.* **10**(3), 637–645 (2022).
- [40] P. Gierschke, C. Grebing, M. Abdelaal, M. Lenski, J. Buldt, Z. Wang, T. Heuermann, M. Mueller, M. Gebhardt, J. Rothhardt, and J. Limpert, Nonlinear pulse compression to 51-W average power GW-class 35-fs pulses at 2- $\mu\text{m}$  wavelength in a gas-filled multi-pass cell, *Opt. Lett.* **47**(14), 3511–3514 (2022).
- [41] N. Nagl, S. Gröbmeyer, V. Pervak, F. Krausz, O. Pronin, and K. F. Mak, Directly diode-pumped, Kerr-lens mode-locked, few-cycle Cr:ZnSe oscillator, *Opt. Express* **27**(17), 24445–24454 (2019).
- [42] E. Slobodchikov and P. F. Moulton, 1-GW-Peak-Power, Cr:ZnSe Laser, *Laser ciences to Photonic Applications* (CLEO, 2011), pp. 1-2, PDPA10.
- [43] S. Vasilyev, J. Peppers, I. Moskalev, V. Smolski, M. Mirov, E. Slobodchikov, A. Dergachev, S. Mirov, and V. Gapontsev, 1.5-mJ Cr:ZnSe Chirped Pulse Amplifier Seeded by a Kerr-Lens Mode-

- Locked Cr:ZnS oscillator, *Laser Congress 2019 (ASSL, LAC, LS&C)*, pp. ATu4A.4.
- [44] A. Villa, A. M. Ross, R. Gotti, M. Lamperti, F. Scotognella, G. Cerullo, and M. Marangoni, Broadly tunable mid-infrared femtosecond pulses directly generated by an optical parametric amplifier, *OSA Contin.* **4**(11), 2837–2844 (2021).
- [45] Y. Yin, X. Ren, A. Chew, J. Li, Y. Wang, F. Zhuang, Y. Wu, and Z. Chang, Generation of octave-spanning mid-infrared pulses from cascaded second-order nonlinear processes in a single crystal, *Sci. Rep.* **7**(1), 11097 (2017).
- [46] Y. Wu, F. Zhou, E. W. Larsen, F. Zhuang, Y. Yin, and Z. Chang, Generation of few-cycle multi-millijoule 2.5  $\mu\text{m}$  pulses from a single-stage  $\text{Cr}^{2+}$ :ZnSe amplifier, *Sci. Rep.* **10**(1), 7775 (2020).
- [47] V. E. Leshchenko, B. K. Talbert, Y. H. Lai, S. Li, Y. Tang, S. J. Hageman, G. Smith, P. Agostini, L. F. DiMauro, and C. I. Blaga, High-power few-cycle Cr:ZnSe mid-infrared source for attosecond soft x-ray physics, *Optica* **7**(8), 981–988 (2020).
- [48] A. Dubietis, G. Jonušauskas, and A. Piskarskas, Powerful femtosecond pulse generation by chirped and stretched pulse parametric amplification in BBO crystal, *Opt. Commun.* **88**(4–6), 437–440 (1992).
- [49] G. Cerullo and S. De Silvestri, Ultrafast optical parametric amplifiers, *Rev. Sci. Instrum.* **74**(1 I), 1–18 (2003).
- [50] D. Brida, C. Manzoni, G. Cirimi, M. Marangoni, S. Bonora, P. Villoresi, S. De Silvestri, and G. Cerullo, Few-optical-cycle pulses tunable from the visible to the mid-infrared by optical parametric amplifiers, *J. Opt. A: Pure Appl. Opt.* **12**(1), 013001 (2010).
- [51] C. Manzoni and G. Cerullo, Design criteria for ultrafast optical parametric amplifiers, *J. Opt.* **18**(10), 103501 (2016).
- [52] A. G. Ciriolo, M. Negro, M. Devetta, E. Cinquanta, D. Faccialà, A. Pusala, S. De Silvestri, S. Stagira, and C. Vozzi, Optical parametric amplification techniques for the generation of high-energy few-optical-cycles IR pulses for strong field applications, *Appl. Sci.* **7**(3), 265 (2017).
- [53] A. Vaupel, N. Bodnar, B. Webb, L. Shah, and M. Richardson, Concepts, performance review, and prospects of table-top, few-cycle optical parametric chirped-pulse amplification, *Opt. Eng.* **53**(5), 051507 (2013).
- [54] C. N. Danson, C. Haefner, J. Bromage, T. Butcher, J. C. F. Chanteloup, E. A. Chowdhury, A. Galvanauskas, L. A. Gizzi, J. Hein, D. I. Hillier,

- N. W. Hopps, Y. Kato, E. A. Khazanov, R. Kodama, G. Korn, R. Li, Y. Li, J. Limpert, J. Ma, C. H. Nam, D. Neely, D. Papadopoulos, R. R. Penman, L. Qian, J. J. Rocca, A. A. Shaykin, C. W. Siders, C. Spindloe, S. Szatmári, R. M. G. M. Trines, J. Zhu, P. Zhu, and J. D. Zuegel, Petawatt and exawatt class lasers worldwide, *High Power Laser Sci. Eng.* **7**, e54 (2019).
- [55] Y. Yin, J. Li, X. Ren, K. Zhao, Y. Wu, E. Cunningham, and Z. Chang, High-efficiency optical parametric chirped-pulse amplifier in  $\text{BiB}_3\text{O}_6$  for generation of 3 mJ, two-cycle, carrier-envelope-phase-stable pulses at 1.7  $\mu\text{m}$ , *Opt. Lett.* **41**(6), 1142–1145 (2016).
- [56] T. Fuji, N. Ishii, C. Y. Teisset, X. Gu, Th. Metzger, A. Baltuska, N. Forget, D. Kaplan, A. Galvanauskas, and F. Krausz, Parametric amplification of few-cycle carrier-envelope phase-stable pulses at 2.1  $\mu\text{m}$ , *Opt. Lett.* **31**(8), 1103–1105 (2006).
- [57] B. E. Schmidt, N. Thiré, M. Boivin, A. Laramée, F. Poitras, G. Lebrun, T. Ozaki, H. Ibrahim, and F. Légaré, Frequency domain optical parametric amplification, *Nat. Commun.* **5**(1), 3643 (2014).
- [58] F. Silva, P. K. Bates, A. Esteban-Martin, M. Ebrahim-Zadeh, and J. Biegert, High-average-power, carrier-envelope phase-stable, few-cycle pulses at 2.1  $\mu\text{m}$  from a collinear  $\text{BiB}_3\text{O}_6$  optical parametric amplifier, *Opt. Lett.* **37**(5), 933–935 (2012).
- [59] I. N. Ross, J. L. Collier, P. Matousek, C. N. Danson, D. Neely, R. M. Allott, D. A. Pepler, C. Hernandez-Gomez, and K. Osvay, Generation of terawatt pulses by use of optical parametric chirped pulse amplification, *Appl. Opt.* **39**(15), 2422–2427 (2000).
- [60] P. Mackonis and A. M. Rodin, OPCPA investigation with control over the temporal shape of 1.2 ps pump pulses, *Opt. Express* **28**(8), 12020–12027 (2020).
- [61] D. Du, X. Liu, G. Korn, J. Squier, and G. Mourou, Laser-induced breakdown by impact ionization in  $\text{SiO}_2$  with pulse widths from 7 ns to 150 fs, *Appl. Phys. Lett.* **64**(23), 3071–3073 (1994).
- [62] B. C. Stuart, M. D. Feit, A. M. Rubenchik, B. W. Shore, and M. D. Perry, Laser-induced damage in dielectrics with nanosecond to subpicosecond pulses, *Phys. Rev. Lett.* **74**(12), 2248–2251 (1995).
- [63] M. Lenzner, J. Krüger, S. Sartania, Z. Cheng, Ch. Spielmann, G. Mourou, W. Kautek, and F. Krausz, Femtosecond optical breakdown in dielectrics, *Phys. Rev. Lett.* **80**(18), 4076–4079 (1998).
- [64] K. H. Hong, S. W. Huang, J. Moses, X. Fu, C. J. Lai, G. Cirimi, A. Sell, E. Granados, P. Keathley, and F. X. Kärtner, High-energy, phase-

- stable, ultrabroadband kHz OPCPA at 2.1  $\mu\text{m}$  pumped by a picosecond cryogenic Yb:YAG laser, *Opt. Express* **19**(16), 15538–15548 (2011).
- [65] N. Thiré, R. Maksimenka, B. Kiss, C. Ferchaud, P. Bizouard, E. Cormier, K. Osvay, and N. Forget, 4-W, 100-kHz, few-cycle mid-infrared source with sub-100-mrad carrier-envelope phase noise, *Opt. Express* **25**(2), 1505–1514 (2017).
- [66] N. Ishii, K. Kaneshima, T. Kanai, S. Watanabe, and J. Itatani, Generation of ultrashort intense optical pulses at 1.6  $\mu\text{m}$  from a bismuth triborate-based optical parametric chirped pulse amplifier with carrier-envelope phase stabilization, *J. Opt.* **17**(9), 094001 (2015).
- [67] G. Cerullo, A. Baltuška, O. D. Mücke, and C. Vozzi, Few-optical-cycle light pulses with passive carrier-envelope phase stabilization, *Laser Photon. Rev.* **5**(3), 323–351 (2011).
- [68] Z. Hong, Q. Zhang, P. Lan, and P. Lu, Generation of few-cycle infrared pulses from a degenerate dual-pump OPCPA, *Opt. Express* **22**(5), 5544–5557 (2014).
- [69] K.-H. Hong, J. T. Gopinath, D. Rand, A. M. Siddiqui, S.-W. Huang, E. Li, B. J. Eggleton, J. D. Hybl, T. Y. Fan, and F. X. Kärtner, High-energy, kHz-repetition-rate, ps cryogenic Yb:YAG chirped-pulse amplifier, *Opt. Lett.* **35**(11), 1752–1754 (2010).
- [70] T. Nubbemeyer, M. Kaumanns, M. Ueffing, M. Gorjan, A. Alismail, H. Fattahi, J. Brons, O. Pronin, H. G. Barros, Z. Major, T. Metzger, D. Sutter, and F. Krausz, 1 kW, 200 mJ picosecond thin-disk laser system, *Opt. Lett.* **42**(7), 1381–1384 (2017).
- [71] P. Mackonis and A. M. Rodin, Laser with 1.2 ps, 20 mJ pulses at 100 Hz based on CPA with a low doping level Yb:YAG rods for seeding and pumping of OPCPA, *Opt. Express* **28**(2), 1261–1268 (2020).
- [72] C. J. Lai, K. H. Hong, J. P. Siqueira, P. Krogen, C. L. Chang, G. J. Stein, H. Liang, P. D. Keathley, G. Laurent, J. Moses, L. E. Zapata, and F. X. Kärtner, Multi-mJ mid-infrared kHz OPCPA and Yb-doped pump lasers for tabletop coherent soft x-ray generation, *Journal of Optics* **17**(9), 094009 (2015).
- [73] I. Sytceвич, A. L. Viotti, C. Guo, J. Vogelsang, F. Langer, A. L’Huillier, and C. L. Arnold, Few-cycle short-wave-infrared light source for strong-field experiments at 200 kHz repetition rate, *Opt. Express* **30**(15), 27858–27867 (2022).
- [74] J. H. Buss, S. Starosielec, M. Schulz, R. Riedel, F. Campi, C. S. Lehmann, S. Witte, and P. M. Kraus, Mid-infrared optical parametric chirped-pulse amplifier at 50 W and 38 fs pumped by a

- high-power Yb-InnoSlab platform, *Opt. Express* **32**(21), 36185–36192 (2024).
- [75] A. Harth, M. Schultze, T. Lang, T. Binhammer, S. Rausch, and U. Morgner, Two-color pumped OPCPA system emitting spectra spanning 15 octaves from VIS to NIR, *Opt. Express* **20**(3), 3076–3081 (2012).
- [76] D. Herrmann, C. Homann, R. Tautz, M. Scharrer, P. St. J. Russell, F. Krausz, L. Veisz, and E. Riedle, Approaching the full octave: noncollinear optical parametric chirped pulse amplification with two-color pumping, *Opt. Express* **18**(18), 18752–18762 (2010).
- [77] L. Xu and E. J. Takahashi, Dual-chirped optical parametric amplification of high-energy single-cycle laser pulses, *Nat. Photonics* **18**(1), 99–106 (2024).
- [78] Z. Hong, F. Hu, X. Fu, W. Cao, Q. Zhang, and P. Lu, Few-cycle 1.9- $\mu\text{m}$  pulse generation via collinear spectrum synthesis in multiple-crystal OPA, *Opt. Lett.* **44**(14), 3438–3441 (2019).
- [79] Y. Fu, B. Xue, K. Midorikawa, and E. J. Takahashi, TW-scale mid-infrared pulses near 3.3  $\mu\text{m}$  directly generated by dual-chirped optical parametric amplification, *Appl. Phys. Lett.* **112**(24), 241105 (2018).
- [80] Y. Fu, K. Midorikawa, and E. J. Takahashi, Towards a petawatt-class few-cycle infrared laser system via dual-chirped optical parametric amplification, *Sci. Rep.* **8**(1), 1–11 (2018).
- [81] L. Xu, B. Xue, N. Ishii, J. Itatani, K. Midorikawa, and E. J. Takahashi, 100-mJ class, sub-two-cycle, carrier-envelope phase-stable dual-chirped optical parametric amplification, *Opt. Lett.* **47**(13), 3371–3374 (2022).
- [82] G. M. Rossi, R. E. Mainz, Y. Yang, F. Scheiba, M. A. Silva-Toledo, S. H. Chia, P. D. Keathley, S. Fang, O. D. Mücke, C. Manzoni, G. Cerullo, G. Cirmi, and F. X. Kärtner, Sub-cycle millijoule-level parametric waveform synthesizer for attosecond science, *Nat. Photonics* **14**(10), 629–635 (2020).
- [83] Y. C. Lin, Y. Nabekawa, and K. Midorikawa, Optical parametric amplification of sub-cycle shortwave infrared pulses, *Nat. Commun.* **11**(1), 3413 (2020).
- [84] A. Alismail, H. Wang, G. Barbiero, N. Altwaijry, S. A. Hussain, V. Pervak, W. Schweinberger, A. M. Azzeer, F. Krausz, and H. Fattahi, Multi-octave, CEP-stable source for high-energy field synthesis, *Sci. Adv.* **6**(7), (2020).
- [85] P. H. Bucksbaum, The future of attosecond spectroscopy, *Science* **317**(5839), 766–769 (2007).

- [86] G. Sansone, E. Benedetti, F. Calegari, C. Vozzi, L. Avaldi, R. Flammini, L. Poletto, P. Villoresi, C. Altucci, R. Velotta, S. Stagira, S. De Silvestri, and M. Nisoli, Isolated single-cycle attosecond pulses, *Science* **314**(5798), 443–446 (2006).
- [87] H. Fattahi, H. Wang, A. Alismail, G. Arisholm, V. Pervak, A. M. Azzeer, and F. Krausz, Near-PHz-bandwidth, phase-stable continua generated from a Yb:YAG thin-disk amplifier, *Opt. Express* **24**(21), 24337–24346 (2016).
- [88] A. Dubietis and A. Matijošius, Table-top optical parametric chirped pulse amplifiers: past and present, *Opto-Electron. Adv.* **6**(3), 220046 (2023).
- [89] B. Pal, *Frontiers in Guided Wave Optics and Optoelectronics* (InTech, 2010).
- [90] V. Jukna, J. Galinis, G. Tamosauskas, D. Majus, and A. Dubietis, Infrared extension of femtosecond supercontinuum generated by filamentation in solid-state media, *Appl. Phys. B* **116**(2), 477–483 (2014).
- [91] N. Ishii, M. Maruyama, K. Nagashima, Y. Ochi, and R. Itakura, Generation and compression of an intense infrared white light continuum in YAG irradiated by picosecond pulses, *Opt. Express* **29**(11), 17069–17076 (2021).
- [92] P. Mackonis, A. Petrulenas, V. Girdauskas, and A. Rodin, Observation of a stable supercontinuum from 1100 nm to 2400 nm in YAG pumped with 1.2 ps pulses for a cost-effective 1 TW-class OPCPA, *8th EPS-QEOD Europhoton Conference* (2018), pp. TuPD4, 2–7.
- [93] A. Špaček, L. Indra, F. Batysta, P. Hříbek, J. T. Green, J. Novák, R. Antipenkov, P. Bakule, and B. Rus, Stability mechanism of picosecond supercontinuum in YAG, *Opt. Express* **28**(14), 20205–20214 (2020).
- [94] N. Thiré, G. Chatterjee, Y. Pertot, O. Albert, G. Karras, Y. Zhang, A. S. Wyatt, M. Towrie, E. Springate, G. M. Greetham, and N. Forget, A versatile high-average-power ultrafast infrared driver tailored for high-harmonic generation and vibrational spectroscopy, *Sci. Rep.* **13**(1), 18874 (2023).
- [95] R. Budriūnas, K. Jurkus, M. Vengris, and A. Varanavičius, Long seed, short pump: converting Yb-doped laser radiation to multi- $\mu$ J few-cycle pulses tunable through 2.5–15  $\mu$ m, *Opt. Express* **30**(8), 13009–13023 (2022).



- [96] G. C. Bhar, U. Chatterjee, and S. Das, Tunable near-infrared radiation by difference frequency mixing in beta barium borate crystal, *Appl. Phys. Lett.* **58**(3), 231–233 (1991).
- [97] B. Teng, J. Wang, Z. Wang, X. Hu, H. Jiang, H. Liu, X. Cheng, S. Dong, Y. Liu, and Z. Shao, Crystal growth, thermal and optical performance of  $\text{BiB}_3\text{O}_6$ , *J. Cryst. Growth* **233**(1–2), 282–286 (2001).
- [98] P. Segonds, B. Boulanger, J.-P. Fève, B. Ménaert, J. Zaccaro, G. Aka, and D. Pelenc, Linear and nonlinear optical properties of the monoclinic  $\text{Ca}_4\text{YO}(\text{BO}_3)_3$  crystal, *J. Opt. Soc. Am. B* **21**(4), 765–769 (2004).
- [99] S. Lin, Y. Tanaka, S. Takeuchi, and T. Suzuki, Improved dispersion equation for  $\text{MgO}:\text{LiNbO}_3$  crystal in the infrared spectral range derived from sum and difference frequency mixing, *J. Quantum Electron.* **32**(1), 124–126 (1996).
- [100] W. Kiefer, Recent Advances in linear and nonlinear Raman spectroscopy I, *J. Raman Spectrosc.* **38**(12), 1538–1553 (2007).
- [101] S. A. Borman, Nonlinear Raman Spectroscopy, *Anal. Chem.* **54**(9), 1021A-1026A (1982).
- [102] A. V. Konyashchenko, L. L. Losev, and S. Y. Tenyakov, Raman frequency shifter for laser pulses shorter than 100 fs, *Opt Express* **15**(19), 11855–11859 (2007).
- [103] A. V. Konyashchenko, L. L. Losev, and V. S. Pazyuk, Femtosecond Raman frequency shifter–pulse compressor, *Opt. Lett.* **44**(7), 1646–1649 (2019).
- [104] A. Z. Grasyuk, Raman lasers, *Sov. J. Quantum Electron.* **4**(3), 269–282 (1974).
- [105] C. Jordan, K. A. Stankov, G. Marowsky, and E. J. Canto-Said, Efficient compression of femtosecond pulses by stimulated Raman scattering, *Appl. Phys. B* **59**(4), 471–473 (1994).
- [106] V. A. Orlovich, Y. I. Malakhov, Y. M. Popov, D. N. Busko, M. B. Danailov, A. A. Demidovich, P. A. Apanasevich, and R. V Chulkov, Raman conversion of femtosecond laser pulses in crystals, *Laser Phys. Lett.* **9**(11), 770–774 (2012).
- [107] J. Reichel, F. Bardou, M. Ben Dahan, E. Peik, S. Rand, C. Salomon, and C. Cohen-Tannoudji, Raman cooling of cesium below 3 nK: New approach inspired by Lévy flight statistics, *Phys. Rev. Lett.* **75**(25), 4575–4578 (1995).
- [108] G. He, Optical phase conjugation: principles, techniques, and applications, *Prog. Quantum Electron.* **26**(3), 131–191 (2002).

- [109] A. M. Zheltikov, The Raman effect in femto- and attosecond physics, *Phys.-Uspekhi* **54**(1), 29–51 (2011).
- [110] R. L. Carman, F. Shimizu, C. S. Wang, and N. Bloembergen, Theory of Stokes pulse shapes in transient stimulated Raman scattering, *Phys. Rev. A* **2**(1), 60–72 (1970).
- [111] A. Agnesi, G. C. Reali, and V. Kubecek, Transient stimulated Raman scattering: theory and experiments of picosecond pulse compression, *Inst. Phys. Conf. Ser.* **1415**(115), 105–108 (1991).
- [112] R. L. Carman, M. E. Mack, F. Shimizu, and N. Bloembergen, Forward Picosecond Stokes-Pulse Generation in Transient Stimulated Raman Scattering, *Phys. Rev. Lett.* **23**(23), 1327–1329 (1969).
- [113] G. Andriukaitis, T. Balčiūnas, S. Ališauskas, A. Pugžlys, A. Baltuška, T. Popmintchev, M.-C. Chen, M. M. Murnane, and H. C. Kapteyn, 90 GW peak power few-cycle mid-infrared pulses from an optical parametric amplifier, *Opt. Lett.* **36**(15), 2755–2757 (2011).
- [114] R. B. Stewart and R. T. V. Kung, A kilohertz repetition rate 1.9  $\mu\text{m}$  H<sub>2</sub> Raman oscillator, *J. Quantum Electron.* **25**(10), 2142–2148 (1989).
- [115] R. Frey, A. de Martino, and F. Pradère, High-efficiency pulse compression with intracavity Raman oscillators, *Opt. Lett.* **8**(8), 437–439 (1983).
- [116] A. McKay, O. Kitzler, and R. P. Mildren, Simultaneous brightness enhancement and wavelength conversion to the eye-safe region in a high-power diamond Raman laser, *Laser Photon. Rev.* **8**(3), L37–L41 (2014).
- [117] S. Yoshikawa and T. Imasaka, A new approach for the generation of ultrashort optical pulses, *Opt. Commun.* **96**(1–3), 94–98 (1993).
- [118] S. Baker, I. A. Walmsley, J. W. G. Tisch, and J. P. Marangos, Femtosecond to attosecond light pulses from a molecular modulator, *Nat. Photonics* **5**(11), 664–671 (2011).
- [119] D. A. Long, *The Raman Effect* (Wiley, 2002).
- [120] C. V. Raman and K. S. Krishnan, A new type of secondary radiation, *Nat.* **121**(3048), 501–502 (1928).
- [121] R. Loudon, The Raman effect in crystals, *Adv. Phys.* **13**(52), 423–482 (1964).
- [122] M. D. Duncan, R. Mahon, L. L. Tankersley, and J. Reintjes, Transient stimulated Raman amplification in hydrogen, *J. Opt. Soc. Am. B* **5**(1), 37–52 (1988).
- [123] R. W. Hellwarth, Theory of Stimulated Raman Scattering, *Phys. Rev.* **130**(5), 1850–1852 (1963).

- [124] R. W. Boyd, A. L. Gaeta, and E. Giese, *Nonlinear Optics* (Springer, 2023).
- [125] A. Penzkofer, A. Laubereau, and W. Kaiser, High intensity Raman interactions, *Prog. Quantum Electron.* **6**(2), 55–140 (1979).
- [126] N. Bloembergen, The Stimulated Raman Effect, *Am. J. Phys.* **35**(11), 989–1023 (1967).
- [127] J. Murray, J. Goldhar, D. Eimerl, and A. Szoke, Raman pulse compression of excimer lasers for application to laser fusion, *J. Quantum Electron.* **15**(5), 342–368 (1979).
- [128] J. Moloney and A. Newell, *Nonlinear Optics* (CRC Press, 2018).
- [129] D. von der Linde, M. Maier, and W. Kaiser, Quantitative Investigations of the Stimulated Raman Effect Using Subnanosecond Light Pulses, *Phys. Rev.* **178**(1), 11–17 (1969).
- [130] W. Hartig and W. Schmidt, A broadly tunable IR waveguide Raman laser pumped by a dye laser, *Appl. Phys.* **18**(3), 235–241 (1979).
- [131] H. G. M. Edwards, D. A. Long, and G. Sherwood, Line widths in the pure rotational Raman spectra of hydrogen and deuterium self-broadened and broadened by foreign gases, *J. Raman Spectrosc.* **22**(11), 607–611 (1991).
- [132] M. Katsuragawa and K. Hakuta, Raman gain measurement in solid parahydrogen, *Opt. Lett.* **25**(3), 177–179 (2000).
- [133] K. Midorikawa, H. Tashiro, Y. Aoki, K. Nagasaka, K. Toyoda, and S. Namba, Room-temperature operation of a para-H<sub>2</sub> rotational Raman laser, *Appl. Phys. Lett.* **47**(10), 1033–1035 (1985).
- [134] V. S. Averbakh, A. I. Makarov, and V. I. Talanov, Stimulated Raman scattering on rotational and vibrational transitions in nitrogen gas, *Sov. J. Quantum Electron.* **8**(4), 472–476 (1978).
- [135] M. A. Henesian, C. D. Swift, and J. R. Murray, Stimulated rotational Raman scattering in nitrogen in long air paths, *Opt. Lett.* **10**(11), 565–567 (1985).
- [136] C. Shen, X. Cai, Y. Sang, T. Zheng, Z. Li, D. Liu, W. Liu, and J. Guo, Investigation of multispectral SF<sub>6</sub> stimulated Raman scattering laser, *Chin. Opt. Lett.* **18**(5), 051402 (2020).
- [137] A. A. Kaminskii, C. L. McCray, H. R. Lee, S. W. Lee, D. A. Temple, T. H. Chyba, W. D. Marsh, J. C. Barnes, A. N. Annanenko, V. D. Legun, H. J. Eichler, G. M. A. Gad, and K. Ueda, High efficiency nanosecond Raman lasers based on tetragonal PbWO<sub>4</sub> crystals, *Opt. Commun.* **183**(1–4), 277–287 (2000).

- [138] Y. Liu, W. You, C. Zhu, M. Li, Y. Sun, X. Yin, D. Chen, Y. Feng, W. Chen, and X. Yang, A review of ns-pulsed Raman lasers based on diamond crystal, *Front. Phys.* **10**, 1054234 (2022).
- [139] S. L. Shapiro and D. H. Auston, *Ultrashort Light Pulses: Topics in Applied Physics* (Springer Berlin Heidelberg, 1977).
- [140] N. J. Everall, J. P. Partanen, J. R. M. Barr, and M. J. Shaw, Threshold measurements of stimulated Raman scattering in gases using picosecond KrF laser pulses, *Opt. Commun.* **64**(4), 393–397 (1987).
- [141] V. Krylov, O. Ollikainen, U. P. Wild, A. Rebane, V. G. Bespalov, and D. I. Staselko, Femtosecond stimulated Raman scattering in pressurized gases in the ultraviolet and visible spectral ranges, *J. Opt. Soc. Am. B* **15**(12), 2910–2916 (1998).
- [142] V. Krylov, V. Bespalov, D. Staselko, A. Rebane, O. Ollikainen, D. Erni, and U. Wild, Stimulated Raman scattering in hydrogen by frequency-doubled amplified femtosecond Ti:sapphire laser pulses, *Opt. Lett.* **21**(6), 381–383 (1996).
- [143] A. G. Shvedko, S. G. Kruglik, P. A. Apanasevich, and V. A. Orlovich, Spectral characteristics of picosecond stimulated raman scattering in high-pressure hydrogen, *Laser Phys.* **11**(3), 377–387 (2001).
- [144] I. G. Koprnikov, A. Suda, and K. Midorikawa, Interference between stimulated Raman scattering and self-phase modulation in pressurized methane in highly transient femtosecond pump regime, *Opt. Commun.* **174**(1–4), 299–304 (2000).
- [145] A. V. Konyashchenko, L. L. Losev, and V. S. Pazyuk, SRS of ultrashort laser pulses with nonlinear phase modulation, *Quantum Electron.* **51**(3), 217–221 (2021).
- [146] V. Krylov, I. Fischer, V. Bespalov, D. Staselko, and A. Rebane, Transient stimulated Raman scattering in gas mixtures, *Opt. Lett.* **24**(22), 1623–1625 (1999).
- [147] A. Major, J. S. Aitchison, P. W. E. Smith, N. Langford, and A. I. Ferguson, Efficient Raman shifting of high-energy picosecond pulses into the eye-safe 1.5- $\mu$  spectral region by use of a KGd(WO<sub>4</sub>)<sub>2</sub> crystal, *Opt. Lett.* **30**(4), 421–423 (2005).
- [148] A. S. Grabtchikov, R. V. Chulkov, V. A. Orlovich, M. Schmitt, R. Maksimenko, and W. Kiefer, Observation of Raman conversion for 70-fs pulses in KGd(WO<sub>4</sub>)<sub>2</sub> crystal in the regime of impulsive stimulated Raman scattering, *Opt. Lett.* **28**(11), 926–928 (2003).
- [149] I. O. Kinyaevskiy, V. I. Kovalev, P. A. Danilov, N. A. Smirnov, S. I. Kudryashov, L. V. Seleznev, E. E. Dunaeva, and A. A. Ionin, Highly efficient stimulated Raman scattering of sub-picosecond laser pulses

- in BaWO<sub>4</sub> for 10.6 μm difference frequency generation, *Opt. Lett.* **45**(8), 2160–2163 (2020).
- [150] S. C. Pinault and M. J. Potasek, Frequency broadening by self-phase modulation in optical fibers, *J. Opt. Soc. Am. B* **2**(8), 1318–1319 (1985).
- [151] L. L. Losev, J. Song, J. F. Xia, D. Strickland, and V. V. Brukhanov, Multifrequency parametric infrared Raman generation in KGd(WO<sub>4</sub>)<sub>2</sub> crystal with biharmonic ultrashort-pulse pumping, *Opt. Lett.* **27**(23), 2100–2102 (2002).
- [152] A. V Konyashchenko, P. V Kostryukov, L. L. Losev, and V. S. Pazyuk, Minimum possible laser pulse duration for SRS, *Quantum Electron.* **47**(7), 593–596 (2017).
- [153] A. V. Konyashchenko, L. L. Losev, V. S. Pazyuk, and S. Y. Tenyakov, Frequency shifting of sub-100 fs laser pulses by stimulated Raman scattering in a capillary filled with pressurized gas, *Appl. Phys. B* **93**, 455–461 (2008).
- [154] D. Wang and Y. Leng, Nonlinear response of hydrogen atom induced by intense few-cycle laser field and its influence on refractive index, *Opt. Commun.* **285**(24), 5462–5466 (2012).
- [155] I. O. Kinyaevskiy, V. I. Kovalev, A. V. Koribut, Ya. V. Grudtsyn, L. V. Seleznev, E. E. Dunaeva, and A. A. Ionin, Efficient SRS of chirped Ti:sapphire laser pulses in BaWO<sub>4</sub> crystals, *Quantum Electron* **52**(3), 278–282 (2022).
- [156] R. C. Swanson, P. R. Battle, and J. L. Carlsten, Quantum statistics of the gain-narrowed Raman linewidth in H<sub>2</sub>, *Phys. Rev. A* **42**(11), 6774–6783 (1990).
- [157] A. I. Vodchits, A. G. Shvedko, V. A. Orlovich, V. P. Kozich, and W. Werncke, Stimulated Raman amplification of ultrashort seed pulses in compressed methane, *J. Opt. Soc. Am. B* **22**(2), 453–458 (2005).
- [158] V. Krylov, A. Rebane, D. Erni, O. Ollikainen, U. Wild, V. Bespalov, and D. Staselko, Stimulated Raman amplification of femtosecond pulses in hydrogen gas, *Opt. Lett.* **21**(24), 2005–2007 (1996).
- [159] O. V Bugarov, A. S. Grabtchikov, Y. I. Malakhov, Y. M. Popov, V. A. Orlovich, and S. A. Tikhomirov, Features of Raman amplification in KGW and barium nitrate crystals at excitation by femtosecond pulses, *L. Phys. Lett.* **9**(11), 786 (2012).
- [160] P. Mackonis, A. Petruenas, A. M. Rodin, V. Girdauskas, and A. Michailovas, Two-stage transient stimulated Raman chirped-pulse

- amplification in  $\text{KGd}(\text{WO}_4)_2$  with compression to 145 fs, *Opt. Lett.* **45**(24), 6627–6630 (2020).
- [161] A. Gladyshev, Y. Yatsenko, A. Kolyadin, V. Kompanets, and I. Bufetov, Mid-infrared 10- $\mu\text{J}$ -level sub-picosecond pulse generation via stimulated Raman scattering in a gas-filled revolver fiber, *Opt. Mater Express* **10**(12), 3081–3089 (2020).
- [162] S. Loranger, P. St. J. Russell, and D. Novoa, Sub-40 fs pulses at 1.8  $\mu\text{m}$  and MHz repetition rates by chirp-assisted Raman scattering in hydrogen-filled hollow-core fiber, *J. Opt. Soc. Am. B* **37**(12), 3550–3556 (2020).
- [163] N. V Didenko, A. V Konyashchenko, P. V Kostryukov, L. L. Losev, V. S. Pazyuk, S. Y. Tenyakov, V. Y. Molchanov, S. I. Chizhikov, and K. B. Yushkov, 40-fs hydrogen Raman laser, *Quantum Electron.* **45**(12), 1101–1104 (2015).
- [164] C. Vicario, M. Shalaby, A. Konyashchenko, L. Losev, and C. P. Hauri, High-power femtosecond Raman frequency shifter, *Opt. Lett.* **41**(20), 4719–4722 (2016).
- [165] V. Raghunathan, D. Borlaug, R. R. Rice, and B. Jalali, Demonstration of a Mid-infrared silicon Raman amplifier, *Opt. Express* **15**(22), 14355–14362 (2007).
- [166] A. Sabella, J. A. Piper, and R. P. Mildren, Diamond Raman laser with continuously tunable output from 3.38 to 3.80  $\mu\text{m}$ , *Opt. Lett.* **39**(13), 4037–4040 (2014).
- [167] O. Kuzucu, Watt-level, mid-infrared output from a  $\text{BaWO}_4$  external-cavity Raman laser at 2.6  $\mu\text{m}$ , *Opt. Lett.* **40**(21), 5078–5081 (2015).
- [168] P. Cheng, J. Zhao, F. Xu, X. Zhou, and G. Wang, Diode-pumped mid-infrared  $\text{YVO}_4$  Raman laser at 2418 nm, *Appl. Phys. B* **124**(1), 1–5 (2018).
- [169] N. Gelbach, Y. Neustadter, M. Henig, R. Nahear, and S. Noach, Two-mJ level, high-energy all-passive  $\text{KGW}/\text{Tm}:\text{YLF}$  Raman laser, *Opt. Lett.* **48**(17), 4444–4447 (2023).
- [170] U. Sheintop, D. Sebbag, P. Komm, S. Pearl, G. Marcus, and S. Noach, Two-wavelength  $\text{Tm}:\text{YLF}/\text{KGW}$  external-cavity Raman laser at 2197 nm and 2263 nm, *Opt. Express* **27**(12), 17112–17121 (2019).
- [171] A. Dubietis, G. Tamošauskas, R. Šuminas, V. Jukna, and A. Couairon, Ultrafast supercontinuum generation in bulk condensed media, *Lith. J. Phys.* **57**(3), 113–157 (2017).
- [172] I. Kinyaevskiy, V. Kovalev, P. Danilov, N. Smirnov, S. Kudryashov, A. Koribut, and A. Ionin, Asymmetric spectral broadening of sub-picosecond laser pulse in  $\text{BaWO}_4$  crystal: interplay of self-phase

- modulation, stimulated Raman scattering, and orientational Kerr nonlinearity, *Opt. Lett.* **46**(3), 697–700 (2021).
- [173] I. O. Kinyaevskiy, A. V Koribut, Y. V Grudtsyn, E. E. Dunaeva, Y. M. Andreev, and A. A. Ionin, Two-color emission of BaWO<sub>4</sub> crystals pumped by 472 nm 0.11 ps laser pulses for frequency conversion into the longwave IR domain, *Laser Phys. Lett.* **17**(10), 105402 (2020).
- [174] M. Frank, S. N. Smetanin, M. Jelínek, D. Vyhlídal, L. I. Ivleva, P. G. Zverev, and V. Kubeček, Highly efficient picosecond all-solid-state Raman laser at 1179 and 1227 nm on single and combined Raman lines in a BaWO<sub>4</sub> crystal, *Opt. Lett.* **43**(11), 2527–2530 (2018).
- [175] M. Frank, S. N. Smetanin, M. Jelínek, D. Vyhlídal, A. A. Kopalkin, V. E. Shukshin, L. I. Ivleva, P. G. Zverev, and V. Kubeček, Synchronously-pumped all-solid-state SrMoO<sub>4</sub> Raman laser generating at combined vibrational Raman modes with 26-fold pulse shortening down to 1.4 ps at 1220 nm, *Opt. Laser Technol.* **111**, 129–133 (2019).
- [176] E. Garmire, F. Pandarese, and C. H. Townes, Coherently Driven Molecular Vibrations and Light Modulation, *Phys. Rev. Lett.* **11**(4), 160–163 (1963).
- [177] Y. Y. Wang, C. Wu, F. Couny, M. G. Raymer, and F. Benabid, Quantum-Fluctuation-Initiated Coherence in Multioctave Raman Optical Frequency Combs, *Phys. Rev. Lett.* **105**(12), 123603 (2010).
- [178] D. Gold, J. Weber, and D. Yavuz, Continuous-Wave Molecular Modulation Using a High-Finesse Cavity, *Appl. Sci.* **4**(4), 498–514 (2014).
- [179] R. B. Stewart and R. T. V. Kung, A kilohertz repetition rate 1.9  $\mu\text{m}$  H<sub>2</sub> Raman oscillator, *J. Quantum Electron.* **25**(10), 2142–2148 (1989).
- [180] A. V Sokolov and S. E. Harris, Ultrashort pulse generation by molecular modulation, *J. Opt. B: Quantum Semiclass. Opt.* **5**(1), R1–R26 (2003).
- [181] N. Zhavoronkov and G. Korn, Generation of single intense short optical pulses by ultrafast molecular phase modulation, *Phys. Rev. Lett.* **88**(20), 203901 (2002).
- [182] M. Dorner-Kirchner, V. Shumakova, G. Coccia, E. Kaksis, B. E. Schmidt, V. Pervak, A. Pugžlys, A. Baltuška, M. Kitzler-Zeiler, and P. A. Carpeggiani, HHG at the carbon K-edge directly driven by SRS red-shifted pulses from an ytterbium amplifier, *ACS Photonics* **10**(1), 84–91 (2023).
- [183] P. A. Carpeggiani, G. Coccia, G. Fan, E. Kaksis, A. Pugžlys, A. Baltuška, R. Piccoli, Y.-G. Jeong, A. Rovere, R. Morandotti,

- L. Razzari, B. E. Schmidt, A. A. Voronin, and A. M. Zheltikov, Extreme Raman red shift: ultrafast multimode nonlinear space-time dynamics, pulse compression, and broadly tunable frequency conversion, *Optica* **7**(10), 1349–1354 (2020).
- [184] T. C. Truong, J. E. Beetar, and M. Chini, Light-field synthesizer based on multidimensional solitary states in hollow-core fibers, *Opt. Lett.* **48**(9), 2397–2400 (2023).
- [185] M. Zhi and A. V Sokolov, Broadband generation in a Raman crystal driven by a pair of time-delayed linearly chirped pulses, *New. J. Phys.* **10**(2), 025032 (2008).
- [186] A. A. Zhdanova, M. Shutova, A. Bahari, M. Zhi, and A. V. Sokolov, Topological charge algebra of optical vortices in nonlinear interactions, *Opt. Express.* **23**(26), 34109–34117 (2015).
- [187] A. Bahari, A. A. Zhdanova, M. Shutova, and A. V. Sokolov, Synthesis of ultrafast waveforms using coherent Raman sidebands, *Phys. Rev. A* **102**(1), 013520 (2020).
- [188] K. Wang, A. A. Zhdanova, M. Zhi, X. Hua, and A. V. Sokolov, Multicolored femtosecond pulse synthesis using coherent raman sidebands in a reflection schem, *Appl. Sci.* **5**(2), 145–156 (2015).
- [189] M. Zhi, K. Wang, X. Hua, H. Schuessler, J. Strohaber, and A. V. Sokolov, Generation of femtosecond optical vortices by molecular modulation in a Raman-active crystal, *Opt. Express* **21**(23), 27750–27758 (2013).
- [190] T. Bartulevicius, L. Veselis, K. Madeikis, A. Michailovas, and N. Rusteika, Compact femtosecond 10  $\mu$ J pulse energy fiber laser with a CFBG stretcher and CVBG compressor, *Opt. Fiber Technol.* **45**, 77–80 (2018).
- [191] P. Mackonis, *Development of a high peak power laser based on solid-state, parametric and stimulated Raman amplifiers* (Vilnius university, 2022).
- [192] D. N. Schimpf, J. Rothhardt, J. Limpert, A. Tünnermann, and D. C. Hanna, Theoretical analysis of the gain bandwidth for noncollinear parametric amplification of ultrafast pulses, *J. Opt. Soc. Am. B* **24**(11), 2837–2846 (2007).
- [193] B. Trophème, B. Boulanger, and G. Mennerat, Phase-matching loci and angular acceptance of non-collinear optical parametric amplification, *Opt. Express* **20**(24), 26176–26183 (2012).
- [194] J. Moses, C. Manzoni, S.-W. Huang, G. Cerullo, and F. X. Kaertner, Temporal optimization of ultrabroadband high-energy OPCPA, *Opt. Express* **17**(7), 5540 (2009).



- [195] P. Wang, Y. Li, W. Li, H. Su, B. Shao, S. Li, C. Wang, D. Wang, R. Zhao, Y. Peng, Y. Leng, R. Li, and Z. Xu, 2.6 mJ/100 Hz CEP-stable near-single-cycle 4  $\mu\text{m}$  laser based on OPCPA and hollow-core fiber compression, *Opt. Lett.* **43**(9), 2197–2200 (2018).
- [196] D. Sanchez, M. Hemmer, M. Baudisch, S. L. Cousin, K. Zawilski, P. Schunemann, O. Chalus, C. Simon-Boisson, and J. Biegert, 7  $\mu\text{m}$ , ultrafast, sub-millijoule-level mid-infrared optical parametric chirped pulse amplifier pumped at 2  $\mu\text{m}$ , *Optica* **3**(2), 147–150 (2016).
- [197] N. Bigler, J. Pupeikis, S. Hrisafov, L. Gallmann, C. R. Phillips, and U. Keller, High-power OPCPA generating 1.7 cycle pulses at 2.5  $\mu\text{m}$ , *Opt. Express* **26**(20), 26750–26757 (2018).
- [198] D. Milam, Review and assessment of measured values of the nonlinear refractive-index coefficient of fused silica, *Appl. Opt.* **37**(3), 546–550 (1998).
- [199] P. Tournois, Acousto-optic programmable dispersive filter for adaptive compensation of group delay time dispersion in laser systems, *Opt. Commun.* **140**(4–6), 245–249 (1997).
- [200] F. Verluise, V. Laude, Z. Cheng, Ch. Spielmann, and P. Tournois, Amplitude and phase control of ultrashort pulses by use of an acousto-optic programmable dispersive filter: pulse compression and shaping, *Opt Lett* **25**(8), 575–577 (2000).
- [201] S. L. Chin, H. L. Xu, Q. Luo, F. Théberge, W. Liu, J. F. Daigle, Y. Kamali, P. T. Simard, J. Bernhardt, S. A. Hosseini, M. Sharifi, G. Méjean, A. Azarm, C. Marceau, O. Kosareva, V. P. Kandidov, N. Aközbek, A. Becker, G. Roy, P. Mathieu, J. R. Simard, M. Châteauneuf, and J. Dubois, Filamentation “remote” sensing of chemical and biological agents/pollutants using only one femtosecond laser source, *Appl. Phys. B* **95**(1), 1–12 (2009).
- [202] L. Bergé, S. Skupin, R. Nuter, J. Kasparian, and J. P. Wolf, Ultrashort filaments of light in weakly ionized, optically transparent media, *Rep. Prog. Phys.* **70**(10), 1633–1713 (2007).
- [203] F. Silva, D. R. Austin, A. Thai, M. Baudisch, M. Hemmer, D. Faccio, A. Couairon, and J. Biegert, Multi-octave supercontinuum generation from mid-infrared filamentation in a bulk crystal, *Nat. Commun.* **3**(1), 807 (2012).
- [204] S. Cheng, G. Chatterjee, F. Tellkamp, A. Ruehl, and R. J. D. Miller, Multi-octave supercontinuum generation in YAG pumped by mid-infrared, multi-picosecond pulses, *Opt. Lett.* **43**(18), 4329–4332 (2018).

- [205] S. H. Nam, G. C. Nagar, D. Dempsey, O. Novák, B. Shim, and K. H. Hong, Multi-octave-spanning supercontinuum generation through high-energy laser filaments in YAG and ZnSe pumped by a 2.4  $\mu\text{m}$  femtosecond Cr:ZnSe laser, *High Power Laser Sci. Eng.* **9**, e12 (2021).
- [206] M. Neuhaus, H. Fuest, M. Seeger, J. Schötz, M. Trubetskov, P. Russbueldt, H. D. Hoffmann, E. Riedle, Zs. Major, V. Pervak, M. F. Kling, and P. Wnuk, 10 W CEP-stable few-cycle source at 2  $\mu\text{m}$  with 100 kHz repetition rate, *Opt. Express* **26**(13), 16074–16085 (2018).
- [207] E. P. Perillo, J. W. Jarrett, Y.-L. Liu, A. Hassan, D. C. Fernée, J. R. Goldak, A. Bonteanu, D. J. Spence, H.-C. Yeh, and A. K. Dunn, Two-color multiphoton in vivo imaging with a femtosecond diamond Raman laser, *Light Sci. Appl.* **6**(11), e17095–e17095 (2017).
- [208] N. G. Horton, K. Wang, D. Kobat, C. G. Clark, F. W. Wise, C. B. Schaffer, and C. Xu, In vivo three-photon microscopy of subcortical structures within an intact mouse brain, *Nat. Photonics* **7**(3), 205–209 (2013).
- [209] D. Kobat, N. G. Horton, and C. Xu, In vivo two-photon microscopy to 1.6-mm depth in mouse cortex, *J. Biomed Opt.* **16**(10), 106014–106014 (2011).
- [210] M.-C. Chen, P. Arpin, T. Popmintchev, M. Gerrity, B. Zhang, M. Seaberg, D. Popmintchev, M. M. Murnane, and H. C. Kapteyn, Bright, Coherent, Ultrafast Soft X-Ray Harmonics Spanning the Water Window from a Tabletop Light Source, *Phys. Rev. Lett.* **105**(17), 173901 (2010).
- [211] C. Vicario, A. V. Ovchinnikov, S. I. Ashitkov, M. B. Agranat, V. E. Fortov, and C. P. Hauri, Generation of 0.9-mJ THz pulses in DSTMS pumped by a Cr:Mg<sub>2</sub>SiO<sub>4</sub> laser, *Opt. Lett.* **39**(23), 6632–6635 (2014).
- [212] D. V. Petrov, I. I. Matrosov, A. R. Zaripov, and A. S. Maznoy, Effects of pressure and composition on Raman spectra of CO-H<sub>2</sub>-CO<sub>2</sub>-CH<sub>4</sub> mixtures, *Spectrochim Acta A: Mol. Biomol. Spectrosc.* **215**, 363–370 (2019).
- [213] X. Cai, M. Xu, Y. Jia, J. Liu, P. Wang, Y. Chen, B. Gai, Y. Tan, H. Cai, and J. Guo, Stimulated vibrational–rotational Raman scattering of hydrogen pumped at a 1064-nm laser, *Appl. Opt.* **62**(5), 1274–1278 (2023).
- [214] Y. Cui, W. Huang, Z. Li, Z. Zhou, and Z. Wang, High-efficiency laser wavelength conversion in deuterium-filled hollow-core photonic

- crystal fiber by rotational stimulated Raman scattering, *Opt. Express* **27**(21), 30396–30404 (2019).
- [215] D. D. Yavuz, D. R. Walker, M. Y. Shverdin, G. Y. Yin, and S. E. Harris, Quasiperiodic Raman Technique for Ultrashort Pulse Generation, *Phys. Rev. Lett.* **91**(23), 233602 (2003).
- [216] A. M. Rodin and A. S. Dementev, Development of a 2-color laser based on high-efficiency Raman amplification for multicolor holography, *Sixth International Symposium on Display Holography* (SPIE, 1998), pp. 211–217.
- [217] R. W. Minck, E. E. Hagenlocker, and W. G. Rado, Stimulated Pure Rotational Raman Scattering in Deuterium, *Phys. Rev. Lett.* **17**(5), 229–231 (1966).
- [218] V. B. Morozov, A. N. Olenin, and V. G. Tunkin, Transformation of strong picosecond pulses in radiation with an extended quasirotational spectrum during self-focusing in high-pressure hydrogen, *J. Exp. Theor. Phys.* **88**(2), 263–271 (1999).
- [219] H. Kawano, Y. Hirakawa, and T. Imasaka, Generation of high-order rotational lines in hydrogen by four-wave Raman mixing in the femtosecond regime, *J. Quantum Electron.* **34**(2), 260–268 (1998).
- [220] M. E. Thomas, S. K. Andersson, T. M. Cotter, and K. T. Constantikes, Infrared properties of polycrystalline magnesium fluoride, *Infrared Phys. Technol.* **39**(4), 213–222 (1998).
- [221] M. J. Dodge, Refractive properties of magnesium fluoride, *Appl. Opt.* **23**(12), 1980–1985 (1984).
- [222] H. Moriwaki, S. Wada, H. Tashiro, K. Toyoda, A. Kasai, and A. Nakamura, Wavelength conversion of quadrupled Nd:YAG laser radiation to the vacuum ultraviolet by anti-Stokes stimulated Raman scattering, *J. Appl. Phys.* **74**(4), 2175–2179 (1993).
- [223] J. Jang and R. M. Stratt, Dephasing of individual rotational states in liquids, *J. Chem. Phys.* **113**(24), 11212–11221 (2000).
- [224] G. V. Venkin, Y. A. Il'inskiĭ, and G. M. Mikheev, Influence of the polarization of radiation on the energy characteristics and threshold of stimulated Raman scattering due to rotational transitions, *Sov. J. Quantum Electron.* **15**(3), 395–397 (1985).
- [225] C. T. Hsieh, N. D. Foltz, and C. W. Cho, Production of the stimulated Raman lines in H<sub>2</sub> gas with a focused laser beam, *J. Opt. Soc. Am.* **64**(2), 202–205 (1974).
- [226] F. Benabid, G. Bouwmans, J. C. Knight, P. St. J. Russell, and F. Couny, Ultrahigh efficiency laser wavelength conversion in a gas-filled hollow core photonic crystal fiber by pure stimulated rotational

- Raman scattering in molecular hydrogen, *Phys. Rev. Lett.* **93**(12), 123903 (2004).
- [227] D. C. Hanna, D. J. Pointer, and D. J. Pratt, Stimulated Raman scattering of picosecond light pulses in hydrogen, deuterium, and methane, *J. Quantum Electron.* **22**(2), 332–336 (1986).
- [228] Á. Börzsönyi, Z. Heiner, A. P. Kovács, M. P. Kalashnikov, and K. Osvay, Measurement of pressure dependent nonlinear refractive index of inert gases, *Opt. Express* **18**(25), 25847–25854 (2010).
- [229] J. Zheng and M. Katsuragawa, Freely designable optical frequency conversion in Raman-resonant four-wave-mixing process, *Sci. Rep.* **5**(1), 8874 (2015).
- [230] K. R. Pandiri, T. Suzuki, A. Suda, K. Midorikawa, and M. Katsuragawa, Line-by-line control of 10-THz-frequency-spacing Raman sidebands, *Opt. Express* **18**(2), 732–739 (2010).
- [231] A. V. Sokolov, D. R. Walker, D. D. Yavuz, G. Y. Yin, and S. E. Harris, Femtosecond Light Source for Phase-Controlled Multiphoton Ionization, *Phys. Rev. Lett.* **87**(3), 033402 (2001).
- [232] I. V. Mochalov, Laser and nonlinear properties of the potassium gadolinium tungstate laser crystal  $\text{KGd}(\text{WO}_4)_2:\text{Nd}^{3+}$ -(KGW:Nd), *Opt. Eng.* **36**(6), 1660–1669 (1997).
- [233] A. A. Kaminskii, H. J. Eichler, K. Ueda, N. V. Klassen, B. S. Redkin, L. E. Li, J. Findeisen, D. Jaque, J. García-Sole, J. Fernández, and R. Balda, Properties of  $\text{Nd}^{3+}$ -doped and undoped tetragonal  $\text{PbWO}_4$ ,  $\text{NaY}(\text{WO}_4)_2$ ,  $\text{CaWO}_4$ , and undoped monoclinic  $\text{ZnWO}_4$  and  $\text{CdWO}_4$  as laser-active and stimulated Raman scattering-active crystals, *Appl. Opt.* **38**(21), 4533–4547 (1999).
- [234] J. Jakutis-Neto, J. Lin, N. U. Wetter, and H. Pask, Continuous-wave Watt-level Nd:YLF/KGW Raman laser operating at near-IR, yellow and lime-green wavelengths, *Opt. Express* **20**(9), 9841–9850 (2012).
- [235] W. H. Lowdermilk and G. I. Kachen, Coherent transient Raman pulse propagation, *Opt. Commun.* **18**(1), 68–69 (1976).
- [236] N. Daher, X. Délen, F. Guichard, M. Hanna, and P. Georges, Raman wavelength conversion in a multipass cell, *Opt. Lett.* **46**(14), 3380–3383 (2021).
- [237] V. P. Kalosha and J. Herrmann, Pulse compression without chirp control and frequency detuning by high-order coherent Raman scattering in impulsively excited media, *Opt. Lett.* **26**(7), 456–458 (2001).
- [238] A. Nazarkin, G. Korn, M. Wittmann, and T. Elsaesser, Generation of multiple phase-locked Stokes and anti-Stokes components in an

- impulsively excited Raman medium, *Phys. Rev. Lett.* **83**(13), 2560–2563 (1999).
- [239] Y.-X. Yan, E. B. Gamble, and K. A. Nelson, Impulsive stimulated scattering: General importance in femtosecond laser pulse interactions with matter, and spectroscopic applications, *J. Chem. Phys.* **83**(11), 5391–5399 (1985).
- [240] J. Schoetz, Z. Wang, E. Pisanty, M. Lewenstein, M. F. Kling, and M. F. Ciappina, Perspective on petahertz electronics and attosecond nanoscopy, *ACS Photonics* **6**(12), 3057–3069 (2019).
- [241] J. Tate, T. Augustine, H. G. Muller, P. Salières, P. Agostini, and L. F. DiMauro, Scaling of wave-packet dynamics in an intense midinfrared field, *Phys. Rev. Lett.* **98**(1), 013901 (2007).
- [242] G. Cirimi, C. Manzoni, D. Brida, S. De Silvestri, and G. Cerullo, Carrier-envelope phase stable, few-optical-cycle pulses tunable from visible to near IR, *J. Opt. Soc. Am.* **25**(7), B62–B69 (2008).
- [243] H. Çankaya, A.-L. Calendron, C. Zhou, S.-H. Chia, O. D. Mücke, G. Cirimi, and F. X. Kärtner, 40- $\mu$ J passively CEP-stable seed source for ytterbium-based high-energy optical waveform synthesizers, *Opt. Express* **24**(22), 25169–25180 (2016).
- [244] G. I. Kachen and W. H. Lowdermilk, Self-induced gain and loss modulation in coherent, transient Raman pulse propagation, *Phys. Rev.* **14**(4), 1472–1474 (1976).
- [245] T. T. Basiev, P. G. Zverev, A. Ya. Karasik, V. V. Osiko, A. A. Sobol, and D. S. Chunaev, Picosecond stimulated Raman scattering in crystals, *J. Exp. Theor. Phys.* **99**(5), 934–941 (2004).
- [246] A. Aboumajd, H. Berger, and R. Saint-Loup, Analysis of the Raman spectrum of SF<sub>6</sub>, *J. Mol. Spectrosc.* **78**(3), 486–492 (1979).
- [247] K. Jamshidi-Ghaleh and H. Masalehdan, Modeling of nonlinear responses in BK7 glass under irradiation of femtosecond laser pulses, *Opt. Quantum Electron.* **41**(1), 47–53 (2009).
- [248] X. Guo, Y. Leng, Y. Li, X. Zou, J. Lu, W. Li, X. Lu, Y. Xu, Y. Liu, and R. Li, Experimental and numerical study on chirped transient stimulated Raman scattering in dispersive medium, *Opt. Commun.* **351**, 85–90 (2015).
- [249] A. G. Papashvili, Y. A. Kochukov, D. P. Tereshchenko, S. N. Smetanin, P. D. Kharitonova, V. E. Shukshin, E. E. Dunaeva, I. S. Voronina, and L. I. Ivleva, Highly transient stimulated Raman scattering in SrMoO<sub>4</sub> under ultrafast laser pumping with a controllable chirp, *Opt. Lett.* **48**(17), 4528–4531 (2023).

- [250] E. C. Welch, S. Ya. Tochitsky, J. J. Pigeon, and C. Joshi, Long-wave infrared picosecond parametric amplifier based on Raman shifter technology, *Opt. Express* **26**(5), 5154–5163 (2018).
- [251] R. Trebino, R. Jafari, S. A. Akturk, P. Bowlan, Z. Guang, P. Zhu, E. Escoto, and G. Steinmeyer, Highly reliable measurement of ultrashort laser pulses, *J. Appl. Phys.* **128**(17), (2020).
- [252] Y.-H. Chen, J. Moses, and F. Wise, Femtosecond long-wave-infrared generation in hydrogen-filled hollow-core fiber, *J. Opt. Soc. Am. B* **40**(4), 796–806 (2023).
- [253] X. L. Cai, C. H. Zhou, D. J. Zhou, J. B. Liu, J. W. Guo, and L. Gui, H<sub>2</sub> stimulated Raman scattering in a multi-pass cell with a Herriott configuration, *Chin. Phys. Lett.* **32**(11), 114207 (2015).
- [254] D. Liu, X. Cai, Z. Li, X. Xia, D. Zhou, G. Li, H. Cai, J. Guo, and Y. Jin, The threshold reduction of SRS in deuterium by multi-pass configuration, *Opt Commun* **379**, 36–40 (2016).
- [255] I. Jovanovic, G. Xu, and S. Wandel, Mid-infrared laser system development for dielectric laser accelerators, *Phys. Procedia.* **52**, 68–74 (2014).
- [256] H. R. Reiss, Limits on tunneling theories of strong-field ionization, *Phys. Rev. Lett.* **101**(4), 043002 (2008).
- [257] B. M. Walsh, H. R. Lee, and N. P. Barnes, Mid infrared lasers for remote sensing applications, *J. Lumin.* **169**, 400–405 (2016).
- [258] S. V. Yakovlev, O. A. Romanovskii, S. A. Sadovnikov, D. A. Tuzhilkin, A. A. Nevzorov, O. V. Kharchenko, and N. S. Kravtsova, Mobile mid-infrared differential absorption lidar for methane monitoring in the atmosphere: Calibration and first in situ tests, *Results Opt.* **8**, 100233 (2022).
- [259] K. V. Kepesidis, M. Bozic-Iven, M. Huber, N. Abdel-Aziz, S. Kullab, A. Abdelwarith, A. Al Diab, M. Al Ghamdi, M. A. Hilal, M. R. K. Bahadoor, A. Sharma, F. Dabouz, M. Arafah, A. M. Azzeer, F. Krausz, K. Alsaleh, M. Zigman, and J.-M. Nabholz, Breast-cancer detection using blood-based infrared molecular fingerprints, *BMC Cancer* **21**(1), 1287 (2021).
- [260] F. Rotermund, V. Petrov, and F. Noack, Difference-frequency generation of intense femtosecond pulses in the mid-IR (4–12  $\mu\text{m}$ ) using HgGa<sub>2</sub>S<sub>4</sub> and AgGaS<sub>2</sub>, *Opt. Commun.* **185**(1–3), 177–183 (2000).
- [261] F. Junginger, A. Sell, O. Schubert, B. Mayer, D. Brida, M. Marangoni, G. Cerullo, A. Leitenstorfer, and R. Huber, Single-cycle multiterahertz

- transients with peak fields above 10 MV/cm, *Opt. Lett.* **35**(15), 2645–2647 (2010).
- [262] Z. Heiner, V. Petrov, V. L. Panyutin, V. V. Badikov, K. Kato, K. Miyata, and M. Mero, Efficient generation of few-cycle pulses beyond 10  $\mu\text{m}$  from an optical parametric amplifier pumped by a 1- $\mu\text{m}$  laser system, *Sci. Rep.* **12**(1), 5082 (2022).
- [263] P. Fuertjes, M. Bock, L. von Grafenstein, D. Ueberschaer, U. Griebner, and T. Elsaesser, Few-cycle 65- $\mu\text{J}$  pulses at 11.4  $\mu\text{m}$  for ultrafast nonlinear longwave-infrared spectroscopy, *Optica* **9**(11), 1303–1306 (2022).
- [264] V. Leshchenko, S. Li, P. Agostini, and L. F. DiMauro, Sub-two-cycle gigawatt-peak-power LWIR OPA for ultrafast nonlinear spectroscopy of condensed state materials, *Opt. Lett.* **48**(19), 4949–4952 (2023).
- [265] Z. Zhu, Y. Liu, J. Ye, J. Tian, T. Wan, J. Bai, Y. Zheng, R. Tan, Z. Li, and X. Su, Gain Measurement of ZnGeP<sub>2</sub> Optical Parametric Oscillator Pulses in a High-Pressure CO<sub>2</sub> Amplifier, *Photonics* **11**(2), (2024).
- [266] H. Huang, X. Xiao, M. Burger, J. Nees, and I. Jovanovic, Ultra-broadband long-wave-infrared pulse production using a chirped-pulse difference-frequency generation, *Opt. Lett.* **47**(13), 3159–3162 (2022).
- [267] B.-H. Chen, E. Wittmann, Y. Morimoto, P. Baum, and E. Riedle, Octave-spanning single-cycle middle-infrared generation through optical parametric amplification in LiGaS<sub>2</sub>, *Opt. Express* **27**(15), 21306–21318 (2019).
- [268] S. Vasilyev, I. S. Moskalev, V. O. Smolski, J. M. Peppers, M. Mirov, A. V. Muraviev, K. Zawilski, P. G. Schunemann, S. B. Mirov, K. L. Vodopyanov, and V. P. Gapontsev, Super-octave longwave mid-infrared coherent transients produced by optical rectification of few-cycle 2.5- $\mu\text{m}$  pulses, *Optica* **6**(1), 111–114 (2019).

## CURRICULUM VITAE

<b>Vardas</b>	Augustinas
<b>Pavardė</b>	Petrulėnas
<b>Gimimo data</b>	1995-04-27
<b>El. Paštas</b>	augustinas.petrulenas@ftmc.lt
<b>Išsilavinimas</b>	2010-2014 Žirmūnų gimnazija, Vilnius 2014-2018 Vilniaus universitetas, Fizikos fakultetas. <i>Bakalauro laipsnis</i> 2018-2020 Vilniaus universitetas, Fizikos fakultetas <i>Magistro laipsnis</i> 2020-2024 Fizinių ir technologijų mokslų centras <i>Doktorantūros studijos</i>
<b>Darbo patirtis</b>	2016-2018 Technikas, <i>Fizinių ir technologijos mokslų centras, Kieto kūno lazerių laboratorija</i> 2018-2023 Inžinierius, <i>Fizinių ir technologijos mokslų centras, Kieto kūno lazerių laboratorija</i> 2023-2025 Jaunesnysis mokslo darbuotojas, <i>Fizinių ir technologijos mokslų centras, Kieto kūno lazerių laboratorija</i>



## UŽRAŠAMS / NOTES

## UŽRAŠAMS / NOTES

## UŽRAŠAMS / NOTES

Vilniaus universiteto leidykla  
Saulėtekio al. 9, III rūmai, LT-10222 Vilnius  
El. p. [info@leidykla.vu.lt](mailto:info@leidykla.vu.lt), [www.leidykla.vu.lt](http://www.leidykla.vu.lt)  
[bookshop.vu.lt](http://bookshop.vu.lt), [journals.vu.lt](http://journals.vu.lt)  
Tiražas 20 egz.